



POLITECNICO
MILANO 1863

**DIPARTIMENTO DI SCIENZE
E TECNOLOGIE AEROSPAZIALI**

**Comprehensive Design Methodology for Metal Aeronautical
Components Produced by Additive Manufacturing**

Ricardo João Dias Ferreira

Thesis to obtain the Master of Science Degree in

Aeronautical Engineering

Supervisor: Prof. Antonio Mattia Grande

Co-supervisor(s): Prof. Giuseppe Sala

Prof. José Miranda Guedes

April 2022

Sommario

Lo scopo di questa tesi è la introduzione completa all'applicazione di una metodologia di progettazione guidata da *Design for Additive Manufacturing* (DfAM) ai componenti aeronautici attraverso una simulazione del processo di *Additive Manufacturing* (AM), nonché lo sviluppo di una metodologia di progettazione relativa alla all'ottimizzazione della topologia e forma, utilizzando soluzioni commerciali, come Abaqus Tosca. La tesi inizia con uno studio sull'ottimizzazione strutturale e la simulazione del processo di AM, e la sua teoria sottostante. Inoltre, l'implementazione del nuovo algoritmo MIMP (*Mass Interpolation Material Penalization*) viene esplorata e confrontata con l'algoritmo SIMP (*Solid Isotropic Material with Penalization*), concludendo la sua efficacia nel trattare i problemi di ottimizzazione della topologia contenenti variabili di progettazione relative alla massa, come risposta di frequenza, raggiungendo la convergenza dove il SIMP fallisce. Inoltre, viene eseguita una simulazione di AM di *benchmarking* al fine di definire una linea guida generale e una serie di strumenti necessari per implementare correttamente una simulazione a bassa risoluzione in Abaqus. I risultati sono in linea con quelli messi a disposizione dal *National Institute of Standards and Technology* (NIST), convalidando quindi la metodologia. La tesi discute inoltre la definizione di un'accurata analisi statica dell'attuale componente utilizzata da Leonardo, dato i suoi risultati influenzano direttamente i requisiti di progettazione, e la corretta definizione della ottimizzazione strutturale in termini di condizioni di carico e contorno. L'ottimizzazione strutturale è definita come un'ottimizzazione della topologia di minimizzazione del volume, per soddisfare l'evoluzione della funzione oggettiva a vincoli concreti di progettazione ingegneristica. SIMP non riesce a raggiungere la convergenza in presenza di vincoli di risposta di frequenza, mentre MIMP converge a un design ben connesso, che seguendo la sua interpretazione di progetto con poliNURBs in Altair Inspire, si traduce in una riduzione di peso del 2,29% rispetto alla componente corrente. L'ulteriore implementazione di un'ottimizzazione della forma per affrontare i requisiti di progettazione dello stress consente di ottenere l'omogeneizzazione dello stress e un peso inferiore, con una notevole riduzione del peso del 5,12%. Infine, il processo di simulazione AM viene applicato a una versione scalata del progetto finale, al fine di valutare sia la stampabilità della parte stessa, sia l'implementazione degli strumenti chiave per definire la simulazione AM. La distorsione della parte appare nelle regioni previste con materiale sporgente, dando ulteriore fiducia ai risultati.

Parole-chiave: Progettazione per manifattura additiva, simulazione di manifattura additiva, ottimizzazione strutturale, minimizzazione del volume, interpolazione di massa penalizzazione del materiale.

Abstract

This thesis aims to serve as a comprehensive introduction to the application of a Design for Additive Manufacturing (DfAM) driven design methodology to aeronautical components through an additive manufacturing process simulation, as well as the development of a design methodology concerning topology and shape optimization utilizing commercial solutions, namely SIMULIA Tosca. The thesis begins with a study on both structural optimization and additive manufacturing process simulation, and its underlying theory. Additionally, the implementation of the new Mass Interpolation Material Penalization (MIMP) is explored, and compared with the widely used Solid Isotropic Material with penalization (SIMP) algorithm, concluding its efficacy in dealing with topology optimization problems containing mass related, frequency response design variables, achieving convergence where SIMP fails to. Furthermore, a benchmarking additive manufacturing simulation is performed in order to define a general guideline and set of tools needed to properly implement a low-resolution additive manufacturing simulation in Abaqus. The results fall in line with the ones made available by the National Institute of Standards and Technology (NIST), therefore validating the methodology. The thesis further discusses the definition of an accurate static analysis of the current bracket in use by Leonardo, as its results directly influence design requirements, and the correct definition of the structural optimization task in terms of boundary and loading conditions. The structural optimization is started by a volume minimization topology optimization, as it allows to cater the objective function evolution to concrete engineering design constraints. SIMP fails to achieve convergence under the presence of frequency response constraints, while MIMP converges to a well-connected design, which following its design interpretation with polyNURBs in Altair Inspire, results in a weight reduction of 2.29% compared to the current component. Further implementation of a shape optimization to tackle stress design requirements allows to achieve stress homogenization and a lower weight, resulting in a considerable 5.12% weight reduction. Finally, the AM simulation process is applied to a scaled version of the final design, in order to both assess the printability of the part itself, as well as the implementation of the key tools to define the AM simulation. Distortion of the part appears at expected regions with overhanging material, further giving the results confidence.

Keywords: Design for additive manufacturing, additive manufacturing simulation, structural optimization, volume minimization, mass interpolation material penalization.

Contents

- Sommario iii
- Abstract v
- List of Tables xv
- List of Figures xix
- Nomenclature xxv

- 1 Introduction 1**
- 1.1 Motivation 1
 - 1.1.1 Clean Sky Programme 2
 - 1.1.2 AMATHO 2
- 1.2 Objectives and Deliverables 2
- 1.3 Thesis Outline 3

- 2 Problem Definition 5**
- 2.1 Recent component redesign 6
- 2.2 Design Restraints 7
- 2.3 Mounting interfaces 7
- 2.4 Hydraulic feed 8
- 2.5 Test loads 8
 - 2.5.1 Servo-actuator loads 9
 - 2.5.1.1 Static strength 9
 - 2.5.1.2 Fatigue life 10
 - 2.5.2 Pressure loads 10
- 2.6 Stiffness and natural frequency requirements 11
 - 2.6.1 Servo-actuator axial stiffness 11
 - 2.6.2 Mounting bosses stiffness 11
 - 2.6.3 First natural frequency 11
- 2.7 Project requirement summary 12

- 3 Structural Optimization Overview 15**
- 3.1 History 15
- 3.2 Introduction to Structural Optimization 16

3.2.1	General Mathematical Formulation	16
3.2.2	Types of Structural Optimization Procedures	17
3.3	Topology Optimization	17
3.3.1	Minimum Compliance Problem	18
3.3.2	Interpolation Methods	19
3.3.2.1	Solid Isotropic Material with Penalization - SIMP	19
3.3.2.2	Mass Interpolation Material Penalization - MIMP	20
3.3.3	Sensitivity Analysis and the Method of Moving Asymptotes	20
3.3.3.1	Method of Moving Asymptotes	21
3.3.3.2	Sensitivity Analysis	21
3.3.4	Volume Minimization Problem	22
3.3.5	Numerical difficulties	23
3.3.5.1	Mesh dependence	23
3.3.5.2	Checkerboarding	23
3.3.5.3	Local optima	24
3.3.6	Filtering techniques	24
3.3.6.1	Sensitivity filtering	24
3.3.6.2	Design Variables Filtering	25
3.4	Shape optimization	25
3.4.1	Multi-objective optimization formulation	26
3.4.2	Shape optimization problem formulation	26
4	Additive manufacturing overview	27
4.1	History	27
4.2	Additive Manufacturing Advantages and Disadvantages	28
4.2.1	Advantages	28
4.2.2	Disadvantages	28
4.3	Additive manufacturing technologies	29
4.3.1	Powder-based Additive Manufacturing Technologies	30
4.3.1.1	Powder-injection Based Additive Manufacturing Technologies	30
4.3.1.2	Powder-bed Based Additive Manufacturing Technologies	31
4.3.2	Support Structures	31
5	Design for Additive Manufacturing overview	33
5.1	Topology Optimisation and Additive Manufacturing	33
5.1.1	Directional Constraints	34
5.1.1.1	Support Structures	34
5.1.1.2	Anisotropy	34
5.1.1.3	Distortion and Residual Stresses	35
5.1.2	Non-Directional Constraints	36

5.1.2.1	Powder Enclosure/Cavity Constraint	36
5.1.2.2	Member/Feature Size Control	37
5.2	Additive Manufacturing Simulation	37
5.2.1	Process Parameters Optimisation	37
5.2.2	Thermal-Mechanical-Metallurgical Coupling Problem	37
5.2.3	Transient Thermal Problem Formulation	38
5.2.4	Heat Source Model	39
5.2.4.1	Concentrated Moving Heat Source Model	39
5.2.4.2	Uniform Heat Source Model	39
5.2.4.3	Goldak Heat Source Model	39
5.2.5	Mechanical Problem Formulation for Residual Stress	39
5.3	Design Process Approach	41
5.3.1	Current Design Process Approach	41
5.3.2	DfAM Guidelines in the Design Process Approach	42
6	Additive Manufacturing Thermal-mechanical Simulation Methodology	44
6.1	AM Process Simulation Workflow	44
6.2	Toolpath-Mesh Intersection	44
6.2.1	Event Series	45
6.2.2	Material Deposition and Progressive Element Activation	45
6.2.3	Moving Heat Flux and Progressive Heating	46
6.3	Abaqus user subroutines and AM modeler plug-in	46
6.3.1	User subroutines	46
6.3.2	AM modeler plug-in	47
6.3.2.1	Data setup	47
6.3.2.2	Model setup	49
6.3.2.3	Simulation setup	49
6.4	AM Simulation Geometry Pre-Processing	49
6.4.1	Printing support design and generation	49
6.4.2	Voxelization and voxel-based meshing	50
6.4.3	Part slicing and scan path information	51
6.4.4	LSR file analysis and translation to INP file format	52
6.5	Low Resolution Thermo-Mechanical Simulation in Abaqus	53
6.5.1	Annealing effects simulation	53
6.5.2	Thermal simulation definition	53
6.5.2.1	Initial and boundary conditions	54
6.5.2.2	Cooling effects	54
6.5.2.3	Job Definition	55
6.5.3	Structural simulation definition	56

6.5.3.1	Initial and boundary conditions	56
6.5.3.2	Job definition	56
6.5.3.3	Support removal	57
6.5.3.4	Post-processing simulation	58
6.6	Benchmarking simulation	58
6.6.1	Part geometry and mesh design	58
6.6.2	Material properties	59
6.6.3	Event series definition	60
6.6.4	Simulation definition in Abaqus	62
6.6.5	Results and discussion	62
6.6.5.1	Time increment	62
6.6.5.2	Residual elastic strain and distortion	64
7	Static analysis and topology optimization implementation	66
7.1	Static strength analysis of the current bracket	66
7.1.1	Bracket assembly	66
7.1.1.1	Contact interaction	67
7.1.1.2	Load application	68
7.1.2	Test equipment and real model	69
7.1.2.1	Bolt and washer models	69
7.1.2.2	Mounting plate model	69
7.1.2.3	Real model assembly	70
7.1.2.4	Interactions	70
7.1.2.5	Preloading	72
7.1.2.6	Boundary condition selection	73
7.1.3	Simplified model	73
7.1.4	Meshing	74
7.1.4.1	Mesh convergence analysis	75
7.1.5	Materials	76
7.1.6	Comparative Results between Real and Simplified Models	78
7.2	Topology Optimization Implementation and Parameter Definition in Abaqus	80
7.2.1	Mesh Influence	80
7.2.2	Material Interpolation Scheme Comparison	81
7.2.2.1	Mesh influence	82
7.2.2.2	Frequency Design Response Influence	82
7.3	Design Interpretation and Conceptualization of Optimization Results	83
7.3.1	Geometry Smoothing	83
7.3.2	Interpretation of smoothed geometry	83

8	Topology optimization results	85
8.1	Topology optimization model preparation	85
8.1.1	Design requirements	85
8.1.2	Geometry and meshing	85
8.1.3	Materials	88
8.1.4	Boundary conditions and load cases	88
8.2	Topology optimization setup	89
8.2.1	Topology optimization task	89
8.2.2	Design responses definition	89
8.2.2.1	Volume	89
8.2.2.2	Axial stiffness	90
8.2.2.3	Eigenfrequency	90
8.2.2.4	Relative stiffness	90
8.2.2.5	Normal stiffness	91
8.2.3	Topology optimization objective and constraints definition	91
8.2.4	Topology optimization trial cases	92
8.3	SIMP and MIMP comparison trial cases	93
8.3.1	Trial case 1	93
8.3.1.1	Topology optimization results	94
8.3.1.2	Post-processing and design realization	94
8.3.1.3	Part validation	96
8.3.2	Trial case 2	97
8.3.2.1	Topology optimization results	97
8.3.2.2	Post-processing and design realization	98
8.3.2.3	Part validation	99
8.3.3	Trial case 3	99
8.3.3.1	Topology optimization results	99
8.3.3.2	Post-processing and design realization	101
8.3.3.3	Part validation	101
8.3.4	Trial case 4	102
8.3.4.1	Topology optimization results	103
8.3.4.2	Post-processing and design realization	103
8.3.4.3	Part validation	104
8.3.5	Comparison and discussion	104
8.4	Relative and normal stiffness constraint effects trial cases	106
8.4.1	Trial case 5	106
8.4.1.1	Topology optimization results	107
8.4.1.2	Post-processing and design realization	107
8.4.1.3	Part validation	108

8.4.2	Trial case 6	109
8.4.2.1	Topology optimization results	109
8.4.2.2	Post-processing and design realization	111
8.4.2.3	Part validation	111
8.4.3	Trial case 7	112
8.4.3.1	Topology optimization results	112
8.4.4	Comparison and discussion	112
8.5	Volume minimization and maximum minimization trial cases	114
8.5.1	Trial case 8	114
8.5.1.1	Topology optimization results	114
8.5.1.2	Post-processing and design realization	115
8.5.1.3	Part validation	115
8.5.2	Comparison discussion and conclusions	116
9	Shape optimization results	117
9.1	Shape optimization workflow	117
9.2	Shape optimization model preparation	117
9.2.1	Design requirements	117
9.2.2	Geometry and meshing	118
9.2.3	Materials	118
9.3	Shape optimization setup	118
9.3.1	Shape optimization task	118
9.4	Initial geometry results	119
9.5	Shape optimization results	120
9.5.1	Design iteration 1	121
9.5.2	Design iteration 2 - final design	122
9.5.3	Discussion and conclusions	124
10	Additive manufacturing simulation results	125
10.1	Geometry preparation	125
10.1.1	Support definition and voxelization	125
10.2	Model preparation	127
10.2.1	Material properties	127
10.2.2	Event series definition	128
10.2.3	Meshing	130
10.2.4	Thermal analysis definition	131
10.2.4.1	Initial and boundary conditions	131
10.2.4.2	Cooling effects	131
10.2.5	Structural analysis definition	131
10.2.5.1	Initial and boundary conditions	131

10.2.5.2 Support removal	132
10.3 Results and discussion	132
10.3.1 Structural simulation results	132
11 Conclusions	135
11.1 Future Work	137
Bibliography	139
A Event series Matlab script	145
B Topology optimization beam solutions	151
B.1 Mesh influence results	151
B.1.1 Mesh influence solution geometries	152
B.2 Material interpolation scheme comparison results	155
B.2.1 Mesh influence results	155
B.2.1.1 Mesh influence solution geometries	156
B.2.2 Frequency design response influence results	157
B.2.2.1 Frequency design response influence solution geometries	158

List of Tables

2.1	Static loads for axial load case 1.	9
2.2	Static loads for bending load case 2.	10
2.3	Fatigue loads.	10
4.1	AM technology classification based on [43–45].	30
6.1	Laser path event series format [10].	45
6.2	Recoater roller event series format.	45
6.3	LSR file format.	52
6.4	Iconel 625 material composition.	59
6.5	Iconel 625 thermal properties.	60
6.6	Iconel 625 mechanical properties.	60
6.7	Contour laser path properties.	60
6.8	Infill laser path properties.	60
6.9	Recoater roller and cooling parameters.	62
7.1	Linear elastic E4340 Alloy Steel properties.	69
7.2	Ti6Al4V ELI linear-elastic properties.	77
7.3	z-direction displacement results comparison.	78
7.4	Von Mises stress results comparison.	78
7.5	Computational time comparison.	80
8.1	Topology optimization load cases considered.	89
8.2	Trial case 1 topology optimization configuration.	93
8.3	Trial case 1 normalized axial stiffness results.	96
8.4	Trial case 1 normalized relative stiffness results.	97
8.5	Trial case 1 normalized normal stiffness results.	97
8.6	Trial case 2 topology optimization configuration.	97
8.7	Trial case 2 normalized axial stiffness results.	99
8.8	Trial case 2 normalized relative stiffness results.	100
8.9	Trial case 2 normalized normal stiffness results.	100
8.10	Trial case 3 topology optimization configuration.	100

8.11 Trial case 3 normalized axial stiffness results.	102
8.12 Trial case 3 normalized relative stiffness results.	102
8.13 Trial case 3 normalized normal stiffness results.	102
8.14 Trial case 4 topology optimization configuration.	102
8.15 Trial case 4 normalized axial stiffness results.	104
8.16 Trial case 4 normalized relative stiffness results.	105
8.17 Trial case 4 normalized normal stiffness results.	105
8.18 Trial case 5 topology optimization configuration.	107
8.19 Trial case 5 normalized axial stiffness results.	109
8.20 Trial case 5 normalized relative stiffness results.	110
8.21 Trial case 5 normalized normal stiffness results.	110
8.22 Trial case 6 topology optimization configuration.	110
8.23 Trial case 6 normalized axial stiffness results.	112
8.24 Trial case 6 normalized relative stiffness results.	112
8.25 Trial case 6 normalized normal stiffness results.	112
8.26 Trial case 7 topology optimization configuration.	113
8.27 Trial case 8 topology optimization configuration.	114
8.28 Trial case 8 normalized axial stiffness results.	116
8.29 Trial case 8 normalized relative stiffness results.	116
8.30 Trial case 8 normalized normal stiffness results.	116
9.1 Shape optimization configuration..	119
9.2 Normalized stress peak result from the initial geometry.	119
9.3 Shape optimization normalized stress objective evolution between cycles 0 (initial) and 10 (final).	120
9.4 Shape optimization design iteration 2 normalized axial stiffness results.	123
9.5 Shape optimization design iteration 2 normalized axial stiffness results.	123
9.6 Shape optimization design iteration 2 normalized axial stiffness results.	123
10.1 Ti-6Al-4V ELI material composition.	128
10.2 Ti-6Al-4V ELI thermal properties.	128
10.3 Ti-6Al-4V ELI mechanical properties.	128
10.4 Contour laser path properties.	128
10.5 Infill laser path properties.	128
10.6 Recoater roller and cooling parameters.	129
10.7 Elements used for both the thermal and the structural simulations, per bracket and sub- strate parts.	131
10.8 Process cooling parameters.	131
B.1 Tabular data of mesh influence on topology optimization of a cantilever beam results. . . .	151

B.2	Tabular data of mesh influence on topology optimization comparison between SIMP and MIMP interpolation schemes.	155
B.3	Tabular data of frequency design response influence on topology optimization comparison between SIMP and MIMP interpolation schemes.	157

List of Figures

1.1	Revenue passenger kilometers (RPK) historical evolution and forecast to the year 2042, based on both international and domestic flights [2].	1
2.1	Current component individual parts.	5
2.2	Optimization individual parts.	6
2.3	Redesigned component individual parts.	6
2.4	Mounting interfaces geometry.	8
2.5	Schematics of both load and center of mass application points, and direction of positive z-direction.	9
2.6	Singular cycle of the dynamic fatigue loads according to table 2.3.	10
2.7	Schematic of the servo-actuator axial stiffness requirement.	11
2.8	Schematic of the mounting bosses stiffness requirements, both relative and normal. . . .	12
3.1	Illustration of Galileo's cantilever beam, from which is understood that the load at the root increases with the square of the beam length [11].	15
3.2	Example of a Michell structure [12].	16
3.3	Examples of structural optimization types [15].	17
3.4	Arbitrary body definition [15].	18
3.5	SIMP interpolation technique penalization with respect to different p values (from 1 to 6). .	20
3.6	<i>Round Table Challenge results</i> [22].	20
3.7	Mesh dependence example on a beam. a) 2700, b) 4800, and c) 17200 elements. [15] .	23
3.8	Checkerboard problem example on a beam. a) Design envelope, b) 400 element solution, and c) 6400 element solution. [15]	24
3.9	Design variable filter representation [30].	25
4.1	Production of AM parts from independent service providers (in millions of dollars [37]). . . .	28
4.2	Economy of scale comparison between AM and traditional manufacturing methods [42]. .	29
4.3	Direct metal deposition device [47].	31
4.4	Selective laser sintering device [48].	32
4.5	Electron beam melting device [49].	32
5.1	Residual stress types and their variation [55].	35

5.2	Crack and distortion caused by residual stress [56].	36
5.3	Residual stress formation mechanisms [57].	36
5.4	Diagram showcasing the multiphysics nature of the AM process (as a thermal-mechanical- metallurgical problem) [41].	38
5.5	Goldak heat source [10].	39
5.6	Proposed design process workflow with DfAM considerations.	43
6.1	Toolpath-mesh intersection geometric options [10].	45
6.2	Schematic of two infinite lines intersecting an element at two different regions.	46
6.3	Create AM Model AM modeler Abaqus window.	47
6.4	Parameter and property table type windows in Abaqus.	48
6.5	Create table collection windows in Abaqus.	48
6.6	Event viewer example with a laser path.	49
6.7	Voxelization process example by [65].	50
6.8	Regionalisation examples.	52
6.9	LSR file example.	52
6.10	INP file example.	52
6.11	Cooling settings windows in Abaqus.	54
6.12	Schematic of partial element activation in an element [10].	55
6.13	Smoothing and temperature interval extension for several scale factors.	56
6.14	Boundary condition applied to the bottom surface of build plate, and the tie constraint interaction between it and the printing part.	57
6.15	STL geometry provided by NIST with four clear parts [63].	58
6.16	Dimensions and meshed geometries of the NIST bridge.	59
6.17	Iconel 625 thermal dependent properties.	61
6.18	Laser path example at a single layer in Autodesk Netfabb.	61
6.19	Layer of elements to be removed through a model change interaction.	62
6.20	Percentage difference of the temperature measured with a single time step per build phys- ical layer, with respect to the high-resolution temperature field. Results are linearly inter- polated over the surface area.	63
6.21	Percentage difference of the temperature measured with two time steps per build physical layer, with respect to the high-resolution temperature field. Results are linearly interpo- lated over the surface area.	63
6.22	Residual elastic strain in the x-direction.	64
6.23	Residual elastic strain in the z-direction.	64
6.24	Path z-direction strain measured at two different heights.	65
6.25	Deflection measured that the part's top ridges.	65
7.1	Connection between upper and lower manifolds through the use of six highlighted bolts.	66
7.2	Contact regions between upper and lower manifolds.	67

7.3	Connection between the load application point and the 6 mounting bosses.	68
7.4	Meshed bolt.	70
7.5	Meshed mounting plate.	70
7.6	Real model assembly.	71
7.7	Find contact pairs windows in Abaqus.	72
7.8	Detailed view of the contact interactions and properties needed for the bolt.	72
7.9	Bolt boundary conditions.	73
7.10	Mounting plate boundary conditions.	74
7.11	Bolt hole boundary conditions.	74
7.12	Connecting fillet boundary condition.	75
7.13	Assembly meshing for different element sizes.	76
7.14	Mesh sensitivity results.	77
7.15	Ti6Al4V ELI plastic properties as a stress strain curve.	77
7.16	Highlight of the path for the von Mises stress measurement.	79
7.17	Von Mises path stress results.	79
7.18	Part to be optimized.	81
7.19	Mesh influence results comparison between element types.	81
7.20	Part to be optimized.	82
7.21	Mesh influence results comparison between SIMP and MIMP.	82
7.22	Frequency design response influence results comparison.	83
7.23	Wrap tool example.	84
7.24	Quadrangulated mesh.	84
8.1	Optimization individual parts.	86
8.2	Hydraulic part.	86
8.3	Updated optimization individual parts.	87
8.4	Meshed topology optimization part.	87
8.5	Boundary conditions.	88
8.6	Edit design response window for the correct definition of the first natural frequency design response.	90
8.7	Schematic of the naming scheme used for both the relative stiffness pairs, and normal stiffness points. Only face 1 is showcased. Face 2 is to the right, and face 3 to the left. . .	91
8.8	Additional coordinate systems to aid the definition of the normal stiffness.	92
8.9	Trial case 1 convergence plot.	94
8.10	Trial case 1 normalized material property result.	94
8.11	Trial case 1 extracted STL mesh file.	95
8.12	Trial case 1 polyNURBS solid result.	95
8.13	Trial case 1 design interpretation result.	96
8.14	Trial case 2 convergence plot.	98

8.15 Trial case 2 normalized material property result.	98
8.16 Trial case 2 extracted STL mesh file.	98
8.17 Trial case 2 design interpretation result.	99
8.18 Trial case 3 convergence plot.	100
8.19 Trial case 3 normalized material property result.	101
8.20 Trial case 3 design interpretation result.	101
8.21 Trial case 4 normalized material property result.	103
8.22 Trial case 4 convergence plot.	103
8.23 Trial case 4 design interpretation result.	104
8.24 Updated bracket redesign.	106
8.25 Trial case 5 convergence plot.	107
8.26 Trial case 5 normalized material property result.	108
8.27 Trial case 4 extracted STL mesh file.	108
8.28 Trial case 5 extracted STL mesh file.	108
8.29 Trial case 5 design interpretation result.	109
8.30 Trial case 6 convergence plot.	110
8.31 Trial case 6 normalized material property result.	111
8.32 Trial case 6 design interpretation result.	111
8.33 Performance metric comparison between trial cases 4, 5, and 6, for both the relative and normal stiffness constraints. The lower the performance metric, the better the result.	113
8.34 Trial case 8 convergence plot.	114
8.35 Trial case 8 normalized material property result.	115
8.36 Trial case 8 design interpretation result.	115
9.1 Meshed shape optimization part.	118
9.2 Normalized stress field under both axial and bending 1 load cases of the initial geometry.	119
9.3 Shape optimization convergence plot.	120
9.4 Shape optimization results, namely the surface vector.	120
9.5 Normalized stress field under both axial and bending 1 load cases of the design iteration 1 geometry.	121
9.6 Highlight of the path for the von Mises stress measurement comparison between initial, and iteration 1 designs.	121
9.7 Normalized path von Mises stress results comparison between initial, and iteration 1 ge- ometries.	122
9.8 Normalized stress field under both axial and bending 1 load cases of the design iteration 2 geometry.	122
9.9 Normalized path von Mises stress results comparison between iteration 1, and iteration 2 geometries.	123
9.10 Showcase of the final design.	124

9.11 Isometric view of the final design.	124
10.1 Edited geometry to accommodate the AM printing process.	126
10.2 Support definition result in Autodesk Netfabb. In blue are highlighted the support structures.	126
10.3 Geometry voxelization process.	127
10.4 Voxel-based geometry.	127
10.5 Some aircrafts.	129
10.6 Laser path example at a single layer in Autodesk Netfabb.	130
10.7 Event series viewer example.	130
10.8 Displacement results of the AM process simulation applied to the bracket component. . .	132
10.9 Cross section view to highlight the contraction happening in the central cylindrical hydraulic system region.	133
10.10 Von mises stress results of the AM process simulation applied to the bracket component.	133
11.1 Von mises stress results comparison under proof bending 1 load case.	136
11.2 Displacement magnitude results comparison under proof bending 1 load case.	136
11.3 Z-direction displacement results comparison under proof bending 1 load case.	137
B.1 C3D8 resulting geometries.	152
B.2 C3D8 resulting geometries.	152
B.3 C3D8 resulting geometries.	153
B.4 C3D8 resulting geometries.	153
B.5 C3D8 resulting geometries.	154
B.6 SIMP mesh influence resulting geometries.	156
B.7 MIMP mesh influence resulting geometries.	157
B.8 SIMP frequency design response influence resulting geometries.	158
B.9 MIMP frequency design response influence resulting geometries.	159

Nomenclature

Abbreviations

3DP 3D printing.

AM Additive manufacturing.

cDLM Continuous digital light manufacturing.

CLIP Continuous liquid interface production.

DB SLA Dual beam stereolithography.

DIW Direct ink writing.

DLP Digital light processing.

EBAM Electron beam additive manufacturing.

EBM Electron-beam melting.

FDM Fused deposition modeling.

FE Finite element.

FFF Fused filament fabrication.

LENS Laser engineered net shaping.

LMD Laser metal deposition.

LOM Laminated object manufacturing.

MIMP Mass interpolation material penalization.

MMA Method of moving asymptotes.

OC Optimality criteria.

SHS Selective laser sintering.

SIMP Solid isotropic material with penalization.

SLA Stereolithography.

SLM Selective laser melting.

SLS Selective laser sintering.

UAM Ultrasonic additive manufacturing.

Chapter 1

Introduction

1.1 Motivation

The latest International Air Transport Association’s (IATA) 20-Year Air Passenger Forecast [1] reveals that air transport passenger numbers could double to 8.2 billion by 2037, with an anticipated 3.5% compound annual growth rate (CAGR) over the next two decades.

In 2019, the aviation sector was responsible for producing 915 million tonnes of CO₂ worldwide, accounting for 12% of all transportation emissions. With the expectation of passenger traffic doubling in the next 20 years, it is on the aeronautical community the duty and strive to pursue the improvement and creation of technology that safeguards the environment and the sustainability of the sector [2].

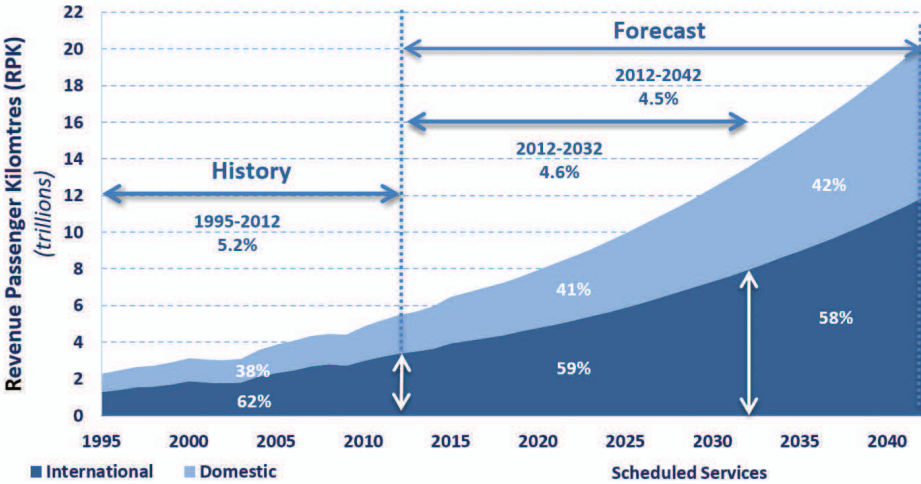


Figure 1.1: Revenue passenger kilometers (RPK) historical evolution and forecast to the year 2042, based on both international and domestic flights [2].

In an European long term effort to address the sustainability of this growth, the Advisory Council for Aeronautics Research in Europe (ACARE) sets in the "Flightpath 2050 - Europe’s Vision for Aviation" [3] a series of targets to be met by 2050. Taking into consideration as baseline a typical new aircraft in the year 2020, a subset of these goals are,

- 75% reduction in CO₂ emissions per passenger kilometre;
- 90% reduction in NO_x emissions;
- 65% reduction in perceived noise emission of flying aircraft.

1.1.1 Clean Sky Programme

Clean Sky launched in 2014, and represents the European Commission efforts to reach and aid the European aeronautical community achieve the Flightpath 2050 goals. By setting key public-private partnerships within this community, Clean Sky 2 allows these institutions to cooperate and develop break-through technology that will contribute to a more competitive and environmentally sustainable European aviation industry [4].

Clean Sky 2 is the new iteration of original programme, aiming at further improvement on the first iteration's foundation. By setting a more stringent set of goals and widening of the accepted initiatives, the programme aims at an acceleration of the technological progress seen in the sector. More concretely, some of the goals directly set by Clean Sky 2 are [4],

- Increase aircraft fuel efficiency, thus reducing CO₂ by between 20 to 30%;
- Reduce aircraft NO_x and noise emissions between 20 to 30% compared to "state-of-the-art" aircraft entering into service as from 2014.

Should be noted that other European programmes are contributing to helping achieve the Flightpath 2050 goals, such as the Single European Sky ATM Research (SESAR) Joint Undertaking, which works towards a more efficient Air Traffic Management (ATM).

1.1.2 AMATHO

Clean Sky's AMATHO (Additive MANufacturing Tilt-rotor HOusing) tackles directly the third goal set by Clear Sky 2. By taking advantage of the Additive Manufacturing potential, it aims at the design and manufacture of a gearbox housing to be utilized by Leonardo Helicopter's Next Generation Civil Tiltrotor (NGCTR). The integration of Additive Manufacturing in the design process opens to the door to reduced weight and optimized performance, saving resources during both manufacturing and flight time.

1.2 Objectives and Deliverables

This thesis aims to explore the potential of applying Design for Additive Manufacturing (DfAM) guidelines in the redesign of an aeronautical component, expanding the design validation process with a thermo-mechanical additive manufacturing (AM) process simulation. Several researches have been developed on the application of topology and shape optimization in a component design phase. For instance, [5] has studied the introduction of these design tools in early phases of a Volvo Cars component development process. With the advancements in AM technology and possibility to produce

complex shapes, these tools saw renewed interest, and integration into DfAM guidelines. While it is a recent research area, extensive investigation has been carried out to explore the potentials of structural optimization in AM components [6], as well as more novel design opportunities, such as design with microstructures [7]. The implementation of thermo-mechanical AM process simulation in the component design workflow has recently seen great interest, as residual stresses and distortion can compromise the quality of the printed component. However, due to the high computational cost of the simulation, research is mostly kept at an academic level [8, 9]. This thesis attempts to provide a proof of concept on the implementation of a thermo-mechanical AM process simulation in an industrial setting and concrete component, opening up the opportunity for broader integration and potential process optimization, which are out of the scope of the thesis.

Moreover, the component redesign process described and developed in this thesis serves as a general baseline procedure guideline for other additively manufactured aeronautical components developed by Leonardo, namely the novel tilt-rotor gearbox housing from the AMATHO project.

Given the recent increased interest in topology optimization and the development of new approaches, it is of extreme importance to understand them and the optimization driving parameters through their implementation in simple problems. For this purpose, Tosca Structure, a structural optimization technology integrated in Abaqus [10], is used. On the aeronautical component, the tool is responsible for offering conceptual designs that fulfil the performance requirements set by Leonardo, with the objective of minimizing the weight of it. It is also responsible for improving the resulting designs through shape optimization, or modification of the surface geometry. The objective is to conclude which optimization parameters provide better results, thus providing a final design proposal to be printed and tested.

To summarize, this project aims to:

- Define a redesign process workflow considering DfAM guidelines, such as structural optimization procedures, and the inclusion of AM process simulation in the design validation phase;
- Provide a good understanding of structural optimization parameters that best fit a redesign project on an aeronautical component with defined performance requirements;
- Implement a part-level AM process simulation to accurately predict residual stresses and distortion, and ultimately provide the required tools and workflow to properly setup the analysis and geometry;
- Analyse and compare different design solutions, providing Leonardo and Politecnico di Milano with the best result for printing and further testing.

1.3 Thesis Outline

This thesis is divided according to the following chapters:

- **Problem definition:** introduces the bracket, namely its current design, useful for comparison purposes and requirement definition. It also describes the project objectives and design requirements;

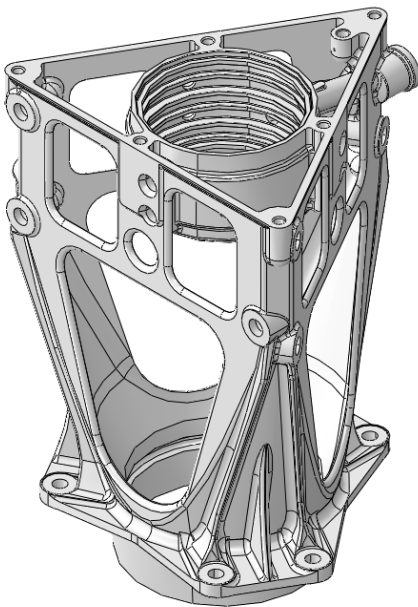
- **Structural optimization overview:** presents an introduction and theory review of the structural optimization processes with relevancy for the current thesis, namely, topology optimization and shape optimization. Additionally, it links the theory of said optimization processes with unique commercial software implementations;
- **Additive manufacturing overview:** briefly explores the concept of additive manufacturing, its history, applications and drawbacks, as well as comparing several different technologies;
- **Design for additive manufacturing overview:** presents in depth state of the art processes to integrate additive manufacturing with structural optimization typical design workflows. Additionally, it explores the inclusion and description of the thermal-mechanical problem and the underlying theory that governs the complex AM process, such that it can be simulated and integrated into the design validation step;
- **Additive manufacturing thermal-mechanical simulation methodology:** introduces the implementation of the supra mentioned thermal-mechanical simulation in a FE analysis, utilizing readily available software tools (for the relevant parties). The process is explored step by step, and the tools detailed. The chapter ends with the application of said steps to a benchmark part with publicly available results, to both compare and validate the methodology;
- **Static analysis and topology optimization methodology:** has a detailed static analysis of the current part, in order to properly define both design requirements, and the topology optimization model. Moreover, it compares the performance of two interpolation techniques, MIMP and SIMP, as well as the introduction of topology optimization setting up procedures to be applied to the bracket part;
- **Topology optimization results:** reports the results obtained from the topology optimization of a set of distinct trial cases, culminating in the choice of a single one based on performance comparison;
- **Shape optimization results:** reports the results obtained from the shape optimization and the design iterations the bracket undergoes until a final geometry is reached;
- **Additive manufacturing simulation results:** the implementation of the part-level (low-resolution) thermal-mechanical AM process simulation is performed on the final design obtained from the shape optimization results. The results are showcased with bigger relevancy to the part distortion.
- **Conclusions:** the design process approach with inclusion of DfAM guidelines is reflected upon based on the results obtained, specifically against the current design part performance. It discusses the practices and their impact, as well as further work.

Chapter 2

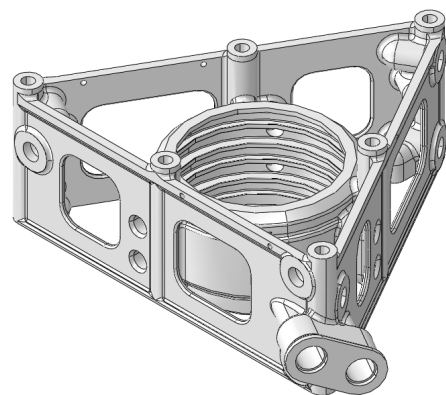
Problem Definition

The target problem of the thesis is the optimum design of an aeronautical component to be employed by Leonardo in an helicopter. To achieve the task, the company has provided a guideline on the performance and volume requirements to be complied with, together with the current component design. As such, a total of four 3D CAD files are provided,

- Current component upper manifold (see figure 2.1(a))
- Current component lower manifold (see figure 2.1(b))
- Design envelope (see figure 2.2(a))
- Fixed elements or mounting interfaces (see figure 2.2(b))

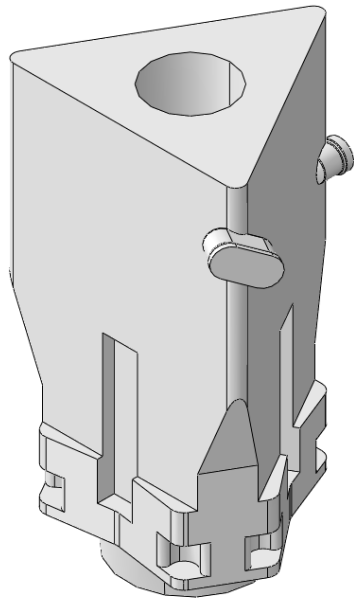


(a) Current component upper manifold.

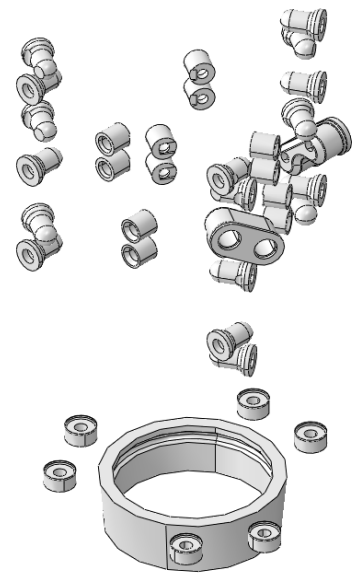


(b) Current component lower manifold.

Figure 2.1: Current component individual parts.



(a) Design envelope.

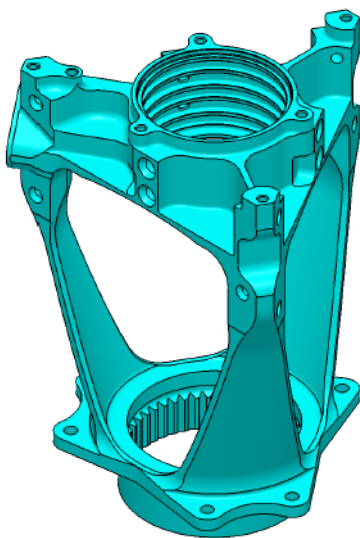


(b) Fixed elements.

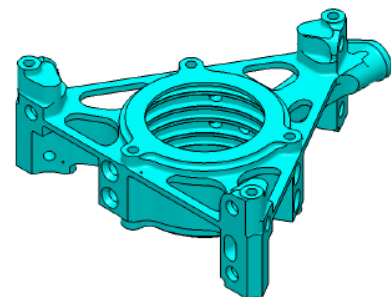
Figure 2.2: Optimization individual parts.

2.1 Recent component redesign

Initially designed in 1985, the servo-actuator bracket as seen several design iterations throughout the years. However, its manufacturing method has either been investment casting or machining from solid, which limited the design to be separated in two different parts, in addition to other minor components that ensure the connection between the two. The original design from 1985, made in investment casting, can be seen in figures 2.1(a) and 2.1(b). The redesign from 2017, which follows a machining from solid manufacturing process can be seen in figures 2.3(a) and 2.3(b).



(a) Redesigned component upper manifold.



(b) Redesigned component lower manifold.

Figure 2.3: Redesigned component individual parts.

2.2 Design Restraints

One of the objectives of the design process is to utilize additive manufacturing technology and integrate both the top and upper manifolds into a single component, reducing the need for connecting components and the assembly complexity. As mentioned, two different volumes are considered, comprising the mounting interfaces, or fixed elements, which shall remain unaltered, and the design envelope, the volume subject to optimization and changes.

2.3 Mounting interfaces

The mounting interfaces present can be divided into categories based on their purpose. The first set of mounting interfaces represents the mounting bosses through which the actuators are connected and loads are transmitted. A total number of eighteen mounting bosses exist, with six existing per face, displayed in a radial pattern in each of the three component's side faces (green elements in figure 2.4).

The second set of mounting interfaces refers to the hydraulic system, representing the inlets, outlets and connection oil ports through which the oil is fed to the three servo-actuators. Each face has four connecting oil ports, which again are radially patterned in each of the three faces, making a total of twelve connection oil ports (red elements in figure 2.4). Four inlet and outlet oil ports exist, but are not displayed in a pattern (orange elements in figure 2.4).

The grounding of the component is done through the support flange, comprised of six bolt holes (purple elements in figure 2.4).

Finally, the cylindrical region, while not load carrying, serves the purpose of properly placing and centring the component in the final assembly (yellow element in figure 2.4).

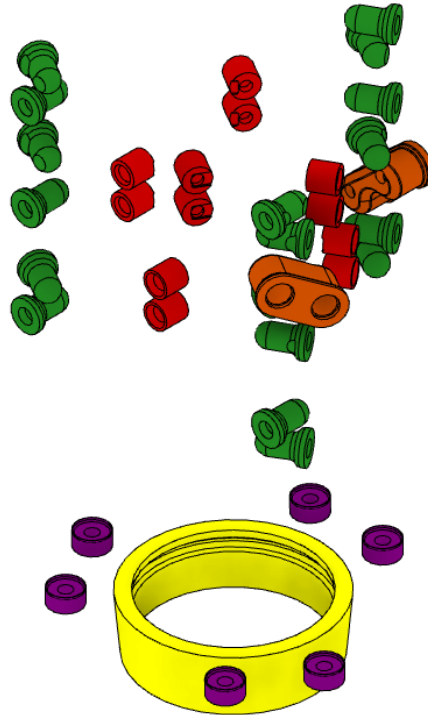


Figure 2.4: Mounting interfaces geometry. Green elements constitute the mounting bosses. Red elements constitute the connection oil ports. Orange elements constitute the oil inlet and outlet ports. Purple elements constitute the mounting bolt holes. Yellow elements constitutes the centring region.

2.4 Hydraulic feed

The hydraulic feed system is designed such that four oil feed levels exist, with each inlet or outlet port connecting to three connection oil ports. The current feeding design conveys the oil from the inlet and outlet ports to the connection oil ports through an inner cylindrical duct, closed by a secondary structure. The ports connect to it through straight ducts. The redesign project guidelines concede freedom over changing the oil ducts, while setting two requirements on the final design. These are,

- The oil ducts must withstand the static and fatigue loads defined;
- The oil ducts must be 100% free of any particle that may become detached from the internal surface, as this could damage the hydraulic actuators.

2.5 Test loads

The loading conditions the component is under result from the both the connected actuator loads, and the pressure loads from the oil ducts.

2.5.1 Servo-actuator loads

The three servo-actuators are connected to the bracket through the eighteen existing mounting bosses, six on each one of the three faces. While information on the actuators is limited, the load application points and centres of gravity are provided (see figure 2.5). For sake of keeping information confidential, the exact location of the load application is not provided and will be referenced to as $d_{AF_{S1}}$, $d_{AF_{S2}}$ and $d_{AF_{S3}}$. Information is also provided on the location of the center of gravity of the servo-actuators, which is offset from the load application point. Once again, to preserve confidentiality, the distance will be referenced to as d_{CG_1} , d_{CG_2} and d_{CG_3} , and the point masses as M_1 , M_2 and M_3 . The test load cases assess both static strength and fatigue life, and the positive force direction is seen in figure 2.5, highlighted by the red arrow.

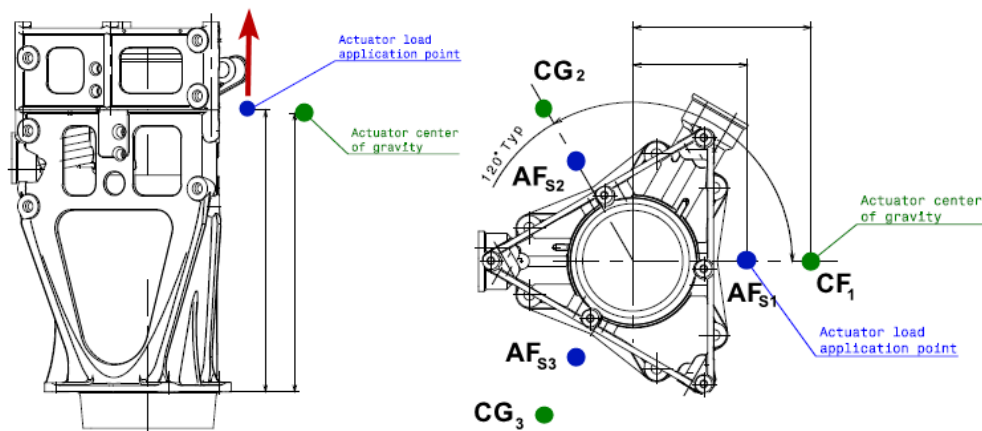


Figure 2.5: Schematics of both load and center of mass application points, and direction of positive z-direction.

2.5.1.1 Static strength

Two different loading conditions are defined to ensure static strength of the component, and both can be seen in tables 2.1 and 2.2. For each, three different loads and requirements are considered, such that, when considering stall and proof loads, no yielding (permanent deformation) shall be present in the component, and when considering the ultimate load, no failure shall happen, but permanent deformation is allowed.

Point	Description	Stall load	Proof load	Ultimate load
		-	No yield	No failure
AF_{S1}	Force SV FWD	AF_S	AF_P	AF_U
AF_{S2}	Force SV REAR RH	AF_S	AF_P	AF_U
AF_{S3}	Force SV REAR LH	AF_S	AF_P	AF_U

Table 2.1: Static loads for axial load case 1.

Point	Description	Stall load	Proof load	Ultimate load
		-	No yield	No failure
AF_{S1}	Force SV FWD	$-AF_S$	$-AF_P$	$-AF_U$
AF_{S2}	Force SV REAR RH	$-AF_S$	$-AF_P$	$-AF_U$
AF_{S3}	Force SV REAR LH	AF_S	AF_P	AF_U

Table 2.2: Static loads for bending load case 2.

2.5.1.2 Fatigue life

The fatigue life assessment is performed through a single load case defined in table 2.3. The three actuator loads are defined by static and dynamic components, and the phase. A wave representation of the loads over a single cycle is represented in figure 2.6.

Point	Description	Static	Dynamic	Phase
AF_{S1}	Force SV FWD	AF_{FS}	$\pm AF_D$	0°
AF_{S2}	Force SV REAR RH	AF_{FS}	$\pm AF_D$	120°
AF_{S3}	Force SV REAR LH	AF_{FS}	$\pm AF_D$	240°

Table 2.3: Fatigue loads.

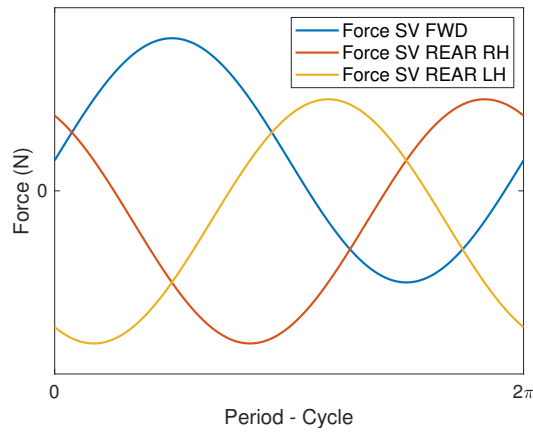


Figure 2.6: Singular cycle of the dynamic fatigue loads according to table 2.3.

2.5.2 Pressure loads

The oil ducts are tested under two dynamic load cases. The first one is defined by a high number of cycles dynamic pressure load, while the second by a single cycle at a higher pressure load. The oil temperature is identical in both cases, and no failure or leakage shall occur.

2.6 Stiffness and natural frequency requirements

2.6.1 Servo-actuator axial stiffness

In order to provide a stiff enough support to the connected servo-actuators, which ensures proper manoeuvrability and accurate helicopter control, a stiffness requirement is defined at each of the actuator load application points, solely in the z (or axial) direction. A graphical depiction of the requirements can be seen in figure 2.7.

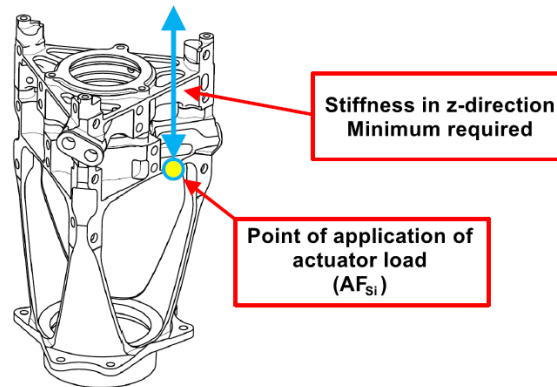


Figure 2.7: Schematic of the servo-actuator axial stiffness requirement.

2.6.2 Mounting bosses stiffness

The second set of stiffness requirements are important to avoid potential distortion of the servo-actuator interface lugs, and are translated to two stiffness requirements on the mounting bosses (see figure 2.8). These are,

- Each mounting boss shall have a relative stiffness within 80% to 120% of the current design, with respect to the directly adjacent bosses;
- Each mounting boss shall have a normal stiffness within 80% to 120% of the current design, with respect to the manifold assembly support flange (the grounded region).

2.6.3 First natural frequency

Given the heavy servo-actuators, the first natural frequency of the component decreases. A minimum natural frequency is then set to ensure proper structural performance. The mass considered for each actuator is applied at the respective centre of gravity and rigidly connected to the mounting bosses.

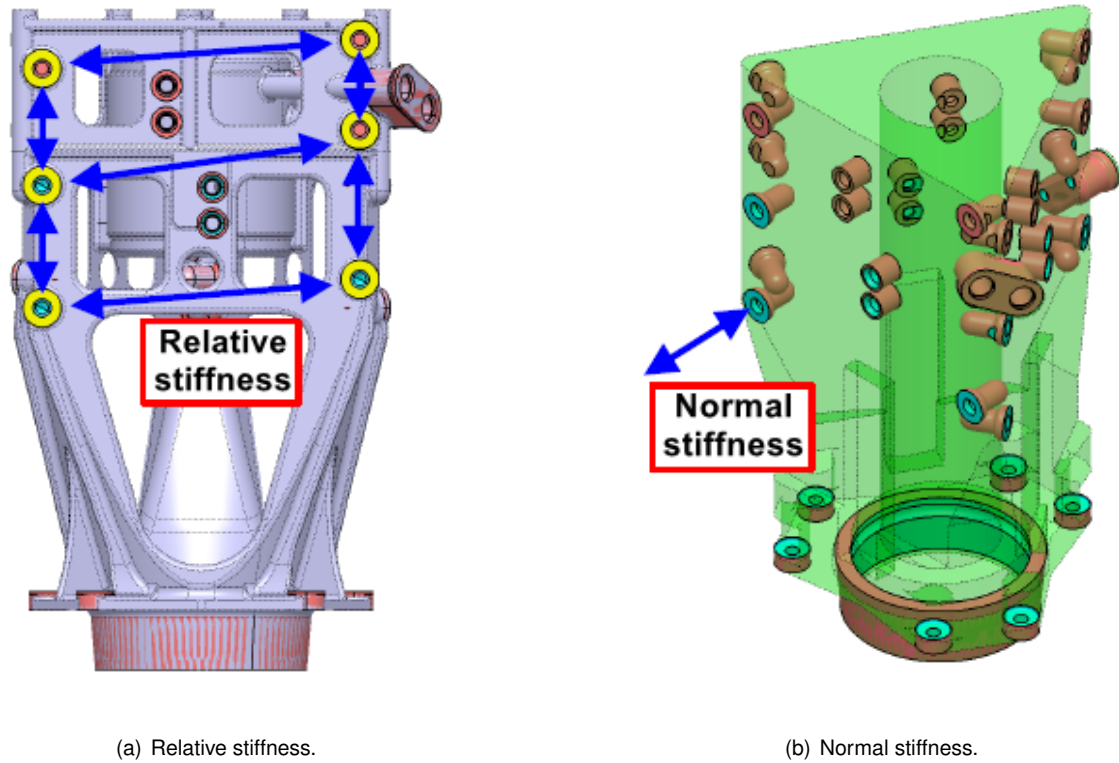


Figure 2.8: Schematic of the mounting bosses stiffness requirements, both relative and normal.

2.7 Project requirement summary

The bracket redesign shall,

- **Fatigue life**

- Withstand N_{cyc}^F ¹ cycles under the dynamic load in 2.6 without failure;

- **Static strength**

- Withstand proof load AF_P without any yielding;
- Withstand ultimate load AF_U without any failure;

- **Pressure loads**

- Withstand N_{cyc}^P ² cycles with each inlet port pressurized at F_1^P ³ with outlet ports closed, without any failure or leakage;
- Withstand a single cycle for T^P ⁴ with each inlet port pressurized at F_2^P ⁵ with outlet ports closed, without any failure or leakage;

- **First natural frequency**

¹ N_{cyc}^F is the non-disclosed limit number of fatigue life cycles
² N_{cyc}^P is the non-disclosed limit number of inlet pressure cycles
³ F_1^P is the non-disclosed high-cycle pressure load
⁴ T^P is the non-disclosed single cycle duration
⁵ F_2^P is the non-disclosed single cycle pressure load

- Have a first natural frequency with a minimum value of w_1 , while connected to the three servo-actuators;

- **Axial stiffness**

- Have a minimum z direction stiffness of K_z^6 at each servo-actuator load application point (AF_{S1} , AF_{S2} and AF_{S1});

- **Mounting bosses stiffness**

- Have each mounting boss with a normal stiffness within 80% to 120% of the current design, with respect to the manifold assembly support flange (the grounded region);
- Have each mounting boss with a relative stiffness within 80% to 120% of the current design, with respect to the directly adjacent bosses.

⁶ K_z is the non-disclosed axial stiffness

Chapter 3

Structural Optimization Overview

3.1 History

"The art of structures is where to put holes"

— Robert Le Ricolais, 1894-1977

With roots back to the 16th century, the problem of optimal design as found itself with an origin alongside structural mechanics. Galileo Galilei (1564-1642), in his famous "Discorsi e Dimostrazioni Matematiche Intorno a Due Nuove Scienze" ("The Discourses and Mathematical Demonstrations Relating to Two New Sciences") from 1638 [11], explored the influence of the shape and size of a body on its strength, namely, he sought after the optimal shape of cantilever beams under load (figure 3.1).

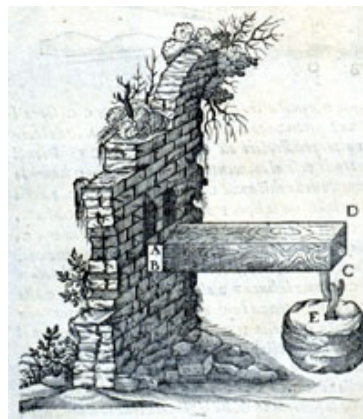


Figure 3.1: Illustration of Galileo's cantilever beam, from which is understood that the load at the root increases with the square of the beam length [11].

With the lack of computational capabilities, initial developments of structural optimization are carried out in an analytical capacity by Anthony George Maldon Michell (1870-1959) in "The limits of economy of material in frame-structures" from 1904 [12]. In his work, Michell explores the concept of minimum compliance trusses (named Michell structures), which guarantee minimum load path for a set of boundary and load conditions (figure 3.2).

With the ever increasing computational capabilities, more complex problems with no analytical solutions are now able to solved through the application of numerical methods to approximate the optimization problem solution.

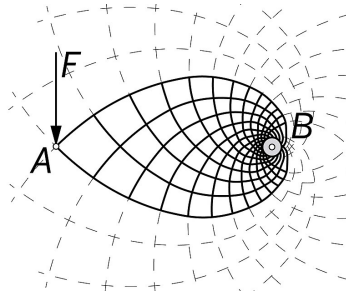


Figure 3.2: Example of a Michell structure [12].

3.2 Introduction to Structural Optimization

Structural optimization is aimed at the search to find the "best" way an assembly of materials can withstand a set of loading and boundary conditions. However, such objective lacks meaning, as the idea of "best" could have multiple different definitions. The search for the minimum weight may be one of those. Another possible objective could be to find the stiffest possible structure. Or even the structure that is most insensitive to buckling or instability. Independently of the objective chosen to guide the optimization process, the inclusion of constraints guide the problem to a well defined solution. Utilizing one of the previous definitions as an example, if the search for the lightest structure is set as the objective of the optimization problem, and no other constraint is placed on the final structure, for example, on the displacement of a certain region, or even on the geometry, the solution results in a null weight structure [13, 14].

Therefore, a more complete definition of the structural optimization problem is the search of the assembly of material that, while respecting a given set of requirements (stiffness, weight, eigenvalues, displacement, etc.), optimally sets the objective of interest, that could be, for example, the stiffness or weight of said structure.

3.2.1 General Mathematical Formulation

In order to formulate a general structural optimization problem, a set of concepts need to be introduced. These are,

- Objective function ($f(x, y)$): represents the objective to be optimized and determines the goodness of each possible design. Typically, it is defined as the volume or compliance of a structure;
- Design variable (x): describes the design, and may represent the geometry of the structure;
- State variable ($y(x)$): depending on the structure, that is, for a given design variable x , the state variable $y(x)$ represents the structural response. This can be the stress, displacement, strain or force.

A general problem takes the form of,

$$\left\{ \begin{array}{l} \text{minimize } f(x, y(x)) \text{ with respect to } x \text{ and } y \\ \text{subject to } \left\{ \begin{array}{l} \text{design constraints on } x \\ \text{state constraints on } y(x) \\ \text{equilibrium constraint} \end{array} \right. \end{array} \right. \quad (3.1)$$

3.2.2 Types of Structural Optimization Procedures

Starting from this formulation, several types of structural optimization problems can be formulated, based on the parametrized geometrical feature. This choice should be based on the structure at hands and on the objectives of the design process. The different types are briefly introduced beneath, accompanied with a graphical representation showcasing the dissimilarities.

- **Sizing optimization:** The design variable x typically represents the cross-sectional areas in a truss structure, or the thickness of a linearly elastic plate. The optimization goal typically falls on stiffness maximization, while satisfying a weight objective and respecting the equilibrium constraint (figure 3.3(a));
- **Shape optimization:** The design variable x is the domain, that is, the goal is now on finding the optimal shape of this domain, such that a given quantity is minimized. For example, the process could be applied to achieve stress homogenization by varying the shape (mesh nodes) of the structure (figure 3.3(b));
- **Topology Optimization:** The design variable x now takes form of the connectivity of the system, being involved in the placement or removal of holes (figure 3.3(c)).

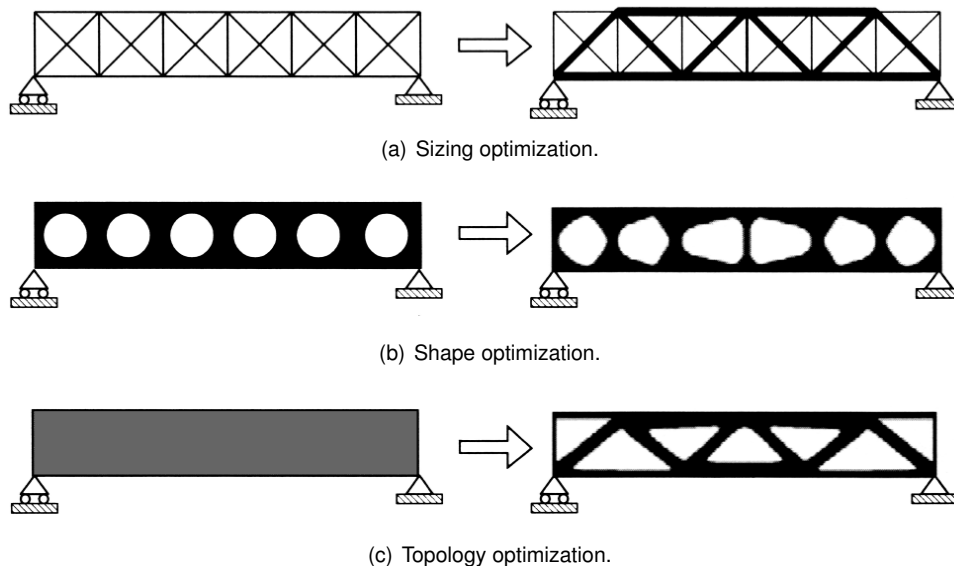


Figure 3.3: Examples of structural optimization types [15].

As will be explored in the chapter 5, these different optimization types have a complimentary relationship between them, since both size and shape optimization handle design with topology and features known *a priori*. Namely topology and shape optimization, which have different strengths, will be used to make the design process as complete as possible.

3.3 Topology Optimization

First introduced by Bendsøe and Kikuchi (1988) [16], where a homogenization method produced an optimal shape and topology of a material composed by individual cells, numerical methods for topology optimization have been extensively studied and developed in several different directions, such as "level set" [17–19], and "evolutionary" [20], to name a few. The evolutionary method, for one, considers element or nodal-based design variables. On the other hand, the level set method utilizes shape derivatives to obtain the optimal topology. While these methods show

promising results, they have not yet seen regular industrial application, limiting them to academic context. However, the density-based approach [15] is currently present in most commercial FEA software with topology optimization capabilities, namely the Solid Isotropic Material with Penalization method. Due to its relevancy and application in this thesis, the SIMP method will be further discussed, including its formulation and limitations.

3.3.1 Minimum Compliance Problem

When dealing with continuum structures, the topology optimization problem can be described as a material distribution problem.

In order to formulate the problem, consider an arbitrary body occupying the domain Ω^{mat} in \mathbb{R}^2 or \mathbb{R}^3 , which represents the optimal subset of materials points that the solution seeks to find. Such domain is part of a larger reference domain Ω , also called ground structure, on which the loads and boundary conditions shall be applied (example of an arbitrary body in figure 3.4).

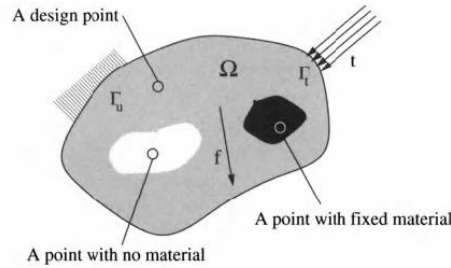


Figure 3.4: Arbitrary body definition [15].

Following the "standard" topology optimization of continuum structures problem, as is described in [15], the minimum compliance problem will be introduced, despite the use of a weight minimization approach in this thesis.

The minimum compliance approach aims at the maximization of the global stiffness of the body considered ($c = k^{-1}$). In a general form, the design problem aims at finding the optimal choice of the stiffness tensor $E_{ijkl}(x)$ over the previously defined domain Ω . The computational nature of the problem leads to a discretisation of both the displacement u and stiffness E fields, by means of finite elements. Considering the variable E constant within each element e , E_e , the minimum compliance problem can be formulated as,

$$\left\{ \begin{array}{l} s.t. \left\{ \begin{array}{l} \mathbf{K}(E_e)\mathbf{u} = \mathbf{f} \\ E_e \in E_{adm} \end{array} \right. \end{array} \right. , \quad (3.2)$$

where \mathbf{f} and \mathbf{u} represent the load and displacement vectors, respectively, and E_{adm} represents the admissible stiffness tensors. The stiffness matrix \mathbf{K} is written as a function of the global element stiffness matrix,

$$\mathbf{K} = \sum_{e=1}^N \mathbf{K}_e(E_e). \quad (3.3)$$

As previously stated, the optimization problem searches for the domain Ω^{mat} , which is achieved by setting points of space in the domain Ω to either voids (absence of material) or material points. Following the discretisation applied, the material-void point definition can be defined through the admissible stiffness tensors. Considering an isotropic material defined by the stiffness tensor E_{ijkl}^0 , the discrete valued design problem is formulated as,

$$E_{ijkl} = \delta_{\Omega^{mat}} E_{ijkl}^0, \quad (3.4)$$

where $\delta_{\Omega^{mat}}$ takes the values,

$$\delta_{\Omega^{mat}} = \begin{cases} 1 & \text{if } x \in \Omega^{mat} \\ 0 & \text{if } x \in \Omega \setminus \Omega^{mat} \end{cases}. \quad (3.5)$$

The design envelope V defines the limit material for the minimum compliance design, represented by the following inequality,

$$\int_{\Omega} \delta_{\Omega^{mat}} d\Omega \leq V. \quad (3.6)$$

A common solution to the problem requires the definition of the stiffness tensor as a function of a continuous variable which becomes the design variable. In this case, the variable to use is the density $\rho(\mathbf{x})$, such that,

$$E_{ijkl}(\rho = 0) = 0, \quad (3.7)$$

and,

$$E_{ijkl}(\rho = 1) = E_{ijkl}^0. \quad (3.8)$$

When $\rho(\mathbf{x}) = 1$, the element considered is filled (solid material), whereas when $\rho(\mathbf{x}) = 0$, the element is a considered to be void. As a continuous function with values between 1 and 0, in order to obtain a pure 0-1 design, the intermediate values need to be evaluated and steered towards one of the extreme values $\rho(\mathbf{x})$ can take, a discrete 0-1 value. Several different interpolation methods have been applied to the problem, namely the penalized, proportional stiffness model, commonly known as Solid Isotropic Material with Penalization (SIMP). However, due to its relevancy to the present thesis, another interpolation methods will be introduced, the Mass Interpolation Material Penalization (MIMP). Should be noted that the method is proprietary under SIMULIA [10], therefore explicit formulation is omitted.

3.3.2 Interpolation Methods

3.3.2.1 Solid Isotropic Material with Penalization - SIMP

Originally developed by [21], based on the approach introduced by [15], the SIMP method has found itself at the forefront of most popular finite element based topology optimization tools. The formulation is as follows,

$$E_{ijkl}(\mathbf{x}) = \rho(\mathbf{x})^p E_{ijkl}^0, \quad p > 1. \quad (3.9)$$

where p is the penalization factor, which penalizes the elements with intermediate densities to the bounds of the interval $\rho \in [\rho_{min}, 1]$ (ρ_{min} is set in order to avoid singularities in the finite element analysis). The equation 3.6 is rewritten as,

$$\int_{\Omega} \rho(\mathbf{x}) d\Omega \leq V, \quad 0 \leq \rho(\mathbf{x}) \leq 1. \quad (3.10)$$

The use of $p > 1$ results in unfavourable intermediate densities, since these stiffness values are now small compared to the volume of the material (the ratio $\frac{stiffness}{volume}$ decreases).

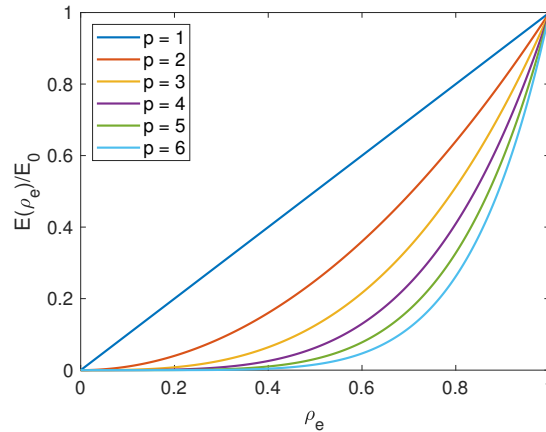


Figure 3.5: SIMP interpolation technique penalization with respect to different p values (from 1 to 6).

3.3.2.2 Mass Interpolation Material Penalization - MIMP

The MIMP algorithm is based on a combination between SIMP for the constitutive material interpolation, and a SIMULIA developed physical density material interpolation. While its definition is proprietary to SIMULIA, its suggested use is in strength optimization with applied stress, either as an objective, or as a constraint. Additionally, it reportedly improves results with mass-related responses, such as frequency, since previously the algorithm would by default change interpolation scheme to PEDE (Niels-Pedersen based approach, also proprietary to SIMULIA [10]).

While academic application is currently non-existent on the method, SIMULIA in its press release showcases the potential of the application of MIMP over SIMP [22]. More specifically, a volume minimization method with stress, frequency and displacement constraints is presented as the *Round Table Challenge* (figure 3.6). As showcased, the application of SIMP for the problem results in lack of convergence and of the 1-0 design that is sought-after to perform design interpretation.



Figure 3.6: *Round Table Challenge* results [22].

3.3.3 Sensitivity Analysis and the Method of Moving Asymptotes

The Optimality Criteria (OC) and the Method of Moving Asymptotes (MMA) are two common methods to solve topology optimization problems with different applications, such that topology optimization software tools offer both depending on the problem. For simple compliance optimization problems with volume constraint, the Optimality Criteria is the ordinary method to employ as it showcases good convergence properties. However, for optimization

problems involving a larger number of constraints and different design objectives, linear programming methods have excellent convergence properties, with particular attention to the Method of Moving Asymptotes.

3.3.3.1 Method of Moving Asymptotes

The Method of Moving Asymptotes is a linear programming algorithm by [23], which solves non-linear and non-convex optimization problems by providing a sequence of convex approximate sub-problems to be solved at each iterative point of the optimization. The method is described below, based on procedures explained in both [13, 23]. Let $F(\mathbf{x})$ be the function to approximate, such that, $\mathbf{x} = (x_1, \dots, x_n)$ are the function variables. The approximation around the iteration point \mathbf{x}^0 is as follows,

$$F(\mathbf{x}) \approx F(\mathbf{x}^0) + \sum_{i=1}^n \left(\frac{r_i}{U_i - x_i} + \frac{s_i}{x_i - L_i} \right), \quad (3.11)$$

where the parameters U_i and L_i define the vertical asymptotes, which are updated at each iteration satisfying,

$$L_i < x_i < U_i. \quad (3.12)$$

The numbers r_i and s_i are defined as,

$$r_i = \begin{cases} (U_i - x_i^0)^2 \frac{\partial F}{\partial x_i}(\mathbf{x}^0) & \text{if } \frac{\partial F}{\partial x_i}(\mathbf{x}^0) > 0 \\ 0 & \text{if } \frac{\partial F}{\partial x_i}(\mathbf{x}^0) < 0 \end{cases}, \quad (3.13)$$

$$s_i = \begin{cases} 0 & \text{if } \frac{\partial F}{\partial x_i}(\mathbf{x}^0) > 0 \\ -(x_i^0 - L_i)^2 \frac{\partial F}{\partial x_i}(\mathbf{x}^0) & \text{if } \frac{\partial F}{\partial x_i}(\mathbf{x}^0) < 0 \end{cases}. \quad (3.14)$$

The following formulation is an extension of 3.2, with the introduction of the SIMP method,

$$\begin{cases} \min_{\rho_e} c(\rho_e) = \mathbf{f}^T \mathbf{u} \\ s.t. \begin{cases} \sum_{e=1}^N \rho_e^p \mathbf{K}_e \mathbf{u} = \mathbf{f} \\ \sum_{e=1}^N v_e \rho_e \leq V, 0 < \rho_{min} \leq \rho_e \leq 1 \end{cases} \end{cases}, \quad (3.15)$$

where the problem is now rewritten solely with respect to the design variables. Applying the MMA to the minimum compliance results in the following optimization sub-problem after an iteration step j ,

$$\begin{cases} \min_{\rho_e} \left\{ c(\rho^j) - \sum_{e=1}^N \frac{(\rho_e^j - L_e)^2}{\rho_e - L_e} \frac{\partial c}{\partial \rho_e}(\rho^j) \right\} \\ s.t. \sum_{e=1}^N v_e \rho_e \leq V, 0 < \rho_{min} \leq \rho_e \leq 1, e = 1, \dots, N \end{cases}. \quad (3.16)$$

3.3.3.2 Sensitivity Analysis

Sensitivity analysis is defined by a problem requiring the definition of the gradients of both the objective and constraint functions, with respect to the design variables. The formulation of the MMA problem requires such an analysis for each iteration, hence its relevance. In order to complete formulation, an example utilizing the minimum compliance with volume constraint problem will be utilized, as it is in [15], to then be generalized to other possible optimization problems, such as weight minimization with displacement constraints, for example.

One effective method to obtain the gradients is through the use of the adjoint method [24], which renders the calculation of the displacement derivatives unnecessary. The Lagrangian functional reads,

$$\mathcal{L}(\rho_e, \mathbf{u}, \boldsymbol{\lambda}) = \mathbf{f}^T \mathbf{u} - \boldsymbol{\lambda} (\mathbf{K} \mathbf{u} - \mathbf{f}), \quad (3.17)$$

such that, if \mathbf{u} satisfies $\mathbf{K} \mathbf{u} - \mathbf{f} = 0$ (true by construction),

$$\frac{\partial c(\rho_e)}{\partial \rho_e} = \frac{d\mathcal{L}(\rho_e, \mathbf{u}, \boldsymbol{\lambda})}{d\rho_e} = \mathbf{f}^T \frac{\partial \mathbf{u}}{\partial \rho_e} + \boldsymbol{\lambda} \frac{\partial \mathbf{K}}{\partial \rho_e} \mathbf{u} + \boldsymbol{\lambda} \mathbf{K} \frac{\partial \mathbf{u}}{\partial \rho_e}, \quad (3.18)$$

that can be further simplified to,

$$\frac{\partial c(\rho_e)}{\partial \rho_e} = (\mathbf{f}^T + \boldsymbol{\lambda} \mathbf{K}) \frac{\partial \mathbf{u}}{\partial \rho_e} + \boldsymbol{\lambda} \frac{\partial \mathbf{K}}{\partial \rho_e} \mathbf{u}. \quad (3.19)$$

The adjoint equation defines $\boldsymbol{\lambda}$ that guarantees the Lagrangian functional does not change locally with a variation of \mathbf{u} , that is,

$$\mathbf{f}^T + \boldsymbol{\lambda} \mathbf{K} = 0, \quad (3.20)$$

which results in,

$$\boldsymbol{\lambda} = -\mathbf{u}^T. \quad (3.21)$$

Finally, the equation 3.19 can be simplified and expanded to the sought-after solution of the problem, that is, the gradient of the objective function $c(\rho_e)$ with respect to the design variable ρ_e ,

$$\frac{\partial c(\rho_e)}{\partial \rho_e} = -\mathbf{u} \frac{\partial}{\partial \rho_e} (\rho_e^p \mathbf{K}_e) \mathbf{u} = -p \rho_e^{p-1} \mathbf{u}^T \mathbf{K}_e \mathbf{u}. \quad (3.22)$$

The presented method is particularly interesting in problems where the number of design variables is large, as is the case in a typical topology optimization problem. Not utilizing the adjoint method, but the direct method instead, would require to obtain the gradients by solving the partial differential equation for each element part of the optimization process, which becomes expensive as the number of design variables increase. The adjoint method cuts down on the computational cost by bypassing the need to solve $dim(\rho_e) + 1$ partial differential equations, and simply calculate equilibrium equation, the adjoint equation to obtain $\boldsymbol{\lambda}$, and finally the equation for the gradient of the objective function with respect to the design variable.

3.3.4 Volume Minimization Problem

One other possible approach to topology optimization is through the definition of a volume minimization procedure [25, 26]. As a volume constraint is imposed in the minimum compliance formulation, as means to impede the solution to be made entirely of material elements ($\rho_e = 1, \forall e = 1, \dots, N_e$), the volume minimization procedure also requires a set of constraints to not allow the entire volume to be made solely out of void elements ($\rho_e = \rho_{min}, \forall e = 1, \dots, N_e$). Typically, volume minimization applications have displacement or stress constraints defined, but can be extended to modal analysis, or a combination of these. The formulation of the optimization under displacement constraint can be defined as,

$$\left\{ \begin{array}{l} \min_{\rho_e} \varphi(\rho) = \sum_{e=1}^N \rho_e v_e \\ s.t. \left\{ \begin{array}{l} \mathbf{K}(E_e) \mathbf{u} = \mathbf{f} \\ \mathbf{u}(\rho) = \bar{\mathbf{u}} \\ 0 < \rho_{min} \leq \rho_e \leq 1 \end{array} \right. \end{array} \right. , \quad (3.23)$$

where $\bar{\mathbf{u}}$ represents the displacement constraint. The problem is solved with the aid of a similar sensitivity analysis formulation, with the key difference that the required gradients are calculated on the constraints themselves ($\mathbf{u}(\rho)$), and not the objective.

3.3.5 Numerical difficulties

Despite the appeal of the topology optimization procedure, the quality control of the obtained solution requires major attention, since the process carries with it several complications that undermine the validity of the solution. Common complications include mesh dependence, checkerboarding and local optimum. The following sections will provide insight into the cause of each problem, and solutions that have been developed and implemented in commercial software tools.

3.3.5.1 Mesh dependence

The SIMP method is inherently mesh dependent, which means that different optimal solutions are found when discretising the domain with diverse mesh densities. [15] explores how the introduction of voids, while maintaining the volume of the structure incurs on an increased efficiency (minimize the objective function) for that particular structure. In a limit condition, the structure develops a geometry comprised of microstructures, typically showcasing non-isotropic properties. In fact, the progressive refinement of the finite element mesh causes a larger number of voids to appear, which leads to the creation of a "fine-scale internal structural lay-out" [15], similar to the microstructures mentioned (figure 3.7).

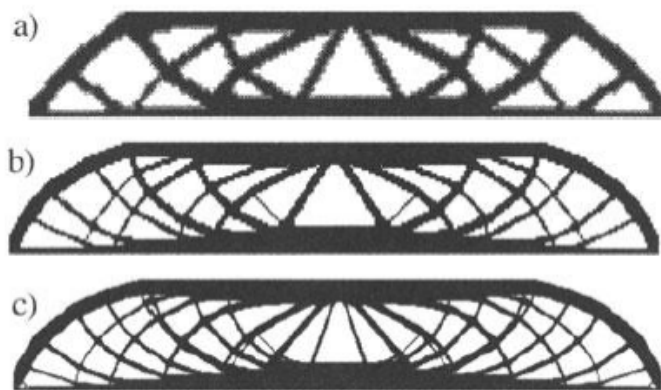


Figure 3.7: Mesh dependence example on a beam. a) 2700, b) 4800, and c) 17200 elements. [15]

3.3.5.2 Checkerboarding

The checkerboarding problem refers to the existence of solid and void elements distributed in a checkerboard like pattern (figure 3.8). Initially, such a region was thought to be an optimal microstructure, but Diaz and Sigmund

(1995) [27], and Jog and Haber (1996) [28], showed that the phenomenon is in fact due to bad numerical modelling, as this pattern has an artificially high stiffness.

Such a solution is highly undesirable, since the elements result connected through a single point, making the solution non manufacturable.

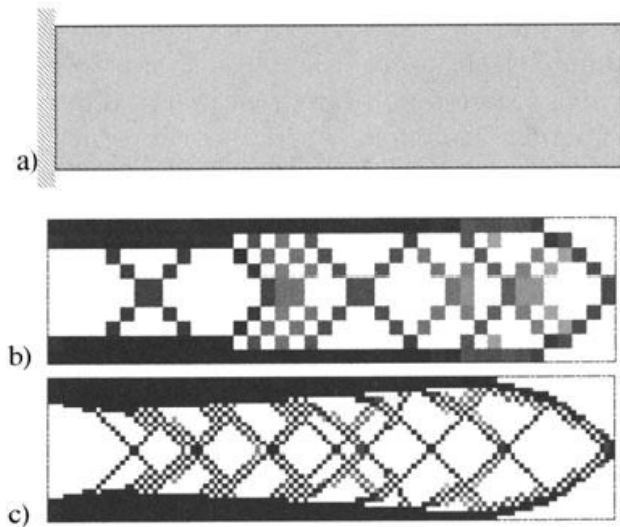


Figure 3.8: Checkerboard problem example on a beam. a) Design envelope, b) 400 element solution, and c) 6400 element solution. [15]

3.3.5.3 Local optima

Most topology optimization are non-convex and have multiple local optima, which are not the global optima, and ultimately lead individually to different solutions by modifying the optimization parameters. It should also be added that different boundary and load conditions, among other design parameters, lead to vastly different solutions.

3.3.6 Filtering techniques

Filters are a common solution that mitigate the extent and appearance of the topology optimization complications mentioned in 3.3.5, namely mesh dependence and checkerboarding. Two are of particular interest given their application in the topology, sensitivities filtering and filtering of the design variables. These are relevant based on the material interpolation algorithm applied. If SIMP is chosen, sensitivities filtering is applied, whereas if MIMP is chosen, design variables filtering is applied to the optimization process. The following two sections will explore the two filtering methods in more detail.

3.3.6.1 Sensitivity filtering

Initially introduced by Sigmund and Petersson (1998) [29], this filtering technique modifies a given element's design sensitivity to be a weighted average between itself and surrounding elements. The formulation for a non-regular mesh (variable element volume) is,

$$\frac{\partial c^{new}}{\partial \rho_e} = \frac{\sum_{i=1}^{N_e} w(\mathbf{x}_i) \rho_i \frac{\partial c}{\partial \rho_i} / v_i}{\frac{\rho_e}{v_e} \sum_{i=1}^{N_e} w(\mathbf{x}_i)}, \quad (3.24)$$

where N_e is the number of elements to be considered for the weighted average, $w(\mathbf{x}_i)$ is the linearly decaying weighting function, and v is the volume of the element to be considered (v_i represents surrounding elements, and v_e the element considered). Such an implementation has proven to be effective in producing mesh independent solutions and mitigating the appearance of checkerboard like geometry, hence its broad presence in topology optimization software tools. In order to avoid numerical singularity, element density must be different from zero, hence the previous definition of a minimum value for the design variable.

3.3.6.2 Design Variables Filtering

Alongside the introduction of new MIMP interpolation technique, also the filtering method has been changed by SIMULIA for this particular technique. The filtering on ρ is performed through the use of the weighted average of the design variables (\mathbf{x}_i). However, the full underlying algorithm is yet to be made available by SIMULIA, as it is currently undergoing several improvement iterations (alongside MIMP). However, the general expression for the design variable filter is defined by [30],

$$\rho_e(\mathbf{x}) = \frac{\sum_{i=1}^{N_e} w_i \mathbf{x}_i}{\sum_{i=1}^{N_e} w_i}, \quad (3.25)$$

where the weighting function w_i can be simply given by a linearly decaying function,

$$w_i = \frac{r_0 - r_i}{r_0}, \quad (3.26)$$

such that r_0 is the filter radius, and r_i the distance between the element of interest and neighbouring (within the filter radius) elements (see figure 3.9).

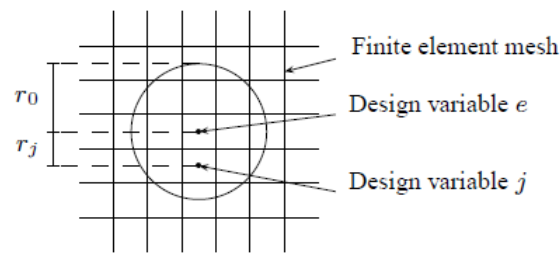


Figure 3.9: Design variable filter representation [30].

3.4 Shape optimization

Shape Optimization is a type of structural optimization that aims at the modification of the boundary domain of a component to achieve a set of objectives. A further distinction can be made between parametric [31] and nonparametric shape optimization [5, 32]. The former type is connected to the CAD parameters of component, such as, distances, radii, sizes, angles, among other significant variables. The optimization procedure is performed

on this set of variables with the goal to minimize or maximize an externally defined objective function. This type of optimization does have some downsides associated with it, namely the fact that the parametrization does not provide *any explicit information about the geometry or topology of the shape's boundaries* [31], which means that the boundary evaluation may fail, and that possible topological changes related to the boundary of the component may possibly invalidate the set boundary conditions.

On the other hand, nonparametric shape optimization is based on implicit parameters, defined from a set of surface nodes from the FE model, named design nodes. The scalar optimization displacements along the local optimization displacement vector of each design node defines the implicit parameters. Compared to a parametrized optimization approach, all possible solutions for the FE discretisation are now possible, since each design node can now be modified during the optimization procedure [5].

3.4.1 Multi-objective optimization formulation

Despite the possibility of considering several load cases during a volume minimization topology optimization analysis, the number of objectives remains singular. However, the consideration of a stress-based shape optimization process, for the same set of load cases, makes the problem a multi-objective one. Therefore, in a simple case, linearly combined based on their weights, such that,

$$f = \sum_{l=1}^N f_l w_l, \quad (3.27)$$

where the objective f_l , for the load case l , is subjected to a weight w_l . A total of N load cases are considered.

3.4.2 Shape optimization problem formulation

The shape optimization problem is formulated following a minimization of the maximum objective consideration, in order to achieve higher overall robustness [10]. It results in, for the respective objective,

$$\begin{cases} \min_x \max |F_j(\mathbf{X} - F_r)| \\ s.t. \Gamma^* \in \Gamma \end{cases} \quad (3.28)$$

F_j is the objective function for a given load case, which depends on the design variable of the shape optimization problem, the displacement vector \mathbf{x} . Γ^* is the design boundary, which should be part of the full geometry boundary Γ . Finally, F_r is the reference objective, which could be the average objective function value from all the design nodes, for example.

Chapter 4

Additive manufacturing overview

Additive manufacturing (AM) defines the wide range of different technologies focused on the 3D printing of objects by successive addition of material. The process is fundamentally different from the conventional subtractive, where the workpiece mass is decreased (e.g. milling, drilling), or formative, where the workpiece mass is conserved (e.g. casting) manufacturing processes, as it is based on a successive layer-wise addition of material, based on the digital Computer Aided Design (CAD) of the original component. Such an approach accomplished the simplification of the manufacturing of complex 3 geometries that previously were simply impossible or involved prohibitive laborious post-processing procedures.

4.1 History

The beginning of additive manufacturing can be traced back to more than a century ago, to the work behind the construction of free-form topographical maps and photo-sculptures from 2D layers [33–35]. Later, following the emergence of computer aided design (CAD) and manufacturing (CAM) in the 1960s, the first concepts for powder fusion [36], photopolymerisation [37] and sheet lamination [38] set the ground work for what are considered modern AM processes [39].

Throughout the proceeding years, with the advances in computational capabilities and increased investment in 3D printing, newer machines and processes appeared, such as fused deposition modelling (FDM) in 1991 [37], laser sintering in 1992 [40] and electron beam melting (EBM) in 1997. The continued investment and research transformed additive manufacturing from a rapid prototyping to industrial final part manufacturing. Alongside these developments, progress was also made in regards to additive manufacturing software and accompanying specific file formatting, such as STereoLithography (STL) and Common Layer Interface (CLI).

Entering the late 2000s, older additive manufacturing process saw defining patents expired, which opened the door to new competing companies to enter the market. This surge, together with the constant growth of additive manufacturing applications (figure 4.1) and the hobby community, drove to an expansion of both the supply and demand in the market. As a result, additive manufacturing is present in a wide range of different fields and applications, from medical, to aeronautical and space applications, to name few [39].

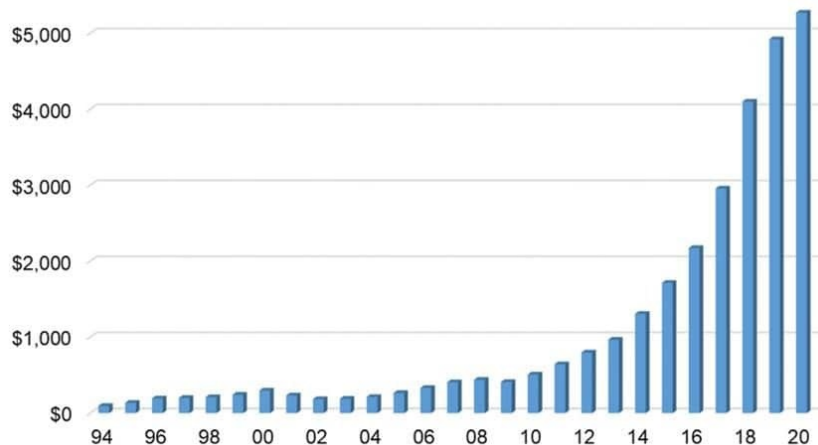


Figure 4.1: Production of AM parts from independent service providers (in millions of dollars [37]).

4.2 Additive Manufacturing Advantages and Disadvantages

In order to better illustrate the new opportunities that have been introduced by additive manufacturing technologies, the main advantages and disadvantages will be summarily presented, since despite its advantages, the technology is still not the right choice for all applications as it still presents several restrictions and problems yet to solve [41].

4.2.1 Advantages

- **Increased geometrical complexity**

Additive manufacturing allows bigger design freedom as it is able to produce highly complex geometries. This in turn means that the light-weighting process is made easier with a lower number of manufacturing constraints. This is specially important in the aerospace and automotive industries, where weight reduction is one of the primary design goals.

- **Reduced material waste**

Compared to conventional manufacturing processes, additive manufacturing proposes the use of less material to build a part with similar mechanical performance. This is due to the introduction of solid material (be in powder or other in its raw form) exactly where it is needed, rather than performing subtractive techniques, for example.

- **Simplified assemblage**

Tied together with the possibility of increased geometrical complexity is the possibility to reduce the number of parts present in an assembly (topic of major importance and relevancy for the scope of this thesis).

- **High customization**

Without the need for moulding or tooling, and consequently production scale, product diversity increases. Such fact seems great implementation in the medical field, where specialized, on-demand, per patient prints are possible.

4.2.2 Disadvantages

- **Limited build size**

The size of the printed component depends entirely on the additive manufacturing machine and technology used, since it is limited to the size of the chamber where it is built.

- **Production and hardware cost**

While the on-demand production represents a plus regarding design freedom, the cost associated is higher compared to conventional manufacturing techniques as the scale increases (figure 4.2). This is due to the steep pricing due to specialized equipment, which include devices responsible to deal with the highly hazardous materials resultant from the the AM process, for example.

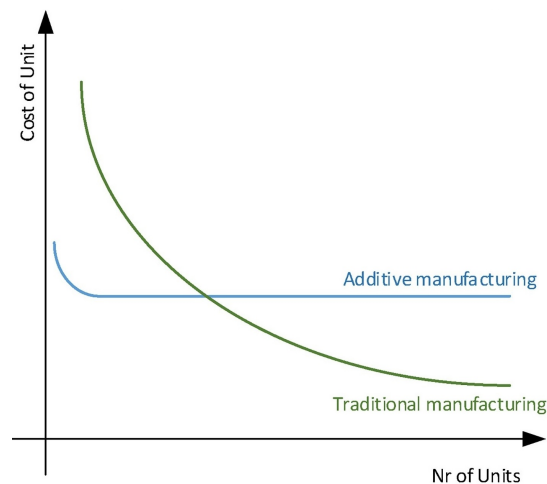


Figure 4.2: Economy of scale comparison between AM and traditional manufacturing methods [42].

- **Mechanical performance**

The anisotropic nature of layer-by-layer production results in parts that might exhibit lower strength and endurance than traditionally manufactured counterparts. Additionally, distortion also poses a serious concern regarding part quality, specially under tight geometrical tolerances. However, post-processing methods exist such that the mechanical shortcomings can be diminished and removed all-together, at the expense of increasing both the manufacturing cost and complexity.

- **Process complexity**

The AM process is reliant on many parameters that heavily impact the quality of the final print. But any change or dynamic setting up of certain parameters requires the modification of several others.

4.3 Additive manufacturing technologies

AM technologies cover a wide range of raw materials, such as titanium, aluminium, steel, nylon and polystyrene, to name a few. Despite the growing numbers of materials treated by AM technologies, each individual one can be processed in different ways. Such diversity introduces complexity when trying to lump and categorize AM technologies. One possible approach is through the one dimensional definition of the raw material used, be it discrete particles, solid sheets, molten material or liquid polymer. Or possibly by the definition of technology used, as it could be lasers, extrusion technology, to name a few.

In order to obtain a more comprehensive classification of existing AM technologies, Pham and Gault (1998) [43] defines a two dimensional classification based on the previous one dimensional classifications. The approach allows to separate technologies that were lumped together in the same category, while having that single property

in common but being ultimately very different. The classification method has later been updated by Gibson et al. (2014) [44] to include modern AM technologies, and a summary can be seen at table 4.1. The horizontal direction defines the generalized channel characteristics, which can be translated to a definition of the method by which the layers are built. On the vertical direction, it has been introduced an additional subdivision based on the ASTM Standard F2792 (2012) [45], which extends the raw material definition to the machine characteristics and the physical transformations it goes through.

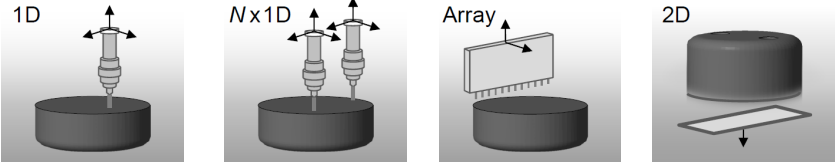
	1D	N x 1D	Array	2D
				
Discrete particles				
Powder bed fusion	SLS, SLM, EBM, DMLS, LMF	-	SHS	-
Directed energy deposition	LENS, EBAM, LMD	-	-	-
Material jetting	-	ColorJet, PolyJet	-	-
Binder jetting	-	-	3DP	-
Molten/viscous material				
Material extrusion	FDM, FFF, DIW	FDM, FFF, DIW	-	-
Liquid polymer				
Vat photopolymerization	SLA	DB SLA	-	DLP, cDLM, CLIP
Solid sheets				
Sheet lamination	LOM, UAM	-	-	-

Table 4.1: AM technology classification based on [43–45].

4.3.1 Powder-based Additive Manufacturing Technologies

The main focus of this thesis is on Powder-based AM technologies dedicated to building metallic parts, and as such, only these will be explored in the following section. The currently most relevant powder-based AM technologies can be divided in powder-bed and powder-injection.

4.3.1.1 Powder-injection Based Additive Manufacturing Technologies

This technology actually presents itself as multifaceted, since it is able to manufacture new components, but also repair damaged ones and apply coatings [46]. A typical technology based on powder-injection is Direct Metal Deposition (DMD) (figure 4.3), which uses a nozzle to inject metal powder that is molten by what is usually a laser, but other heat sources can be used.

Compared with powder-bed based AM technologies that will be introduced in the next section, DMD has a higher printing speed, but the resulting part generally has higher roughness. It also only applies material where needed, therefore there is no surrounding unfused powder, unlike in the powder-bed based AM techniques.

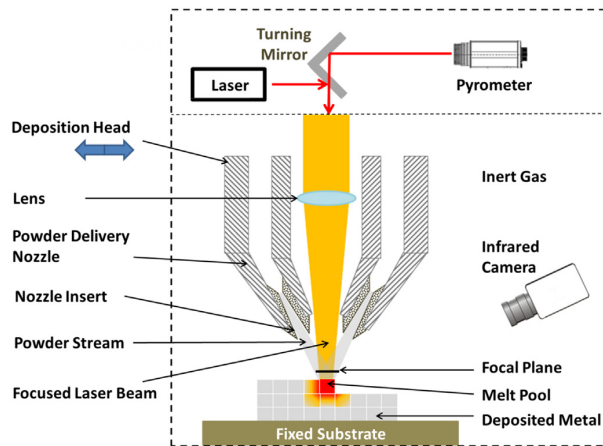


Figure 4.3: Direct metal deposition device [47].

4.3.1.2 Powder-bed Based Additive Manufacturing Technologies

Powder-bed based AM techniques core distinction from the previous technologies is on the use of thin layers of metal powder that are deposited onto the chamber where the part is built. A plate, perpendicular to the build direction, serves as the building starting point. It serves the purpose of holding the manufactured parts, but it also aids in the cooling process. The powder layer is deposited by a roller or a blade, whose function is also of ensuring the layer is uniform throughout. After the powder deposition, the energy source scans the layer through the pre-defined path, binding the powder particles. The plate moves down before the powder deposition process thus closing the cycle that will be repeated until the entire part is built.

The heat source, laser or electron beam, is one the primary differentiators between powder-bed based AM techniques, together with whether the powder is sintered or molten, such that the main powder-bed based AM technologies are defined by these characteristics. These are,

- Selective Laser Sintering (SLS);
- Selective Laser Melting (SLM);
- Electron Beam Melting (EBM).

The melting process that takes place in the SLM technology (see figure 4.4) results in a final part with lower porosity, when compared to the SLS technology, since this one heats the powder to a temperature below its melting point.

While similar in principle to SLS and SLM technologies, EBM uses an electron beam as heat source (see figure 4.5). This translates to a limitation on the materials that can be used as only high electrical conductivity materials can be employed in EBM technology. Due to these different characteristics, EBM presents itself as a more energy absorptivity efficiency technology, together with faster scanning speed and lower costs. In contrast, SLS and SLM technologies have higher precision, smaller grain sizes and better surface resolution.

4.3.2 Support Structures

Support structures are necessary as a temporary auxiliary structure required by most components produced by AM technologies. Together with the workpiece, the support structure also needs to be designed and generated, and has a significant impact on the quality of the final part [50, 51]. Their application depends on the AM technology used and serve two main purposes,

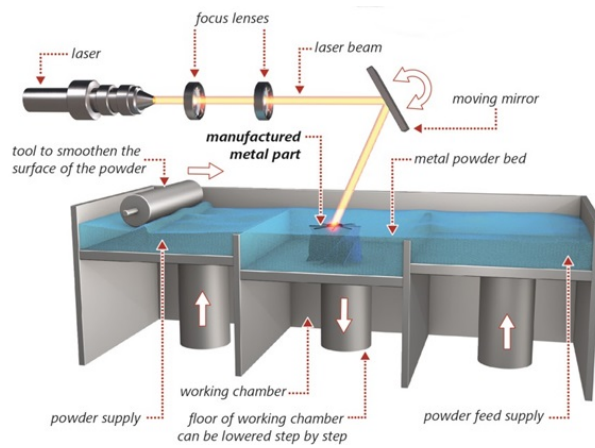


Figure 4.4: Selective laser sintering device [48].

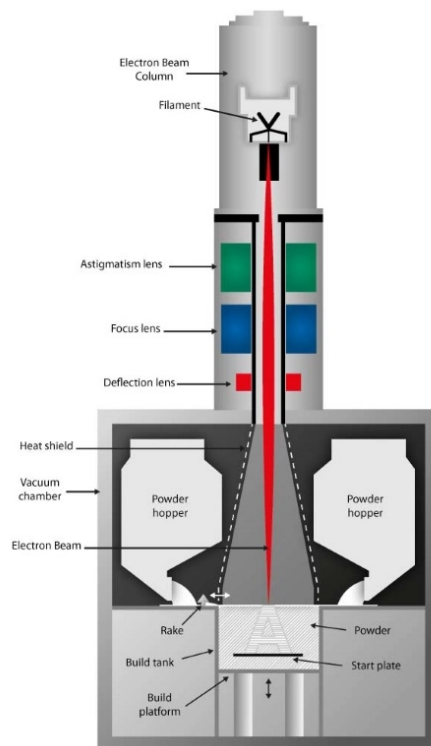


Figure 4.5: Electron beam melting device [49].

- Provide an underlying layer and support for new material to be deposited. It also applies to disconnected features of the geometry and overhangs over a certain angle, to prevent deformations caused by gravity;
- Optimize the temperature field distribution by providing a thermally conductive path away from the melt surface.

Support removal is a time-consuming and complex task, that depending on the design of the part and support placement can be an impossible task, since the machining tools might not be able to reach all surfaces. This makes support structures placement a good candidate for additive manufacturing oriented optimization and the concept will be further explored in the chapter 5.

Chapter 5

Design for Additive Manufacturing overview

AM technologies have seen an intensified presence in the manufacturing of critical components in the medical and aerospace sectors, driving what is now known as a new industrial revolution, or Industry 4.0 [52]. But behind the extended liberty in the design of new parts in AM, a set of guidelines and a structured framework need to be defined to ensure the best possible quality and performance out of these components. These are the Design for Additive Manufacturing (DfAM) guidelines, which focus on various aspects behind the conceptualization, production and post-processing of a part built in AM.

The context and research focus on DfAM includes research on the role of topology optimization and how it takes advantage of the design freedom to construct complex geometries that AM allows, printability of such designs, process parameters impact and control, materials to be used and definition of frameworks to guide the entire process.

The DfAM approach and consideration allows engineers to incorporate the AM potentials to every single step of the design process, as well as better tackle its limitations. In the context of this thesis, mainly topology optimization, printability and process parameters impact will be studied and incorporated into the design process of the aerospace component. Additionally, the design workflow for an aerospace component design will be updated to include the simulation of the additive manufacturing process, adding a new validation step that aims at dressing some of the shortcomings of AM, namely distortion and residual stresses. Ideally, the accurate prediction of these allows to make a more complete assessment on the printability of the final design.

5.1 Topology Optimisation and Additive Manufacturing

Given the ability of AM technologies to print highly complex structures, topology optimisation provides an intelligent way to take advantage of this design liberty. While topology optimisation by itself is a great lightweighting tool, a number of additional considerations can be introduced to, for example, achieve print-ready topology optimisation design. Manufacturing constraints are one of the main current research areas, namely in the design of support-free structures, and well defined boundaries. However, their application is also subjected to scrutiny depending on the application of the structure. In the context of this thesis, as will be further explored in section 8, the introduction of manufacturing constraints is limited to allow the topology optimization process to achieve the defined mechani-

cal performance requirements and the minimum weight possible. This means that, while printability is ensured, a support-free structure is not sought-after.

Reflecting on the AM technologies, namely SLM, and the associated limitations and shortcomings, a few considerations will be explored, together with their applicability in topology optimisation.

On a broad approach, the constraints considered when performing AM-oriented topology optimisation can be divided into two fundamental categories, directional and non-directional, as suggested by [53]. Directional constraints primarily relate and are influenced by the print direction, such as layer-induced anisotropy. On the other hand, non-directional constraints refer to constraints that are not directly influenced by the print direction. One possible example is the presence of enclosures that make it impossible to remove trapped powder (specially important in powder-bed technologies).

5.1.1 Directional Constraints

5.1.1.1 Support Structures

Two separate problems can be interpreted from the need to reduce the need for support structures and the consequent post-processing process to remove them. The first considers a set structure design to which we seek to find the optimal print direction that ensures minimal support structures, while the second seeks to define a structure design that minimizes the amount of support structure needed for a given optimal direction. Ideally, both problems are interconnected and their combination seeks the best possible solution to the support structure minimization problem. However, due to computational limitations, such approach is not the focus, and each problem is treated individually.

The second problem is relevant to the present thesis, as it is possible to consider it and ultimately guide the topology optimization solution. Its implementation is based on a geometrical threshold on the overhang angle of features (at a set distance from self-supported structure) and is present in the topology optimization solver used.

However, the application of this manufacturing constraint drives the solution towards a different optima with increased final weight, and depending on the objective of said part, the minimization of the weight can be more attractive than the reduction of post-processing. Such is the case in components to be applied in the aerospace sector, where lower weight translates to reduced fuel consumption and cost, therefore its application will not be present in this thesis.

The first problem translates into the design of support structures and optimization of the print direction. While the first sub-problem is isolated in the sense that, ideally, no other mechanical property is affected by a support structure design, the print direction has implications on the mechanical properties of the final part and is limited by the chamber and part dimensions.

5.1.1.2 Anisotropy

Layer-wise AM manufacturing technologies introduce anisotropy on the part constructed. More precisely, the in-plane direction (print direction) may exhibit weaker properties that can be modelled through orthotropy properties when defining the material or materials to be used. Despite its apparent impact, isotropic like properties are achievable through proper post-processing treatments, such as heat treatment optimization and hot isostatic pressing, or HIP [54].

5.1.1.3 Distortion and Residual Stresses

Residual stress defines the stress that remains in a part when in equilibrium, mechanical and thermal, with its environment. Different types can occur and are classified according to the scale at which they occur (see figure 5.1).

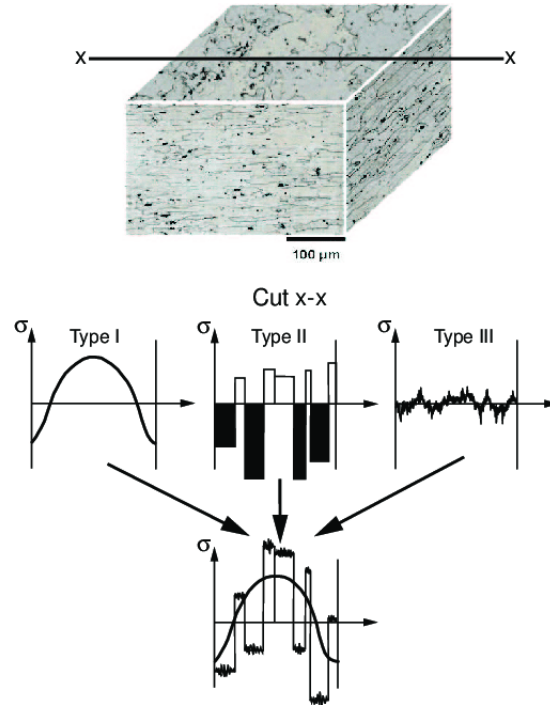


Figure 5.1: Residual stress types and their variation [55].

Type I residual stress, or macroscopic homogeneous residual stress, extend across the length of several crystal grains, and are responsible for large deformations. On the other hand, residual stress of type II, or microscopic homogeneous residual stress, is defined as the grain remaining stress when stress of type I is removed. Finally, type III stress, or microscopic heterogeneous residual stress, have a presence and impact on the atomic scale. Overall, all stress types have a contribution to the total residual stress such that,

$$\sigma_{res} = \sigma^I + \sigma^{II} + \sigma^{III}, \quad (5.1)$$

but the bigger focus of this thesis is on type I residual stress and its impact on the macroscopic quality of an additive manufactured part.

In metal AM, residual stresses have a largely negative presence (opposite to other application such as in tempered glass), and are responsible for distortions and cracks present in the final part, as well as reduced strength caused by pre-existing stresses that are added to external applications (figurefig:crack).

The residual stresses are a consequence of local melting and non-uniform cooling during the manufacturing phase. Two different mechanisms are behind the appearance of residual stresses in AM processes, namely in powder-bed based ones. The first one occurs due to the thermal contraction during the cooling of the molten top layer. The second mechanism is explained by the steep temperature gradient that exists around the laser or electron beam spot.

The first mechanism is directly related to the cooling step that occurs after the introduction of the molten metal pool. Its cooling causes shrinkage, which is held back by the underlying solidified layer. This process introduces

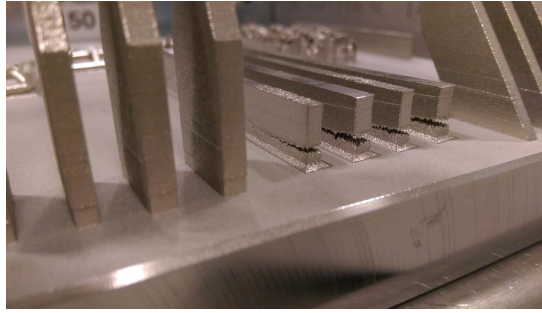
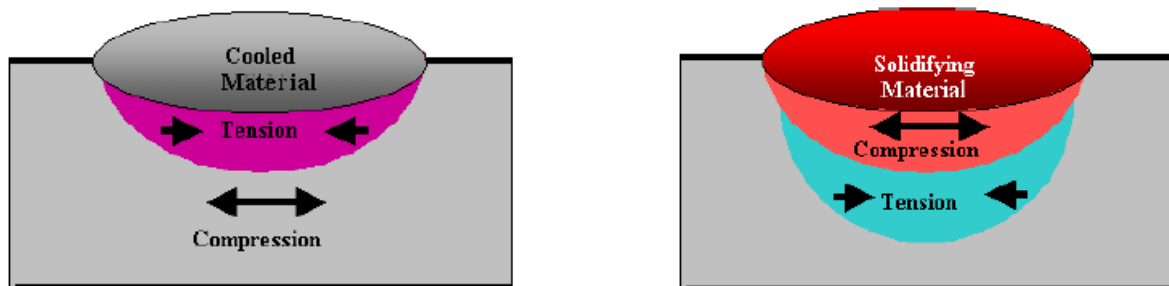


Figure 5.2: Crack and distortion caused by residual stress [56].

tensile stress in the immediate top layer, which in turn causes the appearance of compressive stress in the layers underneath. The process can be seen in figure 5.3(a).

On the other hand, the second mechanism occurs during the heating step and is caused by the quick heating process that occurs on the top layer and the slow heat conduction with the underlying layers, which drives the appearance of large temperature gradients. The expansion of the molten metal top layer is constrained by the cooler underlying solidified layer, which introduces elastic compressive strains, such that when the yield strength is reached, these make the top layer be subjected to plastic compression. The process can be see in figure 5.3(b).



(a) Cooling mechanism.

(b) Heating mechanism.

Figure 5.3: Residual stress formation mechanisms [57].

The problem of prediction of distortion and residual stresses in AM final parts is highly relevant and the research is still in its infancy [41]. Its accurate modelling can be ultimately included in the design workflow of an AM part, as it allows to introduce design modifications and compensation in problematic areas, ultimately leading to a better designed part. Numerical modelling of the problem requires a multi-scale approach to accurately capture the variations that occur at all time and dimension scales.

5.1.2 Non-Directional Constraints

5.1.2.1 Powder Enclosure/Cavity Constraint

With relevancy namely for powder-bed fusion based AM technologies, there is a need to ensure that no enclosed voids are created by the structural optimization or design interpretation steps, as their presence means that power is trapped and requires a cumbersome removal process (if at all possible).

5.1.2.2 Member/Feature Size Control

Similarly to minimum thickness constraints, the member size control aims at defining a limit to how small the members of the topology optimization. Checkerboarding is a potential issue related to the lack of minimum member size, as per section 3.3.5.2, where filtering techniques are also explored in section 3.3.6.

5.2 Additive Manufacturing Simulation

Numerical AM process simulations are an important tool for engineers and researchers to measure and predict the complex evolution of the multi-physics problem and better characterize the process. Due to hardware limitations, these simulations are currently mostly limited to small applications, or the macroscopic and large time scale simulations. Effort has been increasingly placed on utilizing simulation techniques and assumptions to accelerate the process, namely through the definition of a weak coupled thermo-mechanical analysis, and application of FEM specific tools and subroutines (e.g. adaptive mesh refinement and element birth and death).

However, both macro- and micro-scale approaches are important to a complete assessment of the AM process. The micro-scale models are relevant to assess the stability of the melt pool and defects, the interaction between the heat source and the powder bed, phase changes, surface tension, and the thermo-fluid-dynamic melt pool evolution. Due to computational limitations, these are restricted to small and localized simulations, and mostly take advantage of the Discrete Element Model through the implementation of the Lattice Boltzmann Method [58].

On the other hand, and with more relevancy to the context of the thesis, macro-scale models allow the prediction of residual stresses and distortions, and damage prevision, ultimately adding a new layer of completeness to the design validation step, before proceeding with the printing of the final part.

5.2.1 Process Parameters Optimisation

The process parameters that govern the AM process have a big impact on the quality of the printed part and current methods to assess it are based on experimental techniques. The improvement of AM simulation techniques is a positive prospect that allows to reduce both cost and time spent on these experiment, allowing to establish relationships between the process parameters and the quality parameters (e.g. residual stress) of the printed part, and ultimately leading to improved process parameter control.

The work of [41] focuses on the application of AM simulation to define the correlation between parameters such as laser power and heating time, with residual stress. The correlation is defined through the use of an artificial neural network (regression algorithm). The results are applied to a PID controller integrated in the AM simulation, allowing for a tuning that does not utilize several costly and time consuming experiments with the real AM machine.

5.2.2 Thermal-Mechanical-Metallurgical Coupling Problem

The problem of AM simulation is defined by a coupling between three main field (figure 5.4), the thermal, mechanical and metallurgical fields. While the metallurgical field is highly relevant due to the dependence of residual stress and distortion on solid phase transformations that occur during the printing process, its implementation will be limited in the context of this thesis, the focus being on the thermal-mechanical coupling problem.

As previously mentioned, in order to achieve realistic simulation times when dealing with final part designs, several assumptions and simplifications are made, one being the decoupling between both the thermal and mechanical fields. In the coupled model, thermal expansion has an effect on the mechanical properties, and in turn, the thermal

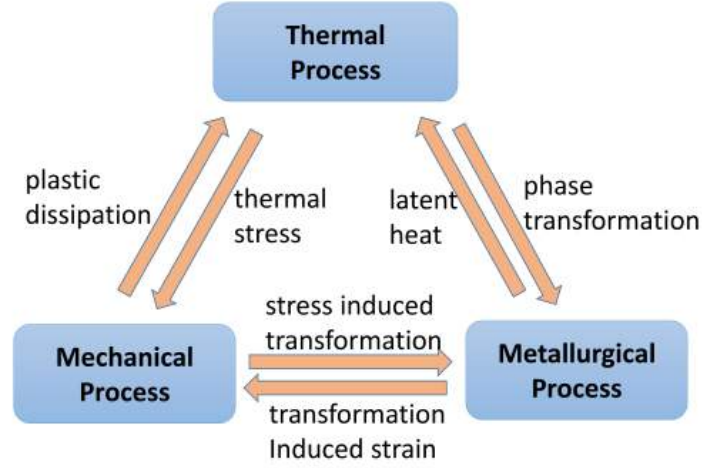


Figure 5.4: Diagram showcasing the multiphysics nature of the AM process (as a thermal-mechanical-metallurgical problem) [41].

expansion also has an effect on the thermal properties. However, it can be approximated that the plastic deformation induced friction heat is much smaller when compared to the thermal energy present in the system, leading to a weakly coupled or uncoupled model that is currently employed in most applications [59–61]. The following chapter will explore the theoretical formulation behind the AM process simulation.

5.2.3 Transient Thermal Problem Formulation

The temperature distribution in both space and time can be modelled by a heat equation,

$$\frac{\partial T}{\partial t} = \frac{k(T)}{c_P(T)\rho} \nabla^2 T + \frac{1}{c_P(T)\rho} \dot{Q}_v, \quad (5.2)$$

where T is the temperature field, $k(T)$ is the thermal conductivity coefficient, $c_P(T)$ is the specific heat, $\rho(T)$ is the density, and \dot{Q}_v is the volumetric heat flux, defined by,

$$\dot{Q}_v = \dot{Q}_{convection} + \dot{Q}_{radiation} + \dot{Q}_{laser}, \quad (5.3)$$

where $\dot{Q}_{convection}$, $\dot{Q}_{radiation}$ and \dot{Q}_{laser} define the volumetric heat flux contributions from convection, radiation and the heat source, respectively. Heat loss through convection happens between the shield gas (used to prevent oxidation) and the convective heat flux is given by,

$$\dot{Q}_{convection} = h(T - T_\infty), \quad (5.4)$$

where h is the convective heat transfer coefficient, and T_∞ is the ambient temperature in the AM machine chamber (shield gas).

Heat loss due to radiation is also present, even in a vacuum chamber setting [62]. Its effect is given by,

$$\dot{Q}_{radiation} = \epsilon\sigma((T - T_{zero})^4 - (T_\infty - T_{zero})^4), \quad (5.5)$$

where ϵ is the emissivity, σ is the Stefan-Boltzmann constant and T_{zero} is the absolute zero of a given temperature scale.

5.2.4 Heat Source Model

The laser heating process can be defined by different models, depending on the complexity of the AM simulation. In case the finite elements of the model are significantly larger than the size of the laser spot, a concentrated moving heat source can be defined. If the size of the finite elements is comparable to the one of the spot size, both the moving uniform heat source and the Goldak distribution models can be utilized.

5.2.4.1 Concentrated Moving Heat Source Model

As the name indicates, this heat source model defines a point energy source simply defined by the power of laser. Its application is suggested when dealing with coarse meshing of the part, such that the finite elements used are significantly larger than the spot size.

5.2.4.2 Uniform Heat Source Model

A commonly used heat source model is the moving uniform heat source, which defines a distribution of heat flux over a finite sized box whose size needs to be defined.

5.2.4.3 Goldak Heat Source Model

The Goldak double-ellipsoid model, like the uniform model, is a volumetric heat source mode, meaning that the changes in power density with respect with penetration depth are considered. The shape is combination of two half-ellipsoids connected over a semi-axis, such that two formulations describe it, depending whether the front or rear quadrants are considered. The model is described as follows,

$$\dot{Q}_{front} = \frac{4\sqrt{3}f_f Q}{abc_f \pi \sqrt{\pi}} \exp\left(-3\left(\frac{x^2}{c_f^2} + \frac{y^2}{a^2} + \frac{z^2}{b^2}\right)\right), \quad (5.6)$$

$$\dot{Q}_{rear} = \frac{4\sqrt{3}f_r Q}{abc_r \pi \sqrt{\pi}} \exp\left(-3\left(\frac{x^2}{c_r^2} + \frac{y^2}{a^2} + \frac{z^2}{b^2}\right)\right), \quad (5.7)$$

where $f_f + f_r = 2$, and f_f and f_r represent the distribution of the heat source at the front or rear, respectively. a , b , c_f and c_r are parameters that define the axes of both ellipsoids. See figure 5.5 for graphical representation of the shape parameters.

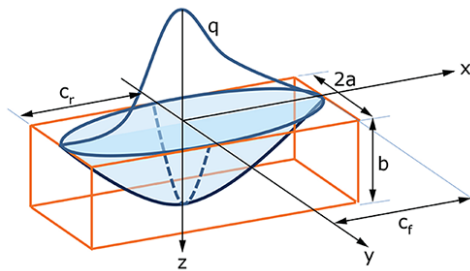


Figure 5.5: Goldak heat source [10].

5.2.5 Mechanical Problem Formulation for Residual Stress

A quasi-static incremental analysis is the approach used to solve the non-linear mechanical analysis problem. The governing conservation equation is expressed as,

$$\nabla \cdot \sigma = 0, \quad (5.8)$$

where σ is the stress tensor. The constitutive model considering elasto-plastic behaviour is given by,

$$\sigma = C\epsilon^e, \quad (5.9)$$

where C is the fourth-order material stiffness tensor, function of the Young's modulus E and the Poisson's ratio ν , and ϵ^e is the elastic strain tensor, which is simplified to the following equation in tensor notation, when considering isotropic material,

$$\epsilon_{ij}^e = \frac{1+\nu}{E}\sigma_{ij} - \frac{\nu}{E}\left(\sum_{k=1}^3\sigma_{kk}\right)\delta_{ij}, \quad (5.10)$$

where δ_{ij} is the Kronecker tensor. The total strain tensor ϵ consists on three parts, the elastic strain ϵ^e , the plastic strain ϵ^p , and the thermal strain ϵ^{th} [41], such that,

$$\epsilon = \epsilon^e + \epsilon^p + \epsilon^{th} = \frac{1}{2}[\nabla\mathbf{u} + (\nabla\mathbf{u})^T]. \quad (5.11)$$

The thermal strain, at a temperature T , is defined by the thermal expansion coefficient α , and the reference temperature T_0 . It is given by,

$$\epsilon^{th} = \alpha(T - T_0)\delta_{ij}. \quad (5.12)$$

To define the yield function criterion, taking into consideration the anisotropy from the AM process, the quadratic Hill yield function is used,

$$f(\sigma) = \sqrt{F(\sigma_{22} - \sigma_{33})^2 + G(\sigma_{33} - \sigma_{11})^2 + H(\sigma_{11} - \sigma_{22})^2 + 2(L\sigma_{23}^2 + M\sigma_{31}^2 + N\sigma_{12}^2)}, \quad (5.13)$$

where σ_{ij} are the normal and shear stress components, and F , G , H , L , M and N , are constant coefficients obtained from experimental testing of the material. They are functions of the anisotropic yield stress ratios, R_{11} , R_{22} , R_{33} , R_{12} , R_{13} and R_{23} , given by,

$$F = \frac{1}{2}\left(\frac{1}{R_{22}^2} + \frac{1}{R_{33}^2} - \frac{1}{R_{11}^2}\right), \quad (5.14)$$

$$G = \frac{1}{2}\left(\frac{1}{R_{22}^2} + \frac{1}{R_{33}^2} - \frac{1}{R_{11}^2}\right), \quad (5.15)$$

$$H = \frac{1}{2}\left(\frac{1}{R_{22}^2} + \frac{1}{R_{33}^2} - \frac{1}{R_{11}^2}\right), \quad (5.16)$$

$$L = \frac{3}{2R_{23}^2}, \quad (5.17)$$

$$M = \frac{3}{2R_{13}^2}, \quad (5.18)$$

$$N = \frac{3}{2R_{12}^2}. \quad (5.19)$$

The yield function is an extension of the von Mises criterion, such that, when all the yield stress ratios are equal to 1 ($R_{11} = R_{22} = R_{33} = R_{12} = R_{13} = R_{23} = 1$), in isotropic yielding conditions, the function is simplified to the von Mises criterion given by,

$$\sigma_{VM} = \sqrt{\frac{1}{2} [(\sigma_{11} - \sigma_{22})^2 + (\sigma_{11} - \sigma_{22})^2 + (\sigma_{11} - \sigma_{22})^2 + 6(\sigma_{12}^2 + \sigma_{23}^2 + \sigma_{31}^2)]}. \quad (5.20)$$

Finally, the enforcement of the von Mises criterion and the Prandtl-Reuss flow rule allow the computation of the plastic strain,

$$f = \sigma_{VM} - \sigma_Y(\bar{\epsilon}_p, T) \leq 0, \quad (5.21)$$

$$\dot{\epsilon}_p = \dot{\bar{\epsilon}}_p \mathbf{a}, \quad (5.22)$$

and,

$$\mathbf{a} = \left(\frac{\partial f}{\partial \boldsymbol{\sigma}} \right)^T, \quad (5.23)$$

where f is the yield function, σ_{VM} is the von Mises stress, σ_Y is the yield strength, $\bar{\epsilon}_p$ and $\dot{\bar{\epsilon}}_p$ are the equivalent plastic strain and equivalent plastic strain, respectively, and \mathbf{a} is the flow vector. The von Mises stress is one of the criteria used to assess the multiaxial stress state of isotropic materials, and is defined by equation 5.20.

5.3 Design Process Approach

The introduction of additive manufacturing in the development process of an aeronautical component brings forth major changes to the "traditional" design workflow. This chapter explores the different steps introduced to utilize, while not to its full extent, DfAM guidelines. Namely, the implementation of the structural optimization process, additive manufacturing constraints, and the printing process simulation for design validation purposes.

5.3.1 Current Design Process Approach

The current design process approach is presented such that structural optimization processes are excluded, and the manufacturing method is casting.

Considering the design process explored in the context of this thesis is an iteration over a previously existing component, a background analysis is performed on said component, as means to provide a baseline comparison for the proposed design iterations, and accurately set the application of loads and boundary conditions.

The definition of the design volume is initially set in order to define the geometrical volume constraint, based on the implementation of the specific component in an assembly setting. Such a geometrical constraint does not consider anything else other than the limit volume that the component can occupy. Starting from it, several different approaches exist to come up with a design that takes into consideration performance requirements, material/volume utilization and manufacturing constraints. The carry-over approach considers designs used in previous projects, rather than searching for a new conceptual design. On the other hand, the search for a new conceptual design generally is based on engineering judgement and a limited application of topology optimization tools. Since the design work is mostly manual, the number of iterations between the design and CAE engineer can be rather large, more so during the validation when critical regions are spotted. The design engineer needs to address these through material compensation, while optimizing other regions through material removal. These steps require a new round of validation and potential design engineer intervention.

Finally, depending on the manufacturing process chosen, additional design considerations need to be applied to the component, which again require validation before finally reaching the final design.

5.3.2 DfAM Guidelines in the Design Process Approach

It should be noted that the introduction of topology optimization and shape optimization processes in the design workflow is not novelty, and has previously aided design engineers. However, in the context of this thesis, DfAM tools are employed to streamline the design process, reducing as much as possible the number of iterations between a design proposal and the validation process, and automatizing the process through a thorough optimization definition and validation procedure.

The proposed design process workflow is represented in figure 5.6. The starting point is entirely the same, consisting on the background analysis performed on the current design. It stands once again to provide a baseline comparison to the proposed design iterations, and aid the accurate definition of loads and boundary conditions application. With it, fixed elements are also defined, which represent volume regions that are not meant to be altered during the design process. These typically are connection regions between other components and can be interpreted as load or boundary condition regions.

With the geometry definition of both the design envelope and fixed elements, the next step is to perform the topology optimization task. Following the conclusions obtained from the static analysis, the loads and boundary conditions are defined on the design envelope and fixed elements. The design objectives and requirements are carefully studied and understood, in order to properly define an optimization procedure that better caters at fulfilling them, be it through the choice of interpolation algorithm, or optimization objective function. Following the topology optimization process, the results are to be interpreted into a solid CAD part, able to be further edited and utilized.

The interpreted geometry is then validated against the requirements set for the topology optimization procedure, namely regarding linear and static events. If the structural performance is not on par with regards to these requirements, a change in the topology optimization task preparation is needed.

Succeeding the validation of the topology optimization design against its requirements, the remaining non-linear requirements are evaluated, namely the fatigue life performance. Shape optimization serves as the perfect candidate to smooth stress peaks and minimize the damage and increase the fatigue life of the component according to the relevant requirements. Additionally, the performance of the part under plastic regime can be assessed and optimize. Additionally, the shape optimization process can be made of several steps, each tackling specific requirements, such as stress peaks, and durability.

With a validated design from the structural optimization process, the design undergoes the typical AM process preparation, namely the introduction of support structures, and definition of process parameters (laser power, speed, and cooling timing, for example). The resulting structure with supports included undergoes a voxelization process, and the process parameters a translation process into the input files needed to accurately model the AM simulation in Abaqus.

The results of the AM simulation highlight the performance of the component under the complex thermal-mechanical-metallurgical simulation, namely opening the possibility to optimize the process with respect to the part itself. However such appreciation is beyond the scope of this thesis, which limits itself to obtaining the results to be compared to experimental ones in the future.

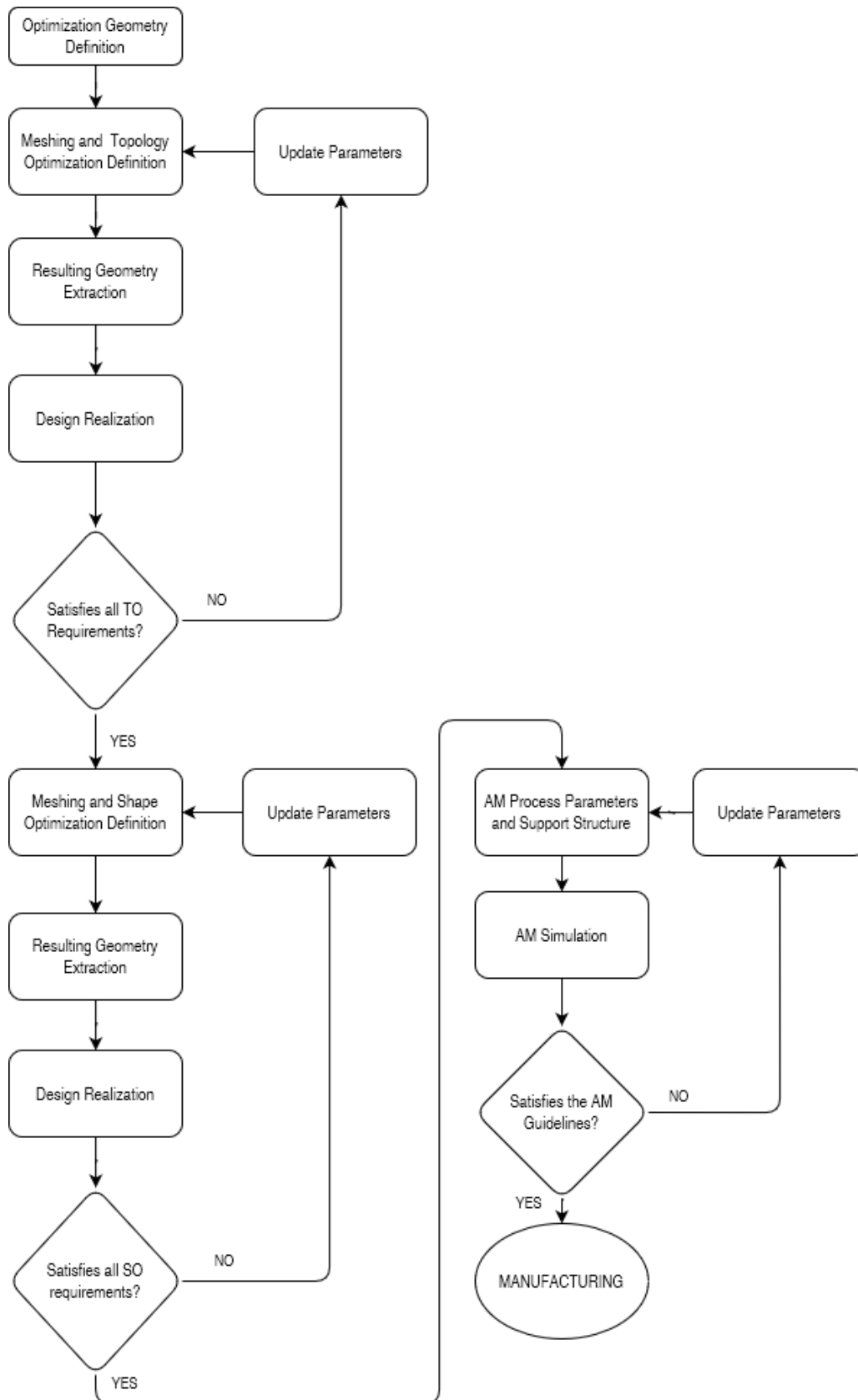


Figure 5.6: Proposed design process workflow with DfAM considerations.

Chapter 6

Additive Manufacturing

Thermal-mechanical Simulation

Methodology

The present chapter focuses on the workflow and pre-processing required to accurately simulate the SLM AM process, together with the application of the methodology to AMB2018-01 Additive Manufacturing benchmark problem defined by the National Institute of Standards and Technology (NIST) [63].

6.1 AM Process Simulation Workflow

The modelling of the SLM process requires the consideration and definition of the following process elements,

- Toolpath/scan path information;
- Progressive material deposition information;
- Thermal-structural material properties;
- Laser/heat input properties;

The implementation into a commercial FEM software While software dedicated to AM simulation exists, it is commonly associated with specific machines, which results license and data format limitations. This added difficulty is overcome with the use of Abaqus and the built-in user subroutines and mesh intersection tools, together with the software Autodesk Netfabb. This last one will be used to both slice the component, and define the scan path based on the AM machine parameters.

6.2 Toolpath-Mesh Intersection

The representation of both the laser source and the recoater roller is done through a toolpath, which is defined by a given geometry following the movement of a reference point along a given path. The main geometries of interest are the point and infinite line, respectively for the laser source and the recoater roller. However others can

be considered for different application, such as the box geometry, useful to characterize the material deposition in polymer extrusion or wire-feed methods. The different geometries can be seen in figure 6.1.

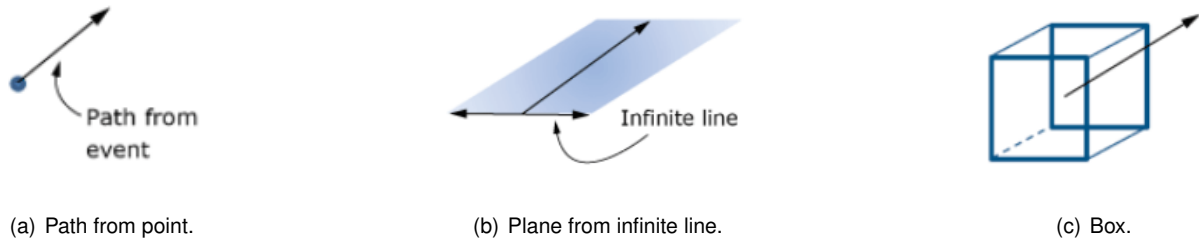


Figure 6.1: Toolpath-mesh intersection geometric options [10].

6.2.1 Event Series

The event series are a functionality in Abaqus that define time and space varying fields, independently of both the mesh and the simulation time increment. The field definition is done through a step function representation, linearly discretised in both space and time. Any event series has a fixed format set for both mandatory time and space definitions, to which a maximum of six user defined fields or dependent variables can be added.

Two event series are of particular interest in the simulation of the powder bed AM method, namely for the definition of the recoater roller motion, and the laser power, both defined in both time and space. The roller event series is used to progressively activate elements, and assumes a boolean dependent variable, such that it is equal to 1 when the roller is passing, and 0 otherwise ("on or off" states) (table 6.2). On the other hand, the laser event series is used to define the laser power such that the laser heat flux can be calculated (table 6.1).

Time (s)	x (mm)	y (mm)	z (mm)	Laser power (mw)
-------------	-----------	-----------	-----------	---------------------

Table 6.1: Laser path event series format [10].

Time (s)	x (mm)	y (mm)	z (mm)	Recoater roller "on or off" state
-------------	-----------	-----------	-----------	--------------------------------------

Table 6.2: Recoater roller event series format.

6.2.2 Material Deposition and Progressive Element Activation

Progressive element activation in Abaqus is employed to simulate the material deposition event that occurs in powder bed-type AM processes, due to the layer-by-layer raw material deposition from each recoater roller passage.

The path taken by the roller is represented by an infinite line moving along the same direction as the roller, defining a plane parallel to the new layer, and perpendicular to the printing direction. Such infinite line intersects the finite element mesh, either partially or fully activating said elements and progressively adding them to the numerical model. Figure 6.2 showcases the intersection of the infinite line with an element, here named as E. The line's path is linear, connecting the points $(X_1, X_2, X_3, \dots, X_n)$, each defined in time $(t_1, t_2, t_3, \dots, t_n)$, and the line moves at constant velocity between these. The event series representing the state of the roller is defined by a boolean "on/off" state. Either the roller is depositing material, or it is not. The toolpath-mesh intersection module is employed merely when the the state of the roller is "on". When an intersection occurs, for affected element, the volume fraction v_i

is defined, corresponding to the ratio between the partial element volume below the plane of the passing element infinite line, and the total element volume.

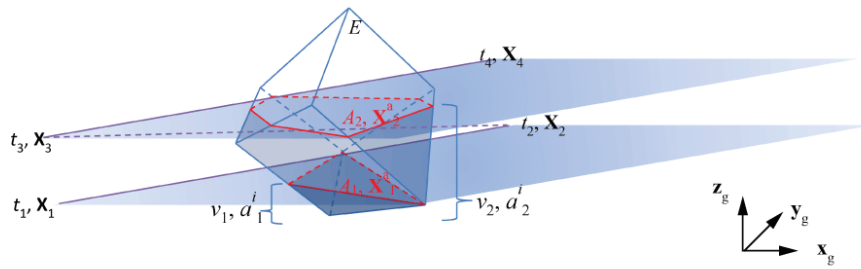


Figure 6.2: Schematic of two infinite lines intersecting an element at two different regions.

6.2.3 Moving Heat Flux and Progressive Heating

The newly deposited layer of raw material is fused due to the passage of the heat source, characteristic of the AM process of interest (laser, electron beam, etc.). This makes the modelling of the heat source essential to properly define the AM process, mainly through its scan path, with regards to power in space and time coordinates, as well as the heat distribution type. The last defining element depends on the simulation scale, such that, for a low resolution resolution simulation (coarse mesh with several layers per element size), a concentrated moving heat flux is a valid approximation; whereas for a high resolution simulation (fine mesh with at least 2 to 3 elements per layer, and 4 to 5 elements in the melt pool for each direction), volumetric heating source yields accurate results, with main emphasis on the use of a Goldak distribution.

6.3 Abaqus user subroutines and AM modeler plug-in

The AM process simulation in Abaqus is aided by the existence of in-house developed user subroutines and the AM modeler plug-in, made publicly available by Abaqus. The details of both tools are explored in this section and detailed as follows.

6.3.1 User subroutines

User subroutines are implemented to increase the capabilities of Abaqus to simulate the AM process [10]. Two particular subroutines are utilized to aid the simulation of both the moving heat flux and the progressive element activation process. These are *UMDFLUX* and *UEPActivationVol*, and the respectively accompanying data setup subroutines *UMDFLUXSetup*, and *UEPActivationSetup*.

UMDFLUXSetup provides the required data structures to the Mesh Intersection Tool, such as mesh and event series details related to the moving heat source at the start of the step. At the beginning of the increment it is once again called to compute the heat flux per element, based on the intersection between the event series laser path and the mesh.

UMDFLUX is responsible for the definition of the heat flux distribution of multiple moving heat sources, continuously with respect to time and space. The subroutine accounts for different heat source models, such as the Goldak heat source model and the concentrated point energy source model (with particular relevancy as it is used in the present thesis). It provides an upgrade over the previously used *DFLUX*, which was restricted to a stationary flux

(that consequently means a transient analysis is not possible), and required element knowledge to define the path of the heat source [10]. On the other hand, *UMDFLUX* allows for a continuous definition of one or more fluxes, that do not depend on the mesh and instead are based on the event series information. For each element, the subroutine obtains the total flux for each event provided by the Mesh intersection Tool during *UMDFLUXSetup*.

UEPActivationSetup, at the beginning of the step, creates and provides to the Mesh Intersection Tool the required data structures to perform the progressive element activation, with accordance to both the mesh and the recoater roller event series. On the other hand, at the start of the increment it triggers the Mesh Intersection Tool to compute the intersection between the recoater roller event series and the mesh for the specific increment time interval. The volume fractions are stored by the Mesh Intersection Tool.

UEPActivationVol obtains the volume fraction previously computed by *UEPActivationSetup* at the start of the increment for each element of interest. The volume fraction increase defines the partial element activation process.

6.3.2 AM modeler plug-in

The AM modeler plug-in is developed and made available by Abaqus, with the main goal of aiding the definition of the necessary keywords that coordinate the extensive data needed by the user subroutines. It requires the previous definition of both thermal and structural models, both the heat source path and recoater roller event series, and the simulation parameters.

The provided user interface first requires the creation of the AM Model, as per the window in figure 6.3. The thermal and structural models, and the printing steps of interest need to be introduced. Secondly, the AM Modeler tree is populated with the different section that define the AM simulation. These are the Data Setup, Model Setup, and Simulation Setup.

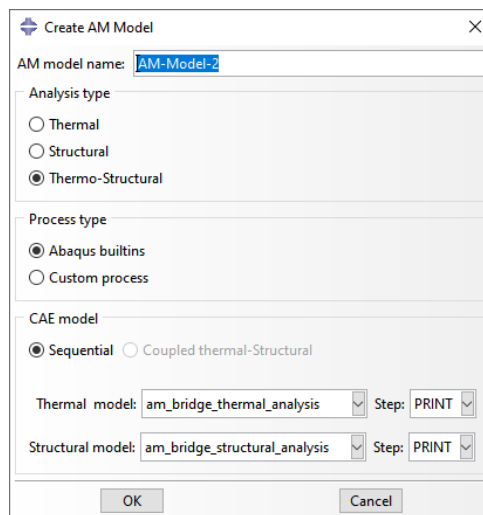


Figure 6.3: Create AM Model AM modeler Abaqus window.

6.3.2.1 Data setup

The Data Setup tab contains the items that allow the definition of the event series (see subsection 6.2.1) required, as well as the parameter tables, property tables, and the respective table collections. The parameter tables used are predefined by the plug-in package and group parameters that do not depend on time, space or material

state. For example, the "ABQ_AM.MaterialDeposition", as seen in figure 6.4(a), groups the parameters referring to the material deposition process, these being the type of process, i.e. recoater roller or bead, and its event series.

On the other hand, property tables group and define parameters dependent on the temperature, field and simulation state variables. As an example seen in figure 6.4(b), the property table "ABQ_AM.AbsorptionCoeff" defines the laser absorption coefficient.

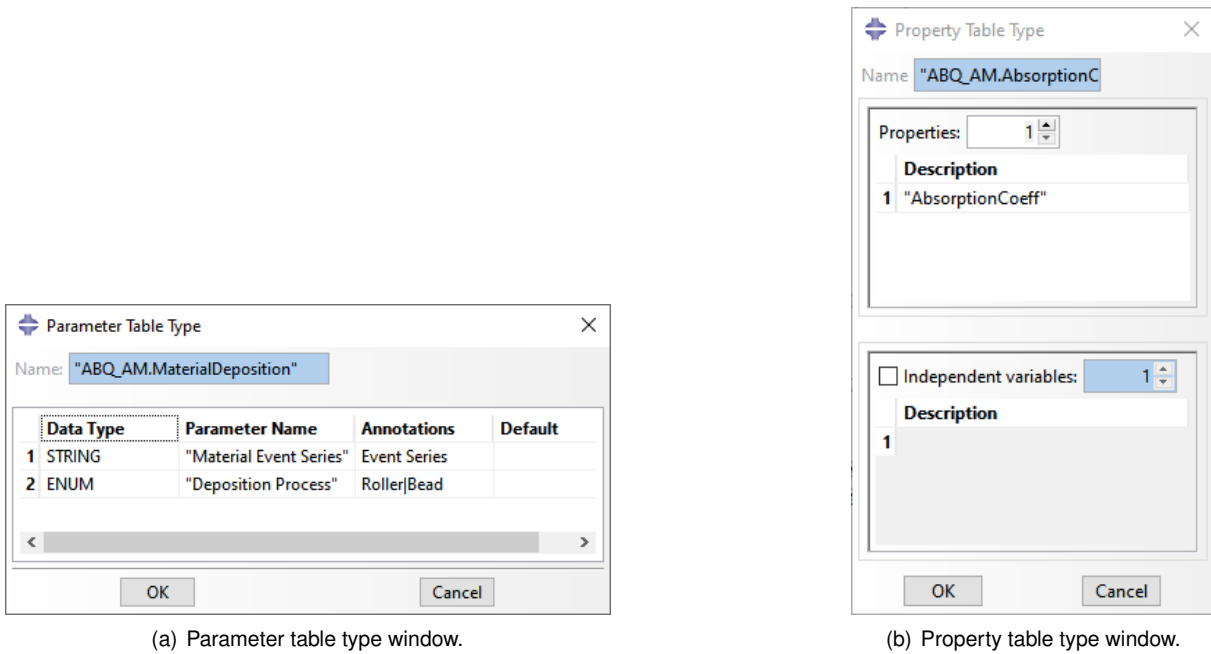


Figure 6.4: Parameter and property table type windows in Abaqus.

Finally, the table collections are a large grouping that encapsulates the previously defined parameter and property tables to be referenced in the user subroutines mentioned in 6.3.1. In these the values and parameters for the previous tables are defined. As an example (see figure 6.5), the "ABQ_AM.Roller" (name defined by user) utilizes both "ABQ_AM.MaterialDeposition" and "ABQ_AM.MaterialDeposition.Advanced", as the parameters tables to be utilized by the respective subroutine.

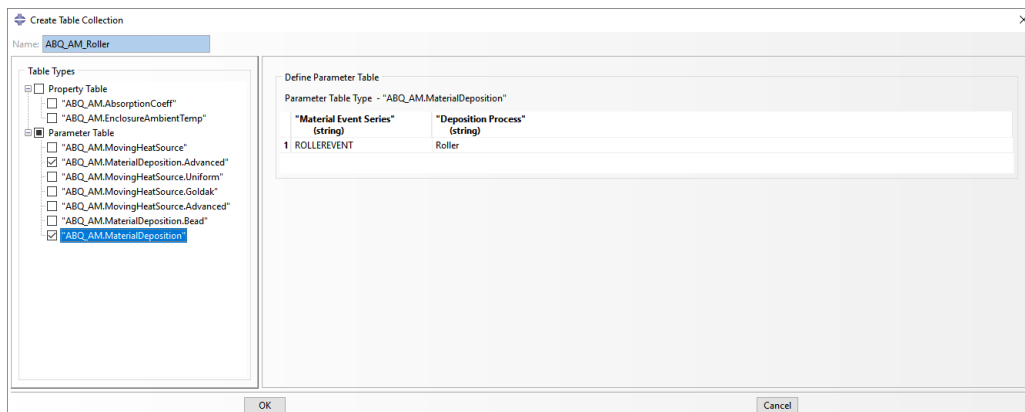


Figure 6.5: Create table collection windows in Abaqus.

6.3.2.2 Model setup

The model setup tab is less extensive than the two other tabs, as it is used solely to select the model parts to be included in the AM process simulation, as well as to graphically visualize the event series data previously introduced, both in time and space, with the model in the background (see figure 6.6).

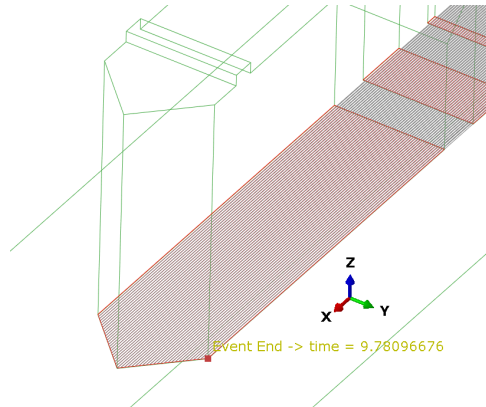


Figure 6.6: Event viewer example with a laser path.

6.3.2.3 Simulation setup

Finally, the simulation setup is used to define the material arrival, and the heating and cooling processes. The material arrival is defined by the recoater roller table collection. Additionally, the heating tab selects the moving heat source table collection, and the cooling tab defines both the convection and radiation cooling process parameters.

6.4 AM Simulation Geometry Pre-Processing

The geometry pre-processing process is divided into three major steps, these being,

- Printing support design and generation;
- Voxelization;
- Part slicing and scan path information.

With the CAD geometry of the part to be printed, firstly the supports need to be designed and generation alongside the part. The generation should result in a new mesh file containing both the original part as well as the support. Following this procedure, the new mesh file is rasterized in order to create a voxelized representation of the part and supports. The result of the procedure is a regular hexahedral element based mesh, constructed along the printing direction. Finally, the resulting mesh can be exported as a STL file and imported again in a slicing software to obtain the scan part information, such as the power, and spatial and time coordinates of the AM process specific heating source.

6.4.1 Printing support design and generation

Despite the importance of the supports during the additive manufacturing process, and the role that the present simulation plays in the optimization and choice between different types, such a focus goes beyond the content of the present thesis.

However, their implementation is still mandatory to accurately simulate the process, and the tool chosen to do so was Autodesk Netfabb. It allows for high customization of both the support structure geometry and topology, as well as the definition of the critical regions that warrant the presence of said support.

6.4.2 Voxelization and voxel-based meshing

The voxelization of a continuous geometry consists on the discrete subdivision of such a geometry into cells or voxels. According to [64], a voxel is defined as *an image of a three-dimensional space region limited by given sizes, which has its own nodal point coordinates in an accepted coordinate system, its own form, its own state parameters that indicates its belonging to some modeled object, and has properties of modeled region*. For our intents and purposes, each voxel is defined by the same geometry of a regular hexahedral finite element, and the volume fraction property. The volume fraction property is a scalar discrete field that characterizes the intersection between a continuous geometry (reference geometry) and a finite element mesh (intersection grid).

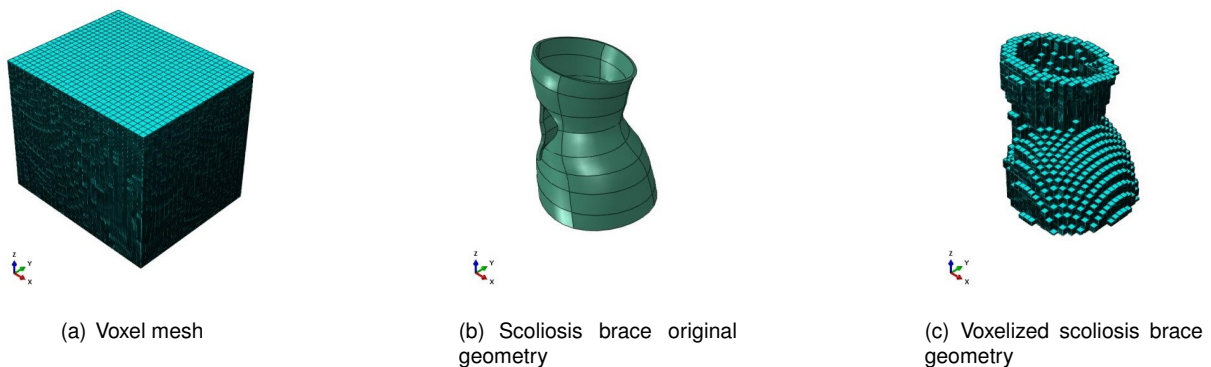


Figure 6.7: Voxelization process example by [65].

The implementation of the voxelization therefore starts with the definition of of the parts needed for the intersection. These are,

- **Reference Geometry:** A CAD file of the part to be printed (see figure 6.7(b)), which will be transformed to a voxel-based geometry;
- **Intersection Grid:** A hexahedral element-based mesh that bounds the reference geometry (see figure 6.7(a)). The elements should have a pair of faces perpendicular to the printing direction, to mimic the progressive layer deposition and facilitate both the progressive element activation, and the heating of the elements from the moving heat flux.

The assembly of both components is such that the intersection grid part completely encapsulates the reference geometry, so that all possible details are captured.

With the definition of the volume fraction of all the grid elements, the ones characterized by a value higher than zero are aggregated into an element set and exported. A MATLAB script (A) was created to extract the element and node set, and create an INP file of an Abaqus importable native mesh.

From the description of the process, its apparent that the quality of the geometrical approximation is dependent on the dimensions of the intersection grid. However a higher resolution intersection grid warrants more computational resources, so a balance must be found such that important details are accurately captured, and the simulation is feasible to be ran in the time frame of this thesis.

Despite further comparisons between conventional meshing with tetrahedral elements, and voxel-based meshing with hexahedral elements being necessary, key features of both methods hold the following items apparent,

- The voxel-based mesh showcases an uniform meshing grid, constructed based on the progressive layer deposition characteristic of a powder bed AM process. The progressive element activation module relies on the intersection between an infinite line and the elements part of each layer. Since the voxel-based mesh is constructed along the printing direction, each element is activated equally to its neighbouring elements in the layer plane, potentially improving convergence of the simulation;
- The conventional mesh does a better job at representing the surface of the part, whereas the voxel-based one exhibits a jagged representation of curved surfaces (see figure 6.7(c)), which can lead to stress concentration spots;
- Given the project workflow, where the resulting surface from the optimization is transformed into a solid CAD file, the solid product of the transformation is characterized by the same surface facets of the surface mesh file, making it a large file to both edit and handle in Abaqus. The transformation to an adequately sized voxel-based mesh means a less complex geometry to work with, as well as less computational resources consuming;
- The likelihood of bad elements being present is reduced with the use of a voxel-based mesh, in spite of the geometrical complexity of the original part.

6.4.3 Part slicing and scan path information

With the aim of achieving a generalized workflow applicable to any machine parameters and complex geometry, it is firstly studied how to take advantage of Autodesk Netfabb's geometry slicing and support structures creation capabilities, as well as the AM process set-up, and import this information into FEM simulation, namely in Abaqus. It should be noted that an open source approach is possible, namely through the use of software based on the Skeinforge tool chain, which allows to slice STL files and convert them into G-Code instructions based on the defined AM process parameters. However, due to the academic access to Autodesk Netfabb's slicing tool, and the software's wider array of output file formats, it was deemed the tool that best fit the project workflow.

The slicing process depends on the geometry itself, part orientation, build direction and printing layer size, which are parameters Netfabb allows to adjust. As these are set, the software proceeds to cut the tessellated triangles such that each layer is made up of closed polygons that constitute the cut surface. These closed perimeters are defined as walls or contours, whereas the inside region is the infill.

The hatch filling geometry is defined through the set of parameters made available in Autodesk Netfabb and is automatically added to each layer. The main parameters of interest that drive the hatch filling creation are the following,

- **Hatch type:**
 - Simple hatching;
 - Stripe hatching;
 - Quad islands;
 - Checkerboard hatching;
 - Radial hatching;

- **Hatch distance:** Distance between consecutive hatch lines;
- **Angle:** Angle of the hatching in the first layer;
- **Angle increment:** Angle increase per consecutive layer basis;
- **Regionalisation:** Splits hatching progress per closed polygon (see figure 6.8).

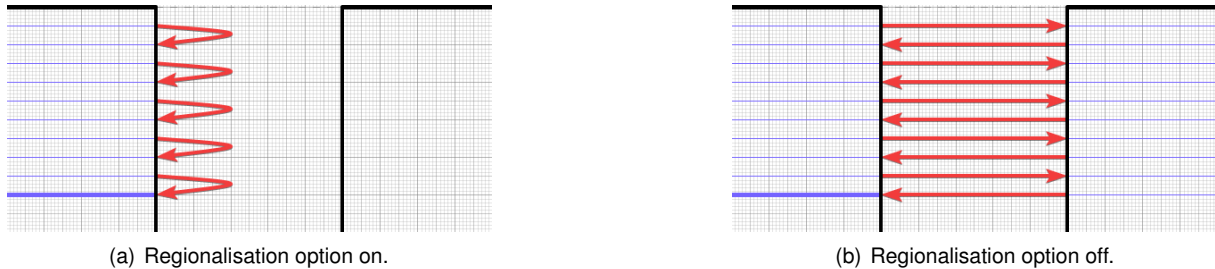


Figure 6.8: Regionalisation examples.

Finally, with the entirety of the scan path defined geometrically, the speed of the laser and its power remain to be set. The parameters can be defined separately for both the contour and the infill, allowing to define the position of the laser both in space and time. The output of the slicing process is chosen to be the laser vector LSR file format.

6.4.4 LSR file analysis and translation to INP file format

The LSR file format (.lsr) was chosen due to its description of the scan path both in time and space, as well as the laser power for each trajectory. While primarily used for a Direct Energy Deposition process workspace, the file format presents the needed data for the SM process simulation concisely, making the translation process as simple as possible. The file has the format showcased in table 6.3, with a practical example in figure 6.9.

Laser Power (W)	Laser Vector (mm)	Start Point (mm)	End Point (mm)	Heat Source Radius (mm)	Deposition Speed (mm/s)	Laser Vector Start Time (s)
-----------------	-------------------	------------------	----------------	-------------------------	-------------------------	-----------------------------

Table 6.3: LSR file format.

```

0.631354,29.600000,22.400000,0.060000,250000.000000
0.631799,29.600000,22.000000,0.060000,0.000000
0.631799,29.600000,22.000000,0.060000,250000.000000
0.633132,30.800000,22.000000,0.060000,0.000000
0.633132,30.800000,22.000000,0.060000,250000.000000
0.633577,30.800000,22.400000,0.060000,0.000000
0.633577,30.800000,22.400000,0.060000,250000.000000

```

Figure 6.9: LSR file example.

On the other hand, the INP file format (.inp) is used to define the event series, and has a set format, where each row is separate entry, with parameters separated by commas, with the format showcased in figure 6.10.

```

250.000 0.000 0.000 -1.000 31.319 24.800 0.060 29.200 24.800 0.060 0.500 900.000 0.044
250.000 0.000 0.000 -1.000 29.200 24.800 0.060 29.200 24.000 0.060 0.500 900.000 0.047
250.000 0.000 0.000 -1.000 29.200 24.000 0.060 28.800 24.000 0.060 0.500 900.000 0.048
250.000 0.000 0.000 -1.000 28.800 24.000 0.060 28.800 22.800 0.060 0.500 900.000 0.048
250.000 0.000 0.000 -1.000 28.800 22.800 0.060 29.200 22.800 0.060 0.500 900.000 0.049
250.000 0.000 0.000 -1.000 29.200 22.800 0.060 29.200 22.400 0.060 0.500 900.000 0.050
250.000 0.000 0.000 -1.000 29.200 22.400 0.060 29.600 22.400 0.060 0.500 900.000 0.050

```

Figure 6.10: INP file example.

The translation between both file formats is done through a MATLAB script (A), which takes as input the LSR file, together with a series of process parameters to be set by the user, such as the roller velocity, inter-layer cooling time and geometrical parameters. The output of the script are the three following files,

- **Laser path and power INP file** - file containing the time and space coordinates, and power of the laser heat source;
- **Recoater roller INP file** - file containing the time and space coordinates, and "on or off" state of the recoater roller;
- **Simulation time increment MAT file** - file containing the simulation time steps to be introduced in Abaqus.

6.5 Low Resolution Thermo-Mechanical Simulation in Abaqus

The AM process is multi-scale defined, both in time and space, such that a simulation of all resolution levels is not feasible with limited computation resources. Depending on the application and area of interest, performing the simulation at a specific level of resolution that yields the results and conclusions needed is satisfactory.

A high resolution approach warrants a fine mesh (typically with an element length comparable to the printing layer size) and small enough time increment, able to capture near-field high temperature gradients, and the active melting and fusion processes. The modelling of the laser source should also match the high resolution approach by providing a detailed laser volumetric energy distribution model, namely through the implementation of a Goldak heat source model. Such an accurate approach is particularly useful to predict material phase transformations and the microstructure evolution of the part during printing, as well as detailed and accurate prediction of residual stresses and distortions, culminating in a complete thermal-mechanical-metallurgical analysis of the AM process. However, the drawback of such a detailed model is the high computational cost associated with it, as well as convergence issues due to the nonlinear and temperature dependent material properties.

In order to achieve a computationally efficient simulation, a lower resolution simulation is proposed, using a coarser mesh (element size larger than than a unitary printing layer thickness), a larger time increment and a concentrated moving heat source model. The larger time increment results in the lumping of the printing events, such that the near-field action is not accurately captured, but instead its effect is averaged and the far-field region is described. Therefore, since the local temperature gradients are not captured, accurate information on the the melting and solidification process is lost. Without additional modelling steps to reintroduce these effects on the simulation, the annealing effect on residual stresses would not be accounted for.

6.5.1 Annealing effects simulation

The annealing effect is introduced through a stress relaxation process that occurring at a relaxation temperature T_{relax} , which can be determined experimentally. As the time step of the low resolution simulation is not enough to capture the high temperature peaks at the melting spot, an initial temperature is applied to each newly activated element, such that it defines the initial thermal contraction during the structural simulation. As such, the value chosen for the present thesis is taken from literature, and specifically for Ti-6Al-4V, it is $T_{relax} = 963K$ [66].

6.5.2 Thermal simulation definition

The uncoupled thermal-mechanical simulation is initialized by the definition of the thermal history of the process. The approach taken in this thesis focuses on a transient thermal analysis, with a duration longer than the one of

the printing of the part itself, to allow for part cooling. However, the time increments are chosen to be large enough such that the simulation is completed in a reasonable amount of time for the time frame of the project, as well as to accurately capture the energy balance of each physical layer.

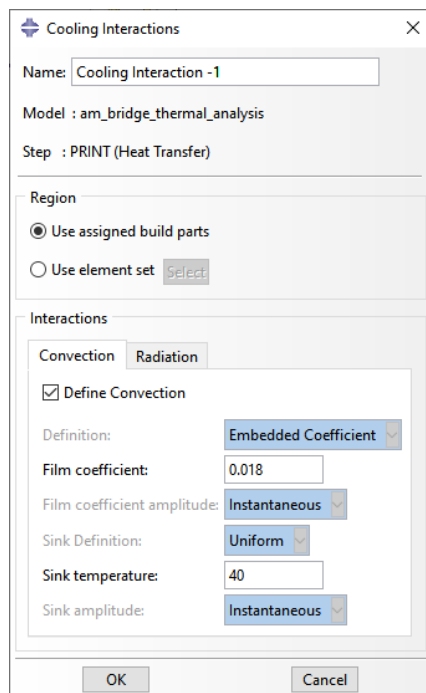
6.5.2.1 Initial and boundary conditions

Both the initial and boundary conditions are essential to accurately represent the temperature evolutions of the part during printing. In order to define substrate process heating, a temperature boundary condition is applied to the bottom of the build plate part T_{sub} . Separately, the powder bed pre-heating effect is defined by a predefined field applied to the entire build plate in the initial step, named T_{pre} .

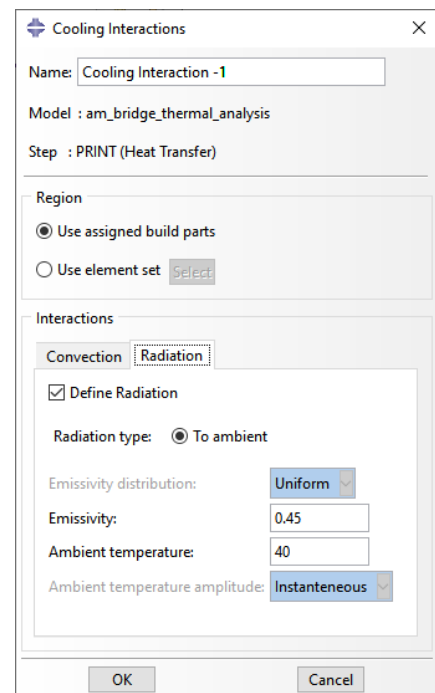
The initial temperature of the deposited powder from each printing layer, T_{part} , is also set through a pre-defined field applied to the printing part.

6.5.2.2 Cooling effects

Progressive cooling is present throughout the entire building process, namely through both convection and radiation effects. Both are defined in Abaqus through the AM plug-in interface in the dialogue box specifically detailing the cooling process of the simulation (see figure 6.11).



(a) Convection tab.



(b) Radiation tab.

Figure 6.11: Cooling settings windows in Abaqus.

Heat loss due to radiation is defined by the ambient temperature, T_{amb} inside the printing chamber (typically the inert gas Argon), as well as the emissivity of the exposed surface of the part, ϵ . On the other hand, heat loss through convection also takes place, with the key-parameter heat transfer or film coefficient, h . It is defined according to the inert gas atmosphere present in the printing chamber.

Partial element activation plays a role on the cooling effects due to both convection and radiation, as it allows to change the exposed surfaces of the elements cut by the activation plane, and apply the effects to said internal

surfaces. For example, in figure 6.12, the partially activated element defined by the nodes $A - B - C - D$ is cut by an element activation plane through the points $I_1 - I_2 - I_3 - I_4$. It is therefore possible to choose the internal surface defined by I_i as the surface through which both convection and radiation effects take place.

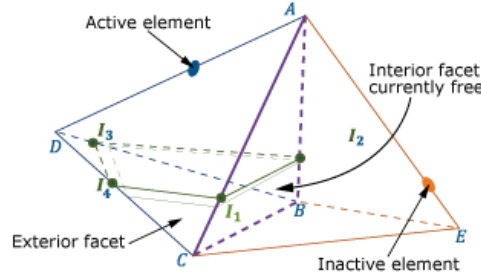


Figure 6.12: Schematic of partial element activation in an element [10].

6.5.2.3 Job Definition

Due to the non-linear material behaviour present in thermo-mechanical AM process simulations, and the potential presence of large deformations and temperature gradients, convergence issues may arise, such that a set of purposeful steps are presented in order to prevent them. Namely in the thermal simulation, potential issues may appear with the use of temperature-dependent material conductivity, and consideration of latent heat effects.

During a low-resolution AM process simulation, melting and solidification effects are not accurately captured, hence they do not pose a potential converge issue. However, with the potential progress to a higher-resolution simulation, a smooth transition or extension of the solidus-liquidus internal energy are available. The smooth transition is governed by the following internal energy, U_θ equation,

$$U_\theta = (L)\xi^3 (10 - 15\xi + 6\xi^2) \quad \text{if } \theta_S \leq \theta \leq \theta_L, \quad (6.1)$$

where,

$$\xi = \frac{\theta - \theta_S}{\theta_L - \theta_S}, \quad (6.2)$$

such that,

$$\frac{\partial U_\theta}{\partial \theta} \Big|_{\theta=\theta_S, \theta_L} = 0, \quad (6.3)$$

where L is the latent heat, θ_S and θ_L are the solidus and liquidus transition temperatures, respectfully.

The interval can also be extended through the use of a scale factor, SF , which defines new solidus-liquidus temperatures. The new temperatures are given by,

$$\begin{cases} \theta_S^{new} = \frac{1}{2} (\theta_S + \theta_L - SF (\theta_L - \theta_S)) \\ \theta_L^{new} = \frac{1}{2} (\theta_S + \theta_L + SF (\theta_L - \theta_S)) \end{cases} \quad (6.4)$$

The plot 6.13 showcases both the smoothing and extension of the temperature interval for several different scale factors.

However, since temperature-dependent conductivity is specified, its non-linearity consequently results in an unsymmetrical system of equations. Therefore, during the step definition, unsymmetric matrix storage and solution scheme can be used to further improve convergence [10].

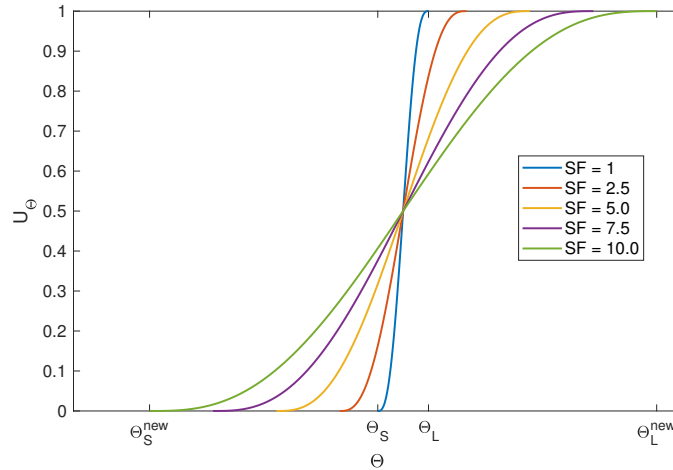


Figure 6.13: Smoothing and temperature interval extension for several scale factors.

6.5.3 Structural simulation definition

Following the sequential uncoupled nature of the AM process simulation in Abaqus, the mechanical field is driven by the results of the thermal simulation.

The same laser-path and recoater roller event series INP files are needed, in order to properly activate the elements. Additionally, the solution ODB file from the thermal simulation is required, as it carries both the time and space temperature field information. Identically, for numerical simplicity, the same mesh geometry is shared between the thermal and structural simulations, with the sole difference being the transformation of heat transfer elements into general 3D solid elements.

6.5.3.1 Initial and boundary conditions

A notable difference between the preprocessing needed for both the structural and thermal simulations under a low-resolution assumption is the need to define the initial temperature of elements as they're activated, as the relaxation temperature, T_{relax} , during the structural analysis.

Contrastingly with the thermal simulation, displacement constraints are needed to ensure that both the part and substrate are properly placed for the structural analysis. In fact, the constraint is applied purely to the building plate. The building part itself is defined through the tie constraint connection with the building plate (see figure 6.14 for schematic of the mechanical boundary condition application to the assembly).

Finally, the results of the thermal simulation are introduced through a predefined field, that refers to the ODB file of the thermal analysis.

6.5.3.2 Job definition

Due to the complexity of the analysis, convergence issues may also arise during the mechanical simulation. More precisely, three main sources of potential divergence are identified, to which solutions to mitigate their impact will also be showcased.

The first regards the heavy distortion that may occur during the simulation. As such, Abaqus allows for inactive elements to follow the deformation of the active ones. While this may in fact lead to improved convergence, according to the results showcased by [67], the resulting distortion is potentially unrealistically high. The same research

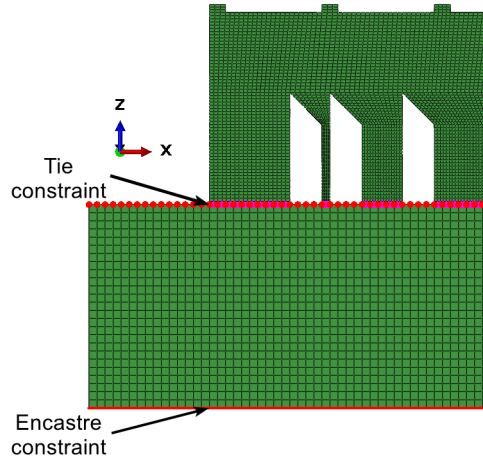


Figure 6.14: Boundary condition applied to the bottom surface of build plate, and the tie constraint interaction between it and the printing part.

also found that the option yields higher runtimes compared to not using the option.

The second source of convergence issues is related to the instantaneous application of thermal strains to the part as the elements are activated. Such circumstances can be viewed as equivalent to the application of an instantaneous load, which can lead to convergence problems. As for mechanical loads there is the possibility to ramp these up over time, the same is permitted by Abaqus during the element activation process. The thermal strain ramping up is linearly defined by the equation,

$$\epsilon^{th}(t) = \begin{cases} \left(\frac{t-t_{act}}{\tau_{th}} \right) \epsilon_0^{th} & \text{if } t_{act} \leq t \leq t_{act} + \tau_{th} \\ \epsilon_0^{th} & \text{if } t > t_{act} + \tau_{th} \end{cases}, \quad (6.5)$$

where t_{act} is the activation time, τ_{th} the expansion time constant defined by the user (equal to twice the initial increment time value by default), $\epsilon^{th}(t)$ the applied thermal strain at time t , and ϵ_0^{th} the strain at the end of the time increment of the element activation. If to be applied instantly, the user should set $\tau_{th} = 0$. The definition of the approximation is entirely dependent on the expansion time constant, with particular attention that it should be smaller than the time needed to process a new physical layer, so that the new layer experiences an accurate, fully-ramped strain-free configuration in the underlying layer.

Finally, an additional source of convergence problems regards the inclusion of plasticity in the material properties when the extrapolation methods are present. It may cause excessive iterations, such that the solution is to disable the extrapolation feature.

6.5.3.3 Support removal

Additionally to the AM process simulation, one can explore the impact of several post-printing processes, such as the support structure removal and heat treatments.

Support removal is performed at a single static step, after the printing step. It is defined by a model change interaction that removes the support structure elements, namely the ones connected to the printed part.

6.5.3.4 Post-processing simulation

In order to reduce residual stresses, and consequently part distortion, heat treatments are commonly performed. They can be added to the AM simulation workflow, however their inclusion will be omitted from the present thesis. Such a task has been developed and applied in [68], with results in line with the expected ones obtained from an experimental heat treated part.

6.6 Benchmarking simulation

With the main goal of establishing and validating the proposed AM process simulation workflow in Abaqus, the 2018 AM-Bench challenges and consequent submissions were studied. Namely, challenge AMB2018-01 was used, as it focused on part deflection and residual elastic strains. More specifically, challenges CHAR-AMB2018-01-PD and CHAR-AMB2018-01-SD target the modelling of part deflection and residual elastic strains, respectively [69].

The challenges and measurements are proposed by the National Institute of Standards and Technology (NIST), to which several dozen submissions have been made. Presently, posteriorly the results of the challenges being evaluated, NIST has made the experimental results publicly available, to which the simulation ones should be compared against. This data provides a baseline example for the AM process simulation implementation defined in the present thesis, with concrete data points to put side-by-side. The challenges also gave origin to several research teams tackling them, contributing to the development and improvement of the AM process simulation space.

6.6.1 Part geometry and mesh design

The geometry is made available as an STL file in the NIST website [63]. The file (present in figure 6.15), contains both the build plate, as well as four identical printing parts equally spaced by 20mm along the Y-axis.

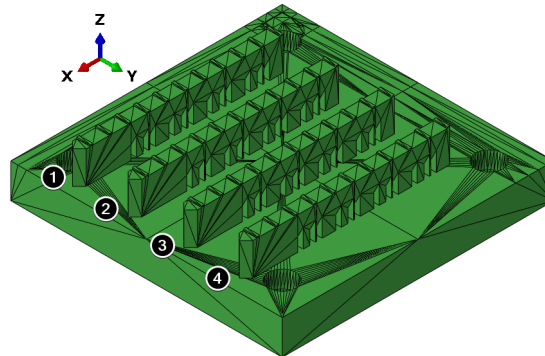


Figure 6.15: STL geometry provided by NIST with four clear parts [63].

However, only one of the parts is needed for the computational assessment, and to be in accordance with the work developed in [70], the mesh files made available by the team were used to define the geometries and mesh used in Abaqus. Both parts are then defined as orphan meshes simply containing nodes, elements and surfaces and sets information, with no geometrical features or associated geometry. The build plate has the dimensions of $90\text{mm} \times 15\text{mm} \times 12.7\text{mm}$ ($x \times y \times z$), and the bridge of $75\text{mm} \times 5\text{mm} \times 12\text{mm}$, comprised of twelve legs, with a total of three different sizes (see figure 6.16(a)).

The assembly is defined by the centring on the bridge part on the top surface of the build plate (see figure 6.16(b)). The surfaces of the two parts are coincident in the contact region, which means no clearance is defined

6.6 outline the considered temperature-independent properties of Inconel 625, whereas the plots 6.17 outline the temperature-dependent properties.

Parameter	Value
Density (tonne/mm ³)	8.44E-9
Absolute zero (°C)	-273.15
Liquidus temperature (°C)	1350
Solidus temperature (°C)	1290
Latent heat of fusion (mJ/tonne)	272E9
Film coefficient (mW/mm ² °C)	0.018
Emissivity	0.45
Absorption coefficient	0.45

Table 6.5: Inconel 625 thermal properties.

Parameter	Value
Yield stress (MPa)	725
Stress ratio - R ₃₃	0.8483
Stress at $\epsilon^p = 0.35$ (MPa)	990

Table 6.6: Inconel 625 mechanical properties.

6.6.3 Event series definition

Both the scan path and recoater roller space and time positions are required as INP files to define the event series to be utilized by Abaqus. The process starts by importing the geometry to Autodesk Netfabb and positioning it according to the same assembly coordinate system utilized in Abaqus, such that the coordinate positions are matching between both software. With the position set, the part can be sliced through the "Slice Part" tool, which initially requires defining the layer size, and the height start and stop positions. The "Slices" tab in the workspace window, allows for the subsequent contour and hatching laser paths to be defined. Additionally, entering the *Slices* environment, allows for the fine tuning and visualization of the path per layer basis, separated into both the contour and filling paths with distinct properties.

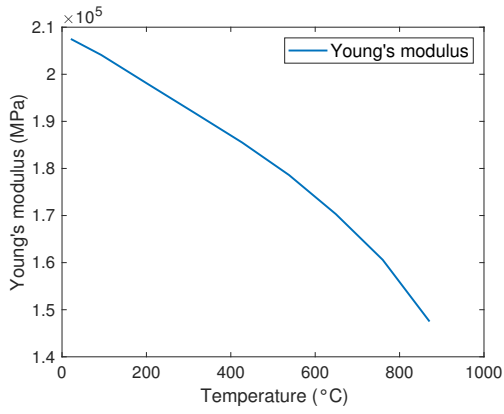
Entering the "Slice" environment, the contour laser path is automatically defined geometrically, but its path and properties are allowed to be defined, such as the laser speed and powder, which allow for a space and time characterization of the contour laser path. The filling laser path is then defined, allowing for different hatching styles to be chosen. Considering the goal of the present assessment is to validate the workflow chosen, the exact scan path suggested by the guidelines in [63], is approximated utilizing the automation tools of Autodesk Netfabb, such that they can be used in a general case, including the bracket part. The parameters that characterize the benchmark build are given in tables 6.7 and 6.8. See figure 6.18 for an example of a sliced layer at height 0.02mm, with both contour and hatching laser paths shown in blue and red, respectively.

Parameter	Value
Power (W)	100
Laser speed (mm/s)	900
Jump speed (mm/s)	900

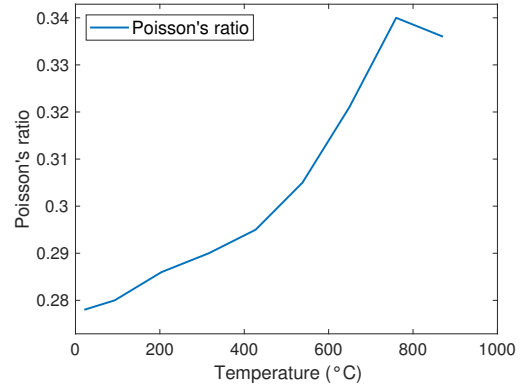
Table 6.7: Contour laser path properties.

Parameter	Value
Hatching	Simple
Hatch distance (mm)	0.1
Angle increment (°)	90
Regionalisation	No
Power (W)	195
Laser speed (mm/s)	800
Jump speed (mm/s)	800

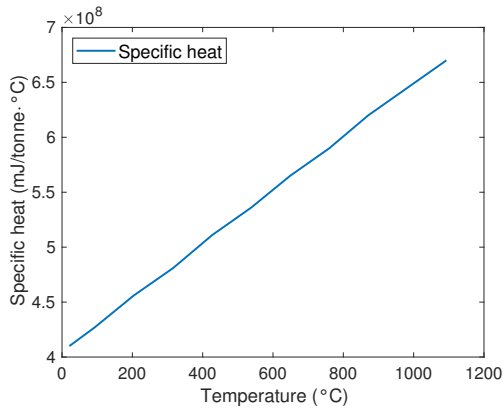
Table 6.8: Infill laser path properties.



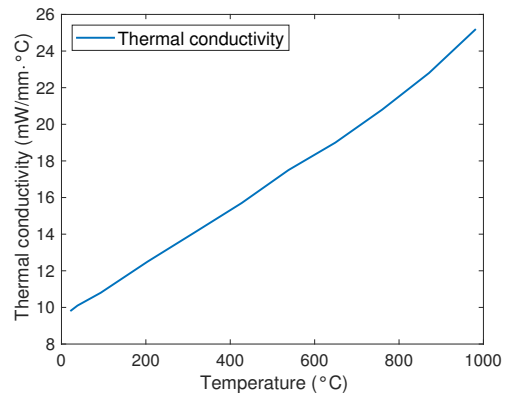
(a) Young's modulus



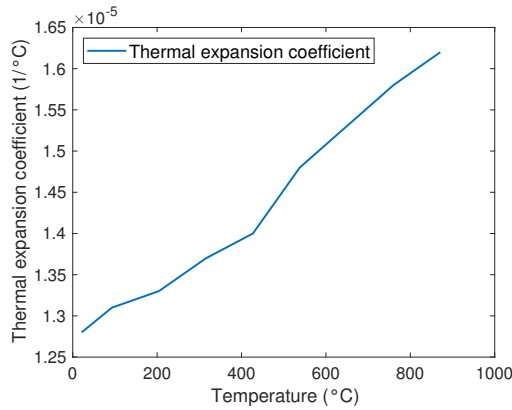
(b) Poisson's ratio



(c) Specific heat



(d) Thermal conductivity



(e) Thermal expansion coefficient

Figure 6.17: Iconel 625 thermal dependent properties.

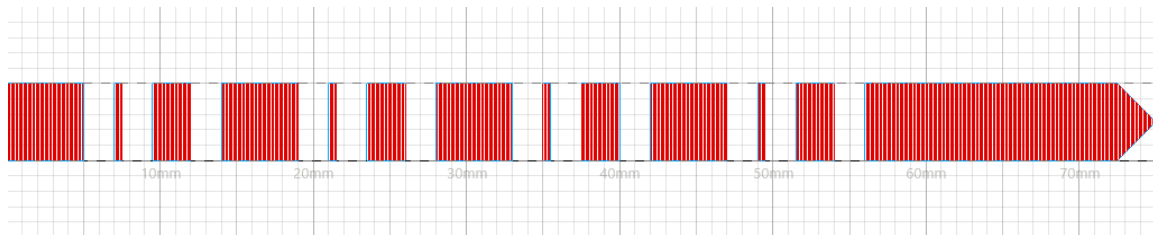


Figure 6.18: Laser path example at a single layer in Autodesk Netfabb.

The paths are exported in the LSR file format. However, the file does not contain information pertaining to the recoater roller passage, nor the cooling and dwell times. In order to keep consistency with the simulation performed by [70], these parameters were obtained from the INP event series files provided at [10]. As such, the additional simulation parameters are included in the MATLAB script (annex A) and are defined in the table 6.9.

Parameter	Value
Recoater roller speed (m/s)	80
Average layer duration	52
Cooling duration (s)	600

Table 6.9: Recoater roller and cooling parameters.

6.6.4 Simulation definition in Abaqus

Both the heat transfer and structural analysis models are prepared before the definition of the AM modeler plugin model, as both models are requested during the initial process. While both models are identical, the structural analysis one contains an additional step entirely dedicated to material removal, representing the separation between the legs and the build plate. This is done through a model change interaction that removes the build plate elements of interest, highlighted in red in figure 6.19.

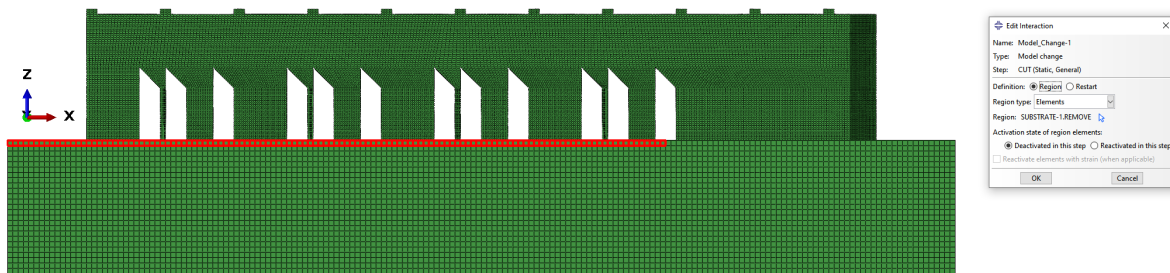


Figure 6.19: Layer of elements to be removed through a model change interaction.

Additionally, the time increment obtained for the Matlab script (annex A) is the same for both analysis for simplicity sake. However, as showcased in [70], these could be different to economize simulation result size, by asking for less output points.

6.6.5 Results and discussion

The benchmark simulation, while serving the main purpose of validating the simulation setup method employed against previously performed analysis and physical tests, it is also expanded to compare the use of a fine time increment with the low-resolution one.

6.6.5.1 Time increment

A time increment comparison is first performed, to better understand the impact of this simulation parameter on the results. Said comparison is performed against a high-resolution thermal analysis where the time increment represents the time needed for the heat source to approximately move the characteristic element length. Due to time restrictions, only a single layer is analysed in the high-resolution simulation. The simulation time sees

a steep increase of 112897.89 over the low-resolution simulation time for the same single-layer analysis, further corroborating the necessity for a low-resolution simulation.

Despite the stark simulation time difference, the nodal temperature difference at the end of the step, at $t = 52.6s$, has a maximum of 5.63%. Additionally, the nodal temperature registered in the low-resolution simulation is higher than the high-resolution one across all measured nodes. Figure 6.20 showcases the nodal temperature percentage error, linearly interpolated over the two dimensional surface that defines the first layer.

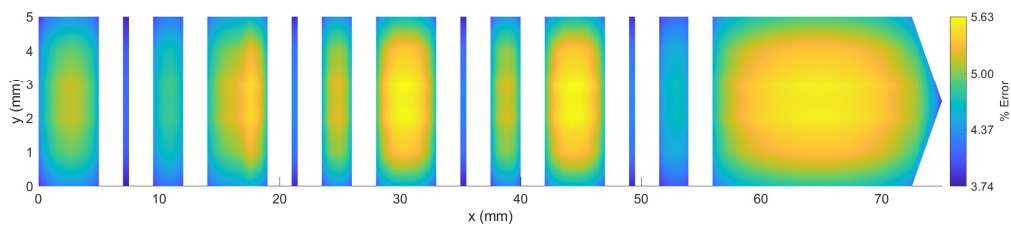


Figure 6.20: Percentage difference of the temperature measured with a single time step per build physical layer, with respect to the high-resolution temperature field. Results are linearly interpolated over the surface area.

The low-resolution simulation, while not accurately capturing the temperature peaks and gradients that are present in the high-resolution one, it does accurately capture the far-field temperature distribution and part cooling. Should be noted that the annealing effects missing are introduced through the relaxation temperature in the structural analysis.

A comparison between the introduction of an additional time step before the recoater roller passage is also performed. The same simulation time of $t = 52.6s$ is considered. Figure 6.21 showcases the nodal temperature percentage error between the extra step, and the high-resolution simulations, linearly interpolated over the two dimensional surface that defines the first layer. The maximum error is reduced by half to 2.81%. Compared to the previous example, the introduction of the step improves the prediction of the temperature on the left side of the part, where the recoater roller has introduced new material at the initial layer temperature. As predicted, the omission of the step averages the input energy and cooling over the entire part for the duration of the whole step. However, due to time constraints, such an approach is not used for the bracket, but it should be further investigated, namely the influence of the new thermal field on the structural analysis, as well as the impact of when the additional step is introduced.

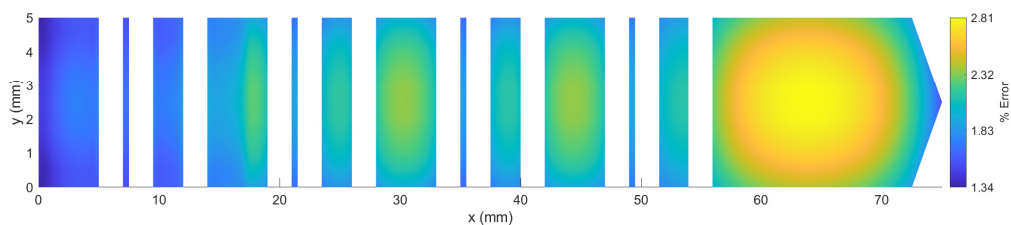


Figure 6.21: Percentage difference of the temperature measured with two time steps per build physical layer, with respect to the high-resolution temperature field. Results are linearly interpolated over the surface area.

6.6.5.2 Residual elastic strain and distortion

Residual elastic strain results, pre-removal of supports, are compared against the benchmark physical test results obtained from x-ray diffraction measurements provided at [63]. Namely, the z and x direction residual elastic strains are obtained at the $y = 2.5\text{mm}$ middle cross-section of the printed part. Figures 6.22(a) and 6.23(a) showcase the residual elastic strain in the x and z-directions, respectively. The residual elastic strain in the x and z-directions provided by NIST can be seen in figures 6.22(b) and 6.23(b), respectively.

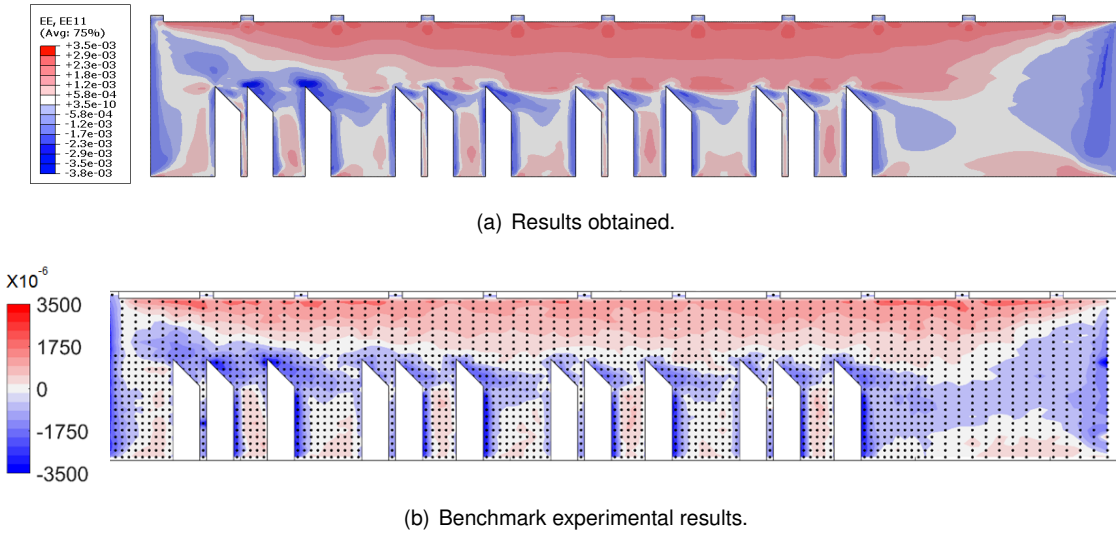


Figure 6.22: Residual elastic strain in the x-direction.

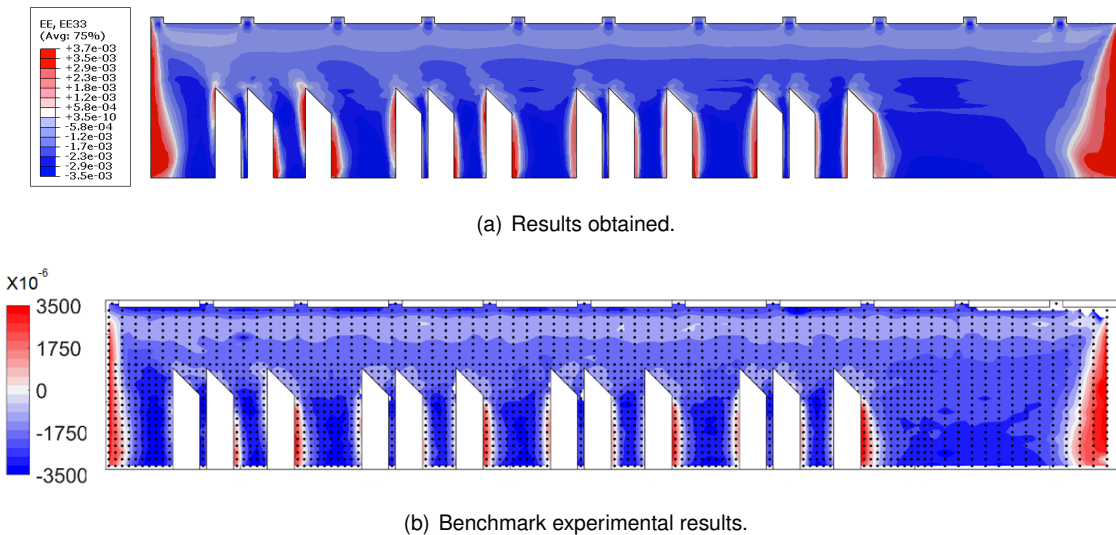


Figure 6.23: Residual elastic strain in the z-direction.

As expected, the obtained results are in close agreement with the experimental data. Namely, in the contour plot in the x direction, the same tension strains are obtained, throughout the main body region, with compressive strains at the edges of the legs.

Furthermore, in the z-direction, agreement is found between the results obtained and the experimental data. While in the x-direction tension strains defined the main body region, now compressive strains occupy the same region. On the other hand, the leg edges are under tension strains.

Additionally, elastic strain in the z-direction path data at $z = 2.75\text{mm}$ (figure 6.24(a)) and $z = 10.75\text{mm}$ (figure 6.24(b)), both at $y = 2.5\text{mm}$, are compared against the NIST benchmark test data. The obtained results showcase good correlation with the tests, at both build heights.

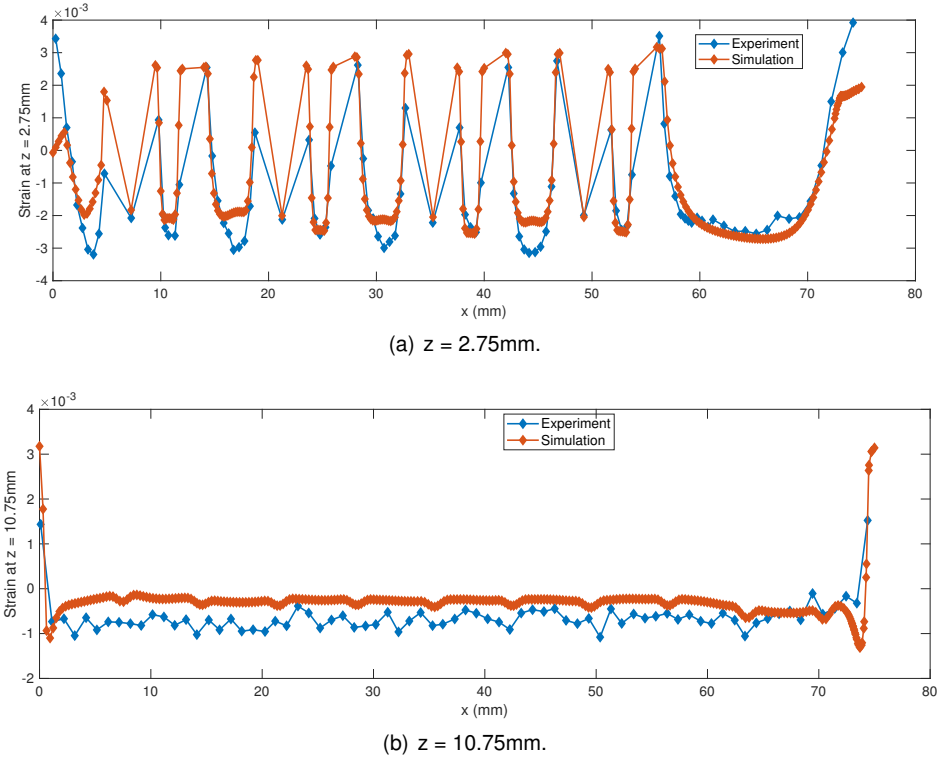


Figure 6.24: Path z-direction strain measured at two different heights.

Finally, distortion is measured at the eleven top ridges found on the part, at $z = 12.5\text{mm}$ in the central plane at $y = 2.5\text{mm}$. The plot in figure 6.25 shows both the benchmark test results and simulation results obtained, again suggesting an reasonably accurate prediction of the part behaviour under AM printing conditions.

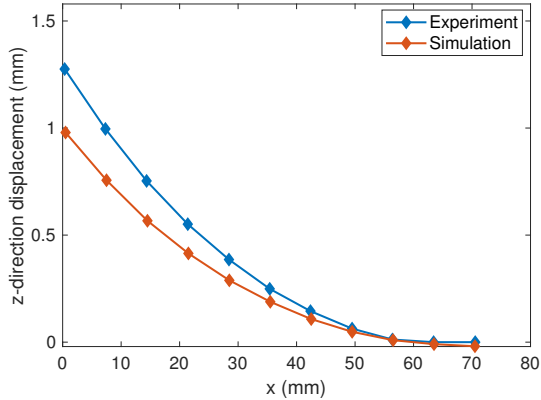


Figure 6.25: Deflection measured that the part's top ridges.

The results suggest that the low-resolution simulation method utilized in this thesis showcases accurate enough results to predict residual strains and part distortion resultant from AM process, at a considerably lower time scale, ideal for large complex geometry, such as the bracket part.

Chapter 7

Static analysis and topology optimization implementation

7.1 Static strength analysis of the current bracket

This section explains the numerical modelling process applied to the current bracket component, as means to accurately evaluate its structural performance and establish a baseline for comparative purposes, and definition of the performance requirements dependent on the current design performance.

7.1.1 Bracket assembly

The current component to be tested was designed in 1985 and is divided into two manifolds, as well as other minor components. These two parts are assembled together through the use of six bolts, which are firstly inserted through the lower manifold part, as depicted by figure 7.1, with the bolt highlighted.

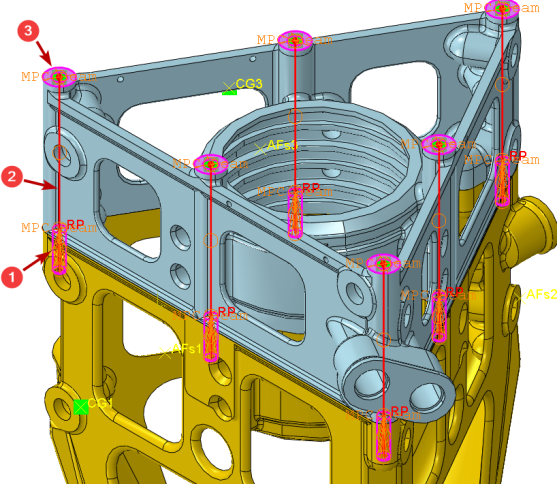


Figure 7.1: Connection between upper and lower manifolds through the use of six highlighted bolts.

While both the upper and lower manifold CAD files are provided, the bolts used to connect the two components are not. A simplified modelling approach is proposed by [72] which will be implemented in the present work. The

bolt has been modelled as rigid wire. Considering the threaded region is present solely in the Upper Manifold part, the bolt was also divided into two separate regions, threaded and unthreaded, which are divided by the Reference Point. It should be noted that the location of the reference point is entirely arbitrary and chosen in this location for simplicity of visualization sake.

The connection between the bolt and the two manifold parts is done through the use of two types of constraints present in Abaqus:

- Kinematic coupling constraint: applied to the unthreaded region of the bolt to simulate the contact between the bolt and the unthreaded walls of the blind hole, belonging to the lower manifold and spanning its entire height (number 2 in 7.1);
- Multi-point constraint: applied in two instances. The first is between the threaded regions of the bolt and the blind hole of the upper manifold, where a beam type MPC is used constraining all degrees of freedom (number 1 in 7.1) The second is placed at the head of the bolt, a beam type MPC constraining all degrees of freedom and simulating the contact between the head of the bolt and top flange of the lower manifold (number 3 in 7.1).

7.1.1.1 Contact interaction

The assembly definition process requires the definition of the contact between the two manifolds. For sake of simplicity and reduced computational time, the contact interaction is defined as a local surface-to-surface discretisation method with a small sliding formulation, as finite sliding formulation ended up in an aborted divergent solution. The master-slave surface relation is born from the differences in mesh refinement and materials present, such that the two main guidelines are to be followed:

- The mesh of the slave surface should be finer;
- In case of both surfaces having similarly dense meshes, then the material difference dictates the master-slave surface pair. The slave surface is chosen such that it is the surface with the softer underlying material.

Given the similarly dense meshes and materials used, the choice of the surface pair is mostly arbitrary and it is represented in figure 7.2.

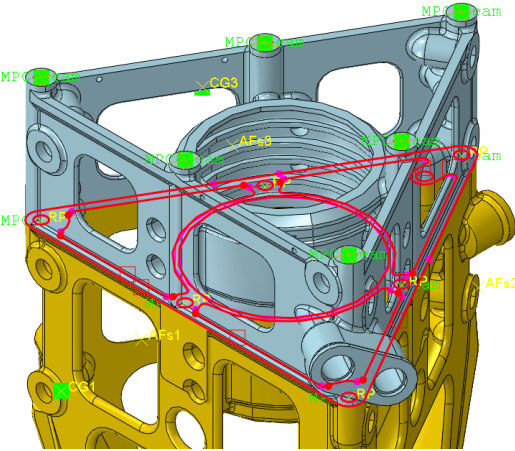


Figure 7.2: Contact regions between upper and lower manifolds.

Moreover, the contact interaction property needs to be defined, and is done so through the introduction of both tangential and normal behaviours. The properties are defined as follows:

- **Tangential Behaviour:**

- Friction formulation: Penalty;
- Directionality: Isotropic;
- Friction coefficient: 0.36 [72];

- **Normal Behaviour:**

- Pressure-overclosure: "Hard" Contact;
- Constraint enforcement method: Default;
- Allow separation after contact: Yes.

7.1.1.2 Load application

The 3 loads are applied to three distinct points. These have been defined as Reference Points, which will be referred to as AF_{S1} , AF_{S2} and AF_{S3} . Compared to the work of [72], a new approach has been taken to simulate the load transfer from the servo-actuator load application point to the mounting bosses. While the modelling of the servo-actuators themselves should yield the most accurate results, as it would take into consideration the stiffness of this part, its geometry and material properties are not provided. As such, the modelling of the connection is done through the use of a Structural Distributing Coupling constraint.

The choice to use this type of constraint is based on the fact that relative motion between the mounting bosses is expected and as such, should be allowed. Such behaviour is not possible using a Kinematic Coupling constraint, as all the nodes belonging to the mounting boss surfaces are coupled to the rigid body motion of the reference nodes (AF_{S1} , AF_{S2} and AF_{S3}). On the other hand, the Structural Distributing Coupling distributes the forces uniformly¹ from AF_{S1} , AF_{S2} and AF_{S3} to the coupling nodes on the mounting bosses surfaces. The average translation of these is coupled to, and drives the motion of the reference nodes. Figure 7.3 showcases the connection to one of the bracket faces.

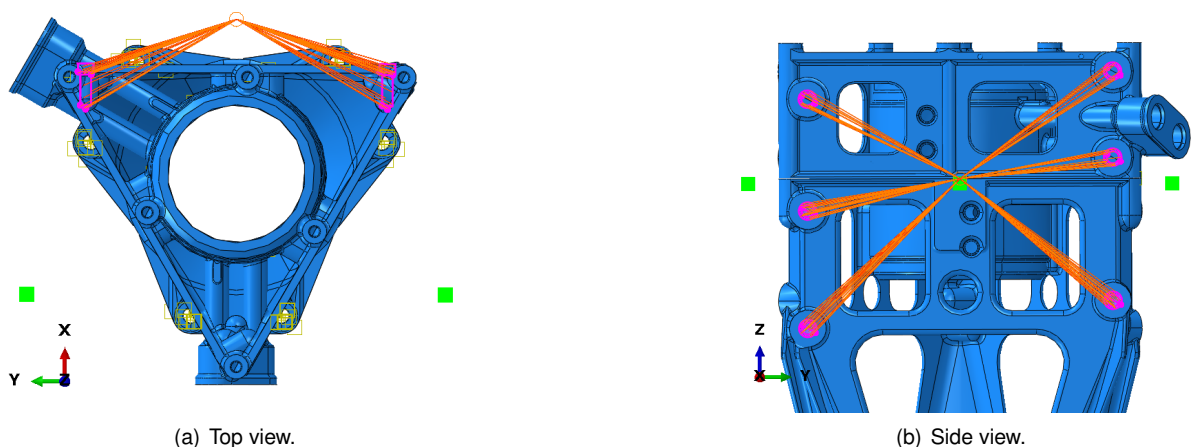


Figure 7.3: Connection between the load application point and the 6 mounting bosses.

¹other weighting methods of distribution exist, such as linear, quadratic and cubic. Since no information is given on this force distribution to the mounting bosses, the uniform weighting method has been chosen for sake of simplicity.

7.1.2 Test equipment and real model

The bracket undergoes testing on a rig designed specifically to assess its structural performance. The schematics of the rig are provided, together with the mounting bolts used. This allows for an accurate prediction of the boundary conditions to use. It is however of interest to simplify the boundary conditions to a point where accuracy is maintained, and computational time is reduced. This thesis expands on the work developed by [72], by introducing the real bolt model and the preloading effect, effectively comparing the complex real boundary condition case to a proposed simplified boundary condition case, and providing legitimacy to its accuracy. The work of [72] also focused on stress homogeneity, since the goal was to perform a fracture analysis on detected critical areas. However, it is of the interest of the present thesis to investigate the influence of the boundary conditions on the displacement field, which will be critical to properly define the optimization constraints. For future reference, the model utilizing both the bolt and the mounting plate will be named real model, whereas the model omitting these components will be regarded as the simplified model.

7.1.2.1 Bolt and washer models

The provided bolt and washer nomenclatures allows to find seller information on the properties of both elements, such that the geometry can be replicated in Abaqus. Both the bolt and the washer have been combined into one single component, which can be seen in figure 7.4. The material choice falls on E4340 Alloy Steel (table 7.1), as it is also documented on the same page. It should be noted that the page is not disclosed for confidentiality purposes.

Parameter	Value
Density (tonne/m ³)	7.85E-09
Young's modulus (MPa)	210000
Poisson's ratio	0.3

Table 7.1: Linear elastic E4340 Alloy Steel properties.

In order to prevent instability, and reduce the simulation time to practical values, the bolt was meshed with linear hexahedral elements with reduced integration (see figure 7.4). The choice results from instability issues using elements with full integration in the the contact regions, and overly long simulation times using quadratic elements. The regular geometry of these regions was also a determining factor in choosing hexahedral elements over tetrahedral elements, with the first allowing for more accurate results.

7.1.2.2 Mounting plate model

A step further towards the realistic modelling of the test rig requires the modelling of the mounting plate where the component bolted to. Considering the cooperation that took place with [72], a similar approach has been taken, but an effort has been made to further simplify the boundary condition problem, namely with a lower number of components. As such, the mounting base is a single part, considered rigid, which also surrounds the conic region present on the upper manifold.

The plate is modelled as a three dimensional deformable body, but with a much higher stiffness and null Poisson's Ratio to replicate a rigid body behaviour compared to the main component. In this case, the stiffness of the mounting plate is three orders of magnitude higher when compared to the stiffness of Ti-6Al-4V used in the bracket.

This component is meshed utilizing quadratic hexahedral elements with reduced integration (see figure 7.5), which proved to not result in a divergent solution, while maintaining reasonable simulation times.

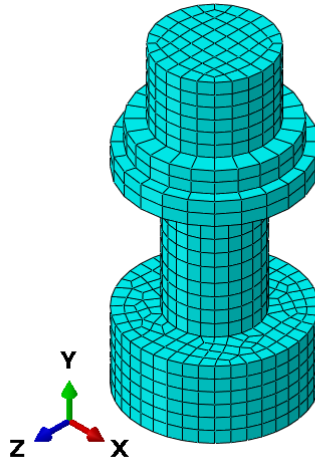


Figure 7.4: Meshed bolt.

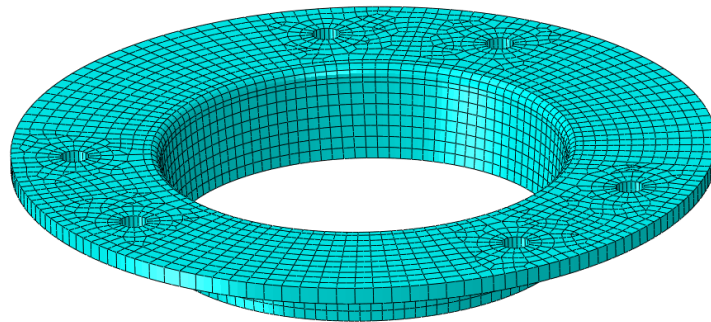


Figure 7.5: Meshed mounting plate.

7.1.2.3 Real model assembly

The previously assembled bracket is completed with the inclusion of the six mounting bolts, and the mounting plate. The full real model assembly can be seen in Figure 7.6(a), and a cut view showcasing the position of the components in figure 7.6(b).

7.1.2.4 Interactions

The introduction of the six bolts and the mounting plate warrant the introduction and definition of new contact behaviour between the new contact surfaces. In order to achieve a convergent solution, several trials have been performed, with the following list showcasing the used contact properties.

- **Frictionless:**
 - Tangential Behaviour:
 - * Friction formulation: Frictionless
- **Hard:**
 - Normal Behaviour:

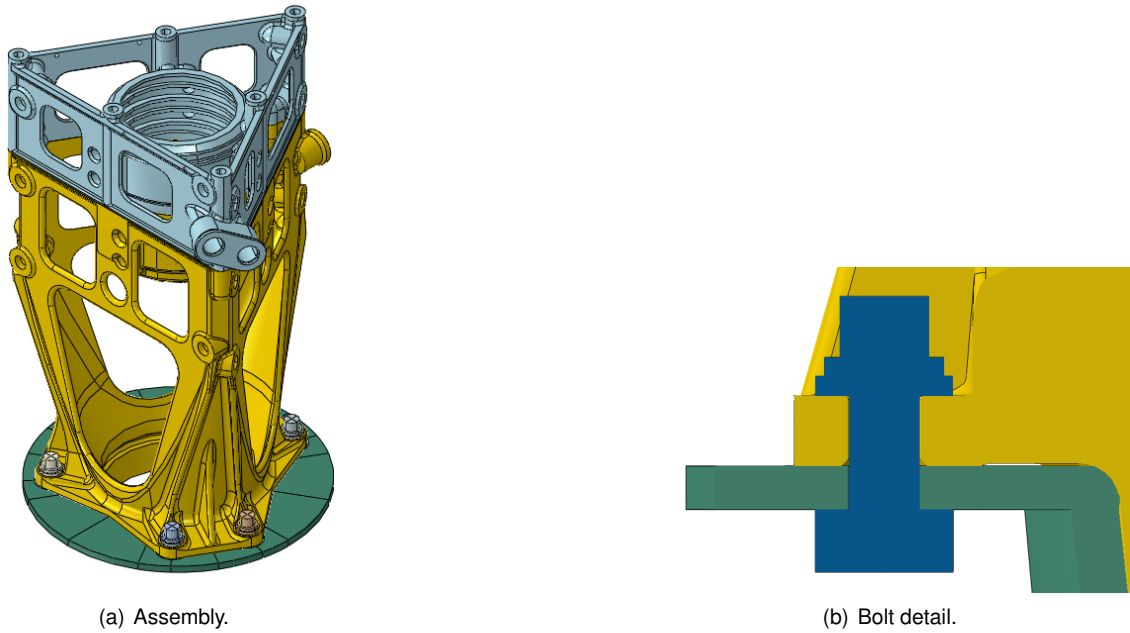


Figure 7.6: Real model assembly.

- * Pressure-overclosure: "Hard" Contact
- * Constraint enforcement method: Augmented Lagrange (Standard)
- * Allow separation after contact: Yes
- * Stiffness value: Default
- * Stiffness scale factor: 1
- * Clearance at which contact pressure is zero: 0

• **Hard-friction:**

- Tangential Behaviour:
 - * Friction formulation: Penalty
 - * Friction Coefficient: 0.41 [73]
- Normal Behaviour:
 - * Pressure-overclosure: "Hard" Contact
 - * Constraint enforcement method: Augmented Lagrange (Standard)
 - * Allow separation after contact: Yes
 - * Stiffness value: Default
 - * Stiffness scale factor: 1
 - * Clearance at which contact pressure is zero: 0

Additionally, the contact pairs need to be defined, and to do so, the "Find Contact Pairs" in Abaqus was used. For a given distance tolerance, it searches the entire model assembly for possible contact pairs of interest, giving the possibility to easily attribute contact properties (see figure 7.7).

The cut view section in figure 7.8 showcases the surface contact pairs introduced by the mounting plate and bolts, together with a labelling table matching each pair with the respective contact property.

The mounting plate has been partitioned to allow for a more regular mesh, and compartmentalize the contact regions to specific areas of interest surrounding the bolts.

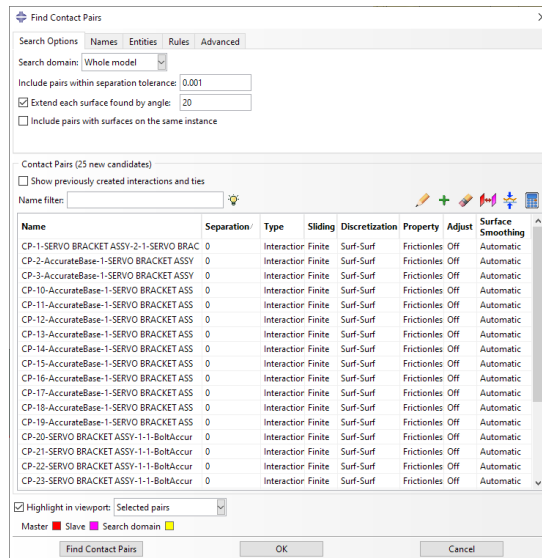


Figure 7.7: Find contact pairs windows in Abaqus.

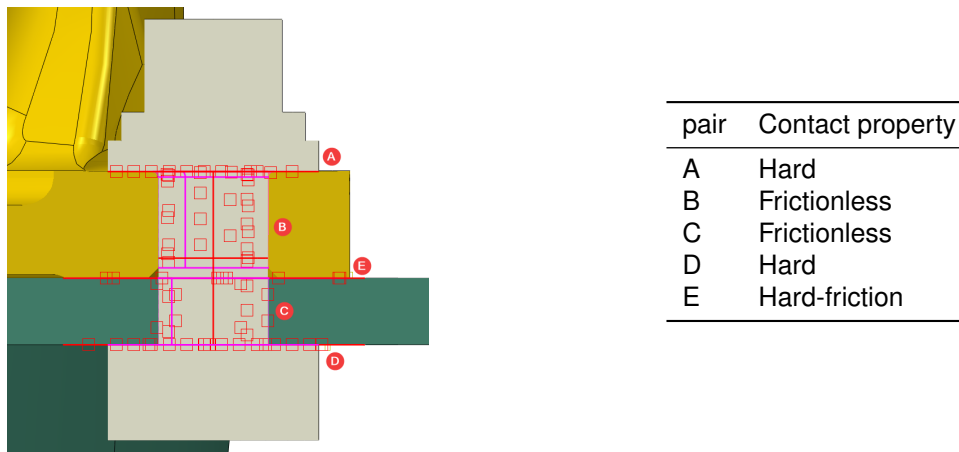


Figure 7.8: Detailed view of the contact interactions and properties needed for the bolt.

7.1.2.5 Preloading

Finally, the bolt preloading is an important modelling step, which ensures the mounting plate and the bracket remain connected, by distributing the load to the mounting plate rather than relying on the bolts to hold the bracket. However, the process was riddled with several numerical errors, which have been mitigated by a careful setting up of the contact properties, meshing, boundary conditions and load application. As such, several modelling techniques have been used to ensure this, ranging from different approaches to the preloading of the bolts, such as defining an initial state of stress in the bolt-shank or utilizing the Abaqus provided bolt load properties. Considering the main goal of the thesis is not on the preloading effect definition, solely the method that yielded stable and physically accurate results will be discussed and presented.

The preloading of the bolts is introduced utilizing the Abaqus bolt load option, which requires an addition set of geometrical definitions within the bolt model itself. Firstly, a surface defining the bolt cross-section must be defined in the bolt. This can be achieved through the partition in the bolt shaft by a user defined plane. In this case, the partition was created halfway through the length of the shaft. Secondly, the bolt axis is defined. While it does not need to be normal to the cross-section previously defined, it has been defined as such in this case, since the load

is to be applied in this direction.

Finally, considering the method chosen is based on the application of a force to the bolt, its magnitude needs to be determined. According to [74], the magnitude of the preload force is 70% of the minimum tensile strength (P_{MTS}) of the bolt. This value is once again provided by the bolt seller page, and is equal to 1.241E9Pa. On the other hand, the bolt cross-section diameter, is defined as 7.9248E-3m, resulting in a cross-section area (A_B) of 4.93249E-5m². With these values, the magnitude of the load can be determined as,

$$F_{bolt} = 0.7 \cdot P_{MTS} \cdot A_B = 42\,850.5\text{ N} \quad (7.1)$$

7.1.2.6 Boundary condition selection

The boundary conditions also play an important role in ensuring that no numerical singularity errors occur, a result of rigid body motion. The constraint applied to the bolt can be considered an artificial boundary condition, since its existence is purely based on the prevention of numerical singularity and it should be deactivated after the preloading step is complete and the contact properties have been activated. However, this approach resulted in aborted simulations due to numerical singularities. As such, the artificial boundary conditions applied to the individual bolts have been maintained throughout the loading steps as well, but have been carefully chosen as not to undermine the physical accuracy of the simulation. The chosen boundary conditions are applied to the most outward top and bottom surfaces of the bolt (see figure 7.9). The displacement degrees of freedom in the x and y directions have been constrained, and so has the rotation degree of freedom in the z axis (the axis with the same direction as the bolt cross-section surface normal).

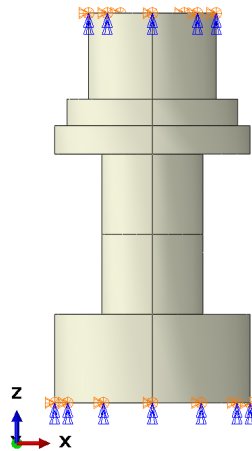


Figure 7.9: Bolt boundary conditions.

The boundary conditions applied to the mounting plate are on the other hand not regarded as artificial, and simply ensure the plate is held in place and maintains symmetric contact with the bracket base and conic regions. Therefore, the lateral regions of the mounting plate have been constrained in all displacement and rotation degrees of freedom (see figure 7.10).

7.1.3 Simplified model

The simplified model consists in an effort to reduce the number of contact interactions, ultimately resulting in a simulation that requires lower computational effort to conclude. With the validation of this model, its implementation

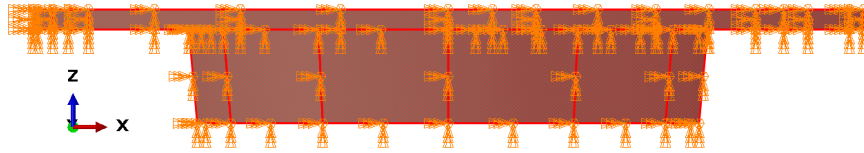


Figure 7.10: Mounting plate boundary conditions.

will be expanded to the optimized model to achieve the same reduced computation effort, more important so given the several number of iterations the optimization task go through. The work of [72] goes into further detail on the choice of simplified boundary conditions and their impact on the stress distribution. The conclusions of said study are employed here, translating into the following boundary conditions.

The washer outer-diameter has been used to define the surface partition that limits the area of effect of the boundary conditions. To this region it has been applied a constraint to the displacement and rotation in the z-axis. Similarly, the underside of this region is constrained in the same manner (see figure 7.11(a)).

On the other hand, the bolt hole is constrained for both displacement and rotation in the x and y directions (see figure 7.11(b)).

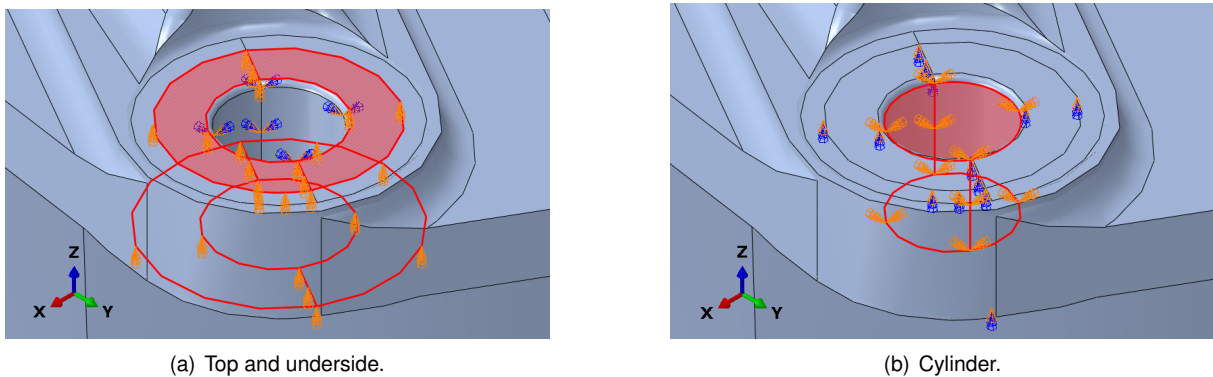


Figure 7.11: Bolt hole boundary conditions.

The last boundary condition to be set exists to ensure connectivity during optimization. Preliminary topology optimization tasks ran by both [75] and this thesis, showcased a decoupling between the conic region in the upper manifold and the remaining part.

As such, in order to introduce consistency between the baseline model and the optimized ones, the boundary condition that ensures continuity has been introduced in the simplified model too. Its impact is meant to be minimal so the filleted region connecting to the conic region has been chosen. This surface is not part of the original fixed element group, but the introduction of a boundary condition forces it to be fixed, ensuring the connection between the design domain and the previously decoupled conic region. This area has the displacement constrained in both the x and y directions (figure 7.12).

7.1.4 Meshing

The meshing process is done utilizing second-order tetrahedral elements, named C3D10 in Abaqus. Given the high geometrical complexity of the component, the use of hexahedral elements was discarded, since a mesh was not able to be defined with this element type, despite its better convergence rate. On the other hand, a fully-integrated linear order tetrahedral element (C3D4) may experience shear locking under bending conditions. It is

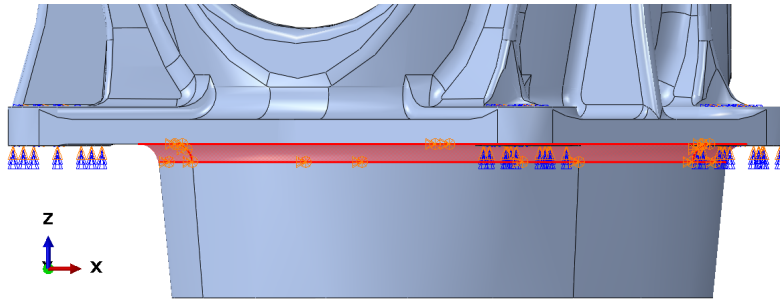


Figure 7.12: Connecting fillet boundary condition.

a consequence of the element numerical formulation that drives the appearance of non-physical "parasitic shear", which turns the elements too stiff in bending-dominant problems where the element length is of the same order of magnitude (or higher) of the geometry wall thickness.

The presence of small details and edges in the original geometry also warrant the use of virtual topology, with the objective of creating a better formed mesh. The effect of "bad" elements is present in both the accuracy of the simulation, but also its convergence and stability. In order to evaluate the quality of the mesh, the Abaqus mesh verification tool is used, which performs mesh quality tests on the elements, based on shape (shape factor, for example) and size metrics (geometric deviation factor, for example).

Using an element size of 4mm, the percentage of elements causing a warning trigger by the Abaqus tool was reduced by 86.41%, from 8.1865% to 1.1126%, yielding this way a substantially better quality mesh and consequently a more accurate solution.

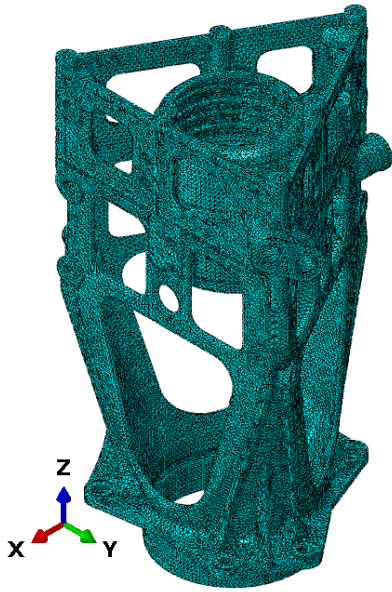
7.1.4.1 Mesh convergence analysis

A sufficiently refined mesh is important to attain accurate simulation results, where in a limit case of infinitesimal element size, the solution converges to the exact solution. However, the increase in mesh density yields an increase in computational resources expended in the simulation, making it important to find an convergence point, that is, when further mesh refinement results in negligible changes in the solution.

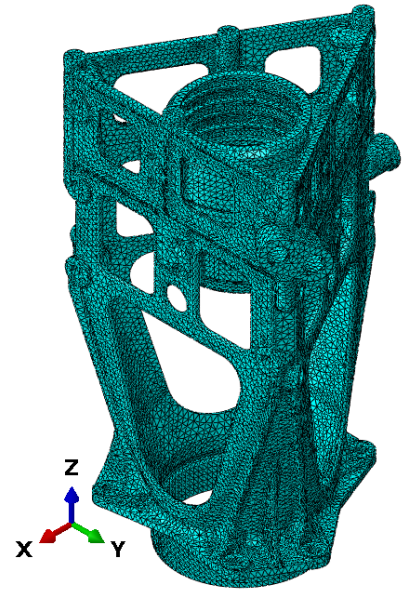
The assessment is performed with the starting point in a mesh with an element size of 4mm, which will be regarded as a normal sized mesh (see figure 7.13(b)). A finer mesh with an element size of 3mm is analysed and referred to as a fine mesh, seeing an increase of approximately 120% in the number of elements (see figure 7.13(a)). Two coarser meshes will be also studied, the first with an element size of 5mm (coarse mesh) which yields an element number reduction of 30% compared to the normal mesh (see figure 7.13(c)), and the second with an element size of 6mm (very coarse mesh), resulting in an element number reduction of approximately 38% compared to the normal mesh (see figure 7.13(d)).

The sensitivity study is performed on both the displacement field measured at the load application point AF_{S3} in the z direction, and the Mises stress peak measured at a critical region highlighted by red in figure 7.14(a). The second load case under proof loading is considered. The results reported are normalized with respect to the very coarse case (figure 7.14(b)).

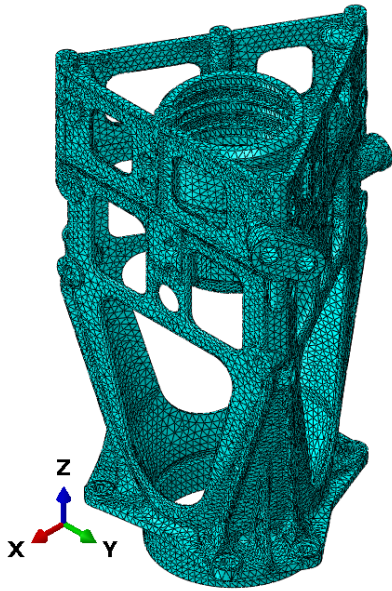
It can be seen that the displacement converges faster than the stress, which is to be expected considering stress relies on displacement gradients calculation. That is, a finer mesh is needed to accurately predict the gradient when compared to an accurate prediction of the local displacement field. The results between the normal and fine meshes are similar with respect to displacement, both plateauing at approximately 1.01. Despite the slower convergence



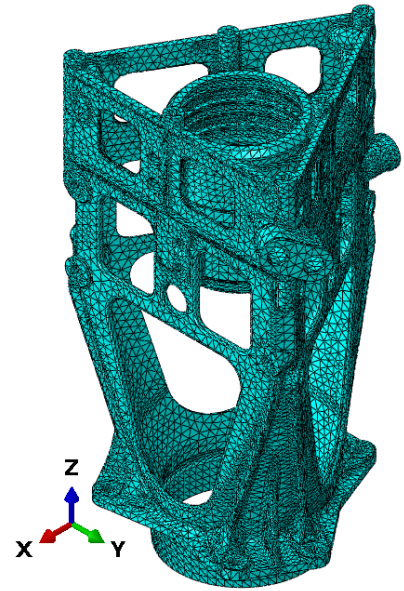
(a) Element size of 3mm.



(b) Element size of 4mm.



(c) Element size of 5mm.



(d) Element size of 6mm.

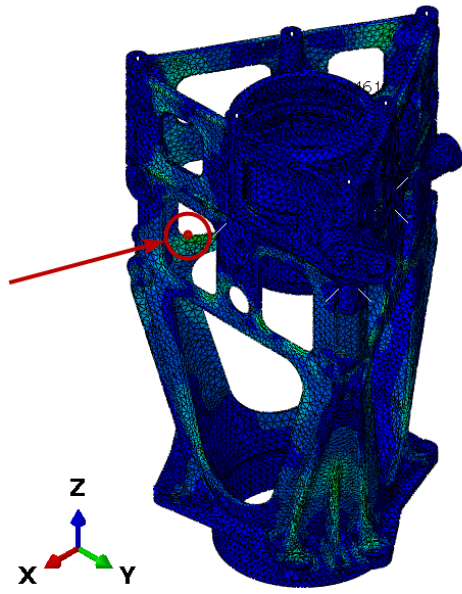
Figure 7.13: Assembly meshing for different element sizes.

rate from the stress, a trend to convergence is noticeable, with the results showcasing negligible differences by staying under a normalized stress value of 1.08 compared to the very coarse mesh case.

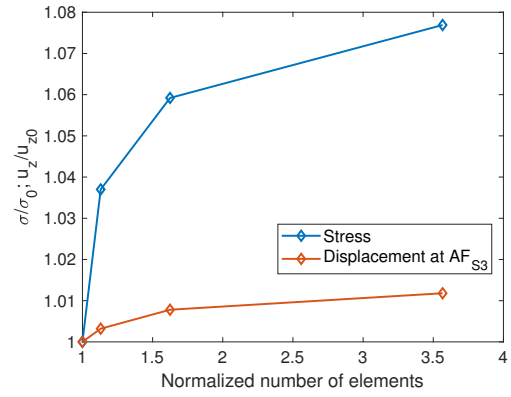
As such, with the present results, it has been decided to continue using the normal mesh (element size of 4mm) throughout the work, namely in the validation of the optimization results, ensuring both accurate results and reasonable low simulation time.

7.1.5 Materials

The material used for the AM printing of the bracket is Ti6Al4V ELI Titanium Alloy, and the properties applicable to this work are sourced from experimental testing performed at Politecnico di Milano. An isotropic assumption is made, despite the material showcasing anisotropic properties under AM printing conditions, namely weaker



(a) Critical stress point.



(b) Normalized von Mises stress and displacement results with respect to the number of elements.

Figure 7.14: Mesh sensitivity results.

performance in the printing direction. Post-processing treatments such as hipping aid at achieving near isotropic properties. The properties are shown in table 7.2, and the stress-strain curve obtained in figure 7.15.

Parameter	Value
Density (tonne/m ³)	ρ
Young's modulus (MPa)	E
Poisson's ratio	ν

Table 7.2: Ti6Al4V ELI linear-elastic properties.

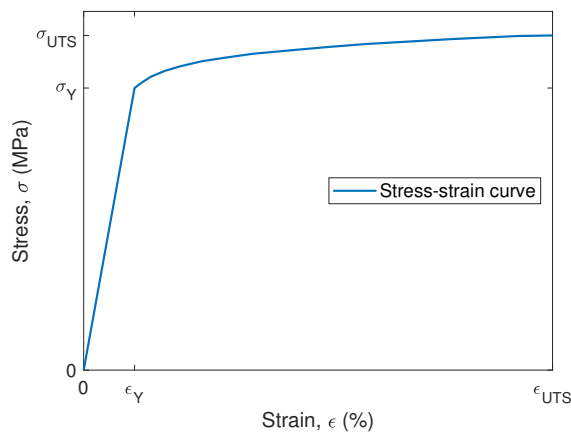


Figure 7.15: Ti6Al4V ELI plastic properties as a stress strain curve.

Moreover, plastic properties are only introduced when assessing the bracket performance under Ultimate loading condition, where yielding is allowed to happen. In order to reduce computational time, the assumption that no

yielding occurs is applied, permitting the use of a linear elastic model of the material for both Stall and Proof loads. Under Ultimate load conditions, the plastic model is utilized.

7.1.6 Comparative Results between Real and Simplified Models

This section is devoted to exploring the results from the comparison between the real and simplified models, namely the comparison between the vertical (z direction) displacements measured at the load application points AF_{S1} , AF_{S2} and AF_{S3} , the stress at the same critical location under scope during the mesh sensitivity analysis (see subsection 7.1.4), and a local and far field path stress distribution to compare the influence of the boundary conditions at different locations.

The first comparison is done on the vertical (z direction) displacements measured at the load application points AF_{S1} , AF_{S2} and AF_{S3} . As shown in table 7.3, the reported results in the simplified case showcase an error of 10% in comparison with the real model, and this peak occurs in the point AF_{S3} during the bending second load case (LC2), which is, given the loading conditions, the load application point that experiences the highest displacement value, being critical and a design requirement to limit this value to a set constraint. It is however noted the overall similar results obtained regarding the displacement field in these critical regions, despite the boundary conditions difference and added parts.

Load	Axial	Bend. 1
AF_{S1}	6.55%	2.29%
AF_{S2}	3.23%	2.53%
AF_{S3}	3.66%	10.08%

Table 7.3: z-direction displacement results comparison.

Focusing on the Von Mises stress distribution, a similar percentage error can be observed in a critical region of the second load case (also observed for the first load case), this time with a peak of 6.15% registered during the first load case. The table 7.4 summarized the obtained results, with the values normalized to the respective load case real model Von Mises stress value obtained, and the percentage discrepancy between the two.

Load	Axial	Bend. 1	Discrepancy
Real model	1	1	6.15%
Simplified model	0.9485	0.9755	2.45%

Table 7.4: Von Mises stress results comparison.

Finally, the Von Mises stress distribution is assessed along a path that spans from the boundary condition region (mounting bolt) to the closest mounting boss (highlighted in figure 7.16). The chosen for the assessment is the one that experiences peak stresses during the second load case, that is, in bending. In fact, the path chosen purposefully crosses a critical corner, which provides a complete insight into how the simplified model handles stress distribution at critical regions.

As shown in figure 7.17(a), regarding the first load case, the difference between both models is more prominent close to the boundary condition region, decreasing to close to null in the far-field. The same can be stated for the second load case (see figure 7.17(a)), where a higher difference is verified in the local region, likely due to the transition between hexahedral elements present in the bolt region, and the tetrahedral elements that constitute

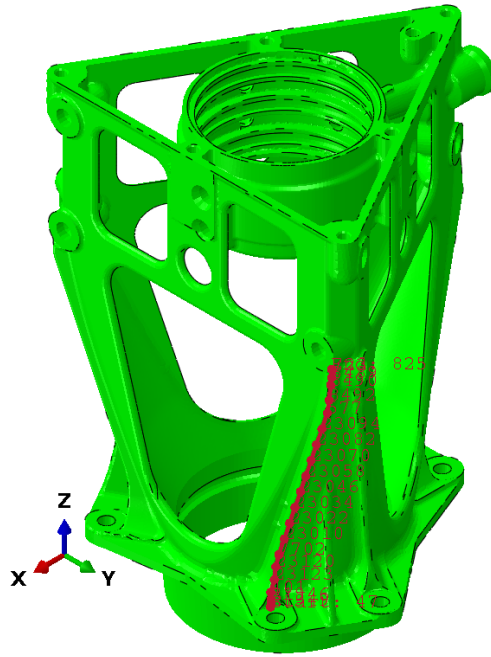


Figure 7.16: Highlight of the path for the von Mises stress measurement.

most of the bracket, because the biggest peak happens at the node shared by both element types. The distinction between near and far-field is done based on the normal distribution of the path past the separating limit. This limit is set based on the 95th percentile of the error, such that the preceding error value does not fall within this set percentile. The exercise is done for both load cases and the limit can be seen in dashed line, which while different, is close in both load cases (0.0753 in the first load case, and 0.1280 in the second load case). The difference between the two models in both load cases does tend to null in the far-field, as shown by the dotted line in both plots. All Von Mises stress values shown are normalized with respect to the peak stress value registered in the real model assessment of the respective load case, while the x axis represents the normalized distance.

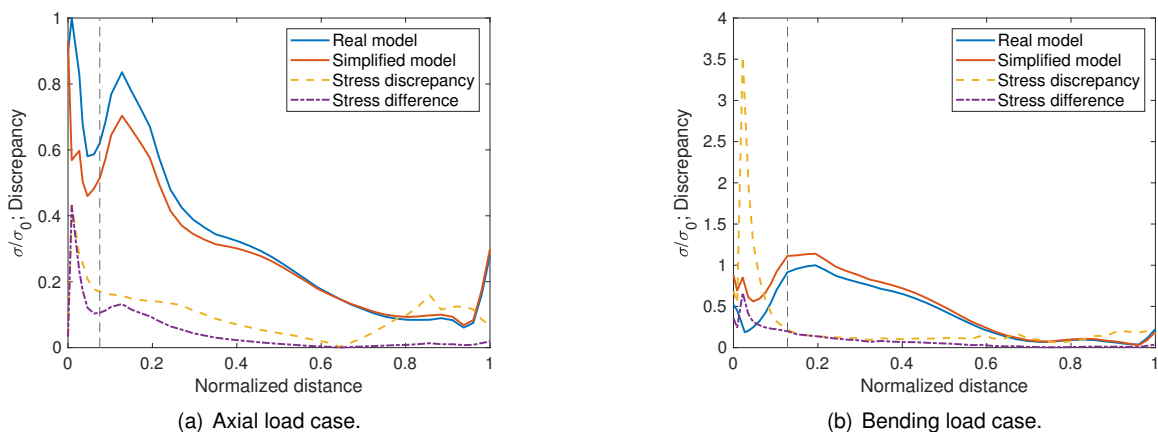


Figure 7.17: Von Mises path stress results.

The total CPU times are also compared (see Table 7.5), further justifying the use of the simplified model given its good accuracy to predict stress, namely in the far-field region, and much lower computational time. The real model, for the first load case, shows approximately a ninefold increase in the total CPU time needed to complete the

simulation, over the simplified model. Similarly, an increase is verified for for the second load case, albeit smaller at a threefold increase, approximately.

Load	Axial	Bend. 1	Discrepancy	Ratio (Real/Simplified)
Real model	296065s	196664s	89%	9.29
Simplified model	37863s	61882s	69%	3.17

Table 7.5: Computational time comparison.

7.2 Topology Optimization Implementation and Parameter Definition in Abaqus

The present section describes the topology optimization workflow employed in the Tosca Structure module in Abaqus, with the objective to create a fundamental understanding of the available tools and parameters that affect the optimization solution. It is also necessary to complement the lacking discussion and application of the MIMP interpolation scheme employed by Tosca starting in 2021, as well as the accompanying new design variable filtering technique. Moreover, while topology optimization has been regularly been adopted through strain energy minimization and volume constraint methods in literature, the present thesis is focused on the implementation of a volume minimization method, since the work of [75] already tackled the same component problem through the conventional strain minimization method extensively.

7.2.1 Mesh Influence

A first analysis is performed on a 3D cantilever beam subjected to a bending load, with the intent to investigate the influence of both element size and type on the optimization solution. The main parameters used for comparison are the final geometry, objective function and constraints, and the total number of cycles needed for convergence.

In order to also developed a clearer understanding of the interactions present in the real component, the cantilever beam model has been defined with the introduction of these. That is, the loaded face is divided into three regions, two loaded at each extreme (top and bottom), and the middle one free. The load itself is defined as a concentrated force at a reference point away from both faces, and connected to each through structural distributing coupling. The load has vertical (positive y-axis) direction, being defined from this point forward as the bending load case (figure 7.18).

The optimization task was defined through a strain energy minimization formulation with volume constraint (lower or equal to 35% of whole model before optimization). The interpolation scheme chosen was SIMP, as during the time said trials were performed there was no access to the MIMP interpolation scheme. All resulting data can be found in annex B.1, alongside the geometries of both the most coarse and fine meshes of each element type.

Plotted in figure 7.19(a) is the objective function of the optimization task, which is the strain energy, for each element type as a function of the total number of elements. It can be noticed that as the number of elements increases, the difference between linear and quadratic elements decreases. The tetrahedral elements showcase poorer performance, which can be attributed to the lack of symmetry that these elements inherently are defined by in contrast with the symmetry of hexahedral elements. In fact, the final geometries for both element types are

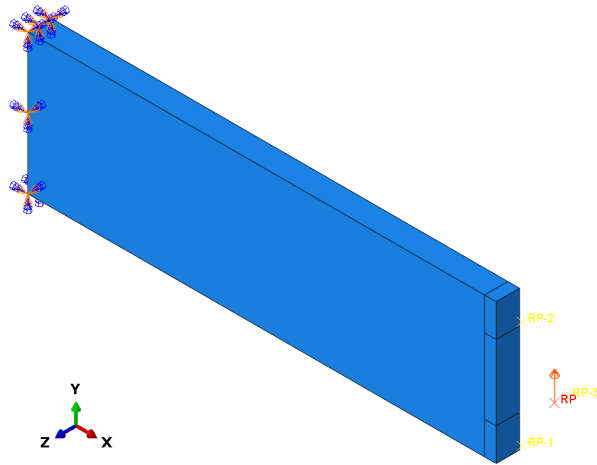


Figure 7.18: Part to be optimized.

different, with the hexahedral meshes showcasing symmetry by the middle plane (xy-plane) as expected, and the tetrahedral mesh example being asymmetric by the same middle plane (see annex ??).

Additionally, the volume constraint is fulfilled in all studied cases, with the maximum error with respect to the 35% constraint being 0.27% (see figure 7.19(b)). For such an optimization task, the best performance indicator to distinguish between optimization solutions is the objective function, or the strain energy in this example, since any other indicators are within marginal differences.

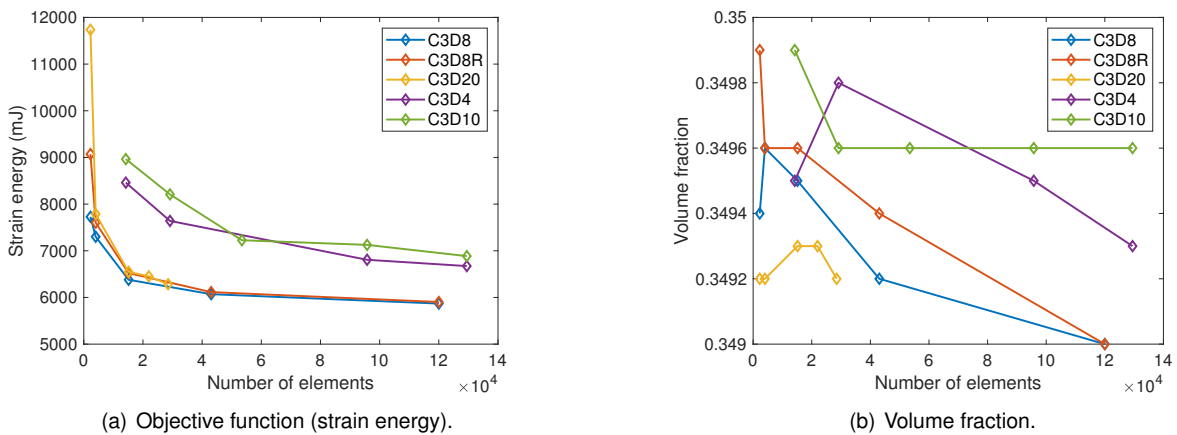


Figure 7.19: Mesh influence results comparison between element types.

7.2.2 Material Interpolation Scheme Comparison

With the interest in defining the most adequate interpolation scheme for the design project at hands, and expand the understanding of the newer MIMP scheme, both SIMP and MIMP schemes are compared through a simple cantilever beam example (see figure 7.20). The left side is constrained in all displacement and rotation directions, while the right side is divided into two segments, the top one loaded by a vertical load, and the bottom one free from any loading or boundary conditions.



Figure 7.20: Part to be optimized.

7.2.2.1 Mesh influence

The optimization task is defined in accordance to the conditions of the real component, that is, a volume minimization task is performed with a displacement constraint at the top right point highlighted in figure 7.20. The plot in figure 7.21(a) showcases the evolution of the solution volume with respect to the number of elements, such that as the mesh refinement increases, the volume decreases, irrespective of the interpolation scheme used. However, the performance of MIMP is lower compared to SIMP for the same number of elements. The same trend is seen in the percentage of gray elements (figure 7.21(b)). For context, gray elements are considered to have a normalized density between 0.2 and 0.8. Ideally, the number of gray elements is close to null, meaning the optimization solution found a 0-1 design with no intermediate densities. The resulting geometries and accompanying data are showcased in annex B.2.1.

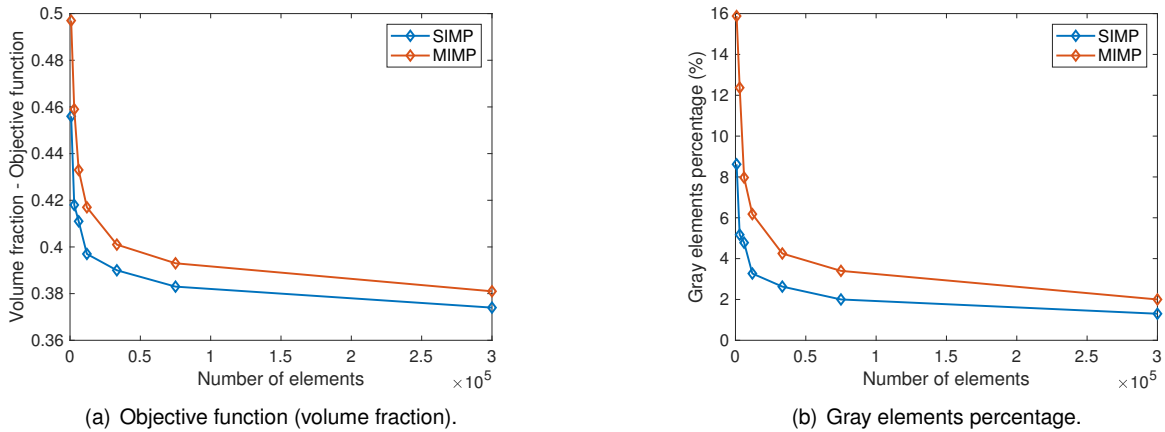


Figure 7.21: Mesh influence results comparison between SIMP and MIMP.

7.2.2.2 Frequency Design Response Influence

MIMP's performance under the presence of frequency design responses is expected to be better compared to the performance of the SIMP scheme. The analysis is performed through the introduction of a minimum frequency constraint, which is changed from 6Hz to 11Hz in unitary steps. Figure 7.22(a) showcases the results obtained, with special emphasis on the frequency constraint. In the optimization performed with SIMP scheme, this constraint is fulfilled up to and including the limit of 9Hz, after which the frequency value overs around the same value of 9.6Hz, despite the minimum limit being above 10Hz. Contrastingly, the MIMP scheme showcases a minimum frequency above the limit in all presented cases, fulfilling the constraint, however with a larger performance margin.

It can also be noted the better performance of SIMP during the cases the frequency is higher than the constraint,

both in terms of volume but also percentage of gray elements. However, the scenario changes starting at 9Hz and up, with MIMP surpassing the quality of the solution in terms of number of gray elements, as can be seen in figure 7.22(b).

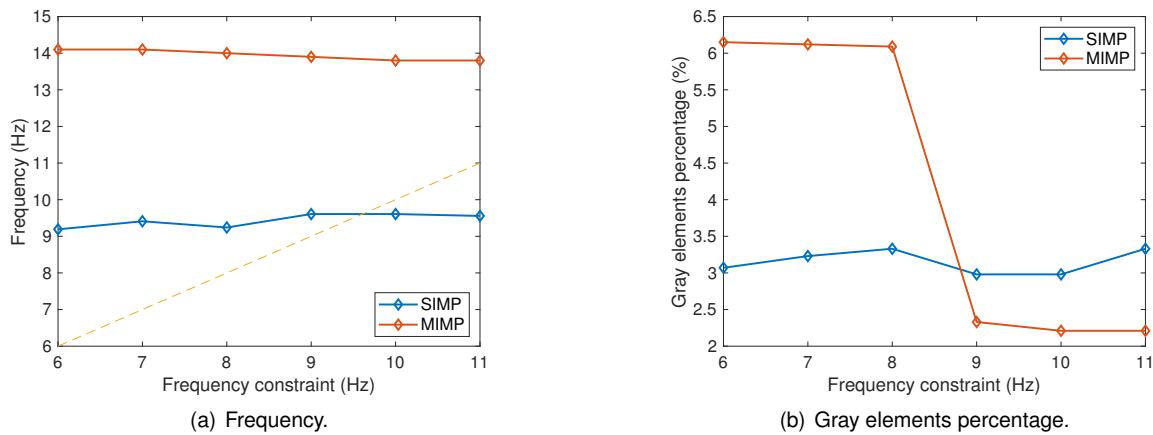


Figure 7.22: Frequency design response influence results comparison.

7.3 Design Interpretation and Conceptualization of Optimization Results

7.3.1 Geometry Smoothing

The optimization results are extracted as a STL file, which represents the surface of the smoothed 3D geometry through tessellated triangles. The process is done with the aid of Tosca Structure.smooth, which generates both the isosurface and its smoothing result.

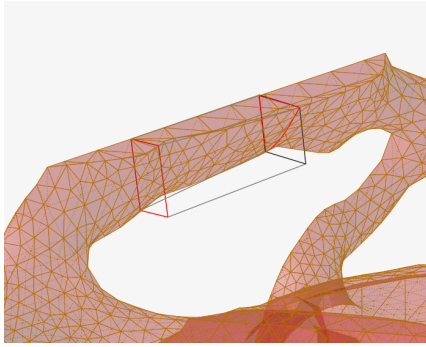
The isosurface is defined by the isovalue, which sets the position of the new surface nodes based on the ratio between interpolated nodal material values defining the element edges. That is, a large isovalue moves the surface node closer to the interior connection node, resulting in a lower model volume. Increasing the isovalue might lead to disconnected geometry, hence a default value of 0.3 is suggested.

The definition of the isosurface still carries surface irregularities and lack of smoothness. An iterative smoothing proceeds the isocut, by further displacing the surface nodes such that the angle between triangles is reduced below a user defined threshold of minimum angle. The higher the number of smoothing cycles, the smoother the resulting geometry. However, this process can lead to shrinkage effects, namely in high curvature regions.

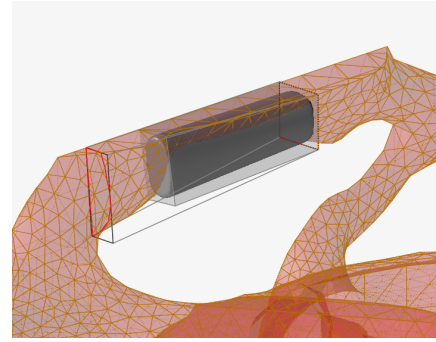
7.3.2 Interpretation of smoothed geometry

The outcomes of the smoothing process are STL files which need to be interpreted into a CAD model able to be modified and prepared for the design validation. For this purpose, the PolyNURBs feature in Altair Inspire was used, allowing to trace over the 3D surface model, creating a smooth geometry, which if closed and not self-intersection, can be exported as a solid model (see figure 7.23 for an example of the use of the wrapping tool).

An alternative solution is the use of re-meshing tools that quadrangulate the existing triangulated polymesh to NURBS in the software Rhinoceros 3D (see figure 7.24), and proceeding to transform the smooth quadrangulated



(a) Selection of the cross-sections to define the two ends of the polyNURBS solid.



(b) Resulting polyNURBS solid.

Figure 7.23: Wrap tool example.

surface file to a solid object in Autodesk Fusion 360. However, this often resulted in open and self-intersecting meshes, and the lack of computational resources did not allow to convert the mesh to solid, proving the method to be very time-consuming. Hence, given the difficulties encountered with this process, PolyNURBs in Altair Inspire was the tool chosen to proceed with the design interpretation process.

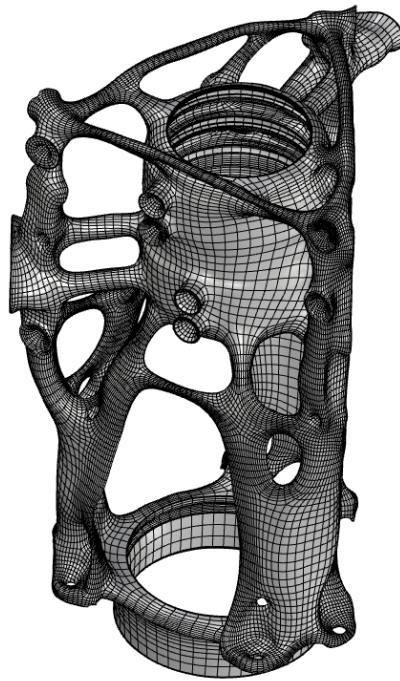


Figure 7.24: Quadrangulated mesh.

Chapter 8

Topology optimization results

In section 7.2, the main tools and parameters available to define a topology optimization process are explored and compared, in order for their impact on the solution to be better understood. This chapter aims at utilizing the results of said section and expanding their use to the actual servo-actuator bracket redesign process.

8.1 Topology optimization model preparation

8.1.1 Design requirements

The design requirements are summarily presented in 2.7. However, the use of a linear FE model warrants the omission of fatigue and dynamic characteristics. Therefore, the relevant structural requirements to be considered in the topology optimization process as requirements are the axial stiffness at the servo-actuator load application points, the relative and normal mounting boss stiffness, and the first natural frequency.

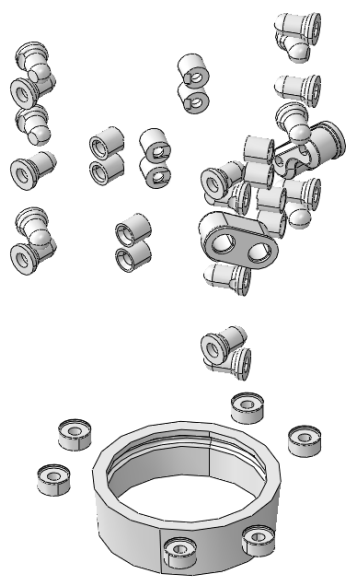
8.1.2 Geometry and meshing

Two files provided by Leonardo are essential to the topology optimization process, which are the design envelope (figure 8.8(c)) and the fixed elements (figure 8.1(b)). However, both need to undergo several changes and fixes before being utilized in Abaqus for the topology optimization process.

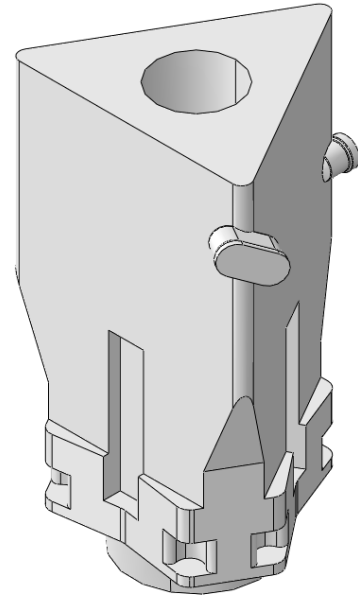
The changes serve three main purposes, the first being the need to improve the quality of the fixed elements, as the ones in figure rebsubfig:dada2 present either missing or broken features, since they are used in the current design of the bracket.

Secondly, the hydraulic region for the present thesis is the same as the current design (see figure 8.2(a)). As such, it is individually created and added to the group of fixed elements, since its addition is essential to accurately predict load transmission and whole design stiffness and frequency response.

Finally, these geometries undergo simplification steps that aim at reducing the necessity for fine mesh regions, and the consequent longer simulation times. Namely, the internal hydraulic region indents and oil canals are removed (see figure 8.2 for comparison between the current hydraulic system and the simplified one). Additionally, the fillet features present on each of the six upper manifold mounting bolt holes are removed, once more to remove the need of fine mesh. The design envelope region is changed in accordance to the fixed elements, such that no internal voids or overlapping regions exist.

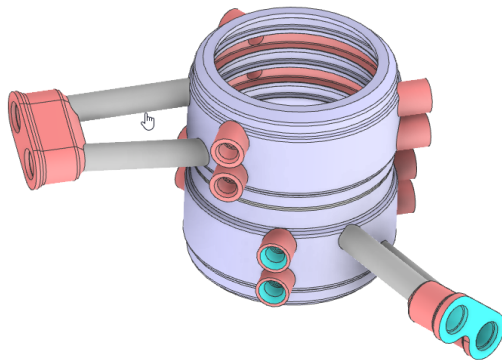


(a) Fixed elements.

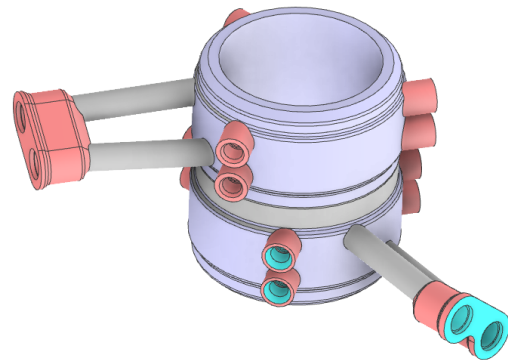


(b) Design envelope.

Figure 8.1: Optimization individual parts.



(a) Hydraulic part of the current design.



(b) Simplified hydraulic part for optimization purposes.

Figure 8.2: Hydraulic part.

Figures 8.3(a) and 8.3(b) show the fixed elements, and design envelope regions, respectively. Additionally, in green are volume regions added to the original geometry, whereas in red are volume regions removed. It should be noted that the entire hydraulic system is in green, despite the part undergoing a simplification process.

The meshing of the part has a significant impact on the topology optimization result, both in terms of element size, but also type. The element type chosen for the topology optimization process is a quadratic tetrahedron element (C3D10). However, due to time constraints and necessity to test several optimization setups, the element size is of 7mm in the regions of most interest, and coarser at 8mm in the regions that are expected to remain both unchanged or entirely absent from the final solution (as per early simulations or intuitive conception). Figure 8.4 shows the meshed part.

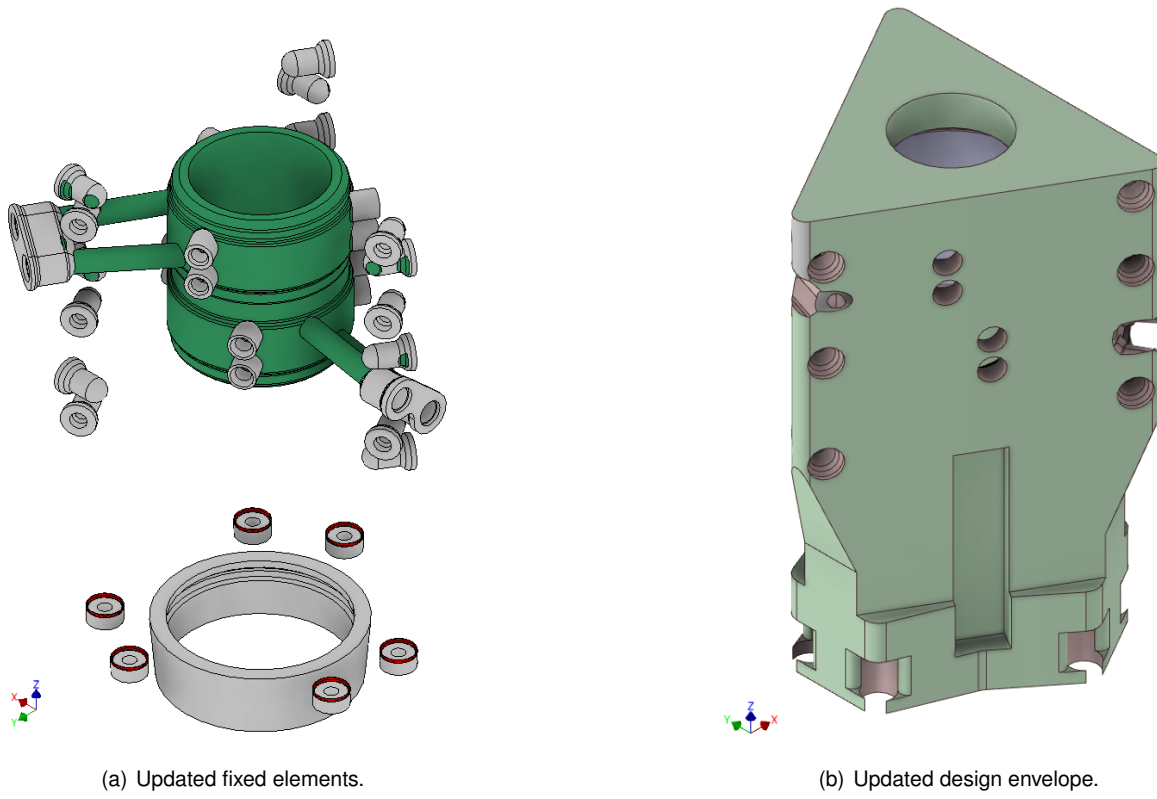


Figure 8.3: Updated optimization individual parts.

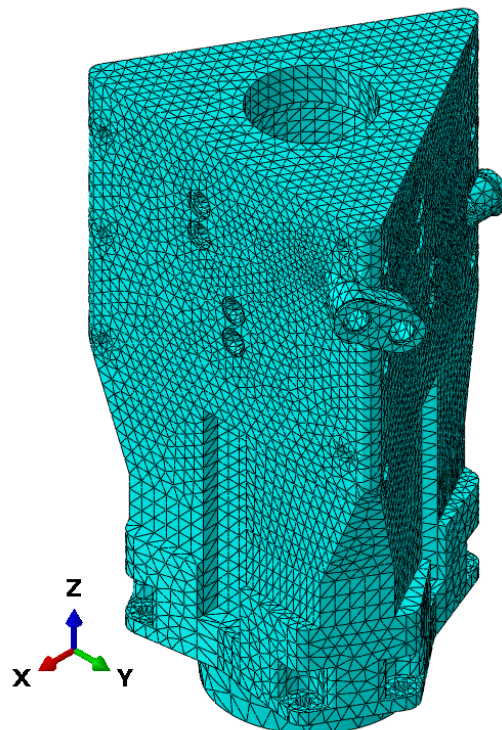


Figure 8.4: Meshed topology optimization part.

8.1.3 Materials

The application of the proof load on all topology optimization simulations performed allows for an elastic material assumption to be applied, therefore reducing computational time and allowing for more test cases to be explored.

The material chosen is Ti6Al4V ELI Titanium Alloy. In summary, the linear-elastic material properties used throughout all topology optimization simulations are defined in table 7.2.

8.1.4 Boundary conditions and load cases

The topology optimization boundary conditions are the same utilized in the simplified model suggested in section 7.1, validated under the static strength analysis of the current bracket design. In order to simulate the attachment of the bracket to the testing rig, translation and rotation constraints are placed on the six bolt holes. Summarily, these are (figure 8.5),

- Bolt hole displacement and rotation constrained in the x and y directions (figure 8.5(a));
- Top and underside bolt hole regions displacement and rotation constrained in the z direction (figure 8.5(b));
- Fillet feature on the conic element displacement constrained in the x and y directions (figure ??).

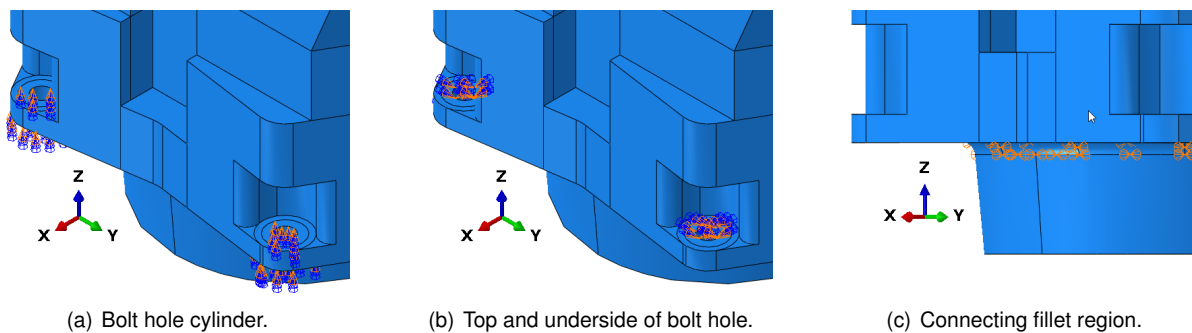


Figure 8.5: Boundary conditions.

Identically, the loads are applied at the same points AF_{S1} , AF_{S2} and AF_{S3} , and connected through a series of Structural Distributing Coupling constraints, connecting each of the load application points to the respective face six mounting bosses. While three load cases are presented by Leonardo's requirement document, only the one referring to the proof condition is taken into consideration. The choice is based on the fact that it represents a critical condition under elastic regime of the material, since the load should be applied and no yielding of the material verified.

Additionally, the symmetry of the solution is bound to the loading of the bracket. If only the static loads presented are applied, the resulting solution is largely non-symmetric, not due to the hydraulic part influence, but due to the fact that only one side of three is loaded in bending. Therefore, two additional bending load cases are introduced in the remaining two sides of the part, totalling four different loading configurations: 1 axial, 3 bending. Table 8.1 summarizes each of the load cases, with AF_P representing the magnitude of the force (considering they're applied solely in the z-direction).

The inclusion of the different load cases is done through a linear perturbation step, rather than a conventional multiple step analysis. This change results in a more efficient analysis, as according to [75], a 87.5% computational time reduction per iteration in a similar analysis. Considering the boundary conditions remain unchanged between all load cases, it is expected for this approach to be more efficient in this application.

Load	Axial	Bend. 1	Bend. 2	Bend. 3
AF_{S1}	AF_P	$-AF_P$	AF_P	$-AF_P$
AF_{S2}	AF_P	$-AF_P$	$-AF_P$	AF_P
AF_{S3}	AF_P	AF_P	$-AF_P$	$-AF_P$

Table 8.1: Topology optimization load cases considered.

Finally, the point masses are applied to the points CG_1 , CG_2 and CG_3 , enumerated in accordance with the load application points. The points are placed at the distances d_{CG_1} , d_{CG_2} and d_{CG_3} , with masses of M_1 , M_2 and M_3 . The connection to the part is simplified, as no information is given on the servo-actuator stiffness or physical model. Once more, to allow relative motion between the mounting bosses, the masses are connected to each through a continuum distributing coupling constraint.

8.2 Topology optimization setup

This section gives an overview of the setting up of the topology optimization task in Abaqus, including the addition of models elements to aid the definition of several design responses and constraints.

8.2.1 Topology optimization task

Both the algorithm and interpolation techniques are selected during the topology optimization task definition. However, it should be noted that the algorithm cannot be changed after the initial setup, whereas the remaining settings can be freely changed. Considering the optimization will focus on a volume minimization process, the general optimization algorithm is used, which conceptually is sensitivity-based.

Two interpolation techniques are explored in the context of this thesis, SIMP and MIMP. While SIMP and its respective settings are available to be modified within the Abaqus GUI, the MIMP interpolation technique is not yet implemented, so its inclusion and definition is done through the simulation input file (INP file format). Therefore, in the case of the SIMP, the penalty factor is kept at a value of 3. By default, this interpolation technique utilizes sensitivity filtering. On the other hand, the MIMP interpolation technique does not make use of penalty factor, such that this is omitted. It does however, by default, make use of a new design variable filtering technique. The remaining settings are kept at default and the same between both techniques, but their impact solution should be assessed on future work.

8.2.2 Design responses definition

The several topology optimization trials will use a different set of design responses, which will be summarily explored and defined in this section.

8.2.2.1 Volume

The volume design response is defined over the entirety of the model, and no further model modification are necessary for its implementation.

8.2.2.2 Axial stiffness

The axial stiffness requirement is translated into a displacement requirement, dependent on the load case in consideration. The design response is individually defined at each servo-actuator load application point as an absolute displacement variable in the z or axial direction. The variable is evaluated at each of the four load cases present, but solely the maximum value is considered for the optimization task.

8.2.2.3 Eigenfrequency

The first natural frequency is evaluated at a separate step with the sole purpose of evaluating the modal response of the part. As such, during the definition of the design response, the modal analysis step should be selected. Additionally, considering only the first eigenfrequency is of interest for the optimization process, the range mode is required to be selected, as well as the upper and lower modes both as 1 (see figure 8.6).

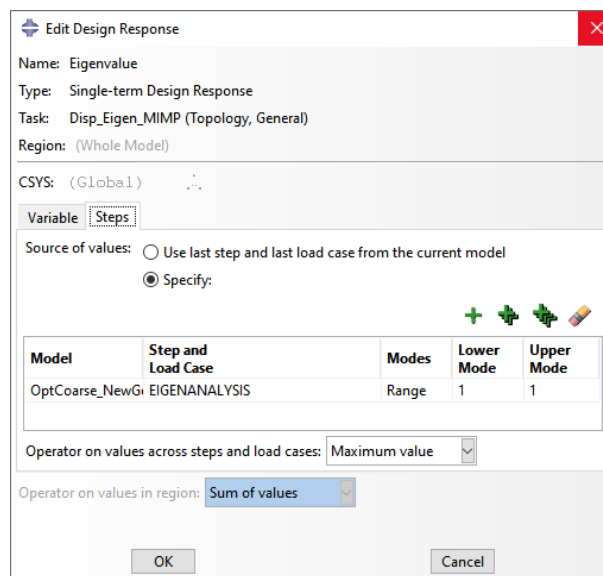


Figure 8.6: Edit design response window for the correct definition of the first natural frequency design response.

8.2.2.4 Relative stiffness

Relative stiffness, such like the axial stiffness, is translated into displacement requirements. However, the design response definition depends on the relative displacement between two elements of the bracket which means a combination must be set.

The relative stiffness is defined between mounting bosses, so a reference point is set at each of these in a relevant location. The center of each mounting boss is chosen, totalling eighteen points. Figure 8.7 showcases the locations of the points in the face that is named as 1. Each point is named from A_i to F_i , with i being the number of each of the three faces (1 to 3).

The single term design responses are selected as absolute displacement variables, individually for each load case. This is because the requirement is given in relative terms to the current part performance, such that it changes depending on the part loading.

The combined term design responses exhibit an unique behaviour when performing an absolute difference operation between two absolute displacement single term design responses. The operation is done between the

individual coordinates, such that,

$$|\Delta u_{\vec{A}B}| = |\vec{u}_A - \vec{u}_B| = \sqrt{(u_{Ax} - u_{Bx})^2 + (u_{Ay} - u_{By})^2 + (u_{Az} - u_{Bz})^2}, \quad (8.1)$$

where \vec{u}_A and \vec{u}_B are the displacement vectors of two nodes A and B. This combined term describes in absolute value the relative displacement between the two nodes. Figure 8.7 showcases the relative displacements pairs that will be considered, specifically in face 1. The pairs are named based on the two points connected, and the face they belong to.

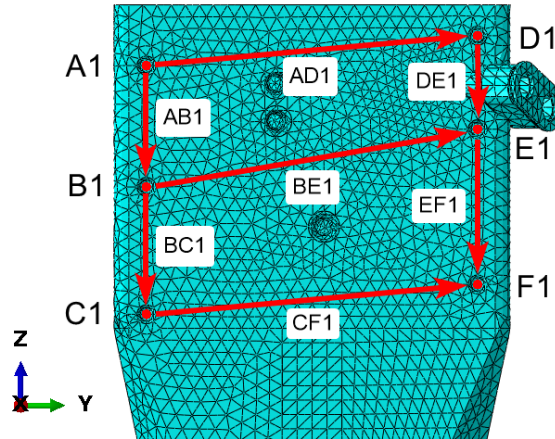


Figure 8.7: Schematic of the naming scheme used for both the relative stiffness pairs, and normal stiffness points. Only face 1 is showcased. Face 2 is to the right, and face 3 to the left.

Due to the high number of design responses to be defined (18 single term, and 21 combined term, totalling 39 design responses), a Python script has been created to automate the process of defining these.

8.2.2.5 Normal stiffness

Finally the normal stiffness, once more translated to a displacement design variable, is measured in the perpendicular direction of each face, at the same mounting boss points defined for the relative stiffness design response. To do so, an approximation is made by introducing two additional coordinate systems, by rotating the global coordinate system 120° and -120° over the z axis. Figure 8.8 showcases the three coordinate systems relevant to assess the normal displacements, with one being the global coordinate system, originally with the x axis perpendicular to face 1.

Similarly to the relative stiffness case, a Python script has been created to automate the definition of these design responses.

8.2.3 Topology optimization objective and constraints definition

The general optimization algorithm present in Abaqus is capable of handling different approaches to optimization, with the most common being strain minimization, constrained by a relative volume fraction. Such an approach is explored on [75]. However, due to the nature of the requirements for the redesign project being displacement related, and the interest in achieving a minimum volume solution to save weight, a volume minimization approach is chosen.

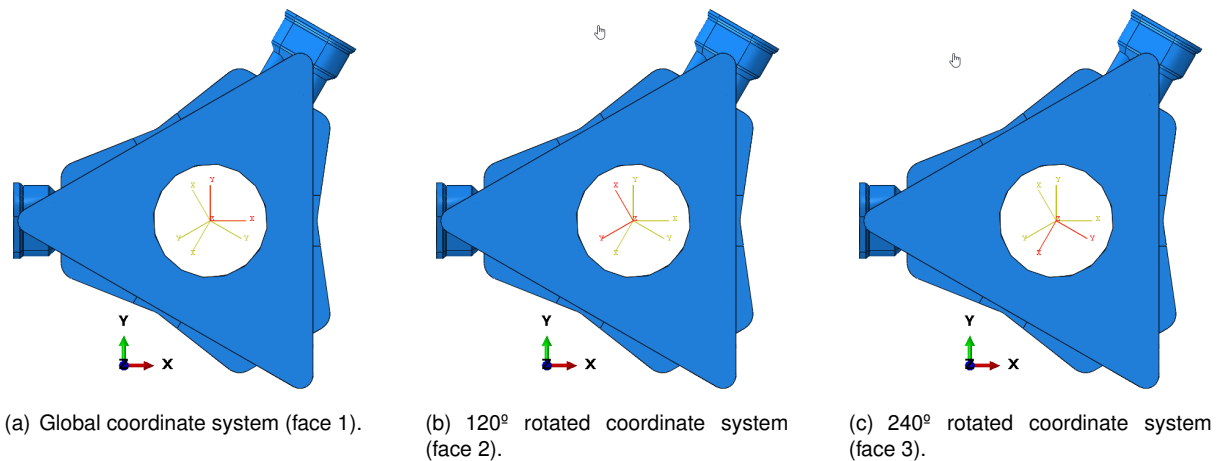


Figure 8.8: Additional coordinate systems to aid the definition of the normal stiffness.

Therefore, all the topology optimization trials and results showcased in this thesis are based on a volume minimization (or minimization of maximum) approach, with different sets and configurations of constraints. These are defined by the numerical limits defined in the requirements section 2.7.

In addition to the design response constraints, geometrical constraints are to be introduced, namely the definition of all the fixed elements as frozen regions which shall remain completely solid and unchanged throughout the optimization process. DfAM guidelines also suggest the consideration of an overhang angle constraint in order to reduce the need for printing supports and post-print processing, however they are not in this present thesis, but their inclusion impact on the solution is suggested for future work. The reasoning behind the decision stands with the lack of information regarding the actual printer to be used, which affects the overhang angle limit characteristics.

The following section explores the studied topology optimization simulations performed, and the different sets of constraints and their definition taken into consideration.

8.2.4 Topology optimization trial cases

The search for a proper topology optimization solution is dependent on the understanding of the requirements, their implementation and impact on the solution performance. While several more topology optimizations have been performed, such as the implementation of the hydraulic system through the addition of a pressure step with stress constraint, and initially solely SIMP optimizations, only a limited amount of relevant results will be showcased.

Summarily, four main topics are tackled, these being,

- **MIMP, and SIMP comparison:** Given the newly addition of MIMP to the interpolation techniques pool provided by Abaqus, it's implementation is compared against the generally used SIMP technique, in order to assess its performance;
- **Eigenfrequency constraint effect:** The approach is particularly relevant to further understand the differences between MIMP and SIMP interpolation techniques, as well as understand the impact an additional constraint and step have on the final solution and its convergence;
- **Relative and normal stiffness constraints effect:** This topic has similar goals as the previous eigenfrequency constraint one, with the additional difference that it is responsible for the introduction of several dozen design responses and constraints. As such, the impact of these is to be assessed, as well as how they are introduced, bringing the solution ever so closer to the final design to be chosen and printed;

- **Volume minimization, and maximum minimization comparison:** Finally, a comparison is performed between the results of the two approaches to the volume minimization problem. However, for the majority of the trial cases presented, the volume minimization approach is chosen as suggested by Abaqus provided documentation.

In order to maintain consistency between the results, the same geometry is used throughout all the trial cases showcased, as well as boundary conditions and loads

The first two presented trial cases also have the objective to assess if the sole inclusion of the three axial stiffness requirements are sufficient to obtain a proper design solution that fulfils the remaining requirements. As the trial cases are presented, the goal is to achieve a more "complete" optimization task (read, all performance requirements are included as optimization constraints) that ultimately converges to a proper solution.

8.3 SIMP and MIMP comparison trial cases

The purpose of the initial set of trial cases is to both understand the fundamental differences between SIMP and MIMP interpolation techniques when applied to a complex geometry and optimization problem, as well as build up the problem towards completeness and slowly add constraints while always validating the performance of the designs.

Four relevant trial cases are defined for the purpose of this assessment, these being trial cases 1, 2, 3 and 4.

- **Trial case 1:** Defined by a volume minimization with axial displacement constraints, it utilizes the SIMP interpolation technique;
- **Trial case 2:** Defined by a volume minimization with axial displacement constraints, however it utilizes the novel MIMP interpolation technique;
- **Trial case 3:** This trial case is identical to trial case 1, with the additional inclusion of a minimum first natural frequency constraint. The SIMP interpolation technique is used;
- **Trial case 4:** This trial case is identical to trial case 2, with the additional inclusion of a minimum first natural frequency constraint. The MIMP interpolation technique is used.

8.3.1 Trial case 1

Table 8.2 summarizes the topology optimization setup and parameters that define the trial case 1. It is a volume minimization optimization task, constrained by the three axial stiffness constraints. The interpolation technique chosen is SIMP with a penalty factor of 3.

Interpolation technique		SIMP
Objective function		Minimize volume
Constraints	Axial displacement	$u_{AFS1}^z \leq u_{axial}$ $u_{AFS3}^z \leq u_{axial}$ $u_{AFS2}^z \leq u_{axial}$

Table 8.2: Trial case 1 topology optimization configuration.

8.3.1.1 Topology optimization results

The analysis converges to a solution in 58 cycles, with the displacement constraints being fulfilled across all load cases. The plot in figure 8.9 showcases the trend of both the objective function, as well as the axial displacements measured at each point, for each of the four load cases. The values shown are normalized by the constraints. As shown, the analysis constraints showcase a fast convergence, despite the volume of the part continuously decreasing and converging at a slower rate. The traction load case showcases the higher stiffness (lower displacement) in the first cycles, converging to the same value as the other load cases as the number of cycles progresses. It's an indication of the detriment of the part response to the traction loading, while keeping it within the performance limits proposed.

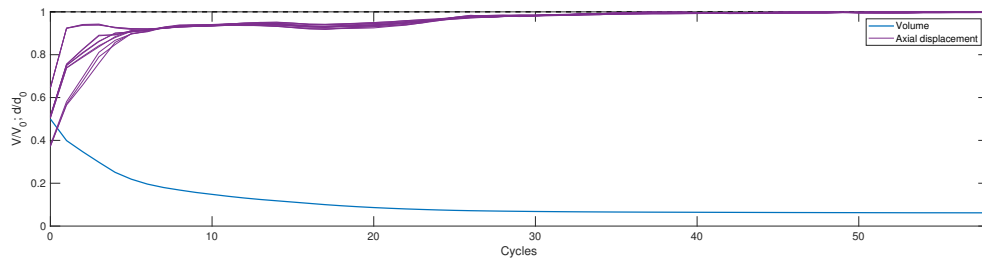


Figure 8.9: Trial case 1 convergence plot.

Figure 8.10 shows the solution of the optimization without any smoothing process being applied. The isosurface is created with the elements that have an intermediate density equal or greater than 0.3. Connectivity exists between all fixed elements of the part, making it a potential good solution for the problem and further validating the use of the isosurface parameter value. Finally, the solution showcases 1.32% of gray elements.

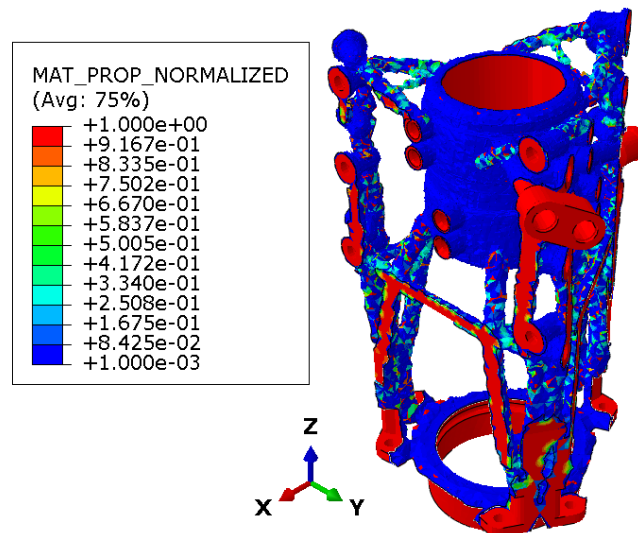


Figure 8.10: Trial case 1 normalized material property result.

8.3.1.2 Post-processing and design realization

Within Abaqus CAE interface, the result of the topology optimization, is extracted through a smoothing process done by Tosca Structure.smooth. The following settings are utilized for the smoothing process applied to all

geometries,

- **Iso value:** 0.5;
- **Reduction percentage:** 0%;
- **Smoothing cycles:** 5;
- **Target volume:** 0;
- **Filtering:** Off.

The resulting STL file (see figure 8.11) is the smoothed geometry. It serves as guideline to the creation of the solid bracket in Altair Inspire through the use of polyNURBS.

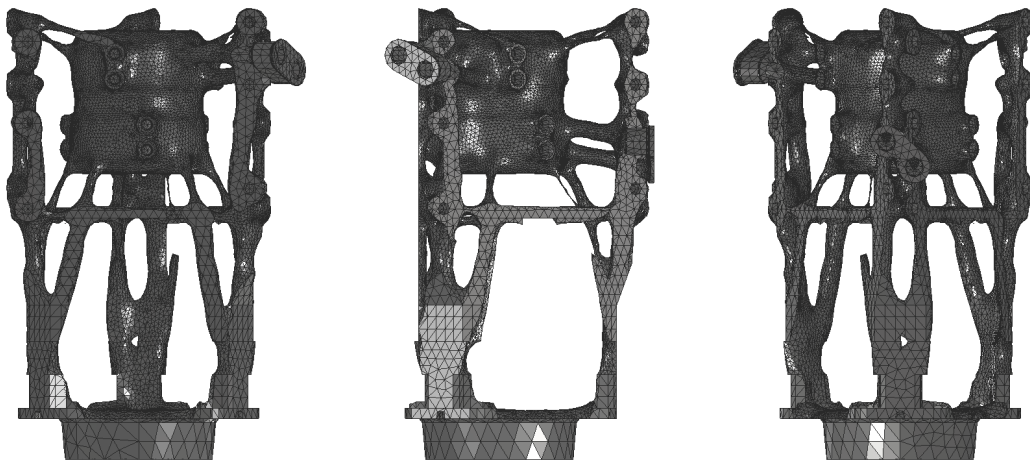


Figure 8.11: Trial case 1 extracted STL mesh file.

The result of the design realization step performed in Altair Inspire can be seen in figure 8.12, which is lacking the post-processing done in Autodesk Inventor, responsible for adding the fixed elements and trimming the volume outside of the design envelope (including the hydraulic system indentations).

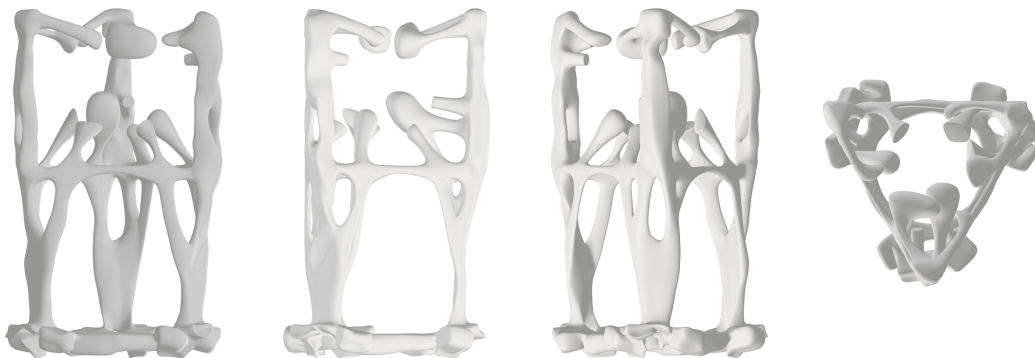


Figure 8.12: Trial case 1 polyNURBS solid result.

Finally, an assembly is created within Autodesk Inventor containing the solid geometry from Altair Inspire, as well as both the set of fixed elements and the design envelope. Through a series of combination features, the final solid part is obtained, with no regions outside the permissible volume. Figure 8.13 showcases the final geometry to be validated under the static and modal analysis in Abaqus.

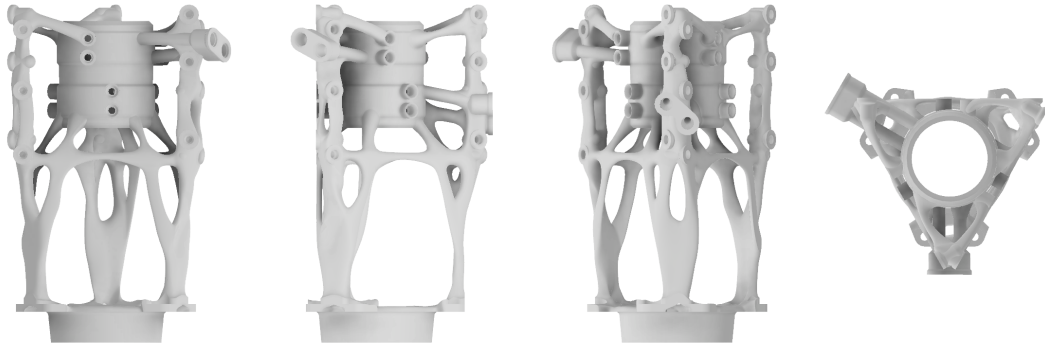


Figure 8.13: Trial case 1 design interpretation result.

8.3.1.3 Part validation

The newly obtained geometry is imported to Abaqus to perform the static and modal analysis that define this solution and allow it to be compared to the next trial cases and the current design bracket. The same loading and boundary conditions are applied to this part, as they were to the current design bracket, and the topology optimization model. That is, the proof loading is applied.

Due to the nature of the topology optimization, the stress results of the optimization solution are solely performed on the final chosen solution that undergoes the shape optimization process that has the intent of smoothing out and reducing stress concentration regions. As such, the performance indicators of interest are the mass, the first eigenvalue, and the axial, relative and normal stiffness values. The mass, and relative and normal stiffness results are normalized against the current design results, as these are compared directly against them. On the other hand, the remaining ones are normalized against the constraints that are imposed.

The mass of the design is, approximately, 0.8456 of the current design bracket, and the axial stiffness results, as per table 8.3, fall well within the requirement.

Load	Axial	Bend. 1	Bend. 2	Bend. 3
AF_{S1}	0.7015	0.7835	0.8718	0.7897
AF_{S2}	0.6970	0.8208	0.7853	0.9090
AF_{S3}	0.6636	0.8694	0.7457	0.7874

Table 8.3: Trial case 1 normalized axial stiffness results.

However, with the lack of any additional constraints on the remaining design responses, their results are not satisfactory. The first eigenvalue is about 0.6847 of the minimum required, a rather high discrepancy which puts in danger the controllability of the aircraft. Additionally, tables 8.4 and 8.5 showcase the normalized relative and normal stiffness results in percentage units, respectively.

Notably, the relative stiffness in all the bending cases is higher than the current design, but outside of the 80% minimum constraint suggested. The same trend has been observed by [75], which might be an indication of similar simulation errors, namely in both the current design simulation due to its two component and connector complexity, and the mesh size used during topology optimization which might poorly predict the displacements.

Load	Axial	Bend. 1	Bend. 2	Bend. 3
AB1	99.86	24.34	28.59	28.07
AD1	327.61	42.02	77.04	54.64
BC1	260.10	41.09	40.53	58.89
BE1	422.19	36.72	31.57	42.53
CF1	133.04	31.75	11.66	33.19
DE1	259.08	49.59	74.36	66.61
EF1	91.15	43.94	31.92	31.79
AB2	111.77	41.16	35.14	41.01
AD2	482.89	41.16	48.95	27.56
BC2	115.40	51.28	39.51	45.83
BE2	100.04	37.73	33.30	14.98
CF2	216.52	39.73	29.67	17.80
DE2	204.26	49.47	57.01	56.54
EF2	244.49	32.12	39.96	30.06
AB3	145.51	34.87	41.79	30.02
AD3	679.22	33.63	41.53	43.18
BC3	179.75	41.77	44.08	37.44
BE3	245.70	31.13	37.15	44.26
CF3	90.54	15.78	30.39	35.71
DE3	275.70	54.10	46.23	35.41
EF3	153.20	27.87	27.19	46.36

Table 8.4: Trial case 1 normalized relative stiffness results.

8.3.2 Trial case 2

Trial case 2 is in everything similar to trial case 1, except for the interpolation technique utilized, this time being MIMP. For simplicity sake, the procedure explanation is simplified as it is similar to trial case 1. Table 8.6 summarizes the topology optimization parameters for trial case 2.

Interpolation technique		MIMP
Objective function		Minimize volume
Constraints	Axial displacement	$u_{AFS1}^z \leq u_{axial}$ $u_{AFS3}^z \leq u_{axial}$ $u_{AFS2}^z \leq u_{axial}$

Table 8.6: Trial case 2 topology optimization configuration.

8.3.2.1 Topology optimization results

With a faster convergence in 32 cycles, trial case 2 results in a high convergence rate for both the objective function and the axial displacement constraints, these trending towards the constraints in all load cases, including the axial one. Figure 8.14 showcases the plot of the design responses trend.

The resulting geometry is similar to the one obtained in trial case 1, with the clear presence of more gray elements, this time making 3.97% of the total elements of the analysis, likely due to the reduced number of cycles.

Load	Axial	Bend. 1	Bend. 2	Bend. 3
A1	267.74	38.90	38.55	41.26
B1	384.12	54.66	43.18	46.95
C1	265.57	69.98	44.60	45.67
D1	179.90	40.29	43.61	50.60
E1	106.80	37.51	39.73	44.72
F1	40.04	36.81	47.28	71.14
A2	1654.11	46.52	50.71	47.01
B2	290.63	49.05	54.44	49.48
C2	65.92	46.25	66.20	50.93
D2	969.49	47.12	40.10	40.66
E2	56.13	44.85	36.35	37.76
F2	462.02	56.35	30.15	44.96
A3	216.33	41.50	37.64	40.52
B3	61.15	44.30	40.08	46.95
C3	57.97	46.63	40.51	53.92
D3	239.48	42.27	43.57	42.88
E3	1253.25	40.33	38.98	41.87
F3	347.97	54.96	77.85	37.13

Table 8.5: Trial case 1 normalized normal stiffness results.

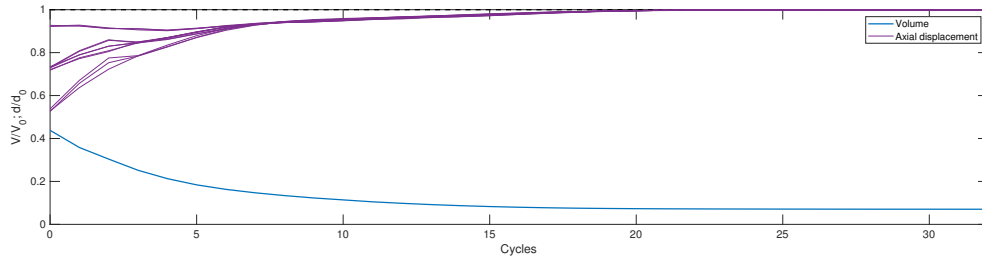


Figure 8.14: Trial case 2 convergence plot.

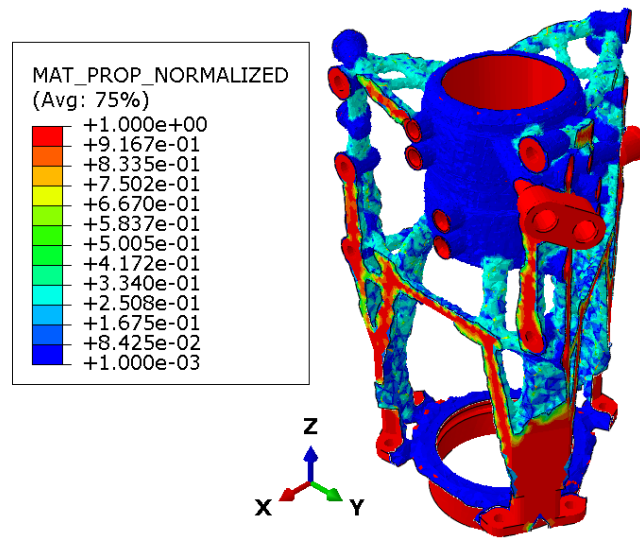


Figure 8.15: Trial case 2 normalized material property result.

8.3.2.2 Post-processing and design realization

Figure 8.16 showcases the smoothed STL geometry obtained from Abaqus as the solution for the optimization process.

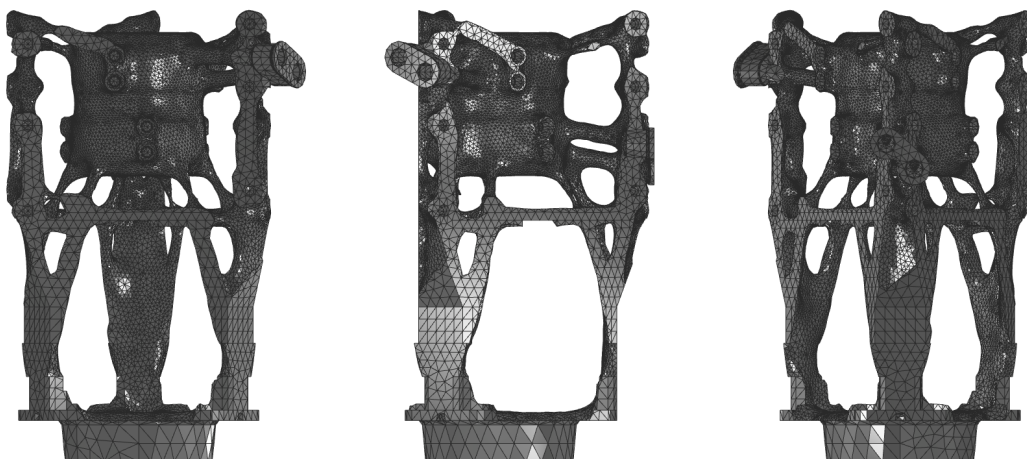


Figure 8.16: Trial case 2 extracted STL mesh file.

Following the same polyNURBS method, the design realization step takes place, and is finalized in Autodesk Inventor to merge with the fixed elements and trim the regions outside of the design envelope volume. The final part is showcased in figure 8.17.

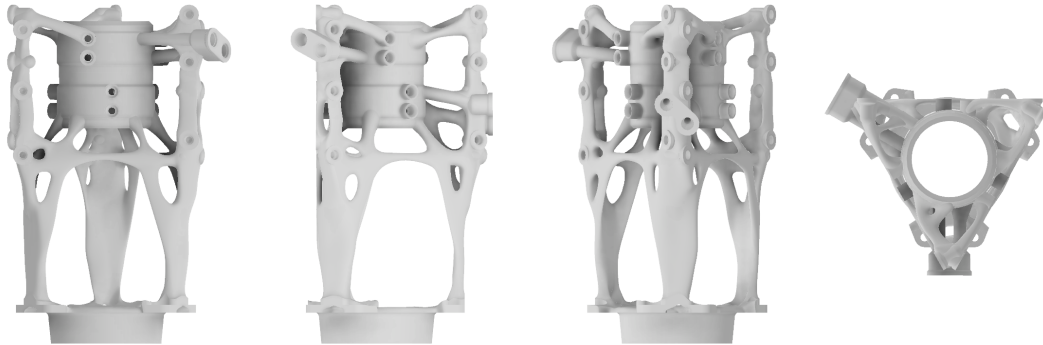


Figure 8.17: Trial case 2 design interpretation result.

8.3.2.3 Part validation

The design interpretation part in figure 8.17 is subjected to a static and modal analysis in Abaqus. The mass of this design is 0.8766 of the current bracket, and the relative stiffness requirements are satisfied, as per table 8.7.

Load	Axial	Bend. 1	Bend. 2	Bend. 3
AF_{S1}	0.6221	0.7166	0.8362	0.7417
AF_{S2}	0.6061	0.7300	0.7257	0.8495
AF_{S3}	0.6219	0.8402	0.7164	0.7458

Table 8.7: Trial case 2 normalized axial stiffness results.

The similarity in results continues with the evaluation of the first natural frequency, now being 0.6953, still a poor result. Tables 8.8 and 8.9 showcase the relative and normal stiffness constraints, respectively.

8.3.3 Trial case 3

Trial case 3 marks the introduction of an additional design response as an optimization constraint. A modal analysis is performed to determine the first natural frequency of the part, to which a minimum value constraint is applied (w_1). The interpolation technique used is once again SIMP with a penalty factor of 3 (see table 8.10 for summary of parameters).

8.3.3.1 Topology optimization results

The introduction of the eigenfrequency constraint highlights the limitations of the SIMP interpolation technique to handle such a problem. While the stiffness constraints converge, the first natural frequency constantly oscillates without achieving any semblance of converge, such that the simulation is aborted at cycle 36 (figure 8.18).

The resulting geometry (figure 8.19) is made of 3.99% gray elements, and it is made of the similar truce-like thin elements that characterize the previous trial cases 1 and 2.

Load	Axial	Bend. 1	Bend. 2	Bend. 3
AB1	106.83	24.12	29.52	29.20
AD1	351.24	42.57	66.60	50.29
BC1	274.90	42.24	43.76	54.53
BE1	420.77	34.79	23.56	41.45
CF1	118.73	29.19	11.54	32.50
DE1	202.68	42.15	63.31	55.69
EF1	96.97	41.03	29.46	29.76
AB2	59.91	33.86	30.49	36.15
AD2	369.03	36.78	41.47	15.90
BC2	132.70	51.40	37.66	42.91
BE2	147.84	33.74	31.79	13.79
CF2	206.66	38.44	29.00	18.56
DE2	240.33	43.20	49.84	49.86
EF2	174.01	28.85	38.31	27.80
AB3	137.28	30.53	39.35	26.03
AD3	604.99	38.26	44.77	41.52
BC3	141.15	38.52	41.95	35.79
BE3	227.36	38.40	37.87	42.87
CF3	81.53	22.31	28.80	34.99
DE3	249.74	52.91	47.12	37.57
EF3	189.52	27.86	28.63	43.63

Table 8.8: Trial case 2 normalized relative stiffness results.

Load	Axial	Bend. 1	Bend. 2	Bend. 3
A1	135.79	41.87	41.84	40.66
B1	278.99	61.43	47.73	45.23
C1	213.49	86.44	51.53	45.59
D1	62.07	38.60	42.22	47.12
E1	321.34	37.68	39.36	42.53
F1	17.65	38.96	49.87	71.32
A2	2145.05	47.07	48.72	45.29
B2	442.90	50.17	56.80	49.49
C2	187.03	49.26	80.15	53.61
D2	1410.63	41.40	45.61	39.15
E2	57.68	38.26	42.36	37.12
F2	287.71	47.20	40.73	45.89
A3	301.34	39.00	34.64	37.98
B3	88.28	42.69	37.14	46.66
C3	79.43	45.90	37.30	57.31
D3	6.70	43.25	46.27	43.48
E3	812.35	41.79	43.11	42.90
F3	323.96	58.98	87.75	39.72

Table 8.9: Trial case 2 normalized normal stiffness results.

Interpolation technique	SIMP
Objective function	Minimize volume
Constraints	Axial displacement $u_{AFS1}^z \leq u_{axial}$
	Axial displacement $u_{AFS3}^z \leq u_{axial}$
	Axial displacement $u_{AFS2}^z \leq u_{axial}$
Eigenfrequency	$\omega \geq \omega_1$

Table 8.10: Trial case 3 topology optimization configuration.

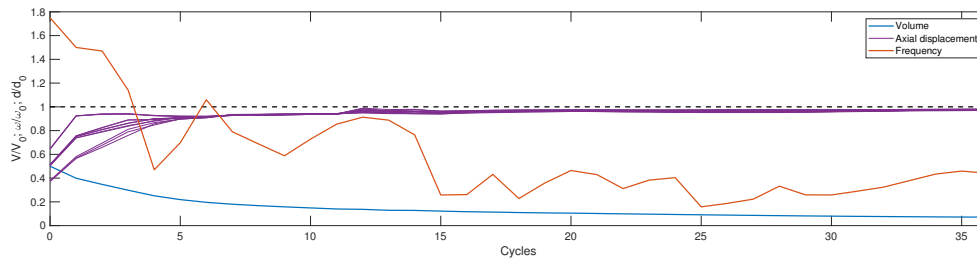


Figure 8.18: Trial case 3 convergence plot.

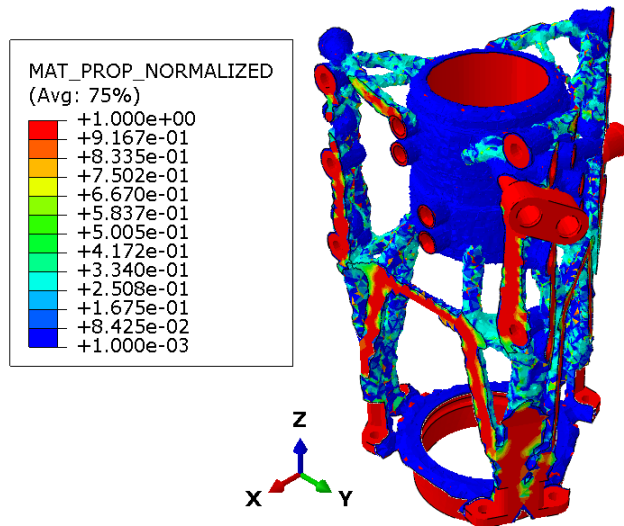


Figure 8.19: Trial case 3 normalized material property result.

8.3.3.2 Post-processing and design realization

The final realized design (figure 8.20) is in every aspect similar to the trial case 1, except for the presence of additional truss-like regions in the top region of the part (highlighted in red), which contribute to a slight increase in both stiffness and first natural frequency, even if far from the requirement set.

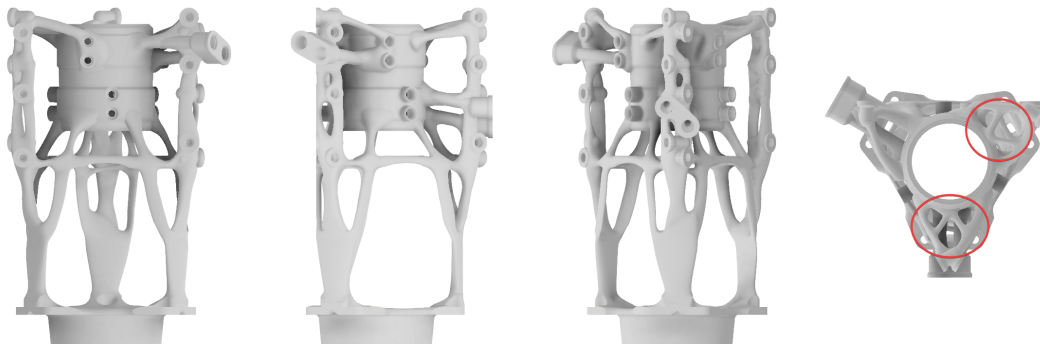


Figure 8.20: Trial case 3 design interpretation result.

8.3.3.3 Part validation

The addition of the eigenfrequency constraint results in the same mass of 0.8556 of the current design, while the first natural frequency stands at 0.7188 of the minimum requirement, still far from fulfilling it.

On the other hand, the axial stiffness showcases once again good results, as shown in table 8.11.

Tables 8.12 and tab:dsahdkj6, respectively, showcase the relative and normal stiffness normalized results, with similar trends shown in the previous trials. That is, stiffness higher than anticipated in bending loading, and lower in axial loading, both far from the 80% to 120% requirements.

Load	Axial	Bend. 1	Bend. 2	Bend. 3
AF_{S1}	0.7648	0.7808	0.8156	0.7996
AF_{S2}	0.7449	0.7913	0.7797	0.8698
AF_{S3}	0.7009	0.8070	0.7169	0.7910

Table 8.11: Trial case 3 normalized axial stiffness results.

Load	Axial	Bend. 1	Bend. 2	Bend. 3
AB1	75.47	21.78	26.09	31.04
AD1	371.53	40.74	43.61	51.00
BC1	245.90	36.98	39.19	52.21
BE1	282.78	37.90	19.77	44.17
CF1	41.84	30.80	10.15	34.89
DE1	422.53	52.81	62.98	51.39
EF1	126.44	44.05	28.88	28.21
AB2	183.94	42.48	29.82	33.22
AD2	460.34	43.26	46.47	31.81
BC2	116.04	44.46	35.46	40.93
BE2	147.57	38.60	33.82	16.84
CF2	162.20	36.83	28.61	21.37
DE2	146.09	50.26	51.46	55.21
EF2	312.89	30.99	43.36	30.64
AB3	158.51	34.65	42.09	30.78
AD3	862.38	26.10	40.64	47.00
BC3	181.82	39.67	45.08	37.33
BE3	274.93	19.93	37.42	48.65
CF3	61.90	10.25	30.73	37.86
DE3	140.45	48.82	40.87	32.53
EF3	177.47	25.60	26.34	48.89

Table 8.12: Trial case 3 normalized relative stiffness results.

Load	Axial	Bend. 1	Bend. 2	Bend. 3
A1	175.31	32.86	35.39	39.48
B1	248.10	46.14	39.54	41.91
C1	110.83	47.75	38.60	38.59
D1	206.95	38.29	38.06	42.63
E1	290.82	35.76	34.44	36.55
F1	70.74	36.41	38.64	47.32
A2	1226.41	38.04	42.60	39.28
B2	139.30	35.06	47.77	42.78
C2	174.38	30.19	59.50	42.84
D2	1376.72	41.83	40.52	37.24
E2	213.31	37.93	38.70	34.00
F2	278.28	40.97	30.21	37.04
A3	293.10	37.44	31.91	37.56
B3	224.27	38.24	32.75	40.40
C3	192.04	37.30	32.29	34.90
D3	215.97	34.83	35.92	38.33
E3	75.39	32.40	31.43	38.71
F3	17.10	38.66	49.62	34.93

Table 8.13: Trial case 3 normalized normal stiffness results.

8.3.4 Trial case 4

Finally, the last trial case of comparison is performed, similar to trial case 3, but utilizing the MIMP interpolation technique. Table 8.14 showcases the optimization parameters taken into consideration.

Interpolation technique	MIMP
Objective function	Minimize volume
Constraints	Axial displacement $u_{AF_{S1}}^z \leq u_{axial}$
	$u_{AF_{S3}}^z \leq u_{axial}$
	$u_{AF_{S2}}^z \leq u_{axial}$
	Eigenfrequency $\omega \geq \omega_1$

Table 8.14: Trial case 4 topology optimization configuration.

8.3.4.1 Topology optimization results

The change in interpolation technique results this time in a different geometry (figure 8.21), namely with clearly thicker elements in the side connection regions of the part, likely responsible for the increase in the first natural frequency. However, the amount of gray elements present is increased to 8.77% despite the good convergence of the solution.

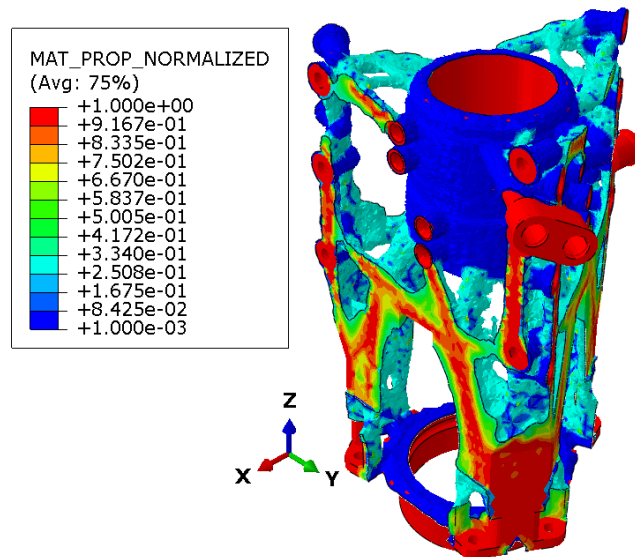


Figure 8.21: Trial case 4 normalized material property result.

The analysis is finished in 42 cycles, and figure 8.22 showcases the convergence plot, which showcases the trend of both the first natural frequency and axial displacements towards the respective constraints.

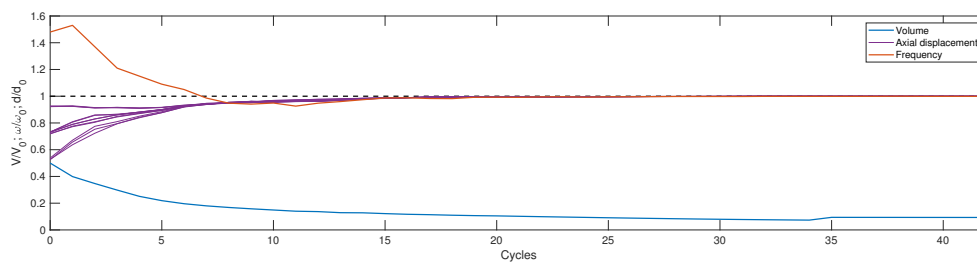


Figure 8.22: Trial case 4 convergence plot.

8.3.4.2 Post-processing and design realization

The design is once more interpreted in Altair Inspire from the ground up, considering the much different design presented. As suggested by the Abaqus results, the geometry has thicker elements and a new design on the lateral connecting regions, highlighted in red in figure 8.23. It does also showcase the same additional truss structure on the top side of the part, as highlighted in the previous trial case.

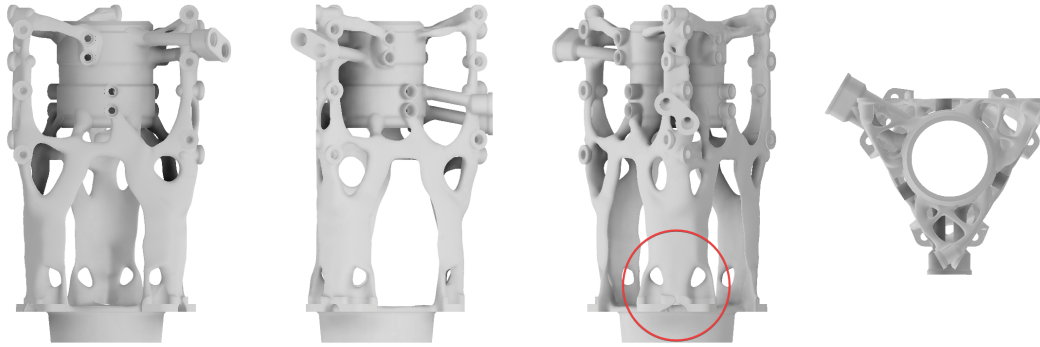


Figure 8.23: Trial case 4 design interpretation result.

8.3.4.3 Part validation

The increased thickness and additional part regions results in a mass of 0.9410 of the current design. The axial stiffness performance (table 8.15) is once more positive, with the requirements being fulfilled in every load case.

Load	Axial	Bend. 1	Bend. 2	Bend. 3
AF_{S1}	0.5993	0.7099	0.7550	0.6444
AF_{S2}	0.6368	0.6940	0.6818	0.7390
AF_{S3}	0.5994	0.7673	0.7100	0.6567

Table 8.15: Trial case 4 normalized axial stiffness results.

Additionally, this is the first trial case where the minimum first natural frequency constraint is verified, this time being 1.2524 of the requirement.

Relative and normal stiffness results are shown in tables 8.16 and 8.17, respectively.

8.3.5 Comparison and discussion

All four trial cases result in proper well connected designs, at volumes lower than the current bracket in use. However, evident differences arise between the use of SIMP and MIMP interpolation techniques.

Between trial cases 1 and 2, the differences are subtle and appear merely in the form of more gray elements with the use of MIMP, likely due to the lower total number of cycles needed. Geometrical differences are small, as the general structure is the same between both. The part is constituted by truce-like elements that carry the loads and connect the mounting bosses to both the hydraulic system and the bolt regions that hold the bracket in place. The presence of the hydraulic element is fundamental to accurately predict the behaviour of the component, such that its omission would yield results with no real meaning.

The introduction of the eigenfrequency constraint highlights the fundamental differences between both interpolation techniques. SIMP outright aborts due to lack of convergence, while MIMP converges and its first natural frequency fulfils the designated minimum requirement. Such is achieved through an entirely new solution geometry. Trial case 3 showcases fairly similar thin truss structures connecting the part elements, as shown in trial cases 1 and 2, suggesting that inadequacy to deal with modal problems. On the other hand, a thicker structure and appearance of new connecting elements is part of MIMP solution. The cost is the clear higher mass.

As such, trial case 4 proves to be able to respect all axial and natural frequency constraints, while maintaining a final volume lower than the current design. However, the remaining relative and normal stiffness requirements

Load	Axial	Bend. 1	Bend. 2	Bend. 3
AB1	80.98	23.62	31.94	29.50
AD1	408.63	38.17	64.39	42.10
BC1	242.41	39.96	37.92	40.16
BE1	336.52	30.02	26.04	34.77
CF1	57.29	26.54	16.28	26.77
DE1	427.31	47.85	60.87	52.22
EF1	127.03	33.64	28.13	25.92
AB2	97.23	32.56	29.24	33.76
AD2	548.68	38.11	40.52	33.04
BC2	183.71	42.90	35.78	33.17
BE2	98.01	32.41	31.02	19.31
CF2	68.27	30.87	26.41	20.99
DE2	299.28	57.14	53.42	54.30
EF2	182.40	28.58	32.61	27.86
AB3	154.11	36.25	36.30	29.00
AD3	627.83	38.72	41.62	36.45
BC3	139.12	31.95	36.95	32.77
BE3	177.75	29.69	32.90	34.80
CF3	31.17	20.53	25.49	28.24
DE3	379.46	59.02	58.36	39.72
EF3	157.71	26.35	26.43	34.77

Table 8.16: Trial case 4 normalized relative stiffness results.

showcases poor performances across all trial cases tested. Considering the same trend is observed in [75], the suspected culprits are both the definition of the requirements themselves in the current design (since they depend directly on the results of the static simulation performed), as well as the displacement approximation considered for these elements, since ideally a unit force displacement load case is applied to each individual mounting boss, which is not feasible considering the number of constraints. However, in order to further improve the performance of the component, these requirements are introduced as constraints in the next trial cases to be performed, with the caveat that they are approximations.

All four designs also contrast vastly with the updated design in the absence of a panel present in all three sides. A step in this direction has already been taken with newer redesign attempts done at Leonardo (see figure 8.24) , where the side panels are also missing, further corroborating the achieved topology optimization designs.

It is also clear that performance is left on the table considering that the first natural frequency of trial case 4 is 1.2524 of the constraint. While further improvements can be performed on this design to reduce the performance gap, due to time limitations, such is only done on the final chosen trial case.

For the proceeding trial cases, MIMP interpolation technique is used over SIMP.

Load	Axial	Bend. 1	Bend. 2	Bend. 3
A1	267.74	38.90	38.55	41.26
B1	384.12	54.66	43.18	46.95
C1	265.57	69.98	44.60	45.67
D1	179.90	40.29	43.61	50.60
E1	106.80	37.51	39.73	44.72
F1	40.04	36.81	47.28	71.14
A2	1654.11	46.52	50.71	47.01
B2	290.63	49.05	54.44	49.48
C2	65.92	46.25	66.20	50.93
D2	969.49	47.12	40.10	40.66
E2	56.13	44.85	36.35	37.76
F2	462.02	56.35	30.15	44.96
A3	216.33	41.50	37.64	40.52
B3	61.15	44.30	40.08	46.95
C3	57.97	46.63	40.51	53.92
D3	239.48	42.27	43.57	42.88
E3	1253.25	40.33	38.98	41.87
F3	347.97	54.96	77.85	37.13

Table 8.17: Trial case 4 normalized normal stiffness results.

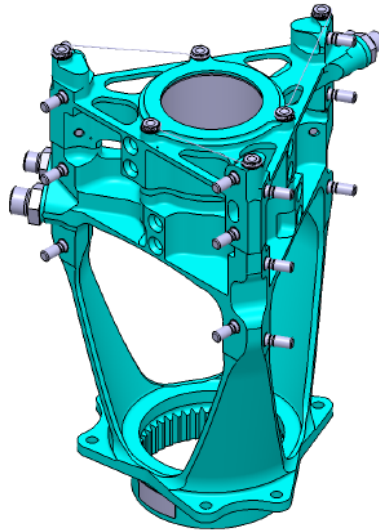


Figure 8.24: Updated bracket redesign.

8.4 Relative and normal stiffness constraint effects trial cases

The next set of trial cases focus on the effect the introduction of relative and normal stiffness constraints have on the topology optimization solution. Trial case 4 serves as the base example to which the constraints are applied.

Ideally, these constraints are applied individually to their respective load case with unitary load, either between the mounting bosses in the case of the relative stiffness, or perpendicular to the face its part of in the case of the normal stiffness. Evidently, the inclusion of additional 39 load cases is not feasible and renders the analysis time way too high, such that the nodal displacement approximation is considered under the already four considered proof load cases.

Three approaches are suggested to the application of the constraints. The first two consider only the maximum displacement constraint (120%) in an attempt to improve the stiffness mainly in the axial case. The inclusion of the minimum displacement constraint does not affect much the results obtained previously in trial cases 1 to 4, where in all the bending load cases, the stiffness shows to be much higher than the current design.

- **Trial Case 5:** For each pair of points (relative stiffness), or single point (normal stiffness), the highest displacement between all load cases is measured and the 120% limit defined. The obtained value is applied as a constraint to each respective design response for all load cases;
- **Trial Case 6:** For each pair of points (relative stiffness), or single point (normal stiffness), the displacement obtained for each load case is measured and the 120% limit defined. The obtained values is applied as a constraint to each respective design response, at each respective load case;
- **Trial Case 7:** The setup is in all similar to trial case 6, with the addition of a minimum displacement constraint (80% limit) in the same design responses, defining both an upper and lower performance boundaries.

8.4.1 Trial case 5

Trial case 5 expands on trial case 4, maintaining the same topology optimization parameters, and adding both relative and normal displacement constraints on the nodal points previously named from A_i to F_i , where $i = 1, 2, 3$. A python script has been used to obtain the constraints from their data storage file, and progressively define both the

design responses as well as the constraints. Table 8.18 summarizes the topology optimization parameters, noting that all the relative and normal displacement constraints have been lumped together for simplicity.

Interpolation technique	MIMP
Objective function	Minimize volume
Constraints	$u_{AFS1}^z \leq u_{axial}$
	$u_{AFS3}^z \leq u_{axial}$
	$u_{AFS2}^z \leq u_{axial}$
	$\omega \geq \omega_1$
	$ \Delta \vec{u} \leq \max(\Delta u_{120\%}) \text{ (all load cases per pair)}$
$ \Delta \vec{u} \leq \max(\Delta n_{120\%}) \text{ (all load cases per point)}$	

Table 8.18: Trial case 5 topology optimization configuration.

8.4.1.1 Topology optimization results

The addition of the normal and relative stiffness constraints have a minimal impact on the topology optimization solution at a first glance. The analysis is constituted by 33 cycles, and according to the convergence plot of figure 8.25, both the axial displacements and first natural frequency converge to the constraints defined, and both the relative and normal displacements, while fulfilling the maximum requirements, converge to values lower than the constraint.

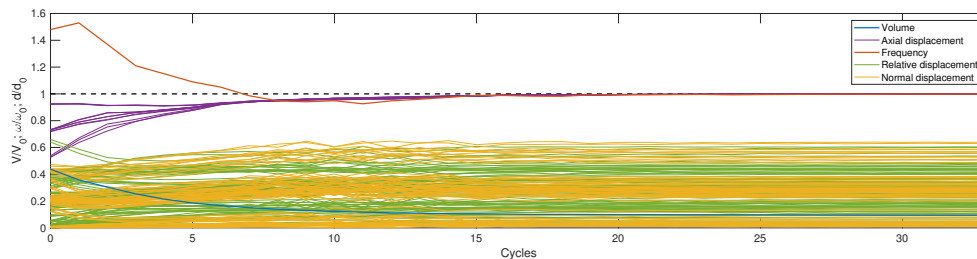


Figure 8.25: Trial case 5 convergence plot.

Figure 8.26 showcases the topology optimization solution through the 0.3 factor isocut.

However, a closer inspection to the STL file extracted from both trial cases 4 and 5 highlights geometrical differences that are subjected to the designer to interpret in Altair Inspire. Figure 8.27 and 8.28 showcase the trial 4 and 5 STL resulting files, respectively. The truss region highlighted in figure 8.27 obtained in trial case 4 does not show up as clearly in trial case 5.

Another highlight of the difference between both designs resides on the different number of gray elements, which equals 9.13%, an increase from the 8.77% from trial case 4.

8.4.1.2 Post-processing and design realization

In an attempt to accurately represent the difference between trials 4 and 5, the geometry is interpreted with the omission of the truss like structure previously highlighted. Figure 8.29 showcases the interpreted design.

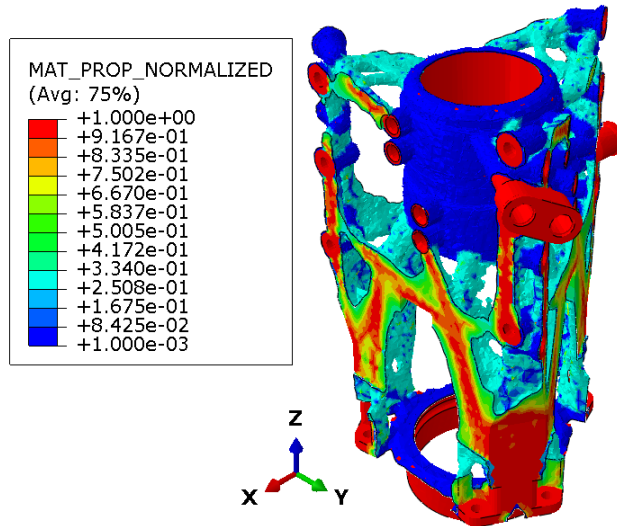


Figure 8.26: Trial case 5 normalized material property result.

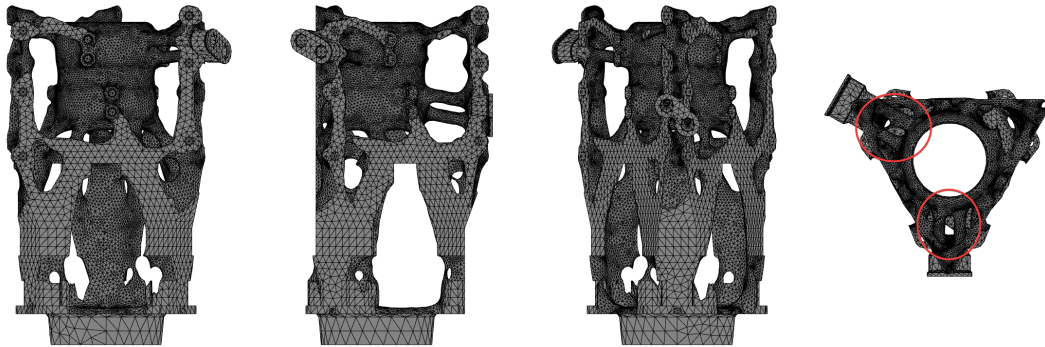


Figure 8.27: Trial case 4 extracted STL mesh file.

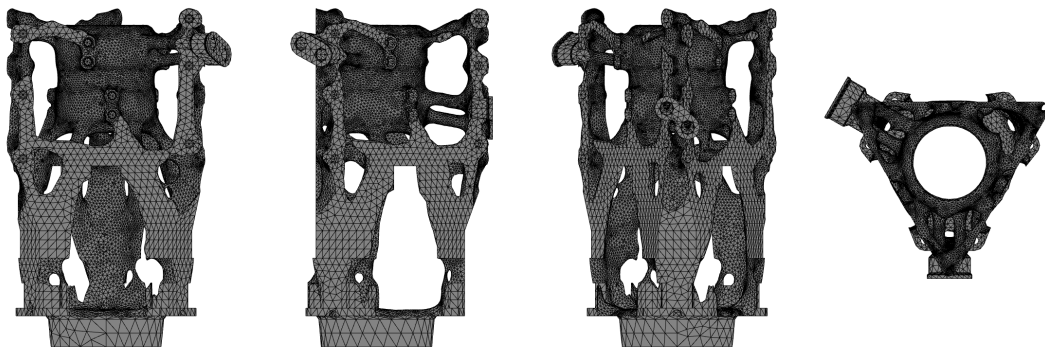


Figure 8.28: Trial case 5 extracted STL mesh file.

8.4.1.3 Part validation

Despite the omission of the truss-like structure, the final mass of the part is 0.9926 of the current design, a 5.5% increase over the mas obtained during trial case 4. This is likely due to the increased thickness in several different spots.

The first natural frequency is 1.2286 of the minimum limit, and all axial displacement constraints are verified

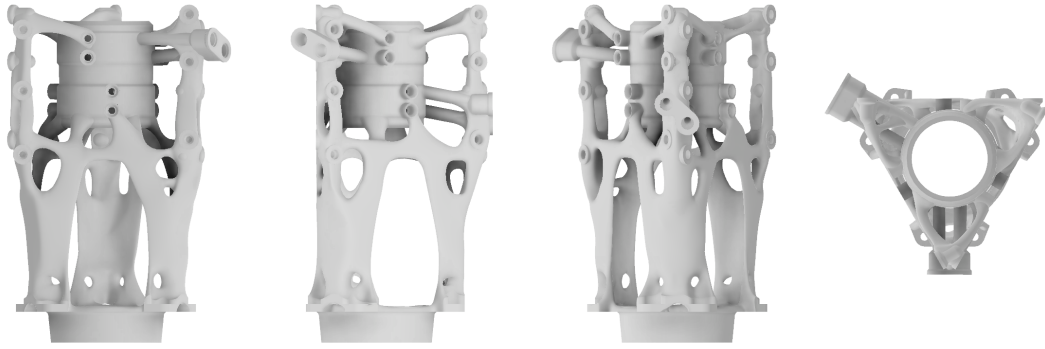


Figure 8.29: Trial case 5 design interpretation result.

(table 8.19), similarly to trial case 4.

Load	Axial	Bend. 1	Bend. 2	Bend. 3
AF_{S1}	0.4964	0.5732	0.6896	0.6128
AF_{S2}	0.4599	0.5735	0.5763	0.6899
AF_{S3}	0.4904	0.6809	0.5672	0.6041

Table 8.19: Trial case 5 normalized axial stiffness results.

Additionally, an improvement is observed across the relative and normal stiffness results (figures ?? and 8.21, respectively), with the part seeing an overall increase of the stiffness when compared to trial case 4. However, specially in the bending load cases, the stiffness increases further away from the upper limit.

8.4.2 Trial case 6

Trial case 6 differs from trial case 5 with the introduction of relative and normal displacement constraints for all load cases independently, and not solely the worst case scenario. However, only the same displacement maximum is once more considered (120% as per requirements). Table 8.22 summarizes the topology optimization parameters considered.

8.4.2.1 Topology optimization results

The analysis runs for 64 cycles, longer than all the previous MIMP topology optimizations performed. A closer look at the convergence plot (figure 8.30), highlights some of the reasoning behind the longer simulation time. Up until cycle 16, several spikes regarding the normal displacement stiffness are highlighted, indicating trouble with convergence. However, after the 16th cycle, the solution shows a convergence trend on all the design responses, including the first natural frequency, axial displacement, and both relative and normal displacements.

The constraint application change results in significant optimization solution changes (figure 8.31). Namely, a new truss-like connecting region appears on the top of the geometry, completely missing from previous optimization results. Additionally, previously existing connections are now missing in preference of others, for the sake of improving the axial load case performance of the component. The solution is made of 6.82% gray elements, a decrease of about 25.30% compared to trial case 5, meaning a performance improvement is achieved. Behind the number of gray elements results might be the increased number of run cycles.

Load	Axial	Bend. 1	Bend. 2	Bend. 3
AB1	48.09	20.58	25.72	27.68
AD1	306.27	33.13	59.61	43.02
BC1	176.87	34.44	32.60	37.55
BE1	259.79	26.07	24.03	33.07
CF1	39.20	21.10	10.76	24.18
DE1	181.71	34.10	55.15	52.68
EF1	81.82	34.77	25.95	25.49
AB2	69.52	30.83	26.94	33.54
AD2	364.69	29.43	36.06	20.59
BC2	89.39	37.47	31.97	34.09
BE2	79.42	24.59	24.45	9.97
CF2	69.77	27.18	22.77	15.32
DE2	207.96	45.10	41.97	45.47
EF2	80.58	24.65	27.26	23.65
AB3	111.99	30.11	30.29	24.39
AD3	537.55	33.23	35.34	32.14
BC3	77.63	28.42	29.65	27.92
BE3	171.52	28.94	28.81	33.29
CF3	49.27	16.08	22.24	26.76
DE3	289.04	47.91	43.56	32.89
EF3	127.06	23.28	22.83	34.07

Table 8.20: Trial case 5 normalized relative stiffness results.

Load	Axial	Bend. 1	Bend. 2	Bend. 3
A1	134.16	29.80	26.78	23.55
B1	181.01	36.29	25.68	23.02
C1	66.42	32.02	20.70	18.41
D1	120.94	24.88	28.19	33.72
E1	16.37	23.98	24.58	26.84
F1	28.68	19.84	21.04	25.16
A2	813.62	27.09	36.25	31.18
B2	77.40	24.71	35.23	28.90
C2	53.28	20.00	25.41	23.33
D2	565.69	28.15	27.28	25.76
E2	103.73	21.13	24.88	22.33
F2	249.99	6.04	23.45	19.93
A3	128.64	24.96	21.86	26.94
B3	174.88	21.91	19.51	26.48
C3	22.24	17.43	15.67	21.59
D3	495.68	27.49	30.92	29.37
E3	195.32	24.52	25.21	26.84
F3	27.09	22.87	26.32	22.95

Table 8.21: Trial case 5 normalized normal stiffness results.

Interpolation technique	MIMP
Objective function	Minimize volume
Constraints	Axial displacement $u_{AFS1}^z \leq u_{axial}$
	$u_{AFS3}^z \leq u_{axial}$
	$u_{AFS2}^z \leq u_{axial}$
	Eigenfrequency $\omega \geq \omega_1$
	Relative displacement $ \Delta \vec{u} \leq \Delta u_{120\%} $ (each load case per pair)
Normal displacement $ \Delta \vec{u} \leq \Delta n_{120\%} $ (each load case per point)	

Table 8.22: Trial case 6 topology optimization configuration.

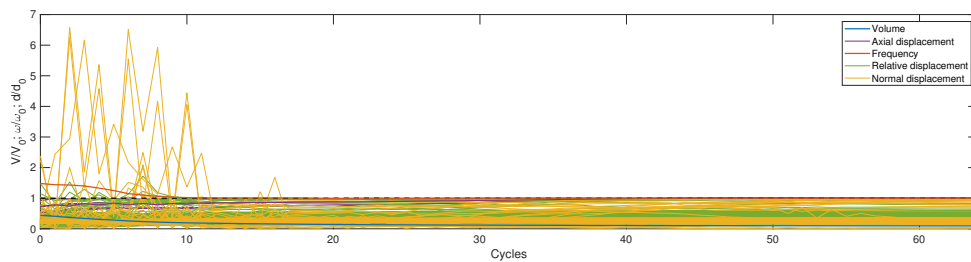


Figure 8.30: Trial case 6 convergence plot.

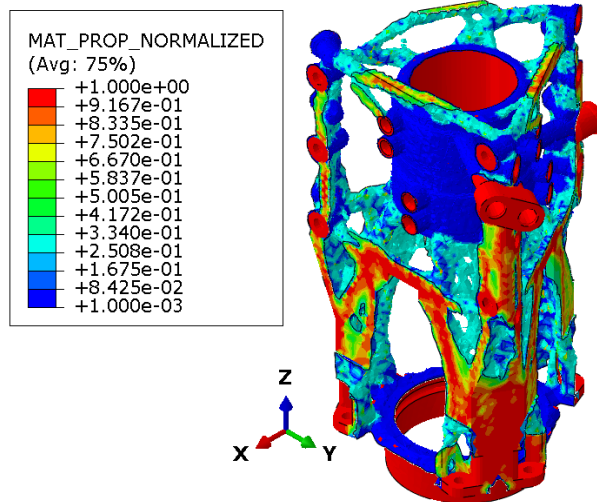


Figure 8.31: Trial case 6 normalized material property result.

8.4.2.2 Post-processing and design realization

Once more in Altair Inspire, the simulation resulting STL file is interpreted using polyNURBS. The interpreted design can be seen in figure 8.32. Highlighted in red is the presence of larger holes in the bottom part of the geometry, different from the previously interpreted geometries and introduces additional lack of symmetry to the part. The hydraulic system is a source of asymmetry in the original geometry to be optimized, namely due to its oil feed and return ports, and their respective connections in two of the three part corners. The presence of a pair of ports in a corner, further reduced the thickness of the connecting elements in that corner, as highlighted in red.

Additionally, a more distinct frame structure is defined on each face, non-existent in previous trial case designs.

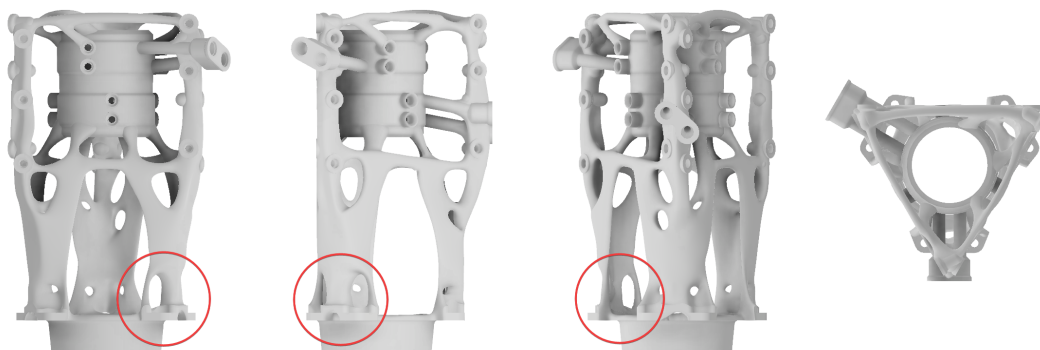


Figure 8.32: Trial case 6 design interpretation result.

8.4.2.3 Part validation

The first solution obtained from design interpretation constitutes 0.9771 of the mass of the current design, despite the newer topology solution. Once more, the first natural frequency is higher than the required minimum, at 1.0319 of this constraint. Similarly, the axial displacements fall well within the requirements, as per table 8.23.

Finally, the inclusion of all constraints to their individual load cases aims at improving the performance under axial loading. Tables 8.24 and 8.25 showcase the results obtained for both relative and normal displacements.

Load	Axial	Bend. 1	Bend. 2	Bend. 3
AF_{S1}	0.5188	0.6663	0.7255	0.5780
AF_{S2}	0.5159	0.6710	0.5751	0.7302
AF_{S3}	0.4668	0.7695	0.6143	0.6220

Table 8.23: Trial case 6 normalized axial stiffness results.

Load	Axial	Bend. 1	Bend. 2	Bend. 3
AB1	53.41	21.27	25.12	31.64
AD1	38.13	34.60	8.97	38.39
BC1	99.60	31.17	30.46	46.73
BE1	158.19	32.26	22.51	29.49
CF1	70.11	28.12	14.05	26.16
DE1	163.19	47.55	48.06	45.94
EF1	64.41	34.85	25.81	24.64
AB2	57.66	34.35	26.38	30.63
AD2	136.12	33.00	39.68	9.17
BC2	129.60	46.18	32.31	32.89
BE2	80.63	32.79	30.44	14.77
CF2	65.07	39.13	29.39	15.44
DE2	127.37	40.45	52.86	41.85
EF2	108.01	29.76	31.25	27.87
AB3	76.93	31.44	34.53	24.22
AD3	225.72	17.88	33.09	32.43
BC3	65.14	36.97	32.45	34.59
BE3	90.53	27.46	29.43	36.79
CF3	53.13	26.91	25.98	30.35
DE3	211.84	50.85	39.67	27.46
EF3	54.96	22.76	21.28	43.57

Table 8.24: Trial case 6 normalized relative stiffness results.

8.4.3 Trial case 7

In an attempt to complete the results obtained in trial case 6, the 80% threshold requirement on relative and normal displacements is also considered. Table 8.26 showcases the analysis parameters.

8.4.3.1 Topology optimization results

The introduction of a lower limit to the displacement on both relative and normal constraints results in an aborted simulation that does not converge, and as such this trial case is dismissed.

8.4.4 Comparison and discussion

Considering the inability to obtain results regarding trial case 7, other than the fact it does not converge to a proper solution, the trial case will not be considered for further discussion.

Trial cases 5 and 6 represent vastly different geometries, with trial 6 displaying lower mass, while performing

Load	Axial	Bend. 1	Bend. 2	Bend. 3
A1	88.73	26.85	27.46	27.50
B1	151.27	28.32	27.23	30.80
C1	55.91	24.18	23.06	24.31
D1	149.89	29.60	28.81	31.65
E1	54.75	24.02	25.39	28.15
F1	48.82	16.42	22.50	32.20
A2	402.54	34.64	27.29	31.15
B2	300.44	37.62	25.91	30.56
C2	105.02	33.66	15.79	27.64
D2	554.02	29.66	30.13	27.82
E2	120.47	25.44	30.87	25.16
F2	13.18	7.18	29.13	20.71
A3	406.26	28.92	25.84	26.69
B3	179.22	26.49	22.97	27.30
C3	44.88	19.56	18.77	17.59
D3	116.77	30.08	28.38	34.25
E3	861.98	26.86	22.61	31.67
F3	201.14	29.08	28.20	24.15

Table 8.25: Trial case 6 normalized normal stiffness results.

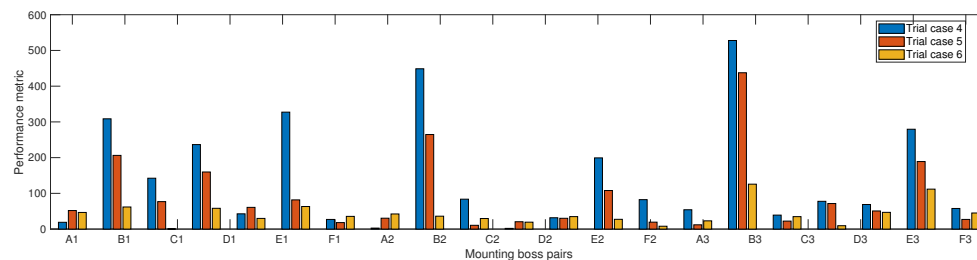
Interpolation technique	MIMP
Objective function	Minimize volume
Axial displacement	$u_{AFS1}^z \leq u_{axial}$ $u_{AFS3}^z \leq u_{axial}$ $u_{AFS2}^z \leq u_{axial}$
Constraints	$\omega \geq \omega_1$ Relative displacement $ \Delta \vec{u} \leq \Delta u_{120\%} $ (each load case per pair) $ \Delta \vec{u} \geq \Delta u_{80\%} $ (each load case per pair) Normal displacement $ \Delta \vec{u} \leq \Delta n_{120\%} $ (each load case per point) $ \Delta \vec{u} \geq \Delta n_{80\%} $ (each load case per point)

Table 8.26: Trial case 7 topology optimization configuration.

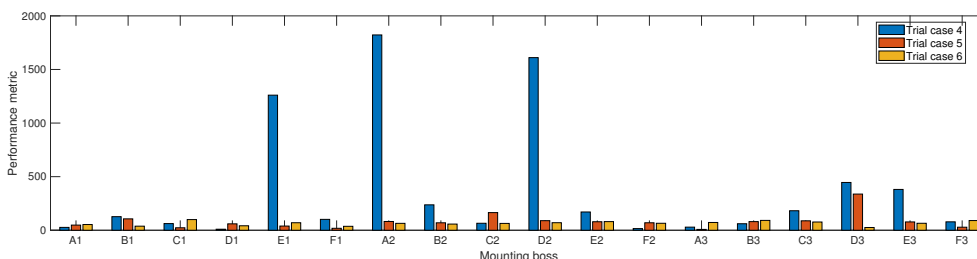
as well or better on the remaining metrics. In fact, when compared to the results obtained from trial case 6, a clear improvement exists regarding the performance of the part under axial loading. Plot 8.33(a) highlights the improvement for the relative displacement, namely in the large spikes that occur in trial case 5. It should be noted that the lower the value, the better the performance metric.

The same trend is found on the comparison between the performance of both trial case's normal displacement on the axial load case. Plot 8.33(b) showcases the results obtained that compare both trial cases. The large peaks are smoothed out, and the overall performance of this parameter is improved with the newer design.

Furthermore, trial 6 represents the better design yet obtained, tackling all requirements set, except for the minimum relative and normal displacements. Compared to trial case 4 under axial load, it achieves better performance regarding both relative and normal displacements, namely in the reduction of the high peaks that are present in trial case 4.



(a) Relative stiffness.



(b) Normal stiffness.

Figure 8.33: Performance metric comparison between trial cases 4, 5, and 6, for both the relative and normal stiffness constraints. The lower the performance metric, the better the result.

In conclusion, the introduction of the constraints per loading case, rather than the worst case scenario does

improve the part performance, and it will be used from this point forward.

8.5 Volume minimization and maximum minimization trial cases

The last set of trial cases are compared, with one being trial case 6, corresponding to the minimization of the volume (the objective function), while trial 8 introduces a volume maximum minimization approach.

8.5.1 Trial case 8

Trial case 8 is entirely similar to trial case 6, as no further changes are done other than the change to maximum minimization of the objective function. The analysis parameters are presented in table 8.27.

Interpolation technique		MIMP
Objective function		Minimize volume
Constraints	Axial displacement	$u_{AFS1}^z \leq u_{axial}$ $u_{AFS3}^z \leq u_{axial}$ $u_{AFS2}^z \leq u_{axial}$
	Eigenfrequency	$\omega \geq \omega_1$
	Relative displacement	$ \Delta \vec{u} \leq \Delta u_{120\%} $ (each load case per pair)
	Normal displacement	$ \Delta \vec{u} \leq \Delta n_{120\%} $ (each load case per point)

Table 8.27: Trial case 8 topology optimization configuration.

8.5.1.1 Topology optimization results

The analysis runs for 63 cycles, similar to the 64 cycles it took trial case 6 to converge to a solution. Also the convergence plot has a similar trend, with peaks smoothing out at around cycle 19, as seen in figure 8.34.

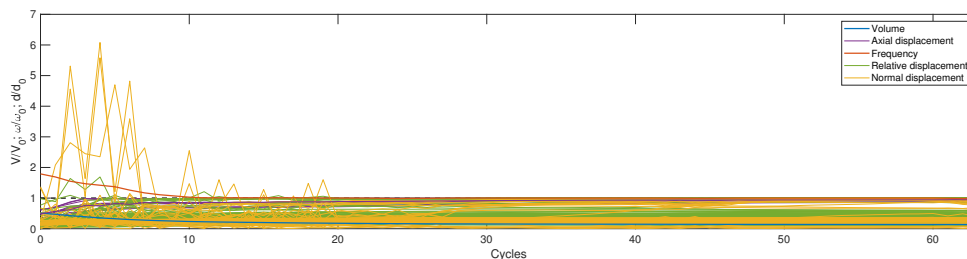


Figure 8.34: Trial case 8 convergence plot.

The resulting geometry (figure 8.35) is entirely similar to the one obtained in trial case 6, with the subtle difference that most elements are suggested to be thicker, likely to increase robustness in the part's response to all load cases and modal constraint. The solution is made of 2.79% gray elements, a major improvement over the 6.82% previously attained in trial case 6.

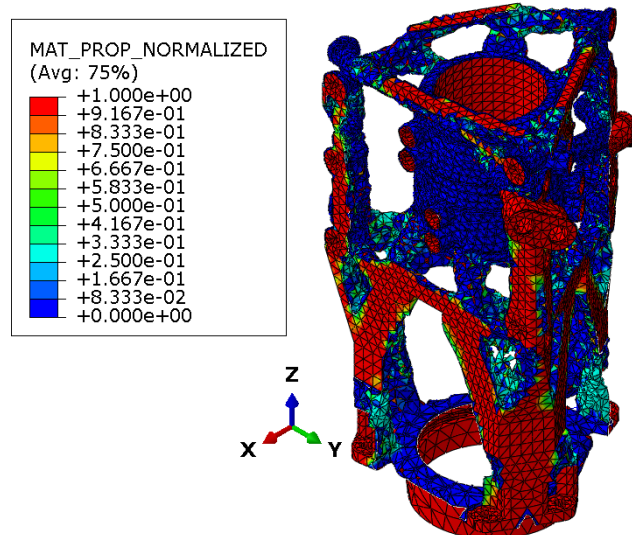


Figure 8.35: Trial case 8 normalized material property result.

8.5.1.2 Post-processing and design realization

As suggested by the Abaqus optimization results, the interpreted geometry is thicker than the results of trial case 6, with subtle changes to small connecting regions. The final solid part can be seen in figure 8.36.

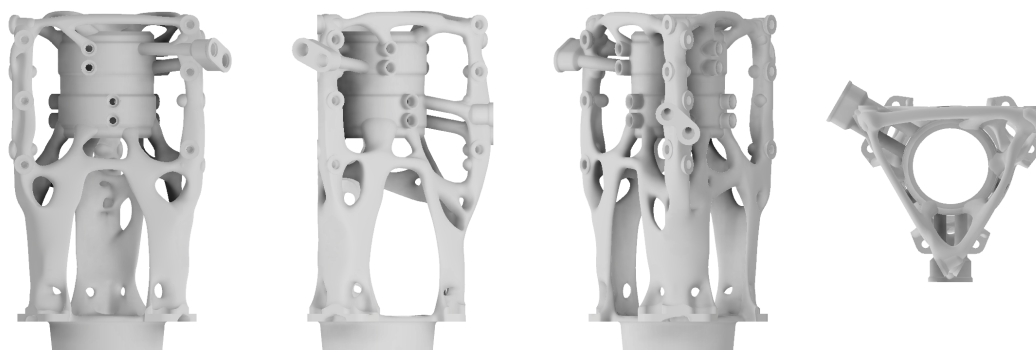


Figure 8.36: Trial case 8 design interpretation result.

8.5.1.3 Part validation

The results of this design are in line with the expected, a stiffer structure with results close to the ones obtained trial case 6, with the downfall being the structure's mass, now higher than the original design, at 1.1267 of the original mass. Also as expected, the increased element thickness and overall mass result in a first natural frequency 1.3114 higher than the requirement, an increase of 27.23% over trial case 6, which already complied with said constraint. Table 8.28 shows the axial displacement constraints, once more fulfilled by a larger margin.

The increased stiffness is also verified on both the relative and normal displacement constraints (tables 8.29 and 8.30, respectively). Regarding the relative displacement constraint, the total number of measurements that do not comply with the requirements improve from 7 in trial case 6, to 2 in trial case 8. Similarly, in the normal displacement constraint, it goes from 10 in trial case 6, to 8 in trial case 8, the number of constraints not fulfilled.

Load	Axial	Bend. 1	Bend. 2	Bend. 3
AF_{S1}	0.4077	0.4504	0.5297	0.4869
AF_{S2}	0.4005	0.4556	0.4797	0.5348
AF_{S3}	0.4243	0.5223	0.4671	0.4795

Table 8.28: Trial case 8 normalized axial stiffness results.

Load	Axial	Bend. 1	Bend. 2	Bend. 3
AB1	53.94	13.48	17.37	23.34
AD1	45.00	25.12	9.31	29.98
BC1	109.43	19.07	20.83	37.02
BE1	153.10	22.55	16.29	22.72
CF1	54.75	17.74	5.64	18.95
DE1	110.71	36.43	36.04	36.28
EF1	64.78	24.10	18.79	17.95
AB2	41.56	24.89	19.29	24.07
AD2	98.12	23.98	28.94	7.97
BC2	92.47	28.04	22.49	23.51
BE2	117.64	23.07	23.27	7.73
CF2	101.63	26.57	20.92	12.23
DE2	83.26	26.18	35.59	32.53
EF2	56.61	19.43	25.36	19.39
AB3	35.00	21.36	27.91	17.76
AD3	89.66	12.74	25.76	27.51
BC3	74.05	23.21	24.63	21.29
BE3	85.68	23.46	23.88	31.57
CF3	49.89	15.30	20.29	23.31
DE3	217.63	30.41	25.77	22.29
EF3	54.85	15.37	14.29	33.34

Table 8.29: Trial case 8 normalized relative stiffness results.

Load	Axial	Bend. 1	Bend. 2	Bend. 3
A1	39.57	17.27	19.22	20.53
B1	118.99	18.61	19.08	23.08
C1	27.18	18.77	16.67	16.35
D1	24.99	18.13	21.11	24.37
E1	493.79	14.62	18.35	21.33
F1	100.37	9.36	15.90	23.61
A2	117.21	21.80	21.46	22.11
B2	179.56	21.11	22.42	20.29
C2	79.63	18.71	17.35	16.92
D2	83.08	16.59	21.59	18.38
E2	123.38	12.90	18.56	15.63
F2	96.33	0.94	15.44	10.45
A3	128.12	17.18	19.70	14.92
B3	185.06	14.00	18.09	11.01
C3	32.41	7.27	14.26	-6.23
D3	288.75	18.98	18.73	23.20
E3	241.87	17.11	15.53	20.56
F3	96.78	16.98	19.48	13.56

Table 8.30: Trial case 8 normalized normal stiffness results.

8.5.2 Comparison discussion and conclusions

The results of the volume maximum minimization approach are compliant with the expected, namely in the increase of overall part stiffness and mass, in order to improve the axial load case performance. However, this results in a geometry with a mass much higher than the current part in use, as well as the volume minimization solution. Despite the mass increase, the overall geometry is entirely similar in its topology, due to the fact that the volume minimization formulation results in a single objective topology optimization, despite the consideration of several load cases.

Considering the approximation nature of the relative and normal displacement constraints, their weight on the decision of the final design is diminished. On the other hand, the final mass is the best performance indicator if the remaining requirements are fulfilled.

Moreover, further mass savings and geometrical improvements are possible with the implementation of a shape optimization analysis that takes into account the effective stress under the suggested loading conditions.

Chapter 9

Shape optimization results

This chapter aims at utilizing the results of said section and expanding their use to the actual servo-actuator bracket redesign process.

This chapter has the main focus on iterating over the results of trial case 6, and reducing the peak stresses, such that the no yielding condition is verified on both static strength proof load cases (axial and bending).

9.1 Shape optimization workflow

Ideally, the shape optimization step is constituted of several optimization iterations. Specifically for the problem at hands, it should,

- Tackle the static strength analysis to reduce stress peaks and hotspot regions under the constraints set for each load case. Which results in a stress reduction shape optimization task;
- Improve the fatigue life performance of the bracket through a durability analysis and reduction. While the durability analysis has been performed in fe-safe, due to time constraints, it has not been included in the shape optimization analysis and as such has been omitted from this thesis. It is however still advised to be performed in future work related to this project, and in general practice when fatigue data is available.

As such, solely one iteration of effective stress reduction is performed, from which several geometrical changes are performed to further reduce the part weight and simultaneously not increase the stress experienced at critical regions. The geometrical changes are performed utilizing the polyNURBs file in Altair Inspire, with the shape optimization results as a guideline to move the surface nodes.

9.2 Shape optimization model preparation

9.2.1 Design requirements

A new set of design requirements is introduced during shape optimization, namely relating to the stress field of the part under given load conditions. The requirements are defined under the static strength item at section 2.7.

9.2.2 Geometry and meshing

The input geometry of the shape optimization analysis is the resulting geometry from trial case 6, as it showcases the better results (lower volume and compliant with the constraints). As several iterations are performed, the newer geometries to be optimized are the result from the previous iteration, in order to further improve the final bracket design.

Considering the main goal of the shape optimization task is the smoothing of stress hotspots, notches and small curvature angles need to be finely meshes in order to accurately report the stress field without non-realistic stress peaks. As such, while the meshing element continues to be a quadratic tetrahedron (C3D10), its average size is now 4mm. Figure 9.1 showcases the initial mesh geometry, prior to any shape optimization.

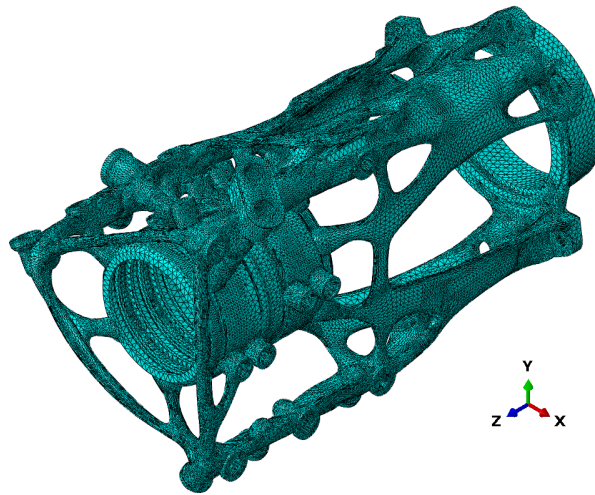


Figure 9.1: Meshed shape optimization part.

9.2.3 Materials

The material used for the shape optimization is an extension of the same used during topology optimization, since the plastic properties of the material are to be considered. Figure 7.15 in subsection 7.1.5 showcases the stress-strain curve of the material utilized in Abaqus.

9.3 Shape optimization setup

The main approach taken in this thesis is to minimize and homogenize stress hotspots that occur during static analysis. Ideally, several steps are needed to tackle all component requirements, namely regarding durability and fatigue life. However, due to the limited time frame of the thesis, only effective stress is tackled in consecutive shape optimization steps.

Additionally, the proof loading case is considered, and not the ultimate, as the behaviour of the component above failure is not accurately modelled.

9.3.1 Shape optimization task

The shape optimization task utilizes the controller based optimality criteria to perform a Von Mises stress maximum minimization, considering the same load cases as in the topology optimization task, one axial, and three

bending. The optimization constraint is defined as a constant volume, that is, the volume fraction should be kept the same. The remaining simulation parameters have been kept default. Table 9.1 summarizes the shape optimization definition and parameters

Algorithm	Condition-based
Objective function	Minmax σ_{VM}
Constraints	Constant volume ($V_f = 1$)
Load case	Axial
	Bend. 1
	Bend. 2
	Bend. 3

Table 9.1: Shape optimization configuration..

9.4 Initial geometry results

In order to provide means of comparison and design evolution, the resulting geometry of trial case 6, prior to any redesign process, has its stress field evaluated.

In fact, the performance of the part under the proof load cases (axial and bending) is positive from a stress field perspective. The peak stress value, normalized to the yield stress, are lower than 1 in both load cases (see table 9.2).

Load	Axial	Bend. 1
Normalized stress peak	0.5061	0.7583

Table 9.2: Normalized stress peak result from the initial geometry.

Figures 9.2(a) and 9.2(b) showcase the normalized stress field on the part under both axial and bending proof load cases, respectively. The stress distribution on the part does not exhibit large and clearly dangerous hotspots, which allows for further reduction of element cross sections. However, after every iteration the first natural frequency is evaluated, since the margin of reduction available is minimal.

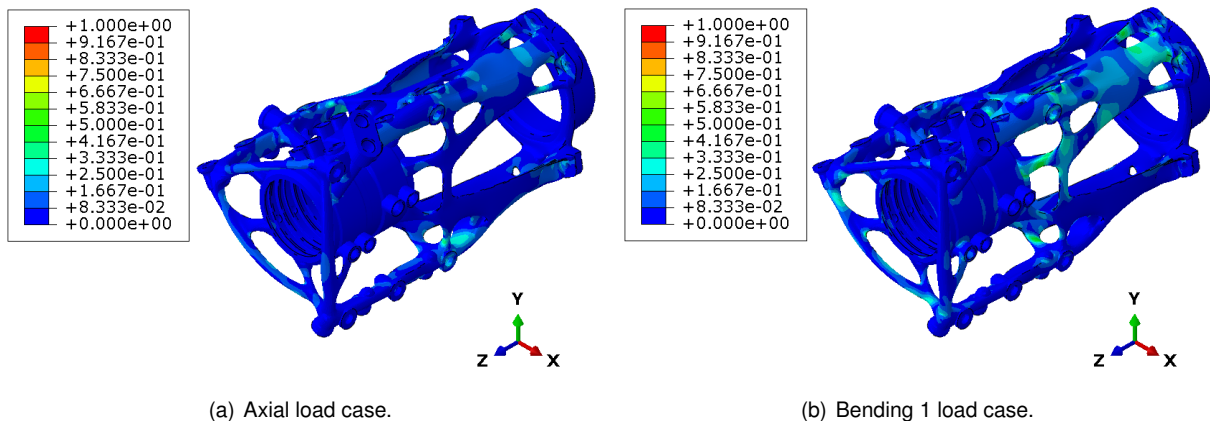


Figure 9.2: Normalized stress field under both axial and bending 1 load cases of the initial geometry.

9.5 Shape optimization results

The shape optimization task runs for 10 cycle until convergence is found. A closer look at the plot of both the objective function and the volume (figure 9.3), showcases the quick convergence found with a controller based shape optimization task, during a stress maximum minimization analysis. The normalized stress objectives for the four load cases considered evolve according to the table 9.3, all being reduced. The objective function itself, a combinations of these values, is decreased from 1.524 to 0.731. The volume is maintained constant, as the constraint intended.

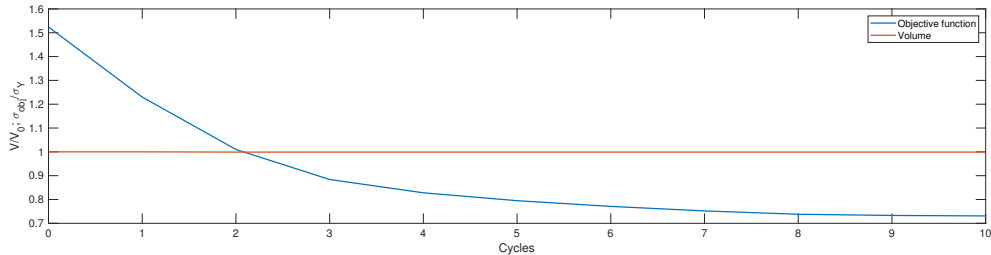


Figure 9.3: Shape optimization convergence plot.

Load case		Axial	Bend. 1	Bend. 2	Bend. 3
Normalized	Cycle 0	0.6271	0.9979	1.6356	1.4382
Stress Objective	Cycle 10	0.5398	0.8512	0.8360	0.7318

Table 9.3: Shape optimization normalized stress objective evolution between cycles 0 (initial) and 10 (final).

Finally the solution is shown in figure 9.4. The regions in red correspond to surface nodes meant to expand outwardly, while the blue regions inwards (increase and reduce thickness, respectively).

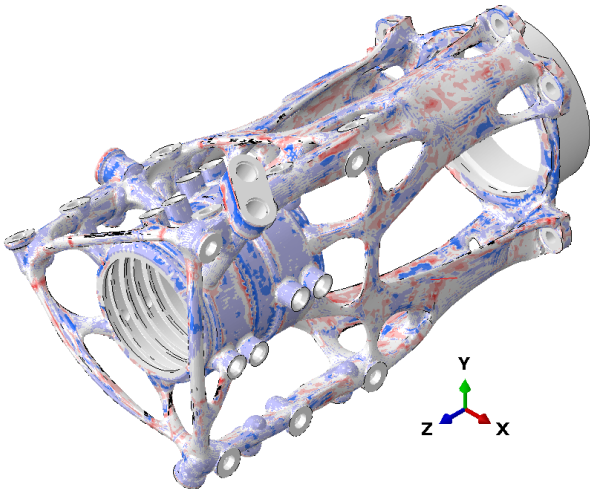


Figure 9.4: Shape optimization results, namely the surface vector.

9.5.1 Design iteration 1

The first design iteration focuses on smoothing out regions highlighted by the shape optimization result. Following its definition, the geometry is tested in Abaqus under proof loading conditions analysed up until now, to evaluate both the stress response, as well as the first natural frequency. Figure 9.5 showcases the normalized stress field under both the axial and bending load cases. Compared to the results of figures 9.2, no evident differences are observed, other than the smoothing out of the stress in the region highlighted in red.

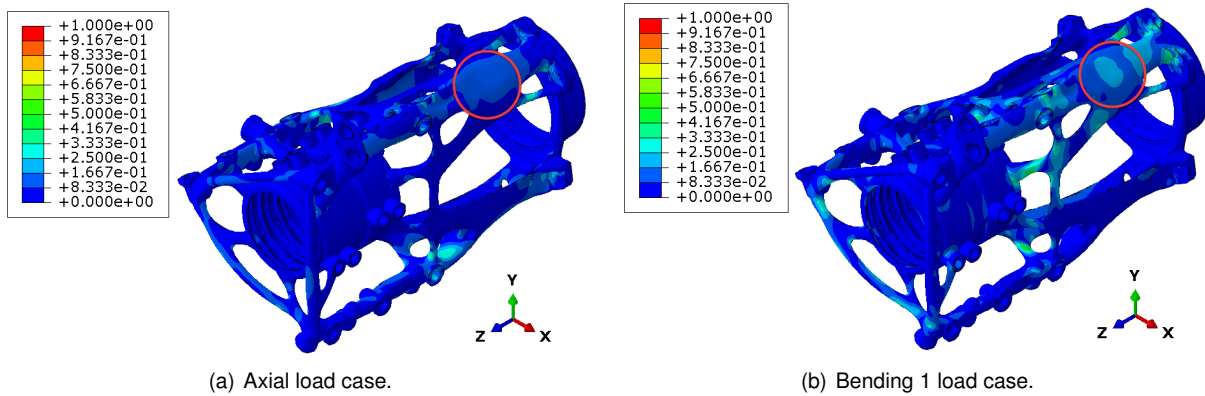


Figure 9.5: Normalized stress field under both axial and bending 1 load cases of the design iteration 1 geometry.

A more concrete mean of comparison is performed, by defining the same path running along the part (as seen in 9.6), and comparing the stresses, for both axial and bending load cases. Point at normalized distance 0 refers to the region closer to the bolt holes. Plots 9.7(a) and 9.7(b) highlight the peak reduction that occurs at the beginning of the path, achieving the sought-after smoothing.

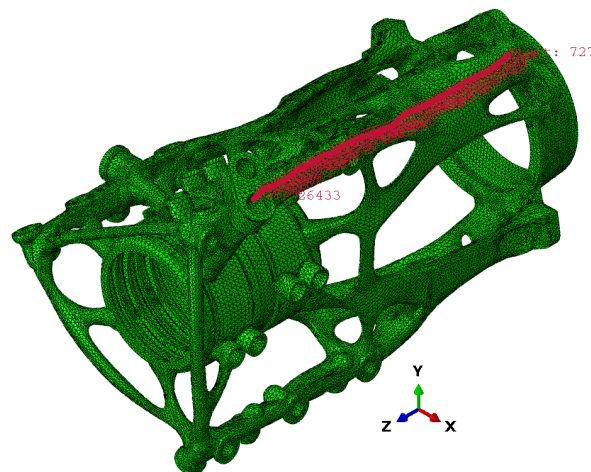


Figure 9.6: Highlight of the path for the von Mises stress measurement comparison between initial, and iteration 1 designs.

The changes made, while positively impacting the stress distribution, also result in a lower mass. The reduction amounts to a 1% decrease, with it being 0.9667 of the original component. The first natural frequency, as expected, also is reduced, but still higher than the minimum required, at 1.0264 of the limit.

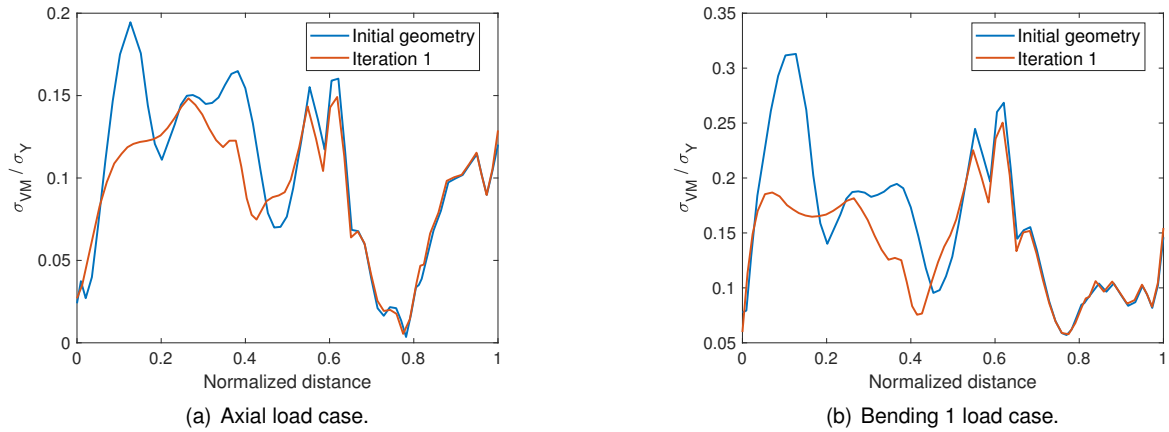


Figure 9.7: Normalized path von Mises stress results comparison between initial, and iteration 1 geometries.

9.5.2 Design iteration 2 - final design

Considering the results obtained from iteration 1, further attempts at mass reduction are attempted, while keeping the properties of the part in check, and fulfils the previously set requirements.

The design changes are done the same way as in iteration 1, through the results of the shape optimization task. Additionally, fillet features in sharp corners are included, to further reduce stress concentration regions (figure 9.8).

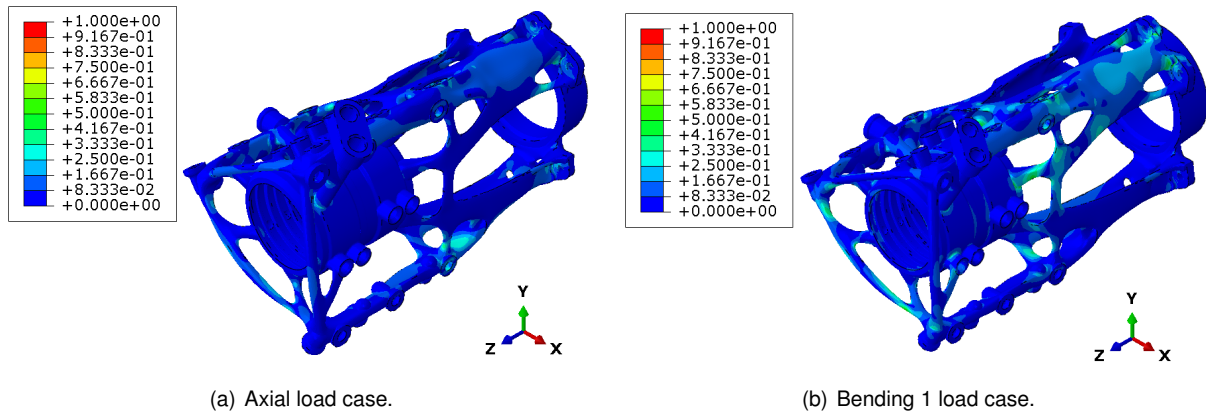


Figure 9.8: Normalized stress field under both axial and bending 1 load cases of the design iteration 2 geometry.

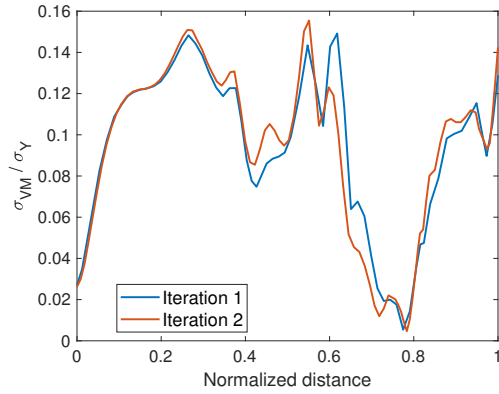
The stress distribution is similar to the one obtained in design iteration 1, as seen by the stress distribution comparison over the same path previously evaluated (figure 9.9).

The changes ultimately result in a geometry with a mass equal to 0.9488 of the original mass, amounting to a 5.12% mass reduction.

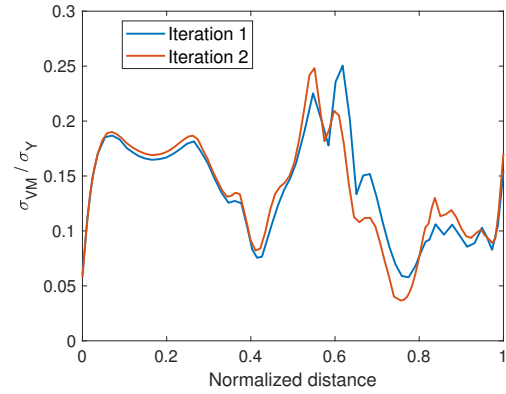
As expected, the further mass reduction results in a lower first natural frequency, now equal to 1.022 of the minimum value, yet still compliant with the requirement.

Regarding axial stiffness, the final design fulfils the requirements as per table 9.4, with little variation from the results of trial case 6, before the shape optimization procedure.

Finally, the relative and normal displacement performance of the final design is given in tables 9.5 and 9.6, respectively.



(a) Axial load case.



(b) Bending 1 load case.

Figure 9.9: Normalized path von Mises stress results comparison between iteration 1, and iteration 2 geometries.

Load	Axial	Bend. 1	Bend. 2	Bend. 3
AF_{S1}	0.4999	0.6203	0.7667	0.6463
AF_{S2}	0.4932	0.6031	0.6396	0.7495
AF_{S3}	0.5361	0.7663	0.6565	0.6460

Table 9.4: Shape optimization design iteration 2 normalized axial stiffness results.

Load	Axial	Bend. 1	Bend. 2	Bend. 3
AB1	67.15	21.07	27.10	30.44
AD1	138.34	31.09	11.92	38.69
BC1	122.10	30.10	33.15	49.83
BE1	113.93	29.23	21.11	29.51
CF1	32.04	25.71	14.61	26.50
DE1	167.31	46.09	51.18	49.59
EF1	71.57	32.17	27.28	25.48
AB2	62.32	33.45	27.91	32.44
AD2	276.24	30.15	42.31	14.77
BC2	101.37	41.67	33.80	33.54
BE2	32.61	30.53	33.08	20.71
CF2	78.68	37.25	31.71	16.56
DE2	164.98	37.93	56.44	42.64
EF2	99.65	30.80	33.13	30.81
AB3	57.98	31.33	36.26	25.66
AD3	430.29	15.78	37.14	34.29
BC3	62.71	38.27	33.97	38.69
BE3	88.98	22.98	32.82	38.50
CF3	35.83	27.89	28.23	32.67
DE3	268.35	50.29	42.80	25.31
EF3	65.02	22.41	23.06	44.93

Table 9.5: Shape optimization design iteration 2 normalized axial stiffness results.

Load	Axial	Bend. 1	Bend. 2	Bend. 3
A1	44.28	26.70	29.75	31.33
B1	140.82	27.51	29.64	35.20
C1	41.73	19.96	25.11	28.09
D1	199.94	31.48	30.48	34.15
E1	332.69	26.71	26.84	29.84
F1	48.13	20.64	23.89	33.35
A2	748.37	28.95	30.06	31.95
B2	1.18	30.57	29.21	30.85
C2	53.36	27.39	19.26	27.63
D2	124.87	28.10	34.54	29.74
E2	46.32	24.36	35.68	27.38
F2	120.52	0.80	33.56	21.99
A3	153.01	28.40	25.15	28.20
B3	50.38	25.81	22.00	28.82
C3	2.04	18.03	18.37	16.23
D3	635.13	28.32	30.52	32.87
E3	105.54	24.96	24.15	30.80
F3	20.77	24.85	27.61	23.82

Table 9.6: Shape optimization design iteration 2 normalized axial stiffness results.

9.5.3 Discussion and conclusions

The inclusion of shape optimization in the design workflow has a positive result in the definition of a part with lower mass, and less significant stress peaks and hotspots. However, the durability of the part is not considered, when its importance is relevant to a well designed component, namely since fatigue life requirements are defined by Leonardo.

Additionally, the convergence of the multi-objective shape optimization, directly from the use of geometry 9.1, highlights the quality of the interpreted design and topology optimization solution. Had the stress peaks been overly high, the shape optimization process would likely diverge, as seen in [5].

Finally, figures 9.10 and 9.11 showcase the geometry to be printed, and the culmination of the structural optimization process applied to an aeronautical component.

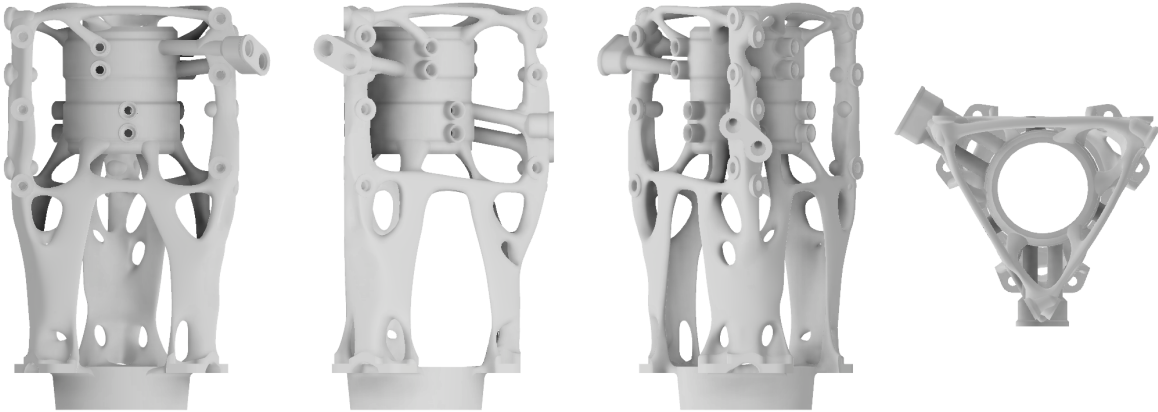


Figure 9.10: Showcase of the final design.

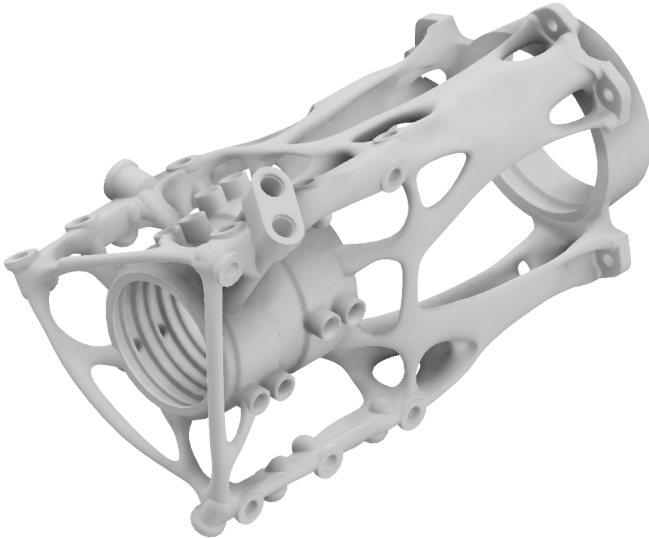


Figure 9.11: Isometric view of the final design.

Chapter 10

Additive manufacturing simulation results

This chapter explores the definition of the AM process simulation that allows for the prediction of part distortion and residual stresses in the AMATHO bracket, utilizing a low-resolution uncoupled thermal-mechanical simulation, with the same methodology implemented in 5.

Considering the lack of information regarding the exact printing properties the part will undergo, the typical printing settings of Ti6Al4V ELI-0406 documented by [76] are used.

10.1 Geometry preparation

The geometry to be analysed is the result of the shape optimization process. Figure 9.11 showcases the geometry in greater detail.

10.1.1 Support definition and voxelization

The initial step to prepare the geometry for the simulation is the definition of its printing supports. In Autodesk Inventor, the holes and indentations of the part are filled with material (see figure 10.1), since post-printing machining is able to handle their creation accurately, and reducing the need to internal support structures in the hydraulic system.

The printing support process is defined in Autodesk Netfabb, proceeding the solid part being imported and converted into a STL file. Additionally, due to the large size of the original part, a scaled analysis is performed. Had this step not been taken, the run time of the simulation would have not been admissible, nor the computational resources enough to handle the large files of data that would define the path of the laser. A scaling of 20% is applied and accepted, after several different scaling factors applied result in unmanageable amounts of data.

Autodesk Netfabb provides automation tools to create support structures depending on the printing process. However, while the studying of the support type impact is important, it is beyond the objective of this thesis. As such, regular hexagonal bar supports are chosen and showcased in figure 10.2 (supports highlighted in blue, with the critical regions shown in red).

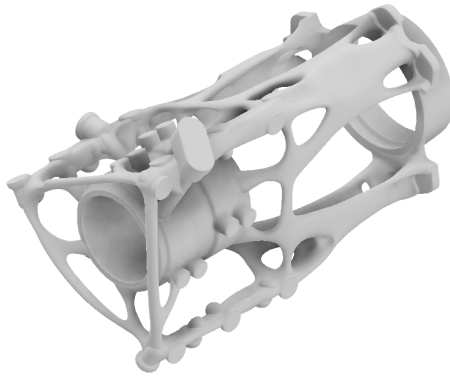


Figure 10.1: Edited geometry to accommodate the AM printing process.

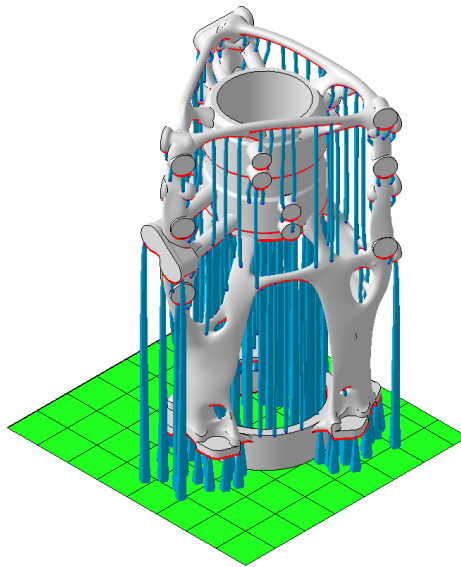


Figure 10.2: Support definition result in Autodesk Netfabb. In blue are highlighted the support structures.

Both the support and part geometries are merged within Autodesk Netfabb and exported as STL, and finally imported to Abaqus as a triangular surface mesh entity.

The voxelization process, in addition to the surface mesh describing the part to voxelize, requires the creation of the intersection grid, a hexahedral element-based mesh "box" that encapsulates the part. A grid with element size 0.4mm is defined, such that each element contains, approximately, 7 physical layers. Figures 10.3(a) and 10.3(b) showcase the surface mesh of the part to be printed, and the intersection grid, respectively, and figure 10.3(c) the part assembly.

Finally, the part intersection translates to the definition of a volume fraction in the grid elements. The ones with a value higher than 0 (intersection took place) are extracted and translated into an INP file, with the aid of a MATLAB script (annex A). The INP file characterizes the node and element sets which allow for the definition of a solid mesh in Abaqus (see figure 10.4).

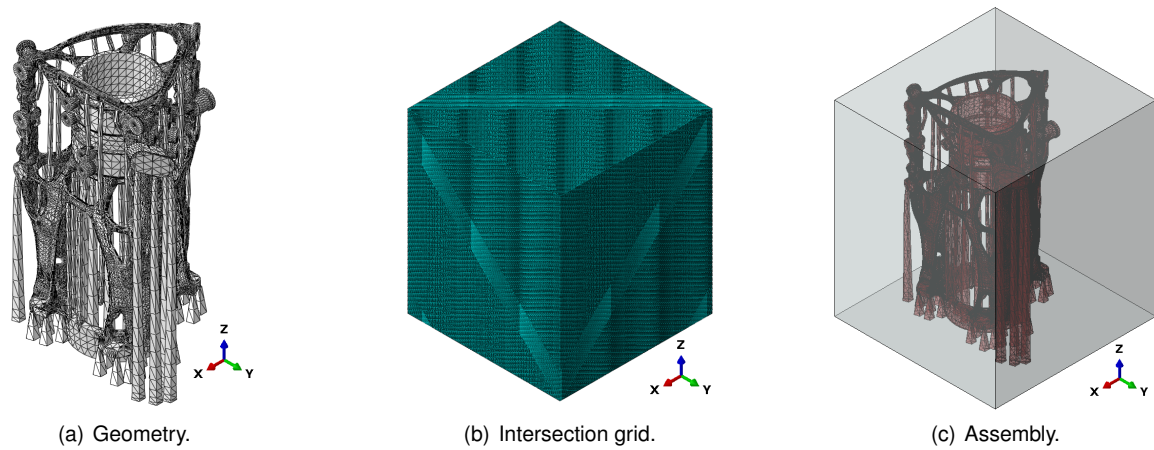


Figure 10.3: Geometry voxelization process.

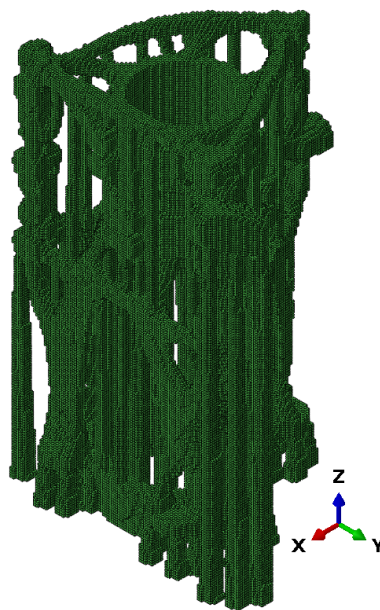


Figure 10.4: Voxel-based geometry.

10.2 Model preparation

With the geometry for the AM simulation constructed, both thermal and structural analysis models are set to be defined in Abaqus. In addition to the printed part itself, a substrate part is defined. It is connected to the printed part through the tie constraint.

10.2.1 Material properties

The widely used Ti-6Al-4V ELI is used, namely with the powder size of $60\mu\text{m}$, as its application in aerospace and defence sectors has been proven, and is used by the AM250 Renishaw machine [76]. The good material's specific strength properties deem it a good candidate material to achieve weight savings in loaded structures. The powder composition is showcased in table 10.1.

The remaining material properties of interest are defined in tables 10.2 and 10.3, and figures 10.5.

The anisotropy yield assumption is defined through the stress ratios of the material, obtained from [76]. As a

Material	Ti	Al	V	Fe	O	C	N	H	Y	Res.
%	Bal.	5.5~6.5	3.5~4.5	≤0.25	≤0.13	≤0.08	≤0.05	≤0.012	≤0.005	≤0.40

Table 10.1: Ti-6Al-4V ELI material composition.

Parameter	Value
Density (tonne/mm ³)	4.48E-09
Absolute zero (°C)	-273.15
Liquidus temperature (°C)	1600
Solidus temperature (°C)	1550
Latent heat of fusion (mJ/tonne)	419E9
Film coefficient (mW/mm ² °C)	0.018
Emissivity	0.201
Absorption coefficient	0.46

Parameter	Value
Stress ratio - R_{33}	0.92 [76]

Table 10.3: Ti-6Al-4V ELI mechanical properties.

Table 10.2: Ti-6Al-4V ELI thermal properties.

simplification, all ratios but R_{33} are equal to 1, while R_{33} is equal to 0.92, representing the worst case of printing direction anisotropy.

Finally, the assumption of a low-resolution requires the definition of the relaxation temperature. The value is extracted from literature as 963K [77].

10.2.2 Event series definition

Both the laser path and the recoater roller define the event series to be utilized in the low-resolution AM process simulation of the AMATHO bracket component. Autodesk Netfabb is used to define the laser path, namely with its slicing tool.

The voxelized geometry is the sliced geometry, where a layer height of 60 μ m is considered, resulting in a total of 1141 physical layers. The printing properties of interest to the laser path characterization are showcased in tables 10.4 and 10.5, with an example of the slicing in figure 10.6, where the first layer is depicted.

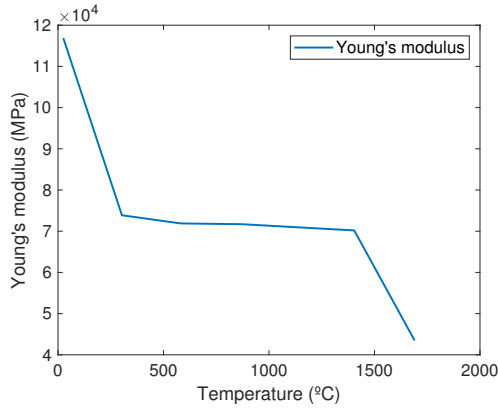
Parameter	Value
Power (W)	250
Laser speed (mm/s)	900
Jump speed (mm/s)	900

Table 10.4: Contour laser path properties.

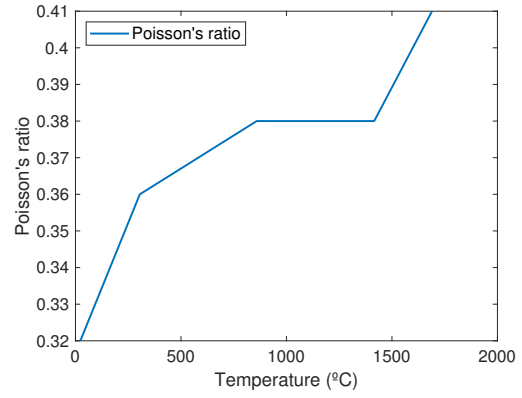
Parameter	Value
Hatching	Simple
Hatch distance (mm)	0.1
Angle increment (°)	90
Regionalisation	No
Power (W)	250
Laser speed (mm/s)	1200
Jump speed (mm/s)	1200

Table 10.5: Infill laser path properties.

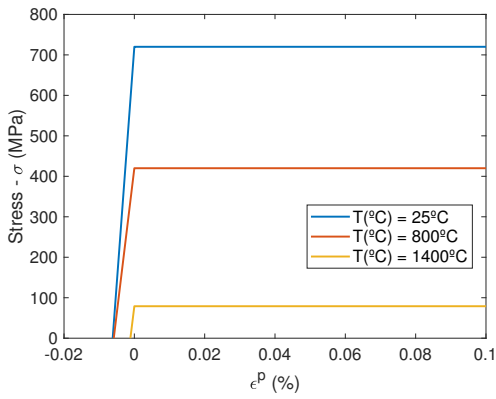
Utilizing the Matlab script in annex A, the LSR file is translated into two event series files (INP file format), one for the laser path and power characterization, and the recoater roller path. Additionally, parameters regarding the cooling process can be set in the script. Namely, the dwell and post-printing cooling times can be set, such that their impact on the simulation can be studied and optimized. Table tab:scalecvvcx has the AM process parameters



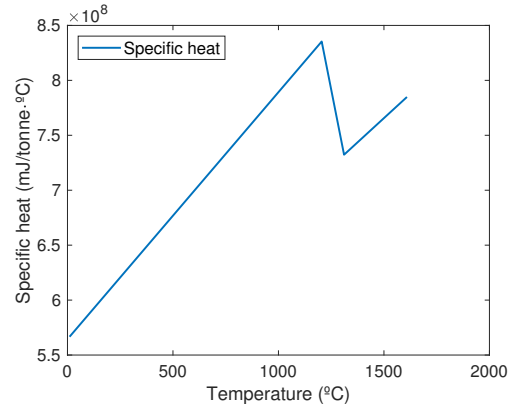
(a) Young's modulus.



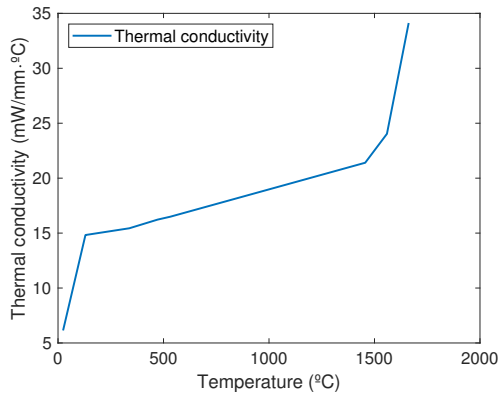
(b) Poisson's ratio.



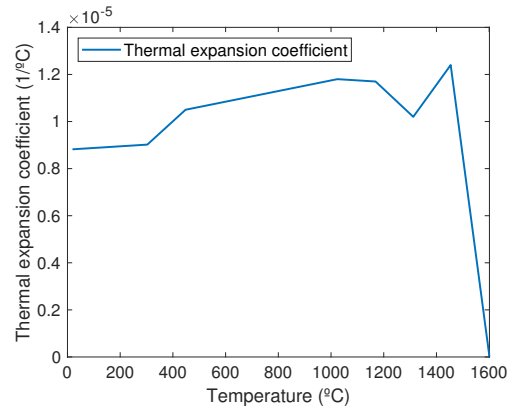
(c) Plastic behaviour.



(d) Specific heat.



(e) Thermal conductivity.



(f) Thermal expansion coefficient.

Figure 10.5: Some aircrafts.

defined in Matlab that influence the event series.

Parameter	Value
Recoater roller speed (m/s)	80
Dwell time (s)	0
Cooling duration (s)	600

Table 10.6: Recoater roller and cooling parameters.

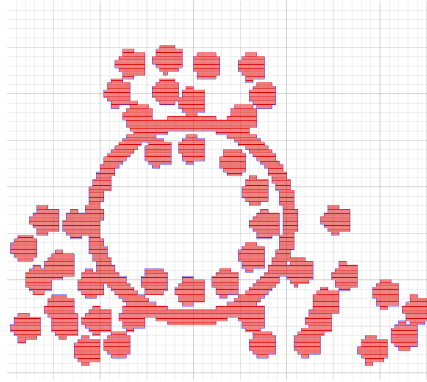
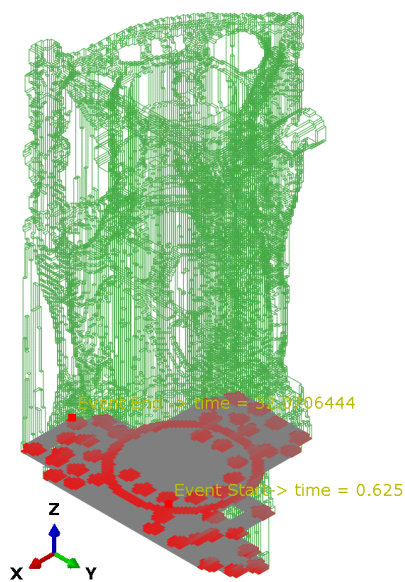
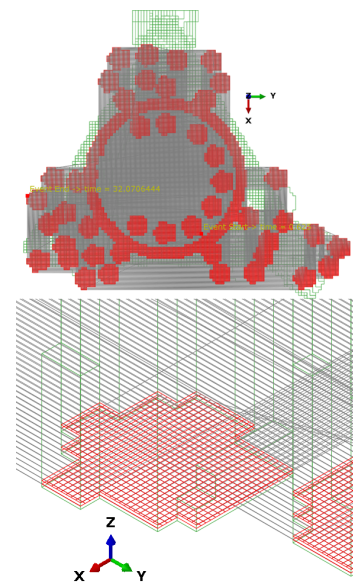


Figure 10.6: Laser path example at a single layer in Autodesk Netfabb.

As the event series files are imported into the AM modeler plug-in in Abaqus, it is possible to verify the accuracy of the files against the wireframe reference of the geometry present in the assembly. For example, in figures 10.7(a) and 10.7(b), it is showcased the path of the laser between $T = 0.625s$ (beginning of the first physical layer) and $T = 32.0706444s$ (end of the second physical layer).



(a) Isometric view.



(b) Detailed view.

Figure 10.7: Event series viewer example.

10.2.3 Meshing

The voxelization process is directly related to the ease of meshing of the part. The imported geometry is a native mesh file with regular hexahedral elements, which ensure constant good quality meshing throughout the entire part, despite the geometrical complexity of the non-voxelized geometry.

Therefore, element types for both the thermal and structural analysis are equal to the ones applied to the benchmarking simulation, as per table 10.7.

Analysis	Part	Element type
Thermal	Bracket	DC3D8
	Substrate	DC3D8
Structural	Bracket	C3D8
	Substrate	C3D8R

Table 10.7: Elements used for both the thermal and the structural simulations, per bracket and substrate parts.

10.2.4 Thermal analysis definition

The transient thermal analysis is defined by time increments at every physical layer deposition (bar the first one), and a post-printing cooling process. The total step duration is $T_{tot} = 12877.6s$.

Considering the coarse mesh size of the part, the concentrated heat source approximation is utilized, in-line with the low-resolution simulation approach.

10.2.4.1 Initial and boundary conditions

Secondly, both the initial and boundary conditions are to be set, depending on the printing process and its parameters. The substrate is heated and kept at a constant temperature, T_{sub} throughout the printing. A value of $T_{sub} = 80^{\circ}C$ is set, based on similarly defined simulations [70]. Identically, the pre-heating temperature of the substrate is kept the same at $T_{pre} = 80^{\circ}C$, this being an initial temperature field defined over the entire substrate part. Finally, the powder temperature is defined as $T_{part} = 40^{\circ}C$, the temperature field is applied to the entire printed part, and initialized per element as they are progressively activated.

10.2.4.2 Cooling effects

The progressive cooling mechanisms described in [70] are similarly applied, with the main process parameters being defined in table 10.8. The film coefficient, h , is set based on typical values defined in previous studies (REF) as $18W/m^2K$. Identically, the emissivity, ϵ , takes the value of 0.201 [68].

Parameter	Value
Ambient Temperature ($^{\circ}C$)	40
Radiation coefficient	0.201
Film coefficient (W/m^2K)	18

Table 10.8: Process cooling parameters.

10.2.5 Structural analysis definition

10.2.5.1 Initial and boundary conditions

An encastre constraint is applied to the bottom surface of the substrate part, fixing all displacement and rotation degrees of freedom. The structural model is defined by a non-linear static analysis step, based on the transient temperature field output from the thermal analysis.

10.2.5.2 Support removal

Despite the implementation of the support removal step during the benchmarking simulation, the complexity of the present geometry requires the definition of an algorithm to automate the selection of the elements to be removed, which has not been the focus of the present thesis. Therefore, the separation of the part itself from the support structure, and both from the building plate are omitted.

However, its implementation is highly suggested for future work expanding on the workflow presented in this thesis.

10.3 Results and discussion

10.3.1 Structural simulation results

The temperature evolution data from the thermal simulation is the basis upon which the mechanical field is defined. However, as previously noted, the temperature field at each node also takes into account the initial relaxation temperature field applied to the nodes of the newly activated elements.

The complexity of both the geometry and the AM process itself lead to an intricate structural behaviour, namely in the cylindrical hydraulic region in the center. As seen in figure 10.8 of the post-printing displacement magnitude field, this region contracts towards its center (see figure 10.9, where the contraction toward the center is seen in both cross-sections of the displacement with respect to x and y-directions, respectively), effectively driving the displacement of the connecting frame. The center of the hydraulic cylinder sees a contraction at a peak of 0.1172mm. Additionally, the geometric complexity and connectivity results in a non-linear variation of the displacement in the printing direction. The part registers its highest displacement peak at a hydraulic system node, with a value of 0.6277mm. The region showcases hanging material with no support structure present, which further justifies its careful and thorough implementation and positioning. Similarly, the oil ports also showcase high distortion, born from the lack of supporting material for the steep hanging angle present.

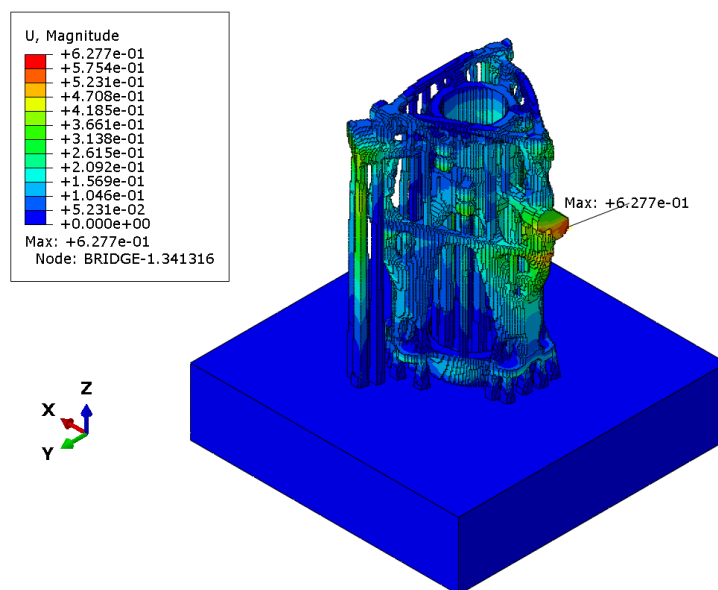


Figure 10.8: Displacement results of the AM process simulation applied to the bracket component.

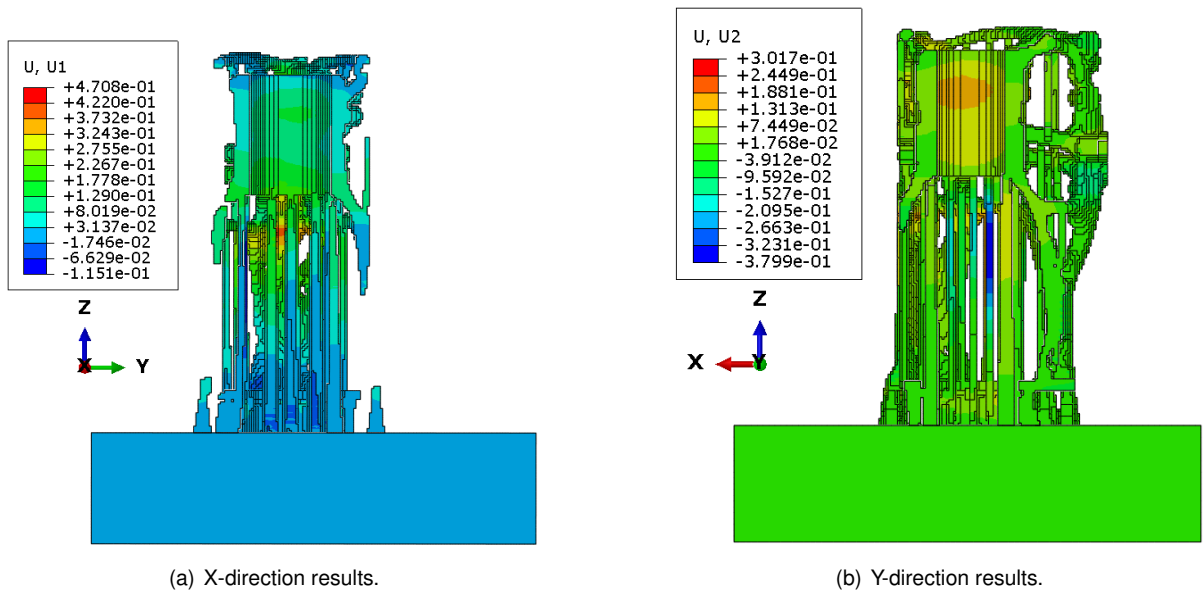


Figure 10.9: Cross section view to highlight the contraction happening in the central cylindrical hydraulic system region.

The illustration of the residual stress is done with the von Mises stress distribution (depicted in figure 10.10). However, the low-resolution nature of the simulation has its drawbacks showcased in the stress distribution, namely the presence of stress concentration points at the surface of the part, result of the voxelization process, causing sharp corners at the part's surface. The region is, as expected, subjected to larger temperature gradients due to the close contact to the cooler elements, such as the inert gas. While displacement is less susceptible to mesh changes, the stress field showcases larger sensitivity, leading to the observed stress peaks at single nodes.

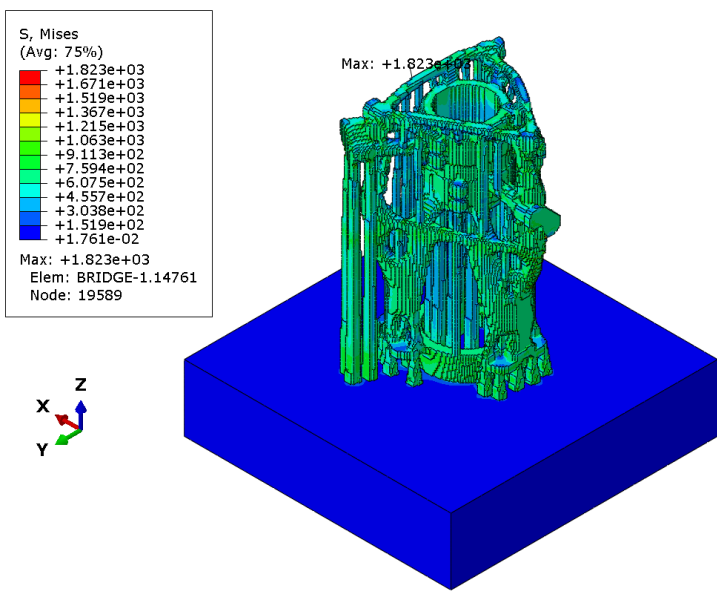


Figure 10.10: Von mises stress results of the AM process simulation applied to the bracket component.

Chapter 11

Conclusions

The bracket provided by Leonardo is compared against the the structural optimization results with the aim of providing a performance comparison between both.

Firstly, it has been shown that the MIMP interpolation method, while based off the SIMP method, achieves both convergence, and better results for the given design constraints. In fact, as suggested by REF, a mass dependent analysis benefits from the use of MIMP, which is in fact verifiable. Comparing the results from trial cases 1 and 2, both volume minimization problems with displacement constraints, they exhibit the same geometry result, bar the increase of gray elements in trial case 2 (from 1.32% with SIMP, to 3.97 with MIMP). Considering the design interpretation is at the discretion of the engineer, the proposed solution being similar at a grand scale, means both are designed the same way.

However, the introduction of the frequency constraint in trial cases 3 and 4 highlights the differences between both interpolation methods. As SIMP struggles to achieve convergence and the frequency constraint oscillates throughout the optimization process, MIMP converges with fair swiftness. By comparing all results, MIMP is chosen to be the interpolation method to be used for the remaining trial cases.

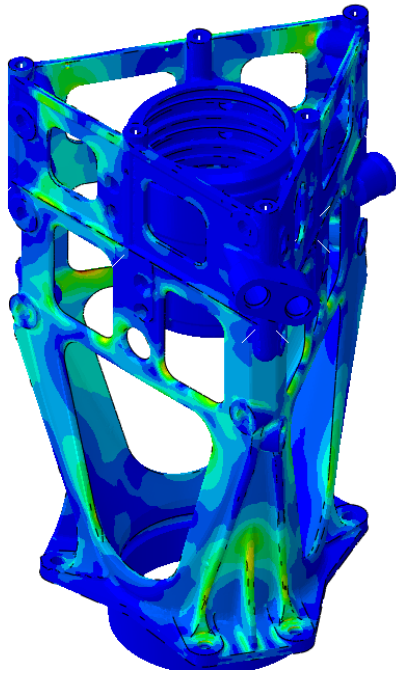
Finally, the introduction of further design constraints in the optimization task results in stark geometrical changes, namely in trial case 6, which showcases a frame surrounding each face, in order to comply with relative displacement constraints between mounting bolts. Considering this, and the final mass of 2.29% the original component, trial case 6 is deemed the best design and the one to undergo further analysis.

In conclusion, regarding the topology optimization process, it has proven to be a powerful tool, able to achieve concrete (1-0) designs, despite the complex set of constraints and objective function. Moreover, volume minimization optimization allows to achieve a design with a mass lower than the original component, while directly targeting real engineering design requirements.

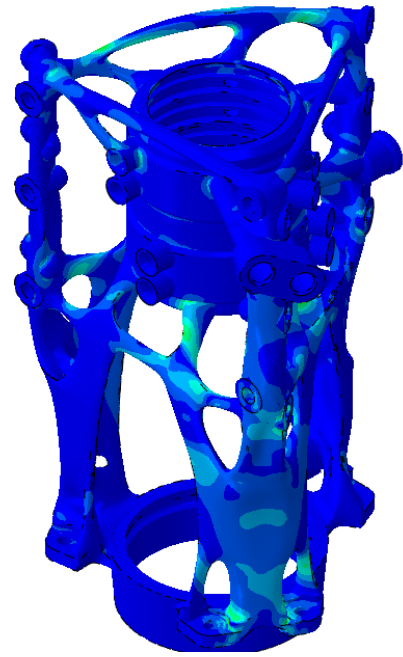
Shape optimization compliments the design process by tackling another set of design requirements, namely the ones pertaining to static strength and fatigue life. However, due to the time frame of this thesis, durability is not considered, but its inclusion is possible within TOSCA, namely with a fe-safe analysis.

The resulting geometry from the applied structural optimization process is seen in figures REF, REF, and 11.3(a), where the stress, displacement magnitude and z-direction displacement fields are showcased, respectively, and compared to the current component performance counterpart. The results are obtained for proof load case under bending. it should also be noted that the scale utilized is entirely identical between the two components.

The final design represents a 5.12% mass decrease compared to the current bracket, while clearly achieving better performance. In fact, while the first frequency is close to the minimum limit (at 1.022 the value), the displace-

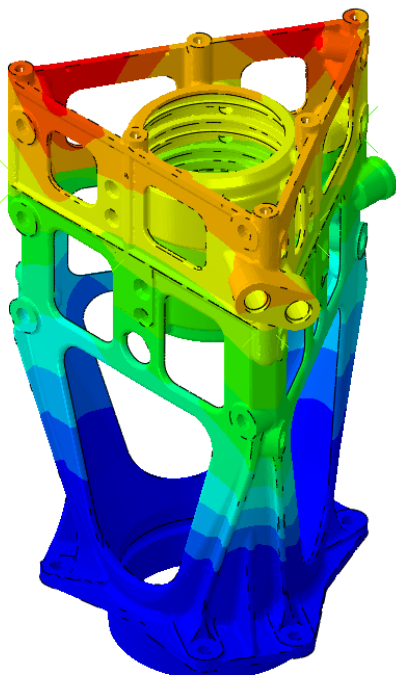


(a) Current design.

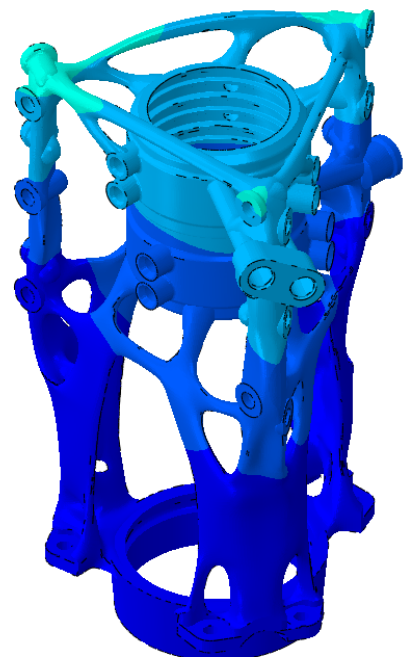


(b) Proposed design.

Figure 11.1: Von mises stress results comparison under proof bending 1 load case.



(a) Current design.



(b) Proposed design.

Figure 11.2: Displacement magnitude results comparison under proof bending 1 load case.

ment performance gap is clear and there is room to further improve it and achieve a larger mass reduction. Such reduction is largely attributed to the DfAM methodology employed, as it allows for a single component design, not limited to typical manufacturing constraints that do not allow for *organic-looking* designs as the one presented.

Finally, an AM process simulation is performed to assess the part's distortion and residual stresses post-printing. It also showcases the application of a series of pre-processing tools, namely voxelization, and Autodesk Netfabb for

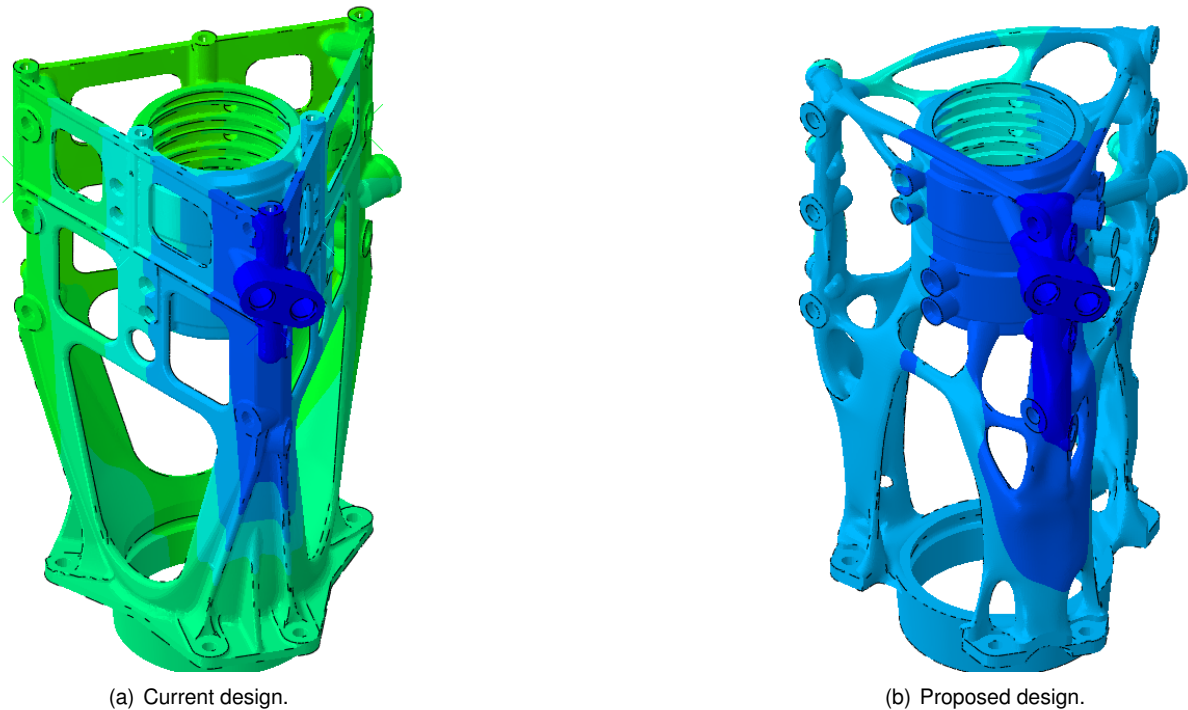


Figure 11.3: Z-direction displacement results comparison under proof bending 1 load case.

the laser path and support structure definition. The workflow presented also eases the implementation of parameter optimization tools that target specific complex engineering problems and geometries, ultimately leading to a control loop based on the simulation results at each printing point.

The results obtained from the AM simulation lack clarity without experimental results to compare against. However, the distortion observed is in fact higher in regions with unsupported overhanging material, as expected. While beyond the scope of this thesis, the presented method allows for a quick transition to a more detailed, high-resolution AM simulation with the scalability of both the the meshing and time intervals considered.

11.1 Future Work

Further work related to structural optimization is suggested to be carried out in the following topics:

- Further investigate the application of the MIMP interpolation method, and its comparison with SIMP, namely with a set of simple geometries and setups that allow for a clearer understanding of the technique's working principle;
-
- Complement the topology optimization analysis with a stress constraint related to the static strength requirements;
- Provide an extensive comparison between the resulting geometries from a minimum compliance with volume constraint topology optimization problem, and the volume minimization formulation employed in this thesis. Namely compare the performance gap between the two, for a minimum compliance problem with a volume constraint equal to the solution of the volume minimization problem;

- Regarding the implementation of DfAM constraints, explore the introduction of overhanging angle constraints based on the AM technology to be utilized;
- Further shape optimization steps are suggested to be employed, namely to further reduce mass and integrate durability analysis and fatigue life improvement. The software fe-safe allows for the fatigue analysis to be exported to Tosca, where the durability may be used as a design objective;
- Inclusion of lattice structures in the component design interpretation and evaluation of its performance.

Finally, regarding the additive manufacturing simulation, the following future work topics are suggested:

- Expand the thermal-mechanical simulation to a thermal-mechanical-metallurgical one, which takes into consideration material phase changes, important to predict Ti-4AL-6V ELI behaviour under the complex heating and cooling conditions;
- Increase the geometrical size of the part to a dimension equal or close to the real one, as more computational resources are made available;
- Carry out the printing of the proposed design to compare the experimental results to the ones obtained from the AM simulation;
- Ultimately, further AM simulations to better understand the impact of simplifications made, and how to optimally define the analysis. Such is suggested cause the scope of the thesis regarding these simplifications is fairly limited, focusing on presenting the tools to aid with the pre-processing, but allowing for both improvement and high customization.

Bibliography

- [1] IATA, International Air Transport Association. Iata's 20-year air passenger forecast. <https://www.iata.org/en/pressroom/pr/2018-10-24-02/>. [Online; accessed April 2022].
- [2] ATAG, Air Transport Action Group. Aviation: Benefits beyond borders. Technical report, 2017.
- [3] European Commission and Directorate-General for Mobility and Transport and Directorate-General for Research and Innovation. Flightpath 2050: Europe's vision for aviation. Technical report, Publications Office, 2011.
- [4] Clean sky 2 - clean aviation joint undertaking. <https://www.clean-aviation.eu/>. [Online; accessed April 2022].
- [5] R. Larsson. Methodology for topology and shape optimization: Application to a rear lower control arm. Master's thesis, Chalmers University of Technology, 2016.
- [6] R. Willner, S. Lender, A. Ihl, C. Wilsnack, S. Gruber, A. Brandão, L. Pambaguian, R. Mirko, E. Lopez, F. Brueckner, and C. Leyens. Potential and challenges of additive manufacturing for topology optimized spacecraft structures. *Journal of Laser Applications*, 32:032012, 08 2020.
- [7] A. Clausen. *Topology Optimization for Additive Manufacturing*. PhD thesis, 2016.
- [8] T. Vaneker, A. Bernard, G. Moroni, I. Gibson, and Y. Zhang. Design for additive manufacturing: Framework and methodology. *CIRP Annals*, 69(2):578–599, 2020.
- [9] Y. Huang, M. C. Leu, J. Mazumder, and A. Donmez. Additive Manufacturing: Current State, Future Potential, Gaps and Needs, and Recommendations. *Journal of Manufacturing Science and Engineering*, 137(1), 2015.
- [10] Dassault Systèmes. Simulia user assistance online, 2022.
- [11] G. Galilei. *The Discourses and Mathematical Demonstrations Relating to Two New Sciences*. 1638.
- [12] A. G. M. Michell. Lviii. the limits of economy of material in frame-structures. *Philosophical Magazine Series 1*, 8:589–597, 1904.
- [13] P. Christensen and A. Klarbring. *An introduction to structural optimization*. Solid Mechanics and its Applications. Springer Netherlands, 1 edition, 2009.
- [14] U. Kirsch. *Structural optimization: fundamentals and applications*. Springer Berlin Heidelberg, 1993.
- [15] M. Bendsoe and O. Sigmund. *Topology Optimization: Theory, Methods, and Applications*. Springer Berlin Heidelberg, 2003.

- [16] M. P. Bendsøe and N. Kikuchi. Generating optimal topologies in structural design using a homogenization method. *Computer Methods in Applied Mechanics and Engineering*, 71(2):197–224, 1988.
- [17] G. Allaire, F. Jouve, and A.-M. Toader. A level-set method for shape optimization. *Comptes Rendus Mathématique*, 334(12):1125–1130, 2002.
- [18] G. Allaire, F. Jouve, and A.-M. Toader. Structural optimization using sensitivity analysis and a level-set method* 1. *Journal of Computational Physics*, 194:363–393, 02 2004.
- [19] M. Wang, X. Wang, and D. Guo. A level set method for structural topology optimization. *Computer Methods in Applied Mechanics and Engineering*, 192:227–246, 2003.
- [20] Y. Xie and G. Steven. A simple evolutionary procedure for structural optimization. *Computers and Structures*, 49(5):885–896, 1993.
- [21] G. I. N. Rozvany, M. Zhou, and T. Birker. Generalized shape optimization without homogenization. *Structural Optimization*, 4:250–252, 1992.
- [22] F. Goetz. Simulia update release 2021 news in toasca, isight and fe-safe. <https://events.3ds.com/simulia-update-release-2021-news-tosca-isight-and-fe-safe>. [Online; accessed April 2022].
- [23] K. Svanberg. The method of moving asymptotes—a new method for structural optimization. *International Journal for Numerical Methods in Engineering*, 24:359–373, 1987.
- [24] G. Allaire. A review of adjoint methods for sensitivity analysis, uncertainty quantification and optimization in numerical codes. *Ingénieurs de l'Automobile*, 836:33–36, 2015.
- [25] G. Yi and Y. Sui. Different effects of economic and structural performance indexes on model construction of structural topology optimization. *Acta Mechanica Sinica*, 31, 09 2015.
- [26] A. Cséfalvi. Volume minimization with displacement constraints in topology optimization of continuum structures. *International Journal of Optimization in Civil Engineering*, 6:447–453, 02 2016.
- [27] A. Díaz and O. Sigmund. Checkerboard patterns in layout optimization. *Structural Optimization*, 10:40–45, 1995.
- [28] C. S. Jog and R. B. Haber. Stability of finite element models for distributed-parameter optimization and topology design. *Computer Methods in Applied Mechanics and Engineering*, 130(3):203–226, 1996.
- [29] O. Sigmund and J. Petersson. Numerical instabilities in topology optimization: A survey on procedures dealing with checkerboards, mesh-dependencies and local minima. *Structural Optimization*, 16:68–75, 08 1998.
- [30] E. Holmberg, B. Torstenfelt, and A. Klarbring. Stress constrained topology optimization. *Structural and Multidisciplinary Optimization*, 48:33–47, 2013.
- [31] J. Chen, V. Shapiro, K. Suresh, and I. Tsukanov. Shape optimization with topological changes and parametric control. *International Journal for Numerical Methods in Engineering*, 71:313 – 346, 2007.
- [32] R. Meske, J. Sauter, and E. Schnack. Nonparametric gradient-less shape optimization for real-world applications. *Structural and Multidisciplinary Optimization*, 30:201–218, 2005.

- [33] J. Beaman. Historical perspective. *JTECIWTEC Panel Report on Rapid Prototyping in Europe and Japan*, pages 737–760, 1997.
- [34] D. L. Bourella, J. J. Beaman, M. C. Leub, and D. W. Rosenc. History of additive manufacturing and the 2009 roadmap for additive manufacturing : Looking back and looking ahead. 2009.
- [35] S. S. D. D. T. Pham. *Rapid Manufacturing The Technologies and Applications of Rapid Prototyping and Rapid Tooling*. Springer, 2001.
- [36] P. A. L. Ciraud. Method and device for manufacturing any articles from any mettable material - de2263777a1 patent. <https://patents.google.com/patent/DE2263777A1/en>. [Online; accessed April 2022].
- [37] W. Associates. Wohlers report 2021. <https://wohlersassociates.com/2021report.htm>. [Online; accessed April 2022].
- [38] T. Nakagawa. Blanking tool by stacked bainite steel plates. *Press Technique*, pages 93–101, 1979.
- [39] M. K. Thompson, G. Moroni, T. Vaneker, G. Fadel, R. I. Campbell, I. Gibson, A. Bernard, J. Schulz, P. Graf, B. Ahuja, and F. Martina. Design for additive manufacturing: Trends, opportunities, considerations, and constraints. *CIRP Annals*, 65(2):737–760, 2016.
- [40] M. Shellabear and O. Nyrhilä. Dmls-development history and state of the art. *Proceedings of the 4th LANE 2004, Sept. 22.-24, 2004*.
- [41] S. Chen. *Investigation of FEM numerical simulation for the process of metal additive manufacturing in macro scale*. PhD thesis, 2019.
- [42] A. Busachi, J. Erkoyuncu, P. Colegrove, F. Martina, C. Watts, and R. Drake. A review of additive manufacturing technology and cost estimation techniques for the defence sector. *CIRP Journal of Manufacturing Science and Technology*, 19:117–128, 2017.
- [43] D. Pham and R. Gault. A comparison of rapid prototyping technologies. *International Journal of Machine Tools and Manufacture*, 38(10):1257–1287, 1998.
- [44] B. S. Ian Gibson, David Rosen. *Additive manufacturing technologies: 3D printing, rapid prototyping, and direct digital manufacturing*. Springer, second edition, 2014.
- [45] A. S. F27982. *Standard terminology for additive manufacturing technologies*. ASTM International, West Conshohocken, PA, 2012.
- [46] M. Ahsan. Modelling and analysis of laser direct metal deposition of ti-6al-4v alloy. 2011.
- [47] S. M. Thompson, L. Bian, N. Shamsaei, and A. Yadollahi. An overview of direct laser deposition for additive manufacturing; part i: Transport phenomena, modeling and diagnostics. *Additive Manufacturing*, 8:36–62, 2015.
- [48] E. Yasa. Understanding adopting selective laser melting of metallic materials. *Solid Freeform Fabrication 2018: Proceedings of the 29th Annual International*, 2018.

- [49] Y. Zhang, Q. Chen, G. Guillemot, C.-A. Gandin, and M. Bellet. Numerical modelling of fluid and solid thermomechanics in additive manufacturing by powder-bed fusion: Continuum and level set formulation applied to track- and part-scale simulations. *Comptes Rendus Mécanique*, 346(11):1055–1071, 2018. Computational methods in welding and additive manufacturing Simulation numérique des procédés de soudage et fabrication additive.
- [50] K. Hu, S. Jin, and C. C. Wang. Support slimming for single material based additive manufacturing. *Computer-Aided Design*, 65:1–10, 2015.
- [51] J.-P. Järvinen, V.-P. Matilainen, X. Li, H. Piili, A. Salminen, I. Mäkelä, and O. Nyrhilä. Characterization of effect of support structures in laser additive manufacturing of stainless steel. *Physics Procedia*, 56:72–81, 08 2014.
- [52] U. M. Dilberoglu, B. Gharehpapagh, U. Yaman, and M. Dolen. The role of additive manufacturing in the era of industry 4.0. *Procedia Manufacturing*, 11:545–554, 2017. 27th International Conference on Flexible Automation and Intelligent Manufacturing, FAIM2017, 27-30 June 2017, Modena, Italy.
- [53] K. Söderhjelm. Topology optimization for additive manufacturing. Master’s thesis, Lund University, 2017.
- [54] R. Condruz, G. Matache, A. Paraschiv, T. Frigioescu, and T. Badea. Microstructural and tensile properties anisotropy of selective laser melting manufactured in 625. *Materials*, 13:4829, 2020.
- [55] S. Nervi. A mathematical model for the estimation of the effects of residual stresses in aluminum plates /. 2005.
- [56] B. O’Neal. Swanson school of engineering and aerotech partner to refine metal additive manufacturing with fast computational modeling. <https://3dprint.com/146259/swanson-aerotech-metal-am/>, 2016. [Online; accessed April 2022].
- [57] P. Withers. Residual stress and its role in failure. *Reports on Progress in Physics*, 70:2211, 2007.
- [58] A. Cattenone, S. Morganti, and F. Auricchio. Basis of the lattice boltzmann method for additive manufacturing. *Archives of Computational Methods in Engineering*, 27:1109–1133, 2020.
- [59] B. Cheng, S. Shrestha, and K. Chou. Stress and deformation evaluations of scanning strategy effect in selective laser melting. *Additive Manufacturing*, 2016.
- [60] M. Zain-ul abdein, D. Nelias, J.-F. Jullien, and D. Deloison. Prediction of laser beam welding-induced distortions and residual stresses by numerical simulation for aeronautic application. *Journal of Materials Processing Technology*, 209:2907–2917, 2009.
- [61] F. Kong and R. Kovacevic. 3d finite element modeling of the thermally induced residual stress in the hybrid laser/arc welding of lap joint. *Journal of Materials Processing Technology - J MATER PROCESS TECHNOL*, 210:941–950, 2010.
- [62] W. Sames, F. List, S. Pannala, R. Dehoff, and S. Babu. The metallurgy and processing science of metal additive manufacturing. *International Materials Reviews*, 61:1–46, 2016.
- [63] National Institute of Standards and Technology. 2018 am-bench test descriptions for amb2018-01. <https://www.nist.gov/ambench/amb2018-01-description>, 2018. [Online; accessed April 2022].

- [64] C. I. Shchurova. A methodology to design a 3d graphic editor for micro-modeling of fiber-reinforced composite parts. *Advances in Engineering Software*, 90:76–82, 2015.
- [65] D. Fradl, J. Panditaratne, J. Bi, R. Fu, and V. Oancea. Finite element simulation of the multi jet fusion (mjf™) process using abaqus. 2017.
- [66] M. Gouge and P. Michaleris. *Thermo-Mechanical Modeling of Additive Manufacturing*. Elsevier, 2018.
- [67] R. Deering. Additive manufacturing part level distortion sensitivity analysis within abaqus on a thin-walled , tubular structure. 2018.
- [68] M. J. Abarca. Development of a low fidelity process model for additive manufacturing. Master’s thesis, Faculdade de Engenharia da Universidade do Porto, 2020.
- [69] L. Levine, B. Lane, J. Heigel, K. Migler, M. Stoudt, T. Phan, R. Ricker, M. Strantza, M. Hill, F. Zhang, J. Seppala, E. Garboczi, E. Bain, D. Cole, A. Allen, J. Fox, and C. Campbell. Outcomes and conclusions from the 2018 am-bench measurements, challenge problems, modeling submissions, and conference. *Integrating Materials and Manufacturing Innovation*, 28, 2020.
- [70] Y. Yang, M. Allen, T. London, and V. Oancea. Residual strain predictions for a powder bed fusion inconel 625 single cantilever part. *Integrating Materials and Manufacturing Innovation*, 8:294–304, 2019.
- [71] Special Metals Corporation. Inconel alloy 625 material data. 2013.
- [72] G. Baffioni. Static and fracture analysis of an additively manufactured aeronautical part. Master’s thesis, Politecnico di Milano, 2019.
- [73] J. Qu, P. Blau, T. Watkins, O. Cavin, and N. Kulkarni. Friction and wear of titanium alloys sliding against metal, polymer, and ceramic counterfaces. *Wear*, 258:1348–1356, 2005.
- [74] Design of steel structures, part 1-8: Design of joints. 2005.
- [75] G. R. Garbujo. Topology optimization of a helicopter servo bracket for am production. Master’s thesis, Politecnico di Milano, 2020.
- [76] Renishaw. Ti6al4v eli-0406 powder for additive manufacturing. 2017.
- [77] P. M. Michael Gouge. *Thermo-Mechanical Modeling of Additive Manufacturing*. Butterworth-Heinemann, first edition, 2017.

Appendix A

Event series Matlab script

```
1 %% PARAMETERS INTIALIZATION %%
2
3 %y is roller movement direction
4
5 initialT = X;
6 initialX = X;
7 initialY = X;
8 initialZ = X; %layer size
9 initiallaserPower = 0;
10 initialrollerState = 0;
11 rollerSpeed = X; %(m/s)
12 rollerDistance = X; %(mm)
13 dwellIT = 0; %(s)
14 durationCooling = X; %(s)
15
16 fileName = ('Filename.lsr ');
17
18 %% READ CLI FILE %%
19
20 fid=fopen(fileName);
21 tline = fgetl(fid);
22 i = 1;
23 while ~feof(fid)
24     if tline(1) ~= '#' %# represent comments
25         Data(i) = textscan(tline, '%f ');
26         i = i + 1;
27     end
28     tline = fgetl(fid);
29 end
```

```

30 fclose(fid);
31
32 %% ROLLER AND LASER EVENT SERIES %%
33
34 % Roller as soon as the infill is done (same time)
35 % Cooling period after each hatching period
36
37 xrollerOn = 0;
38 xrollerOff = rollerDistance;
39 yroller = 0;
40 sizeData = length(Data);
41 layerHeight = 0;
42 rollerI = 0;
43 laserI = 1;
44 stepI = 1;
45 currentT = 0;
46
47 for dataJ = 1:sizeData
48     %Laser Coordinates (beginning of laser path)
49     laserX(laserI) = Data{1, dataJ}(5);
50     laserY(laserI) = Data{1, dataJ}(6);
51     laserZ(laserI) = Data{1, dataJ}(7);
52
53     %Laser Coordinates (ending of laser path)
54     laserX(laserI + 1) = Data{1, dataJ}(8);
55     laserY(laserI + 1) = Data{1, dataJ}(9);
56     laserZ(laserI + 1) = Data{1, dataJ}(10);
57
58     if Data{1,dataJ}(7) ~= layerHeight
59         if dataJ ~= 1
60             timeStep(stepI) = currentT + (rollerDistance/rollerSpeed)/2;
61             stepI = stepI + 1;
62         end
63
64         layerHeight = Data{1, dataJ}(7);
65
66         % Roller passage happens right after
67         rollerI = rollerI + 1;
68
69         rollerT(rollerI) = currentT;
70         rollerState(rollerI) = 1;
71

```

```

72     rollerX(rollerI) = initialX;
73     rollerY(rollerI) = initialY;
74     rollerZ(rollerI) = layerHeight;
75
76     rollerX(rollerI + 1) = rollerDistance;
77     rollerY(rollerI + 1) = initialY;
78     rollerZ(rollerI + 1) = layerHeight;
79
80     % Start new laser passage right after roller
81     currentT = currentT + (rollerDistance/rollerSpeed);
82
83     rollerI = rollerI + 1;
84     rollerT(rollerI) = currentT;
85     rollerState(rollerI) = 0;
86
87     laserT(laserI) = currentT + dwellIT;
88
89     else
90         %Time between consecutive points based on laser speed
91         bx = laserX(laserI - 1);
92         by = laserY(laserI - 1);
93         bz = laserZ(laserI - 1);
94         ex = laserX(laserI);
95         ey = laserY(laserI);
96         ez = laserZ(laserI);
97
98         distancePath = sqrt((ex-bx)^2 + (ey-by)^2 + (ez-bz)^2);
99         speedPath = Data{1, dataJ - 1}(12);
100
101         currentT = currentT + distancePath/speedPath;
102         laserT(laserI) = currentT;
103     end
104
105
106     laserState(laserI) = Data{1, dataJ}(1) * 1000;
107
108     % Distance Traveled
109     laserD = sqrt((laserX(laserI + 1) - laserX(laserI))^2 + (laserY(laserI + 1) -
110         laserY(laserI))^2 + (laserZ(laserI + 1) - laserZ(laserI))^2);
111     currentT = currentT + (laserD/Data{1, dataJ}(12));
112     laserT(laserI + 1) = currentT;

```

```

113     laserState(laserI + 1) = 0;
114
115     laserI = laserI + 2;
116 end
117
118 %% Final cooling process
119
120 timeStep(stepI) = currentT;
121 for p = 1:3
122     timeStep(stepI + p) = timeStep(stepI + p - 1) + durationCooling;
123 end
124
125 %% Print to each file
126
127 formatSpecLaser = "%f,%f,%f,%f,%f\n";
128 formatSpecRoller = "%f,%f,%f,%f,%f\n";
129
130 [~, fileName, ~] = fileparts(fileName);
131 nameLaser = append(fileName, "_Laser.inp");
132 nameRoller = append(fileName, "_Roller.inp");
133 nameStep = append(fileName, "_Step");
134
135 laserID = fopen(nameLaser, 'w');
136 rollerID = fopen(nameRoller, 'w');
137
138 for k = 1:length(laserT)
139     fprintf(laserID, "%f, ", laserT(k));
140     fprintf(laserID, "%f, ", laserX(k));
141     fprintf(laserID, "%f, ", laserY(k));
142     fprintf(laserID, "%f, ", laserZ(k));
143     fprintf(laserID, "%f\n", laserState(k));
144 end
145
146 for l = 1:length(rollerT)
147     fprintf(rollerID, "%f, ", rollerT(l));
148     fprintf(rollerID, "%f, ", rollerX(l));
149     fprintf(rollerID, "%f, ", rollerY(l));
150     fprintf(rollerID, "%f, ", rollerZ(l));
151     fprintf(rollerID, "%f\n", rollerState(l));
152 end
153
154 timeStep = timeStep';

```

```
155 save(nameStep, 'timeStep');  
156  
157 fclose('all');
```


Appendix B

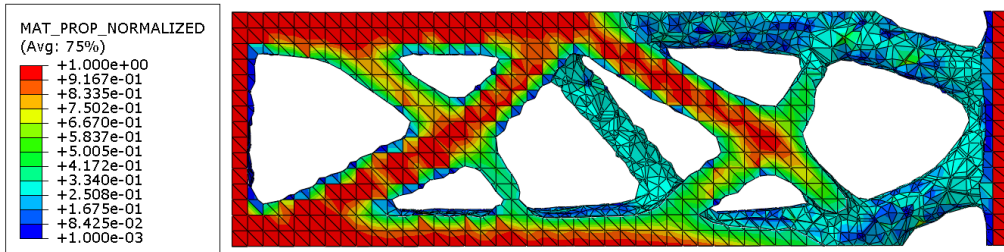
Topology optimization beam solutions

B.1 Mesh influence results

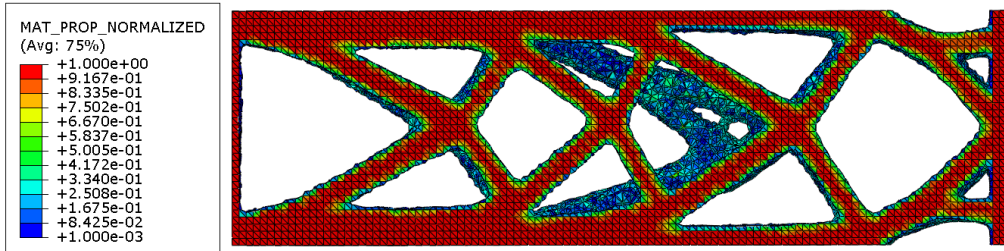
Element type	Number of elements	Cycles	Objective function	Volume fraction
C3D8	2250	81	7727.26	0.3494
	4020	48	7300.76	0.3496
	15150	45	6378.65	0.3495
	43043	44	6070.14	0.3492
	120000	45	5868.76	0.3490
C3D8R	2250	83	9071.69	0.3499
	4020	37	7602.55	0.3496
	15150	36	6521.47	0.3496
	43043	43	6114.73	0.3494
	120000	44	5902.36	0.3490
C3D20	2250	36	11735.96	0.3492
	4020	38	7786.30	0.3492
	15150	44	6548.34	0.3493
	21978	48	6452.06	0.3493
	28500	44	6284.07	0.3492
C3D4	14200	50	8460.67	0.3495
	29132	54	7639.91	0.3498
	95755	47	6807.25	0.3495
	129458	44	6672.42	0.3493
C3D10	14200	44	8964.24	0.3499
	29132	63	8208.30	0.3496
	53451	52	7225.63	0.3496
	95755	47	7126.50	0.3496
	129458	46	6885.77	0.3496

Table B.1: Tabular data of mesh influence on topology optimization of a cantilever beam results.

B.1.1 Mesh influence solution geometries

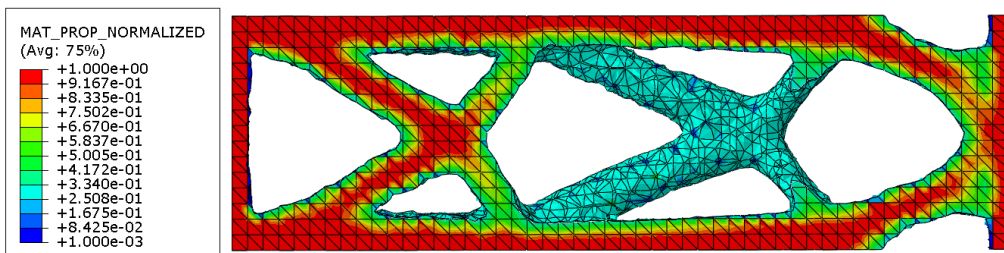


(a) 2250 elements.

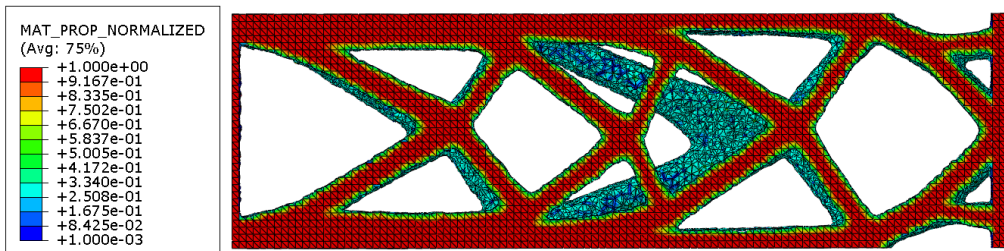


(b) 120000 elements.

Figure B.1: C3D8 resulting geometries.

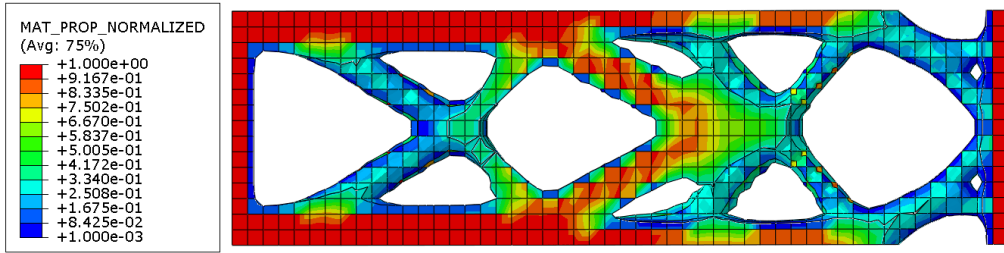


(a) 2250 elements.

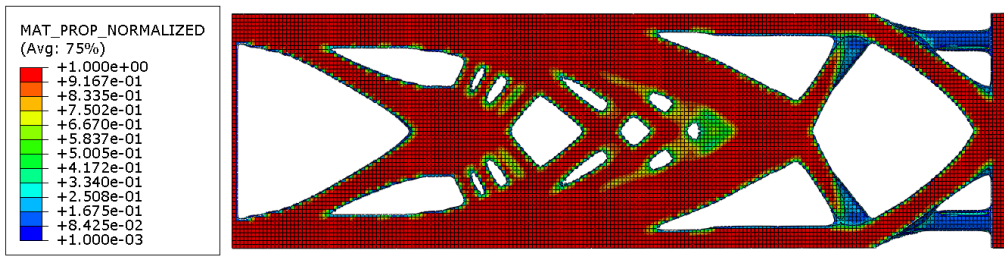


(b) 120000 elements.

Figure B.2: C3D8 resulting geometries.

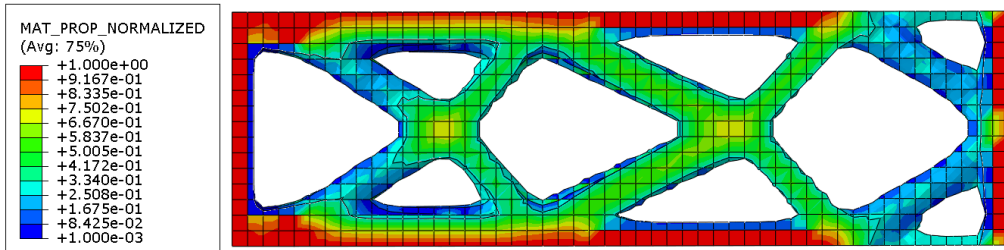


(a) 2250 elements.

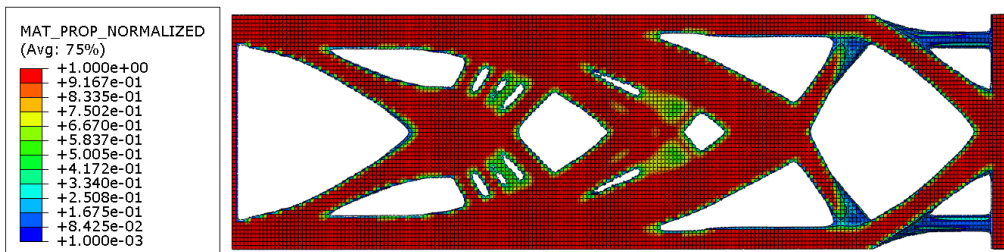


(b) 28500 elements.

Figure B.3: C3D8 resulting geometries.

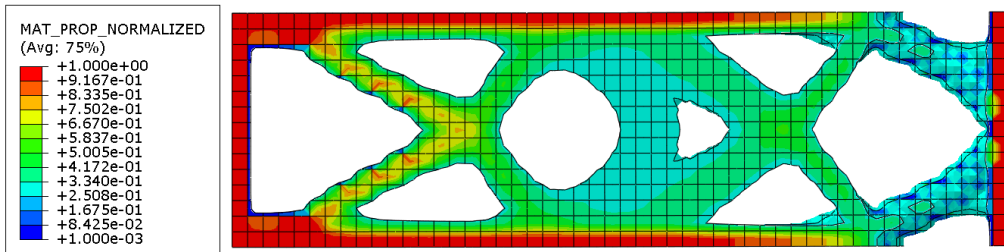


(a) 14200 elements.

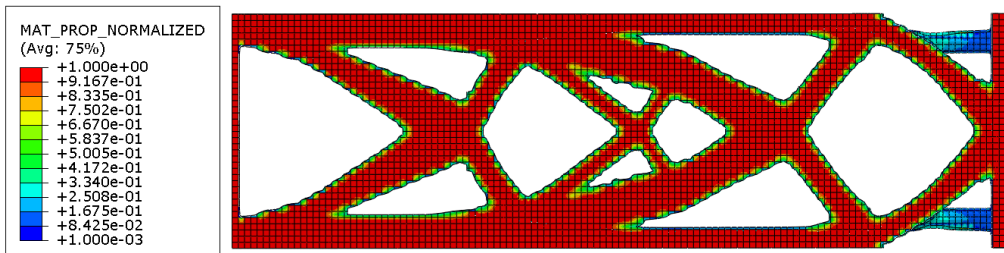


(b) 129458 elements.

Figure B.4: C3D8 resulting geometries.



(a) 14200 elements.



(b) 129458 elements.

Figure B.5: C3D8 resulting geometries.

B.2 Material interpolation scheme comparison results

B.2.1 Mesh influence results

Algorithm	Number of elements	Cycles	Volume fraction	Normalized displacement	Gray elements percentage (%)
SIMP	800	44	0.4966	1.0003	15.88
	3000	45	0.4593	0.9999	12.37
	6149	45	0.4329	0.9997	7.97
	12000	45	0.4167	0.9999	6.18
	33300	44	0.4008	0.9998	4.25
	75000	46	0.3929	0.9998	3.40
	300000	47	0.3813	0.9998	2.00
MIMP	800	62	0.4562	0.9988	8.62
	3000	47	0.4184	0.9988	5.17
	6149	50	0.4105	0.9998	4.78
	12000	52	0.3973	1.0006	3.27
	33300	50	0.3905	0.9998	2.63
	75000	50	0.3826	0.9998	2.00
	300000	54	0.3737	1.0000	1.30

Table B.2: Tabular data of mesh influence on topology optimization comparison between SIMP and MIMP interpolation schemes.

B.2.1.1 Mesh influence solution geometries

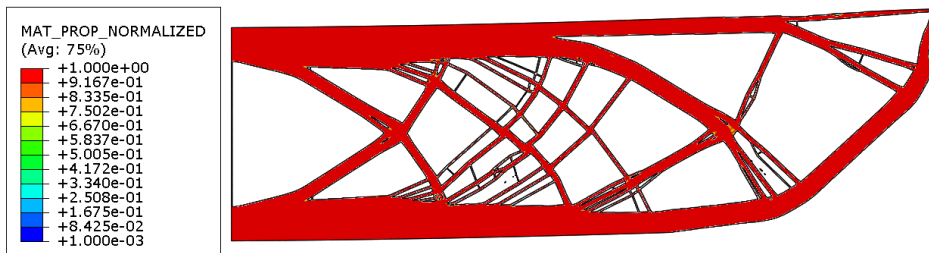
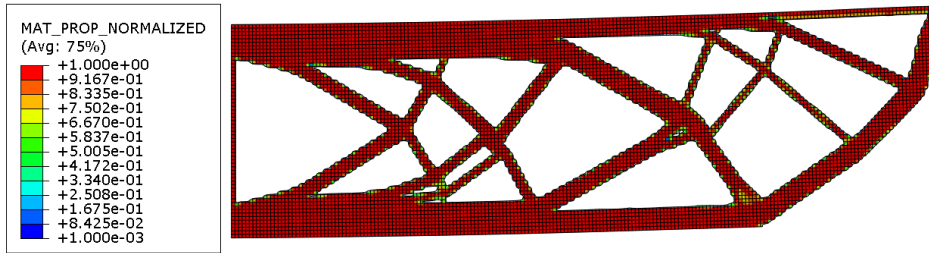
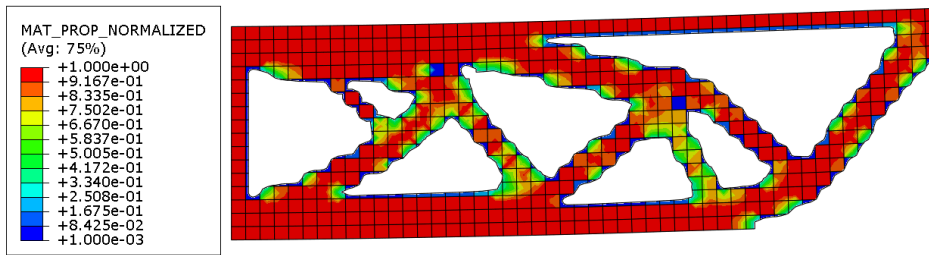


Figure B.6: SIMP mesh influence resulting geometries.

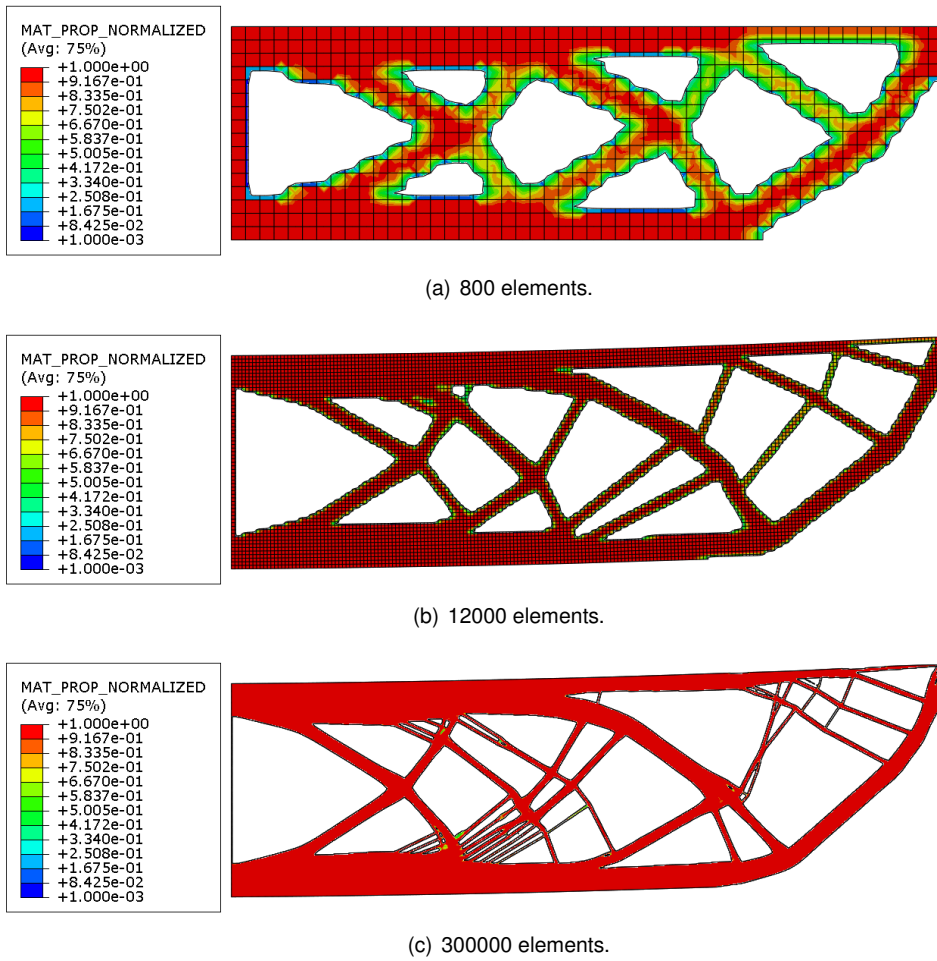


Figure B.7: MIMP mesh influence resulting geometries.

B.2.2 Frequency design response influence results

Algorithm	Frequency constraint (Hz)	Cycles	Volume fraction	Normalized displacement	Frequency (Hz)	Gray elements percentage (%)
SIMP	6	45	0.3600	0.9999	14.10	6.15
	7	45	0.3600	0.9999	14.10	6.12
	8	45	0.3596	0.9998	14.04	6.09
	9	40	0.3660	0.9999	13.86	2.33
	10	40	0.3673	0.9998	13.84	2.21
	11	40	0.3673	0.9998	13.84	2.21
MIMP	6	51	0.3361	0.9997	9.19	3.07
	7	45	0.3378	0.9992	9.41	3.23
	8	47	0.3367	1.0000	9.24	3.33
	9	46	0.3382	0.9999	9.61	2.98
	10	46	0.3382	0.9999	9.61	2.98
	11	46	0.3411	0.9997	9.56	3.33

Table B.3: Tabular data of frequency design response influence on topology optimization comparison between SIMP and MIMP interpolation schemes.

B.2.2.1 Frequency design response influence solution geometries

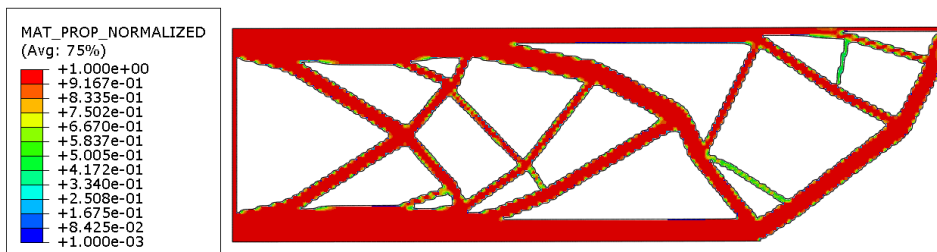
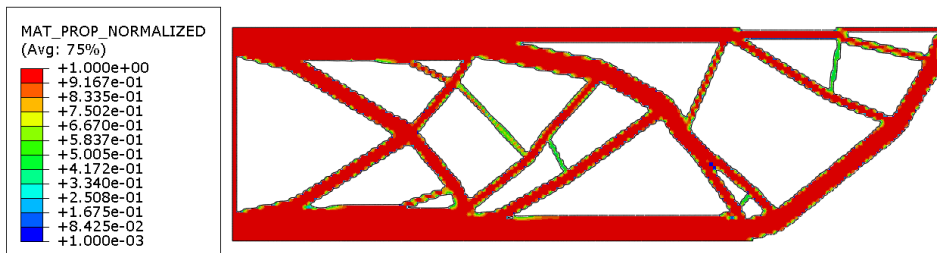
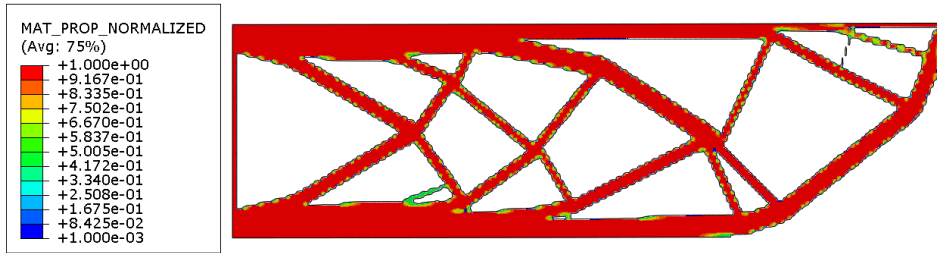
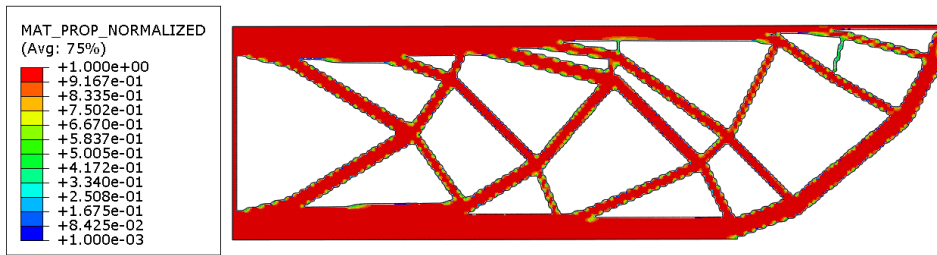
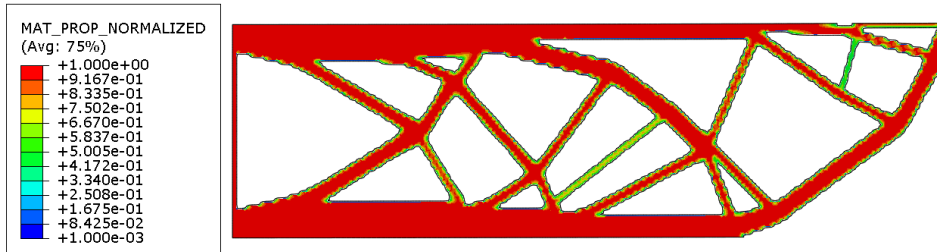
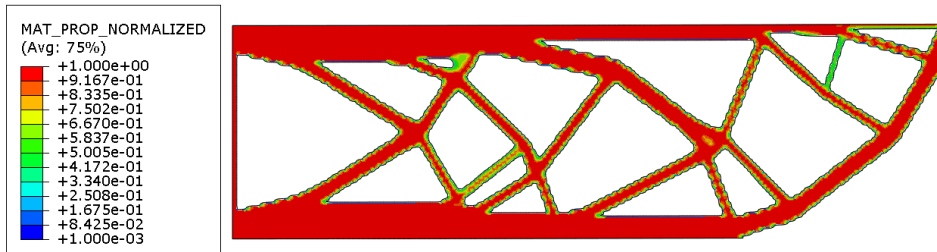


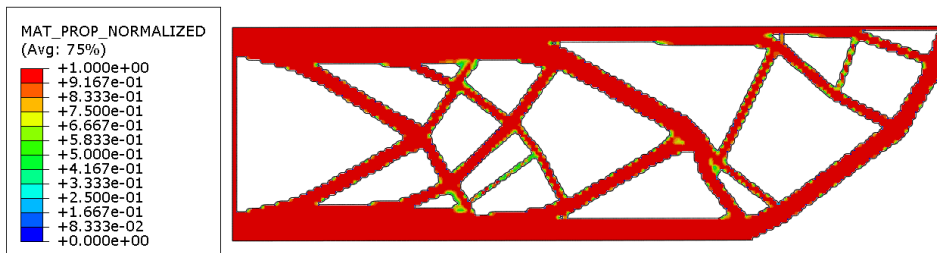
Figure B.8: SIMP frequency design response influence resulting geometries.



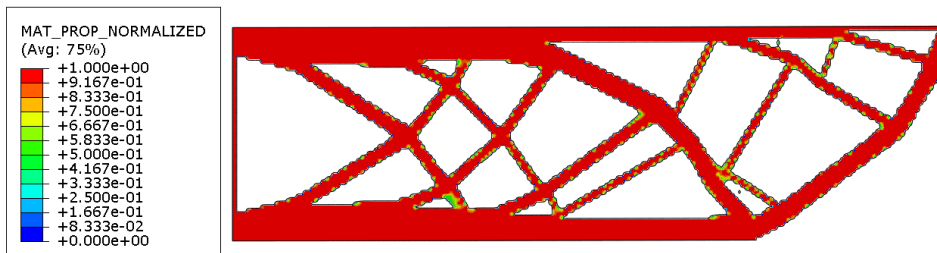
(a) 6Hz.



(b) 8Hz.



(c) 9Hz.



(d) 11Hz.

Figure B.9: MIMP frequency design response influence resulting geometries.

